

NORTHWESTERN UNIVERSITY

Chemical Functionalization of PEG-*b*-PPS Nanocarriers for Applications
in Targeted and Sustained Delivery

A DISSERTATION

SUBMITTED TO THE GRADUATE SCHOOL
IN PARTIAL FULFILLMENT OF THE REQUIREMENTS

for the degree

DOCTOR OF PHILOSOPHY

Field of Biomedical Engineering

By

Nicholas Blaise Karabin

EVANSTON, ILLINOIS

September 2019

© Copyright by Nicholas Blaise Karabin 2019
All Rights Reserved

ABSTRACT

Chemical Functionalization of PEG-*b*-PPS Nanocarriers for Applications in Targeted and Sustained Delivery

Nicholas Blaise Karabin

Nanomaterials are broadly defined as materials that exhibit at least one dimension that is less than 1,000 nm. Encompassed within nanomaterials are a class of constructs known as nanocarriers, which are applied as delivery vehicles for both encapsulated and covalently bound payloads. Poly(ethylene glycol)-*block*-poly(propylene sulfide) (PEG-*b*-PPS) is an amphiphilic block copolymer (BCP) that has been utilized for the self-assembly of a variety of nanocarriers. Since it was first described in 2001, studies concerning the chemical functionalization of PEG-*b*-PPS BCPs for the alteration of nanocarrier surface characteristics have been limited. The objective of this work was to 1) expand the pool of functionalized PEG-*b*-PPS BCPs for the preparation of nanocarriers with diverse surface characteristics and 2) to explore the potential benefits afforded by these surface functionalities in both passive targeting and sustained nanocarrier delivery. This study explores the synthesis of a variety of functionalized-derivatives of PEG-*b*-PPS and utilizes several of these BCPs for the preparation of nanocarriers. The role of PEG-*b*-PPS nanocarrier surface chemistry is explored in the context of protein adsorption and cell interactions. Finally, a proof-of-concept study depicting how nanocarrier surface chemistry can be exploited for sustained delivery is described.

An array of techniques was utilized in these investigations. Morphological and size characterization of the nanocarriers was performed prior to *in vitro* assessments of nanocarrier immunogenicity and cytotoxicity. Nanocarrier-cell associations *in vitro* were quantified via flow cytometry and explored through differences observed in the amount and composition of protein adsorbed to the nanocarrier surface. Finally, constructs for sustained nanocarrier delivery were prepared and investigated *in vivo*. Nanocarrier release was observed through intravital fluorescence imaging and cellular uptake was assessed through flow cytometric analysis.

I have developed and executed several previously unexplored synthetic pathways for the preparation of functionalized PEG-*b*-PPS. I have found that surface modification of PEG-*b*-PPS nanocarriers can impact their immunogenicity and cellular interactions, the latter highlighting the potential of using surface chemistry to tailor nanocarrier uptake. Furthermore, surface chemistry was shown to alter both the quantity and composition of adsorbed proteins. Lastly, I demonstrated that functionalized PEG-*b*-PPS nanocarriers could be the basis of a sustained nanocarrier delivery system. Therefore, I conclude that the surface functionality of PEG-*b*-PPS nanocarriers is a useful design characteristic for nanocarrier performance. Selection and successful incorporation of an appropriate chemistry can permit further construct optimization and investigation into previously unattainable applications.

ACKNOWLEDGEMENTS

There have been a lot of failures and small triumphs in the pursuit of this work. I have been fortunate to have a great support system, both professionally and personally, and I would like to take this opportunity to acknowledge all the people who have helped me through my graduate studies over the years. First, I would like to thank my committee: Dr. Neha Kamat, Dr. Patrick Kiser, and Dr. Bin Zhang. As my graduate studies have progressed, I've gained some perspective into the many responsibilities encompassed within a professorship. In addition to their responsibilities to their own labs, these professors have commitments to the students they teach and the departments they serve. As such, their time is scarce. I'm thankful that, when I chose to seek their advice or input, they were always willing to find a time to meet. Over the course of my graduate studies, they have provided valuable input on my projects and helped me to approach some of my research related problems with a new perspective.

I would like to thank my PI, Dr. Evan Scott, for without whom this chapter in my life may not have happened. I was not a highly sought-after doctoral student after my undergraduate studies. A combination of limited options and personal constraints led me to Northwestern to initially pursue a M.S. Evan gave me an opportunity in his lab at a time when my confidence was certainly at a low. He welcomed me into the team and treated me like the doctoral students starting at the same time. His patience, openness, and willingness to allow me to dictate my research path, even as a Master's student, gave me confidence that this was the career path where I belonged. I feel very fortunate to have had a PI that has always made me feel supported and heard. I am grateful for the chance that Evan took on me, and I simply hope that he feels content with the contribution I've made to his lab.

In the Scott lab, I've had the chance to work with a lot of great individuals who are not only fantastic scientists but incredible people as well. First, I'd like to thank my good friend Sean Allen. Sean: you're one of the smartest and most creative people I've met. While having you to bounce ideas off has been great, one of the best parts of this process has been getting to know you as a friend. You have a way of making even the most challenging/banal parts of the job fun, and I'm excited to see what the future holds for you. I'd like to thank Dr. Sharan Bobbala. Sharan: you're a great scientist and your passion for the work

we do is inspiring. Like Sean, your friendship made the work environment a lot of fun and I wish you nothing but the best. Next, I'd like to thank Molly Frey and Mike Vincent. Molly and Mike: while we started working together late in my time in the lab, it has been a lot of fun collaborating with both of you. I would like to thank Dr. Diana Velluto. Diana trained the first cohort of students. She was a fantastic teacher and I'm grateful for the selflessness she showed in delaying her own research to get everyone up and running. Lastly, I'm grateful for the collaborative and open work culture of the Scott lab. As such, I'd like to thank all the members: Dr. Fanfan Du, Dr. Yu-Gang Liu, Dr. Sijia Yi, Jacqueline Burke, Dina Kats, Sophia Li, Mallika Modak, and Trevor Stack. Thank you all for your help, input, and for enduring my incessant whistling!

Lastly, I've been fortunate to have a very supportive family throughout my studies. I can say for certain that the love and support I've received from my family are two of the biggest reasons I have made it this far. First, I would like to thank my parents, Anna and Dick, who have been two of the biggest influences in my life. Mom: your encouragement started me down this path at the age of seven. You raised me to be well-rounded and to appreciate the various aspects of life, and for that, I'm forever grateful. Dad: thank you for setting the example you did as a father/scientist. You brought aspects of your work home, which made talking about science a lot of fun. Your discipline and commitment to be at home for your family have shaped, in part, my understanding of what it means to be father/husband/professional and I thank you for that example. I'd like to thank my brother Alex, whose relentless pursuit of his own dreams has been an inspiration to me. Next, I would like to thank the Steffa family, particularly my parents-in-law, Cathy and Joe, and my sister-in-law, Kate. You have all rooted for me as much as anyone. Thank you for always encouraging me to follow my aspirations.

Most importantly, I'd like to thank my wife, Christine, for her endless support during this process. These six years have required you to make so many sacrifices. You gave up your life in Boston to give our relationship a chance while I pursued my M.S. You've lost out on time with family and friends at home to move here. And now that we have a daughter, the time you sacrifice with her to provide for our family is even more meaningful. Thank you for giving up so much so that I could pursue this dream. This achievement is as much your success as it is mine.

LIST OF ABBREVIATIONS

633-BCP	DyLight 633 Conjugated BCP
755-BCP	DyLight 755 Conjugated BCP
Ag ₂ O	Silver (I) Oxide
APC	Antigen Presenting Cell
BCN	Bicontinuous Nanosphere
BCP	Block Copolymer
Bn	Benzyl Group
Bn-Br	Benzyl Bromide
BODIPY	Boron-Dipyrromethene
BSA	Bovine Serum Albumin
CBA	Cytometric Bead Array
CD	Cluster of Differentiation
CDCl ₃	Deuterated Chloroform
cDCs	Classical Dendritic Cells
CH ₃ COSH	Thioacetic Acid
CH ₃ ONa	Sodium Methoxide
CIJ	Confined Impingement Jets
CMC	Critical Micelle Concentration
CO ₂	Carbon Dioxide
CryoSEM	Cryogenic Scanning Electron Microscopy
CryoTEM	Cryogenic Transmission Electron Microscopy
CXCL	C-X-C Motif Chemokine Ligand
DBCO	Dibenzocyclooctyne
DCM	Dichloromethane
Dil	1.1'-Dioctadecyl-3,3',3'-Tetramethylindocarbocyanine Perchlorate
DLS	Dynamic Light Scattering

DMF	Dimethylformamide
DMSO-d ₆	Dimethyl Sulfoxide-d ₆
DNA	Deoxyribonucleic Acid
DSA	Drop Shape Apparatus
dTHP-1 Cells	Macrophage-Like Differentiated THP-1 Cells
EDTA	Ethylenediaminetetraacetic Acid
ELS	Electrophoretic Light Scattering
EPR	Enhanced Permeation and Retention
EQ	Equivalent
ET ₃ N	Triethylamine
FBS	Fetal Bovine Serum
FM	Filomicelle
FNP	Flash Nanoprecipitation
fPEG	Hydrophilic Mass Fraction
FT-IR	Fourier Transform Infrared
G'	Storage Modulus
G''	Loss Modulus
GLC-TEM	Graphene Liquid Cell Transmission Electron Microscopy
GM-CSF	Granulocyte-Macrophage Colony-Stimulating Factor
GPC	Gel Permeation Chromatography
H&E	Haematoxylin and Eosin
H ₂ O	Water
H ₂ O ₂	Hydrogen Peroxide
HBSS	Hank's Balanced Salt Solution
He-Ne	Helium-Neon
HEPES	4-(2-Hydroxyethyl)-1-Piperazineethanesulfonic Acid)
HLA	Human Leukocyte Antigen

HPLC	High Performance Liquid Chromatography
IACUC	Institutional Animal Care and Use Committee
IFN	Interferon
IL	Interleukin
IVIS	Intravital Imaging System
K ₂ CO ₃	Potassium Carbonate
KI	Potassium Iodide
LPS	Lipopolysaccharide
MALDI	Matrix Assisted Desorption Ionization
MC	Micelle
MCP	Monocyte Chemoattractant Protein
MeO	Methoxy Group
MFI	Median Fluorescence Intensity
MHC	Major Histocompatibility Complex
miRNA	Micro RNA
MMP	Matrix Metalloproteinase
mPEG	Poly(Ethylene Glycol) Monomethyl Ether
MPS	Mononuclear Phagocyte System
mRNA	Messenger RNA
MsCl	Methanesulfonyl Chloride
MTT	3-(4,5-Dimethylthiazol-2-yl)-2,5-Diphenyltetrazolium Bromide)
MW	Molecular Weight
N ₂	Nitrogen
N ₃	Azide Group
NETs	Neutrophil Extracellular Traps
NH ₂	Amine Group
NHS	N-Hydroxysuccinimide

OD	Optical Density
OH	Hydroxyl Group
OMs	Mesylate Group
ρ	Packing Parameter
PAMPs	Pathogen-Associated Molecular Patterns
PBI	Perylene Bisimide
PBMC	Peripheral Blood Mononuclear Cell
PBS	Phosphate Buffered Saline
PC	Protein Corona
PCL	Poly- ϵ -Caprolactone
pDCs	Plasmacytoid Dendritic Cells
PDIs	Polydispersity Indices
PDS	Pyridyl Disulfide
PEG- <i>b</i> -PPS	Poly(Ethylene Glycol)- <i>block</i> -Poly(Propylene Sulfide)
PEOX	Poly(2-Ethyl 2-Oxazoline)
PGA	Poly(Glycolic Acid)
Phos	Phosphate Group
PLA	Poly(Lactic Acid)
PLGA	Poly(Lactic-co-Glycolic Acid)
PMA	Phorbol 12-Myristate 13-Acetate
POCl ₃	Phosphorous (V) Oxychloride
PPO	Poly(Propylene Oxide)
PRRs	Pattern Recognition Receptors
PS	Polymersome
PTCDA	Perylene-3,4,9,10-Tetracarboxylic Dianhydride
r.t.	Room Temperature
R848	Resiquimod

RBF	Round Bottom Flask
R _f	Relative Mobility
RNA	Ribonucleic Acid
ROIs	Regions of Interest
ROS	Reactive Oxygen Species
RPMI	Roswell Park Memorial Institute
s.d.	Standard Deviation
s.e.m.	Standard Error of the Mean
SAXS	Small Angle X-ray Scattering
SDS-PAGE	Sodium Dodecyl Sulfate Polyacrylamide Gel Electrophoresis
SEAP	Secreted Alkaline Phosphatase
siRNA	Small Interfering RNA
ssDNA	Single Stranded DNA
TA	Thioacetate Group
TCR	T Cell Receptor
TEA	Triethylamine
T _g	Glass Transition Temperature
TGF	Transforming Growth Factor
Th	Helper T
THF	Tetrahydrofuran
TLR	Toll-Like Receptor
TNF	Tumor Necrosis Factor
Treg	Regulatory T Cells
TsCl	p-Toluenesulfonyl Chloride
VS	Vinyl Sulfone Group

TABLE OF CONTENTS

Abstract	3
Acknowledgements	5
List of Abbreviations	7
Table of Contents	12
List of Figures	18
List of Table	23
 CHAPTER 1	
1. Introduction: Dissertation Overview and Literature Review	24
1.1. Dissertation Overview	24
1.1.1. Objectives.....	24
1.1.2. Dissertation Outline	24
1.2. Literature Review	25
1.2.1. Introduction to Nanomaterials	25
1.2.2. A Brief History of Self-Assembled Systems	25
1.2.3. Self-Assembly of Polymeric Nanocarriers	27
1.2.4. Amphiphilic Polymers Commonly Investigated for Biomedical Applications	28
1.2.5. Poly(ethylene glycol)- <i>block</i> -poly(propylene sulfide)	30
1.2.6. PEG- <i>b</i> -PPS Nanocarriers	33
1.2.7. Origins and Evolution of Nanocarrier-based Drug Delivery Systems	35
1.2.8. Immunobiology	37
1.2.9. The Conundrum of Targeting Antigen Presenting Cells	41
1.2.10. Nanocarrier Physicochemical Characteristics Influence Biological Identity	44
1.3. Scope of this Dissertation	45
1.4. Publication Information	45
 CHAPTER 2	
2. Synthesis of Functionally Diverse PEG- <i>b</i> -PPS BCP	47

		13
2.1.	Abstract	47
2.2.	Introduction	47
2.2.1.	PEG- <i>b</i> -PPS: Innovations and Limitations	47
2.2.2.	Synthesis of Heterotelechelic PEG	50
2.3.	Materials and Methods	51
2.3.1.	Chemicals	51
2.3.2.	Synthesis of Functionalized mPEGs	51
2.3.3.	Synthesis of Bn-PPS- <i>b</i> -PEG-OMe BCPs	52
2.3.4.	Synthesis of Heterobifunctional PEG	53
2.3.5.	Synthesis of Bn-PPS- <i>b</i> -PEG-OH BCPs	54
2.3.6.	Synthesis of Bn-PPS- <i>b</i> -PEG-VS BCPs	54
2.3.7.	Synthesis of Bn-PPS- <i>b</i> -PEG-Phos BCPs	55
2.3.8.	Synthesis of Bn-PPS- <i>b</i> -PEG-OMs BCPs	56
2.3.9.	Synthesis of Bn-PPS- <i>b</i> -PEG-N ₃ BCPs	56
2.3.10.	Synthesis of Bn-PPS- <i>b</i> -PEG-NH ₂ BCPs	57
2.3.11.	Polymer Characterization	57
2.4.	Results and Discussion	58
2.4.1.	Synthesis of Bn-PPS- <i>b</i> -PEG-OMe BCPs	58
2.4.2.	Synthesis of α -tosylate- ω -hydroxyl-PEG	64
2.4.3.	Synthesis of Bn-PPS- <i>b</i> -PEG-OH BCPs	67
2.4.4.	Synthesis of Bn-PPS- <i>b</i> -PEG-VS BCPs	68
2.4.5.	Synthesis of Bn-PPS- <i>b</i> -PEG-Phos BCPs	71
2.4.6.	Synthesis of Bn-PPS- <i>b</i> -PEG-NH ₂ BCPs	75
2.5.	Conclusion	81
2.6.	Acknowledgements	83
2.7.	Publication Information	83

CHAPTER 3

3.	Exploring Combinations of Nanocarrier Surface Chemistry and Morphology for	
	Passive Targeting	84
3.1.	Abstract	84
3.2.	Introduction	84
3.2.1.	Nanocarrier Synthetic versus Biological Identity	84
3.2.2.	Passive Targeting with PEG- <i>b</i> -PPS Nanocarriers.....	86
3.2.3.	Combining Physicochemical Characteristics to Influence Cellular Interactions ..	89
3.3.	Materials and Methods	91
3.3.1.	Chemicals	91
3.3.2.	Preparation of FMs and MCs via Thin-Film Hydration.....	91
3.3.3.	Preparation of PSs via Flash Nanoprecipitation.....	91
3.3.4.	Morphologic Confirmation via Cryogenic Transmission Electron Microscopy	91
3.3.5.	Confirmation of Nanocarrier Morphology via Small Angle X-ray Scattering	92
3.3.6.	Spherical Nanocarrier Characterization via Dynamic Light Scattering (DLS	92
3.3.7.	Zeta Potential Assessment via Electrophoretic Light Scattering (ELS)	92
3.3.8.	Endotoxin Testing	93
3.3.9.	Assessment of Nanocarrier-Induced Cytokine Secretion	93
3.3.10.	Assessment of Nanocarrier-Induced Complement Activation	93
3.3.11.	THP-1 Culture Conditions	94
3.3.12.	THP-1 Differentiation to Macrophage-like Phenotype	94
3.3.13.	Immature Dendritic Cell Differentiation from Human Monocytes	94
3.3.14.	Assessment of Nanocarrier Cytotoxicity	95
3.3.15.	Cellular Uptake of Nanocarriers <i>in vitro</i>	95
3.3.16.	Nanocarrier Incubation with and Isolation from Human Plasma	97
3.3.17.	Assessment of Total Protein Adsorption	97
3.3.18.	Quantification of relative Protein Abundances via Densitometry	98

3.4.	Results and Discussion	99
3.4.1.	Physicochemical Characterization of PEG- <i>b</i> -PPS Nanocarriers	99
3.4.2.	Assessment of the Inherent Inflammatory Activity of PEG- <i>b</i> -PPS Nanocarriers	105
3.4.3.	Uptake of PEG- <i>b</i> -PPS Nanocarriers by the MPS	110
3.4.4.	Assessment of Total Protein Adsorption	117
3.4.5.	Relative Abundances of Proteins Adsorbed to PEG- <i>b</i> -PPS Nanocarriers	121
3.5.	Conclusion	124
3.6.	Acknowledgements	125
3.7.	Publication Information	126
CHAPTER 4		
4.	Leveraging BCP Functionality for Sustained Nanocarrier Delivery	128
4.1.	Abstract	128
4.2.	Introduction	128
4.2.1.	The Case for Sustained Nanocarrier Delivery	128
4.2.2.	Limitations of Current Sustained Delivery Platforms for Nanocarriers	129
4.2.3.	Dynamic Self-assembly Behavior of BCPs	130
4.2.4.	Oxidation Sensitivity of PEG- <i>b</i> -PPS Permits Morphological Transitions	131
4.3.	Materials and Methods	132
4.3.1.	Chemicals	132
4.3.2.	Preparation of FM Assemblies	132
4.3.3.	Cryogenic Transmission Electron Microscopy (CryoTEM)	132
4.3.4.	Graphene Liquid Cell Transmission Electron Microscopy (GLC-TEM)	133
4.3.5.	Small Angle X-ray Scattering (SAXS)	133
4.3.6.	Preparation of Ethyl Eosin- and Dil-loaded FM-scaffolds	134
4.3.7.	Cryogenic Scanning Electron Microscopy (CryoSEM)	134
4.3.8.	Rheological Analysis of FM-scaffolds	135

		16
4.3.9.	Photoinduced Oxidation of FM-scaffolds <i>in vitro</i>	135
4.3.10.	Accelerated Degradation of FM-scaffolds <i>in vitro</i>	136
4.3.11.	Characterization of Released MC	136
4.3.12.	Animals	136
4.3.13.	<i>In vivo</i> MC Release from Subcutaneously Injected FM-scaffolds	137
4.3.14.	<i>In vivo</i> Degradation of Subcutaneously Injected FM-scaffolds	137
4.3.15.	Assessment of Immune Cell Biodistribution of Released MCs	138
4.3.16.	Histological Analysis	139
4.4.	Results and Discussion	139
4.4.1.	Characterization of PEG- <i>b</i> -PPS FM and their Transition to MC	139
4.4.2.	Thermodynamic Modelling of FM-to-MC Transition	145
4.4.3.	FM-scaffold Preparation and Characterization	149
4.4.4.	Oxidation of FM-scaffolds for Induced Release of MCs <i>in vitro</i>	152
4.4.5.	Release of Intact MCs from FM-scaffold <i>in vivo</i>	158
4.4.6.	Sustained FM-scaffold Release of MCs for Immune Cell Uptake	164
4.5.	Conclusion	170
4.6.	Acknowledgements	172
4.7.	Publication Information	173
 CHAPTER 5		
5.	Summary of Work and Future Directions	174
5.1.	Summary of Work	174
5.1.1.	Synthesis of Functionally Diverse PEG- <i>b</i> -PPS BCPs	174
5.1.2.	Exploring Surface Chemistry for the Passive Targeting of PEG- <i>b</i> -PPS Nanocarriers	175
5.1.3.	Leveraging Surface Functionalized Nanocarriers for Sustained Delivery	176
5.2.	Future Directions	177
5.2.1.	Additional PEG- <i>b</i> -PPS BCPs Worth Investigating	177

5.2.2.	Deconvoluting Morphology-Associated Characteristics in PEG- <i>b</i> -PPS Nanocarrier Uptake	179
5.2.3.	Research Directions for FM-scaffolds	179
5.2.4.	PEG- <i>b</i> -PPS Nanocarriers for Active Targeting	181
5.3.	Curriculum Vitae	184
	REFERENCES	188
	APPENDIX A	221

LIST OF FIGURES

Figure 1-1. Illustration of diblock copolymer configuration as a result of its packing parameter.

Figure 1-2. Relationship between nanocarrier morphology and the hydrophilic mass fraction of PEG-*b*-PPS.

Figure 1-3. Depiction of how nanocarrier physicochemical properties can indirectly influence T cell function.

Figure 2-1. Synthetic pathways used to generate methoxy group terminated PEG-*b*-PPS BCPs.

Figure 2-2. Representative ^1H NMR for mPEG₄₅-OMs in CDCl₃.

Figure 2-3. Representative ^1H NMR for mPEG₄₅-TA in CDCl₃.

Figure 2-4. Gel permeation chromatography (GPC) chromatograms of mPEG derivatives.

Figure 2-5. Synthetic pathway used to generate hydroxyl-terminated PEG-*b*-PPS BCPs.

Figure 2-6. Representative ^1H NMR for Bn-PPS₄₄-*b*-PEG₄₅-OMe in CDCl₃.

Figure 2-7. GPC chromatograms of methoxy group functionalized BCPs.

Figure 2-8. Representative ^1H NMR for PEG₄₅-OTs in DMSO-*d*₆.

Figure 2-9. GPC chromatograms of tosylate-functionalized PEG.

Figure 2-10. Representative ^1H NMR for Bn-PPS₄₄-*b*-PEG₄₅-OH in CDCl₃.

Figure 2-11. Synthetic pathways used to generate functionally diverse PEG-*b*-PPS BCPs.

Figure 2-12. Representative ^1H NMR for Bn-PPS₄₃-*b*-PEG₄₅-VS in CDCl₃.

Figure 2-13. GPC chromatograms of vinyl sulfone-functionalized BCPs.

Figure 2-14. Representative NMR spectra of Bn-PPS₃₉-*b*-PEG₂₃-Phos in CDCl₃.

Figure 2-15. GPC chromatograms of phosphate-functionalized BCPs.

Figure 2-16. Representative ^1H NMR for Bn-PPS₃₇-*b*-PEG₂₃-OMs in CDCl₃.

Figure 2-17. Representative ^1H NMR for Bn-PPS₄₃-*b*-PEG₂₃-N₃ in CDCl₃.

Figure 2-18. Representative ^{13}C NMR for Bn-PPS₄₃-*b*-PEG₂₃-N₃ in CDCl₃.

Figure 2-19. FT-IR spectra of azide- and amine-functionalized BCPs.

Figure 2-20. GPC confirmation of azide-functionalization.

Figure 2-21. Representative ^1H NMR for Bn-PPS₄₃-*b*-PEG₂₃-NH₂ in CDCl₃.

Figure 2-22. Representative ^{13}C NMR for Bn-PPS₄₃-*b*-PEG₂₃-NH₂ in CDCl₃.

Figure 2-23. GPC chromatograms for the series of BCPs used to prepare Bn-PPS₄₃-*b*-PEG₂₃-NH₂.

Figure 3-1. Cellular biodistributions of PEG-*b*-PPS nanocarriers following intravenous administration.

Figure 3-2. Cellular biodistributions of PEG-*b*-PPS nanocarriers following subcutaneous administration.

Figure 3-3. Schematic of PEG-*b*-PPS BCPs and the corresponding nanocarriers formed.

Figure 3-4. Synthetic pathway used to generate methoxy, hydroxyl, or phosphate terminated BCPs.

Figure 3-5. CryoTEM micrographs with overlaid histograms of particle hydrodynamic diameters for PSs and MCs.

Figure 3-6. Morphologic characterization of PEG-*b*-PPS nanocarriers.

Figure 3-7. Zeta potential measurements of PEG-*b*-PPS nanocarriers.

Figure 3-8. PEG-*b*-PPS nanocarrier-induced secretion of inflammatory cytokines.

Figure 3-9. Individual donor cytokine profiles following 4 and 20 h incubations of nanocarrier formulations with whole blood.

Figure 3-10. PEG-*b*-PPS nanocarrier-induced complement activation.

Figure 3-11. Cytotoxicity assessment of nanocarrier formulations with THP-1 monocytes.

Figure 3-12. Conditions and process flow for *in vitro* uptake studies.

Figure 3-13. Assessment of nanocarrier agglomeration upon protein adsorption.

Figure 3-14. Cellular uptake of nanocarriers in the absence or presence of plasma proteins.

Figure 3-15. Quantification of total adsorbed protein and zeta potential changes following plasma incubation.

Figure 3-16. Quantification and identification of adsorbed protein following plasma incubation.

Figure 4-1. Graphical depiction of a composite nanocarrier-hydrogel system.

Figure 4-2. Schematic of propylene sulfide oxidation.

Figure 4-3. Synthetic pathway used to generate PEG-*b*-PPS BCPs used in Chapter 4.

Figure 4-4. Characterization of PEG-*b*-PPS FMs and visualization of micelle budding.

Figure 4-5. Additional cryoTEM micrographs of micelle budding.

Figure 4-6. Graphene liquid cell-TEM micrographs capture FM-to-MC budding in real time.

Figure 4-7. Confirmation of the FM-to-MC transition through small angle X-ray scattering (SAXS).

Figure 4-8. Thermodynamic modeling and interfacial measurements of oxidation based cylinder-to-sphere transitions.

Figure 4-9. ¹H NMR confirmation of PEG-*b*-PPS oxidation for DSA experiments.

Figure 4-10. Graphical representation of crosslinked FM-scaffolds.

Figure 4-11. Rheological characterization of PEG-*b*-PPS FM-scaffolds.

Figure 4-12. CryoSEM confirms FMs maintain their cylindrical structure upon crosslinking.

Figure 4-13. Graphical depiction of the *in vitro* photo-oxidation of ethyl eosin-loaded FM-scaffolds.

Figure 4-14. Loading efficiency of ethyl eosin within FMs.

Figure 4-15. Characterization of MCs released from ethyl eosin-loaded PEG-*b*-PPS FM-scaffolds *in vitro*.

Figure 4-16. Light-induced degradation of ethyl eosin-loaded PEG-*b*-PPS FM-scaffolds *in vitro*.

Figure 4-17. H₂O₂ induced degradation of Dil-loaded PEG-*b*-PPS FM-scaffolds *in vitro*.

Figure 4-18. Graphical depiction of modular PEG-*b*-PPS FM-scaffold preparation for *in situ* scaffold crosslinking and *in vivo* delivery.

Figure 4-19. CryoTEM confirmation of FM morphology for DyLight incorporating structures.

Figure 4-20. Intravital fluorescence imaging (IVIS) of cumulative MC release over 7 days.

Figure 4-21. *Ex vivo* manipulation of an *in situ* crosslinked FM-scaffold.

Figure 4-22. Cellular colocalization of encapsulated and covalently attached dyes suggest intact MC release *in vivo*.

Figure 4-23. Additional flow cytometric analysis from the colocalization experiment.

Figure 4-24. Complete IVIS image set for 28-day *in vivo* degradation study.

Figure 4-25. *In vivo* sustained release from *in situ* crosslinked FM-scaffolds over one month.

Figure 4-26. Additional flow cytometric analysis of the immune cell populations of the draining lymph nodes from the 28-day *in vivo* degradation study.

Figure 4-27. Additional flow cytometric analysis of the immune cell populations of the spleen, liver, and inguinal lymph nodes from the 28-day *in vivo* degradation study.

Figure 4-28. Histological analysis of the injection site.

Figure 4-29. Comparison of mouse masses between treatments over the course of *in vivo* degradation study.

Figure 5-1. Proposed alternative synthetic pathway for preparing amine-functionalized PEG-*b*-PPS BCPs.

Figure 5-2. Flow cytometric analysis for the *in vitro* cell uptake of peptide-conjugated nanocarriers.

Figure A-1. Determination of the protein:polymer ratio for use in the protein adsorption studies.

Figure A-2. Identification of a protein concentration assay with minimal interference by PEG-*b*-PPS polymer.

Figure A-3. Human plasma protein concentration and calibration curves used for the A660 assay.

Figure A-4. Ultracentrifugation of plasma proteins without nanocarriers.

Figure A-5. Representative calibration curves used to determine the molecular weight of stained protein species.

LIST OF TABLES

Table 2-1. Summary of innovative PEG-*b*-PPS BCPs for enhanced nanocarrier function.

Table 2-2. Summary of PEG syntheses.

Table 2-3. Summary of MeO-BCP syntheses used for nanocarrier formation.

Table 2-4. Summary of BCP syntheses used for polymersome formation.

Table 2-5. Summary of BCP syntheses used for filomicelle formation.

Table 2-6. Summary of BCP syntheses used for micelle formation.

Table 3-1. Physicochemical characteristics of spherical nanocarriers.

Table 3-2. Physicochemical characteristics of cylindrical nanocarriers.

CHAPTER 1

Introduction: Dissertation Overview and Literature Review

1.1. Dissertation Overview

1.1.1. Objectives

Since first being synthesized and described by the Hubbell lab in 2001, poly(ethylene glycol)-*block*-poly(propylene sulfide) (PEG-*b*-PPS) has been actively studied and investigated for applications in drug and vaccine delivery. Innovative alterations to the originally described block copolymer (BCP) have largely focused on the hydrophobic block, and as such, alterations to the hydrophilic block, and consequently, the surface of self-assembled PEG-*b*-PPS nanocarriers, have been limited. This work details the design and execution of previously unexplored synthetic pathways for the preparation of functionally diverse PEG-*b*-PPS BCPs and investigates a select few of these PEG-*b*-PPS BCPs for applications in passive targeting and sustained delivery.

1.1.2. Dissertation Outline

Chapter 1 will provide the reader with an overview of concepts central to the work described within and will include a discussion on polymer-based nanoparticulate delivery systems with a focus on PEG-*b*-PPS nanocarriers. A short overview describing the study of self-assembled systems will be followed by an introduction to the amphiphile characteristic often used to describe or predict the aggregate morphology of BCPs. Lastly, a brief introduction on immunobiology will be provided, which will be of importance in understanding how nanocarriers are identified and cleared *in vivo* and how nanocarrier physicochemical characteristics can be shaped to govern their cellular interactions. Chapter 2 will detail my efforts in expanding the variety of functional groups that can be incorporated on the hydrophilic terminus of PEG-*b*-PPS. Chapter 3 concerns how combinations of the physicochemical characteristics of PEG-*b*-PPS nanocarriers, namely morphology and surface chemistry, can be used to achieve differential uptake in human immune cells *in vitro*. Changes in nanocarrier uptake are explored along with changes to the biological identity of the nanocarriers following their exposure to human plasma. Chapter 4 explores how

the preparation of PEG-*b*-PPS nanocarriers displaying synthetic moieties can be leveraged for the development of a sustained nanocarrier delivery platform. Finally, Chapter 5 provides a summary of my doctoral work and introduces some future directions that may be of interest to those working on PEG-*b*-PPS.

1.2. Literature Review

1.2.1. Introduction to Nanomaterials

Nanotechnology is a steadily growing area of focus that has permeated into a diverse range of disciplines that spans across engineering and into the physical and life sciences. As a result of this expansion into varying fields, terminologies concerning nanotechnology and its products, nanomaterials, have experienced definitional multiplicity leading to debate over how such technologies should be classified. Regulatory and governmental agencies have defined nanomaterials as those materials that exhibit one or more dimensions between 1 and 100 nm [1], striking general agreement with the material sciences community that has gravitated toward sub-100 nm sizes to describe nanoscale materials [2]. But, researchers whose focus is geared toward the life sciences have applied a broader definition describing nanomaterials as those materials exhibiting one dimension that is less than 1,000 nm [2, 3]. The broad definition of nanomaterials encompasses a diverse array of constructs that include hard or solid core nanoparticles, such as metallic nanoparticles [4] or quantum dots [5], as well as soft nanocarriers, which include lipid and polymer-based systems. Within this dissertation, I will limit the scope of our discussion to soft nanocarriers that exhibit a single dimension that is less than 1,000 nm as I introduce both the history of and the central concepts governing their self-assembly.

1.2.2. A Brief History of Self-Assembled Systems

Molecular self-assembly is an omnipresent process that is involved in many of our day-to-day tasks. From the surfactants that form soap bubbles when we clean to the phospholipids that compose our cell membranes, self-assembly is an integral process in our lives. Molecular self-assembly is the spontaneous organization of predefined components through non-covalent interactions that results in the formation of a well-defined structure [6, 7]. In the instance of nanocarrier self-assembly, the predefined

component is an amphiphile. Amphiphiles are molecules that exhibit defined regions that are either polar or non-polar [8]. As a general principle, polar molecules are soluble in polar solvents and non-polar molecules are soluble in non-polar solvents [8]. As such, molecules like amphiphiles, that contain both polar and non-polar regions, will orient themselves in such a way that they minimize the interaction of a given region with its anti-solvent [8]. As this dissertation will focus on the self-assembly of amphiphiles in aqueous environments, I will utilize the terms hydrophilic, or “water-loving,” and hydrophobic, or “water-fearing,” to describe their polar and non-polar regions, respectively [9].

Some of the simplest molecular examples of amphiphiles include phospholipids and surfactants, a term derived from “surface active agents.” Surfactants, which include sodium lauryl sulfate, are often encountered in our daily lives as components of household cleaning products and shampoos [10]. Surfactant self-assembly has been observed and studied since the early 20th century. In 1913, James McBain coined the term “micelle” to describe the surfactant aggregates that form in and alter the bulk properties of soap solutions [11, 12]. From McBain’s pioneering work, research efforts initially focused on aggregate characterization and the identification of the diverse morphologies that could be prepared [12, 13]. By the 1970s, a quantitative thermodynamic understanding of why surfactant micelles form had been achieved [12, 14-16]. And just as the self-assembly behavior of surfactant and lipid systems began to be understood, advancements in polymerization techniques, namely living anionic polymerization, permitted the preparation of synthetic block copolymers (BCPs) [17]. BCPs are an established class of copolymer that consist of at least two chemically distinct monomers that are segregated into discrete segments (i.e. blocks) within the same macromolecule [18]. These blocks may differ significantly in their chemical nature, and like their lipid counterparts, BCPs can be composed of distinct hydrophilic and hydrophobic segments. As such, amphiphilic BCPs can also undergo self-assembly in aqueous solutions [19]. While amphiphilic BCPs have been observed to form comparable nanostructures to previously established surfactant systems [20, 21], they exhibit certain characteristics that make them advantageous in comparison to their surfactant and lipid analogues. In general, the higher molecular weight of BCP systems with respect to lipids has been attributed to altering the physicochemical characteristics of their self-assembled structures [22, 23]. These alterations, which include increased mechanical toughness [22] and decreased permeability [24], can be

beneficial for drug delivery applications. Furthermore, the versatility, amenability to post-polymerization modification, and structural diversity presented by BCPs afford the experimenter with the opportunity to design and tailor at the material level in an effort to control the characteristics of the self-assembled structure [18]. These advantages coupled with the continued strides made in both synthetic and preparative techniques, ensure that BCPs remain an actively studied and highly promising avenue for applications within the drug delivery space.

1.2.3. Self-Assembly of Polymeric Nanocarriers

The aqueous self-assembly behavior of amphiphilic BCPs, like surfactants, is driven in part by the hydrophobic effect. When a single BCP molecule exhibits two regions with antithetical affinities for water, the molecule will be reoriented so that water can maximize its interactions with itself [14, 25]. In doing so, the water molecules experience a gain in entropy [26]. In the process of water maximizing its self-interactions, the amphiphilic molecule's hydrophobic region is shielded either through its interaction with a nonaqueous interface (i.e. air) or its interaction with like-structured molecules. For the latter interaction to occur, the concentration of the amphiphile must exceed a minimum threshold known as the critical micelle concentration (CMC), which may also be defined at the critical association constant for polymeric micelles [27]. At concentrations below the CMC, BCPs exist as molecularly dissolved unimers, or individual BCP molecules. At concentrations equal to or greater than the CMC, the BCP exhibits aggregate behavior wherein multimolecular micelles exist in equilibrium with unimers [27]. Lower BCP CMC values, associated with more stable systems, are correlated with increased hydrophobic chain lengths [28] and the hydrophobicity of the core forming block [29].

Amphiphilic BCPs have been observed to self-assemble into a diverse array of nanoscale morphologies. Commonly observed morphologies include spherical micelles (MCs) [29, 30], cylindrical micelles known as filomicelles (FMs) [31], vesicles known as polymersomes (PSs) [22, 23, 32], and cubic structures called polymeric bicontinuous nanospheres [33, 34]. The morphology assumed by the BCP system is dictated by a reduction in free energy realized through the stretching of the hydrophobic block that comprises the nanostructure core, the interfacial tension that exists between the core and surrounding

solvent, and the repulsion between hydrophilic polymer blocks that comprise the corona [35]. These parameters are influenced through the formation method used to prepare the nanostructure, solution conditions, and, of course, the BCP chemistry and architecture [36].

Researchers have utilized the packing parameter or critical packing factor (p), a dimensionless number originally applied to assess the structure of self-assembled lipids in solution, to ascertain why specific BCPs self-assemble into certain morphologies. The packing parameter is defined as:

$$p = \frac{V}{a_o l_c}$$

Where V represents the volume of the hydrophobic domain, a_o is the surface area of the hydrophilic moiety, and l_c the critical length of the hydrophobic segment [37-39]. In lipid systems, defined value ranges of p correspond to the formation of inverted structures, lamellae/vesicles, cylinders, and spheres [38]. When $p > 1$, the formation of inverse structures, such as bicontinuous nanospheres, is observed [40]. When $p = 1$, planar lamellae are formed; when $1/2 \leq p < 1$, flexible lamellae and vesicles; when $1/3 < p < 1/2$, cylindrical micelles; and when $p \leq 1/3$ spherical micelles are obtained [9, 19, 21]. **Figure 1-1** depicts the BCP configuration for each range of p . In lipid systems, the variables that define p can be calculated, permitting researchers to design low molecular weight surfactants and phospholipids with an expected aggregate behavior [41]. The chemical and architectural diversity afforded by BCPs has made the development of a single, generalizable equation predictive of a given BCP's aggregate behavior nearly impossible. As such, a characteristic known as the hydrophilic mass fraction (f_{PEG}), defined as the ratio of the molecular weight of the hydrophilic block to the molecular weight of the BCP, has been more widely applied to define the phase behavior of BCP systems in practice [23, 37].

1.2.4. Amphiphilic Polymers Commonly Investigated for Biomedical Applications

Amphiphilic BCPs employed for the formation of nanocarriers designed for biomedical applications must be biocompatible. Biocompatibility has been defined as “the ability of a biomaterial to

perform its desired function with respect to a medical therapy, without eliciting any undesirable local or systemic effects in the recipient or beneficiary of that therapy, but generating the most appropriate beneficial

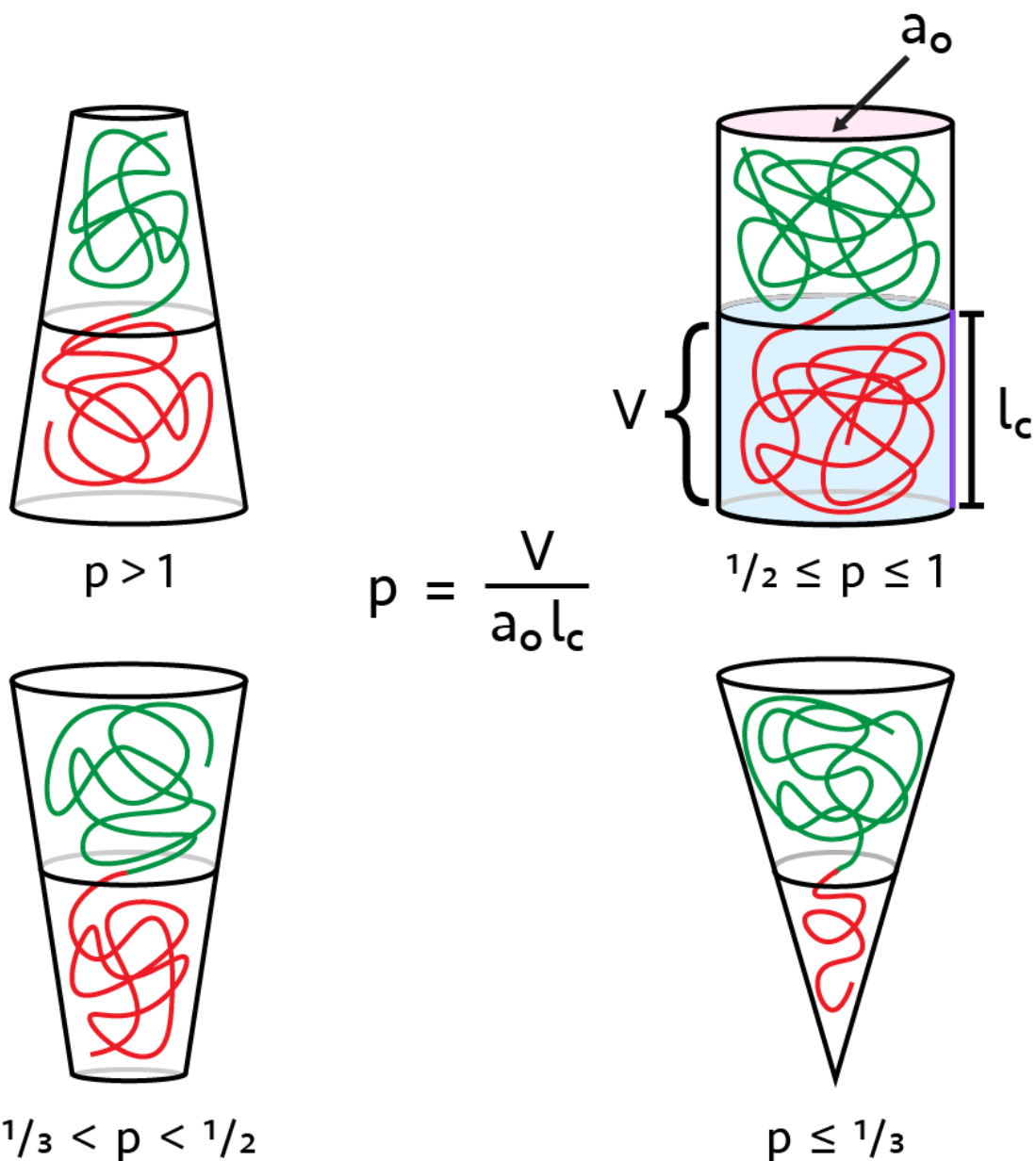


Figure 1-1. Illustration of diblock copolymer configuration as a result of its packing parameter.

Red and green represent the hydrophobic and hydrophilic blocks, respectively. Diblock copolymer configuration for packing parameter, p , values corresponding to the formation of (clockwise from top left) bicontinuous nanospheres, polymersomes, micelles, and filomicelles.

cellular or tissue response in that specific situation, and optimising the clinically relevant performance of that therapy” [42]. Nanocarrier biocompatibility relates to the construct’s cytotoxicity [43], hemocompatibility [44], and immunotoxicity [45]. While selection of a biocompatible BCP does not guarantee the preparation of a biocompatible nanocarrier, it is certainly a logical starting point. Often considered along with the biocompatibility of a construct is its clearance mechanism. The inefficient clearance and subsequent accumulation of nanocarriers remain a concern within the field due to the potential impact on construct toxicity [46, 47]. To mitigate such concerns, many nanocarriers are prepared using BCPs that are bioresorbable or biodegradable. Biodegradable polymers, which can be naturally-derived or synthetic, contain hydrolytically or enzymatically labile bonds along their backbones [48]. The presence of these cleavable bonds permits the efficient metabolism and clearance of the polymer [49], which in turn mitigates the potential for toxicity related to nanocarrier accumulation. There are several classes of biodegradable polymers that have been incorporated in BCPs for the formation of nanocarriers, the most common being aliphatic polyesters [49]. Aliphatic polyesters include poly(lactic acid) (PLA), poly(glycolic acid) (PGA), poly(lactic-co-glycolic acid) (PLGA), and poly- ϵ -caprolactone (PCL), all of which have been studied extensively in nanoparticulate delivery systems [50, 51].

1.2.5. Poly(ethylene glycol)-*block*-poly(propylene sulfide)

While there exists a plethora of unique amphiphilic BCPs in the literature, the material utilized for the research encompassed within this dissertation is poly(ethylene glycol)-*block*-poly(propylene sulfide) (PEG-*b*-PPS). Initially described by Napoli et al. in 2001, PEG-*b*-PPS is a relatively young BCP [52]. Inspired by a wave of publications describing the aggregate behavior of a series of poly(ethylene oxide)-*block*-poly(propylene oxide)-*block*-poly(ethylene oxide) BCPs (commonly referred to as Pluronics® or poloxamers) in the late 1990s [53-55], Napoli et al. sought to synthesize a structural analog to these BCPs [52, 56]. As PEG-*b*-PPS exhibited a similar chemical identity to the poloxamers described in the literature, it was anticipated that it too would demonstrate similar aggregate behavior. But the change in the utilized hydrophobic block, which amounts to replacing the oxygen atoms with sulfurs within the hydrophobe’s

backbone, resulted in a BCP with several unique characteristics over its predecessor. To understand why PEG-*b*-PPS was utilized, I will introduce some of the benefits imparted by each of its respective blocks.

One of the primary advantages of PEG-*b*-PPS over poloxamer is the enhanced stability of its self-assembled structures. As was discussed previously, the stability of self-assembled nanostructures can be assessed through the amphiphile's CMC, with lower CMC values indicative of a more stable self-assembled structure. Cerretelli et al. demonstrated that the CMC of PEG-*b*-PPS is substantially lower than the CMC of analogous poloxamers [57]. Through a combination of complementary fluorescence-based measurements, it was determined that PEG-*b*-PPS BCPs exhibited CMC values that were one to two orders of magnitude lower than comparable poloxamers. As these changes in the CMC were observed in instances when poly(propylene sulfide) (PPS) and poly(propylene oxide) (PPO) were of similar block lengths, it was understood that the decreased CMC was due to the increased hydrophobicity of the PPS [57]. This increase in hydrophobicity can be understood by simply comparing the electronegativities of sulfur and oxygen (2.58 versus 3.44), which explains the relatively low dipole moments of thioethers [58].

Some of the benefits afforded through the utilization of PPS can be explained through a discussion of the glass transition temperature. At temperatures greater than the glass transition temperature (T_g) an amorphous polymer will exist in a viscous or rubbery state while at temperatures below T_g the polymer will exist in a glassy or brittle state [59]. The characteristic differences associated with the two states can be understood in the context of chain interactions, where polymer chains above the T_g are unhampered by interactions with neighboring chains and thus more fluid and flexible [59]. PPS ($T_g \approx -46^\circ\text{C}$ [60]) has a comparable, albeit higher, T_g than PPO ($T_g \approx -75^\circ\text{C}$ [61]). The increase in the T_g for these atomically similar polymers can be explained by the lack of or weakly contributing hydrogen bonds formed by the sulfur atoms within the PPS backbone [62]. The T_g of the utilized polymer is important for both understanding the physical characteristics of the self-assembled structure and how it needs to be processed. For example, the T_g of the selected hydrophobic block has been shown to influence the fluidity and permeability of the aggregate structure [63, 64]. It has also been shown to influence the release of encapsulated molecules from said structures [65, 66].

Importantly, the T_g has been implicated in the hydration of polymer during nanostructure formation. Polymers that exhibit a high T_g may require elevated temperatures to permit proper aggregate formation and processing [67]. As such, one important benefit afforded by the selection of PPS, namely through its low T_g , is that diverse nanostructures can be readily prepared under ambient conditions [56]. Other hydrophobic polymers commonly used in nanostructure-forming BCP systems, which include PLGA [68, 69], PLA [67, 70], and polystyrene [71-73], typically exhibit a T_g that exceeds 37°C [59, 74]. As such, these BCPs may require heat or a fluidizing cosolvent for the preparation of a given aggregate structure [67, 75]. But there are alternative hydrophobes that compare favorably to PPS with respect to T_g . In addition to PPO, which was discussed previously, the commonly used PCL [76, 77] has a T_g of approximately -60°C [78]. Thus, the decision to utilize PPS must involve more than just considerations of nanostructure formation and processing alone.

PPS differentiates itself from more commonly used hydrophobic blocks like PPO and PCL because of its sensitivity to oxidation. Although relatively stable under aerobic conditions, the sulfur atoms present in thioethers, like PPS, can react with powerful oxidants, such as those classified as reactive oxygen species (ROS) [79]. In such instances, the sulfides are oxidized to high-dipole-moment sulfoxides and, eventually, sulfones [58]. This oxidation induced shift in polarity coupled with the ability of sulfoxides and sulfones to undergo hydrogen bonding [80] results in an increase in PPS hydrophilicity. This oxidation responsive behavior is of central importance for the application of PPS in a biological context. First, the oxidation of PPS allows for amphiphilic PEG-*b*-PPS to be safely excreted when applied *in vivo*. As PEG-*b*-PPS is oxidized, aggregate morphologies are destabilized as the increase in BCP hydrophilicity shifts f_{PEG} higher [60, 81]. Alterations in f_{PEG} induce sequential transitions in morphology, which have been captured through cryogenic transmission electron microscopy [60, 82]. Over time, this oxidative process can result in unimolecular micelles that exhibit hydrodynamic radii (~3 nm) that are sufficiently small to be renally excreted [60, 83]. Secondly, the oxidation sensitivity of PPS permits intracellular delivery of encapsulated molecules. It is commonly known that cells employ ROS in endolysosomal pathways to destroy pathogens [84]. As such, the oxidative species generated for these biological processes can be coopted for inducing

the intracellular release of an encapsulated payload. This concept of intracellular payload release has been demonstrated in PEG-*b*-PPS nanocarriers using both active [82] and passive oxidative stimuli [34].

While certainly more commonplace, the decision to utilize PEG as the hydrophilic block within this BCP system has been beneficial. PEG, since it was first proposed as a means of reducing protein immunogenicity by Dr. Frank Davis in the 1970s [85], has become ubiquitous within the field of biomaterials. From a synthesis standpoint, PEG is ideally suited because it exhibits a backbone that is inert to most chemical reactions, it is soluble in a variety of organic solvents as well as water, it displays terminal functional groups that are amenable to chemical modification, and it can be synthesized with a low polydispersity [86]. Furthermore, its non-toxic nature, when synthesized at a molecular weight greater than 600 Da [87], has made it a useful choice for a wide variety of biomedical applications [88]. Central to its selection in the subfield of nanocarrier-based drug delivery is the ability of PEG to mitigate non-specific protein adsorption [89, 90] and increase circulation time [91]. These “stealth” properties stem from PEG forming a dense array of polymer on the surface of the colloidal nanocarrier [92]. Water molecules in the surrounding solution form hydrogen bonds with the oxygen atoms of the PEG backbone resulting in a hydration shell around the nanocarrier that sterically hinders protein adsorption [93]. As such, PEG is often considered the “gold standard” of hydrophiles for BCP systems designed for biological applications [87].

1.2.6. PEG-*b*-PPS Nanocarriers

PEG-*b*-PPS has been observed to form four stable nanocarrier morphologies (**Figure 1-2**). As discussed previously (Section 1.2.3.), forming the various nanocarrier morphologies is in large part controlled by the BCP's f_{PEG} . Cerritelli et al. explored the relationship between f_{PEG} and morphology for PEG-*b*-PPS for two commonly used nanocarrier formation methods and, in doing so, established a large portion of the PEG-*b*-PPS morphological diagram [57]. This work established that vesicular PSs ($0.2 < f_{PEG} < 0.3$), cylindrical FMs ($0.37 \leq f_{PEG} \leq 0.39$), and spherical MCs ($f_{PEG} \geq 0.45$) could all be stably prepared with PEG-*b*-PPS. In addition, it highlighted the importance of the selected formation technique as differences in the morphological diagrams were observed for nanocarriers formed using thin film hydration versus solvent dispersion. The importance of formation method was further highlighted by Allen et al. in their pioneering

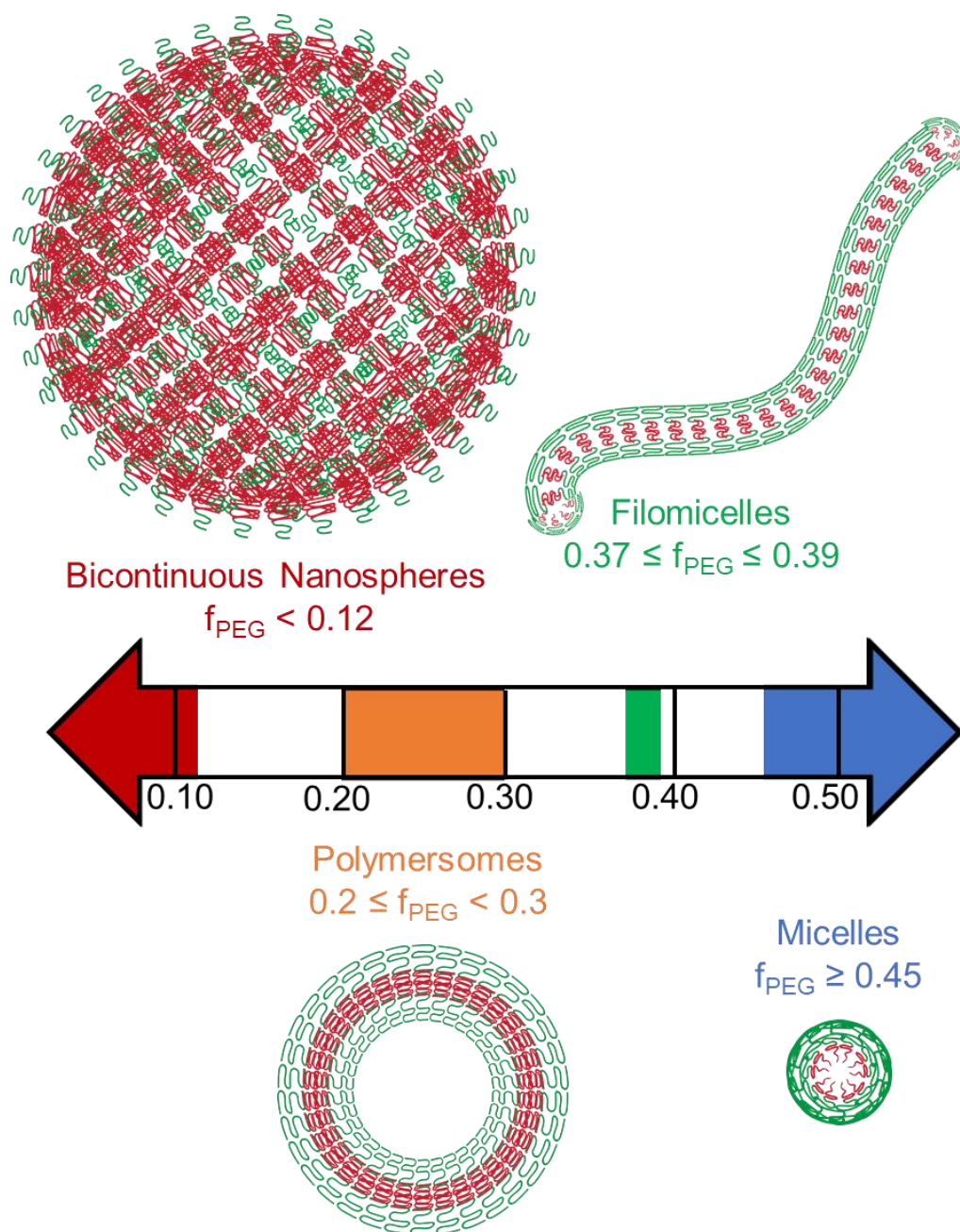


Figure 1-2. Relationship between nanocarrier morphology and the hydrophilic mass fraction of PEG-*b*-PPS. Hydrophilic mass fraction, f_{PEG} , ranges corresponding to the self-assembly of PEG-*b*-PPS bicontinuous nanospheres ($f_{\text{PEG}} < 0.12$; red), polymersomes ($0.20 \leq f_{\text{PEG}} < 0.30$; orange), filomicelles ($0.37 \leq f_{\text{PEG}} \leq 0.39$; green), and micelles ($f_{\text{PEG}} \geq 0.45$; blue).

work demonstrating the formation of soft self-assembled nanocarriers through flash nanoprecipitation (FNP) [94]. FNP permitted the formation of previously inaccessible PEG-*b*-PPS nanocarriers. Of the previously unreported morphologies, bicontinuous nanospheres (BCNs), which form when $f_{PEG} < 0.12$, are of continued interest. While all four morphologies share a comparable synthetic identity, they vary both in their physical characteristics [34, 95] and encapsulation capabilities [33, 94]. As such, the decision to employ a specific nanocarrier morphology for a given application is in part informed by these differences.

1.2.7. Origins and Evolution of Nanocarrier-based Drug Delivery Systems

Dr. Richard Feynman has been credited with the conceptualization of the field of nanotechnology, and consequently, the field of nanomedicine, with his 1959 seminar, “There’s Plenty of Room at the Bottom” [96]. In his talk, he proposed the idea of being able to “swallow the surgeon” as he described a futuristic vision where nanoscale devices could be used for both the non-invasive diagnosis and treatment of disease at the cellular level. While we have yet to achieve the nanoscale surgeons he envisioned, we are attempting to address the overarching concepts he put forth with the current generation of nanocarriers. Drug encapsulation within nanocarrier-based delivery systems display four primary benefits over the application of the molecule in its free form [97-100]. First, nanocarriers enhance the bioavailability of compounds that are poorly soluble [97]. The hydrophobic domain of self-assembled nanocarrier systems is capable of encapsulating non-polar molecules. Thus, nanocarriers encapsulating hydrophobic drugs, like many taxanes [101], are essentially stable colloidal suspensions of the encapsulated molecule and, as such, can be administered intravenously. Second, nanocarriers have the potential to increase drug efficacy through targeted delivery. Targeted delivery approaches for nanocarrier therapeutics include both passive [102] and active [103] targeting strategies. In both instances, the goal is to alter the distribution of the encapsulated molecule and concentrate its delivery within a cellular target. When successful, the total amount of drug applied for a given therapy may be reduced as a higher percentage of the drug reaches its target. Furthermore, the preferential accumulation of the encapsulated molecule within the desired target reduces the accumulation of drug within healthy tissue, which can result in reduced toxicity [104, 105]. Third, nanocarriers provide a means of protecting sensitive payloads. Novel approaches are being sought

for therapies centered around the delivery of nucleotides, like messenger RNA (mRNA) [106], and proteins [107]. These payloads, which are susceptible to a variety of degradative processes when applied *in vivo* [107, 108], achieve some protection when confined within a delivery construct. Finally, nanocarriers enhance the probability of achieving dual or combinatorial delivery to a cellular target. This benefit has largely been explored in the context of chemotherapy. Tumors exhibit a high level of heterogeneity [109] and the malignant cells that comprise them have shown an ability to develop multi-drug resistance over time [110]. To address these characteristics, combinatorial treatments have been explored [111]. But, the effectiveness of multidrug cocktails has been impeded by pharmacokinetic interactions that enhance their toxicity [112] and an inability to colocalize the treatments within the cellular targets [111]. But, as nanocarriers can stably encapsulate multiple therapeutic agents, they offer a promising avenue to address this issue.

As alluded to in the discussion concerning the benefit of concurrent delivery, many of the advantages afforded by nanocarriers have been explored in the development of cancer therapies. As such, the cellular targets have often been the malignant cells that comprise a portion of the tumor. Nanocarrier-based cancer therapies have often relied on a passive targeting strategy known as the enhanced permeation and retention (EPR) effect [102, 113]. The EPR effect was first coined by Maeda in the 1980s and describes the phenomenon where hyperpermeable tumor vasculature permits macromolecules to extravasate to the interstitial space of tumors and accumulate due to a lack of functional lymphatic vessels [114]. But, it should be noted that differences between the vasculature and tumor microenvironment of murine models and humans have made this phenomenon somewhat controversial [114, 115]. Regardless, the EPR effect was long relied upon for development of nanocarrier-based cancer therapies, and the constructs employed in these treatments were designed with the intention of minimizing detection from the mononuclear phagocyte system (MPS) [116]. The MPS, which is comprised of monocytes, macrophages, and dendritic cells [117], is the surveillance system responsible for detection and elimination of foreign debris and pathogens [118]. By escaping this system, conventionally designed nanocarriers can achieve increased circulation time, which maximizes the benefits afforded by the EPR effect. But, as our understanding of the immune system has progressed, we have come to realize the pivotal role the immune

system plays in the progression of a variety of different diseases [119, 120]. Now, rather than constructing nanocarriers such that they avoid interacting with the immune system, engineering principles are being applied to the design of nanocarriers with the intention of defining how they interact with the immune system. This nascent field of immunoengineering [121] looks to build off the knowledge accrued in the development of conventionally applied cancer nanomedicines. But before discussing its potential implications, a brief introduction to the cell types that comprise the immune system is required.

1.2.8. Immunobiology

This section is intended to provide the reader with a primer on the immune system. Its purpose is to introduce background knowledge that is relevant to the rationale behind and potential significance of the work described in this dissertation. It is by no means intended to be a comprehensive description of this rapidly evolving field.

The immune system is the multilayered defense system that protects an individual from exogenous (pathogenic bacteria, fungi, parasites, and viruses) and endogenous (malignant cells) threats. At the most basic level, the immune system can be broken down into three layers: structural and physiological barriers, the innate immune system, and the adaptive immune system [122]. As our first line of defense, we rely on physical barriers (i.e. keratinized skin and mucociliary clearance [123, 124]), chemical barriers (i.e. low pH of the stomach), and secreted proteins (i.e. antimicrobial peptides [125] and the complement system [126]) to neutralize external pathogens. But when these initial defenses fail, our body turns to the cellular components of the immune system to sequester and eliminate pathogens. The innate immune system responds within minutes following exposure to a pathogen. Pathogenic microbes express evolutionarily conserved structures, known as pathogen-associated molecular patterns (PAMPs), that the cells of the innate immune system recognize through several families of receptors known as pattern recognition receptors (PRRs) [127]. The cells of the innate immune system include basophils, dendritic cells, eosinophils, macrophages, mast cells, natural killer cells, and neutrophils. I will limit the discussion of the innate immune system to the four primary phagocytic cells: neutrophils, monocytes, macrophages, and dendritic cells.

Neutrophils, which are also termed polymorphonuclear leukocytes because of their multi-lobed nuclei, are the most abundant white blood cell in the human circulatory system. They are the first cell type recruited to sites of inflammation or infection [128] and are tasked with pathogen elimination. Typically, neutrophils rely on three mechanisms for pathogen elimination: phagocytosis, degranulation, and neutrophil extracellular traps (NETs) [129]. Following activation, neutrophils become highly phagocytic [130]. Upon sequestering a microorganism in the phagosome, neutrophils may eliminate the pathogen through the release of ROS or antibacterial peptides [129]. Alternatively, the antibacterial peptides mentioned above may be released for extracellular pathogen elimination through a process known as degranulation [131]. Finally, neutrophils may employ NETs, which are extracellular fibers of neutrophil DNA decorated with antimicrobial proteins, to ensnare and degrade extracellular pathogens [132]. Neutrophils, while integral to innate immunity, play a relatively short-lived role. In the process of pathogen elimination, neutrophils actively recruit additional immune cells such as monocytes and macrophages to the site of inflammation [133].

Monocytes are one of the primary cells of the MPS. They, like neutrophils, develop in the bone marrow and are the primary mononuclear phagocyte in the human circulatory system [134]. In humans, monocytes account for ~10% of circulating leukocytes where as in mice they account for only 4% [135]. Three monocyte subsets have been identified in humans and two primary subsets have been identified in mice based on their differential expression of cell surface markers [135]. Classical monocytes, identified as cluster of differentiation (CD) 14^{low}CD16⁻ in humans and Ly6C^{hi} in mice, are considered pro-inflammatory [136] and circulate in the blood before they extravasate into infected or inflamed tissue [137]. Classical monocytes are moderately phagocytic [138] and are capable of differentiating into either macrophages or dendritic cells [139]. Non-classical monocytes, identified as CD14^{dim}CD16⁺ in humans and Ly6C^{lo} in mice, are sometimes referred to as “patrolling monocytes” [135]. They typically reside in the vasculature and play roles in maintaining homeostasis, the induction of pro-inflammatory responses, and wound healing [136, 140]. Finally, humans exhibit a third pro-inflammatory subset, known as intermediate monocytes, that are identified as CD14⁺CD16⁺ [135]. While classified as a professional phagocyte, monocytes have limited

antigen-presenting capabilities [134]. This characteristic puts them in stark contrast with the remaining two members of the MPS: macrophages and dendritic cells.

Macrophages are a highly heterogeneous population of cells, present in almost all organs, that contribute to both maintaining homeostasis and host defense [141]. This heterogeneity, in part, stems from their origins, the diverse tasks they conduct, and their adaptation to the local microenvironment where they reside [141]. For example, tissue resident macrophages, which include alveolar macrophages of the lungs, Kupffer cells of the liver, Langerhans cells of the skin, microglial cells of the brain, and red pulp macrophages of the spleen (to name a few), are both phenotypically and functionally distinct [142]. Irrespective of these differences, macrophages collectively exhibit a highly phagocytic nature and, like monocytes, contribute to the functioning of the MPS. Adding to the complexity of the various macrophage functions is the concept of macrophage polarization. Both tissue resident and monocyte-derived macrophages can be activated to one of two states, labeled M1 or M2, in response to variable stimuli in their environment [143, 144]. M1 macrophage polarization is induced through microbial stimuli, like PAMPs, or cytokines, such as tumor necrosis factor (TNF), and results in a pro-inflammatory state [145]. M2 polarization occurs in response to interleukin-4 (IL-4) and IL-13 [146]. These alternatively activated macrophages are believed to play a role in wound healing [146] and, under certain circumstances, can be anti-inflammatory [147]. While this binary classification of macrophage polarization is useful due to its simplicity, it should be noted that macrophage polarization should realistically be viewed as a continuum, with cells existing in a variety of states between the classic and alternative states described [145].

Furthermore, macrophages are classified as a professional antigen presenting cell (APC). APCs are a class of cells capable of presenting peptides for the activation of T cells [148]. Professional APCs share several characteristics that make them particularly suited for this function. These characteristics include the ability to efficiently acquire/process antigens and the ability to display several surface markers, including the constitutive expression of major histocompatibility complex (MHC) class II (human leukocyte antigen (HLA)-DR, HLA-DQ, and HLA-DP in humans), for effective T cell interactions

[149]. Given their functional diversity, ability to both promote and resolve inflammation through cytokine secretion, and their position as a professional APC, macrophages represent an interesting cellular target.

Dendritic cells are the third cellular component of the MPS. Upon their development in the bone marrow, dendritic cells traffic to nonlymphoid organs where they reside [150]. Immature dendritic cells, which exhibit a variety of PRRs, are highly phagocytic [151]. This phagocytic capacity is lost when dendritic cells undergo maturation in response to PAMPs or alternative inflammatory signals. Mature dendritic cells migrate from their resident tissue to draining lymphoid organs for antigen presentation [150]. Among the professional APCs, dendritic cells are considered the most adept at this function and unique in their ability to prime naïve CD4⁺ T cells [150]. Dendritic cells can be further classified as either classical dendritic cells (cDCs) or plasmacytoid dendritic cells (pDCs) [152]. In both mice and humans, cDCs are highly effective at phagocytosing, processing, and presenting antigen, including through cross-presentation mechanisms [153]. Antigen cross-presentation is the process of displaying exogenous antigen on MHC class I molecules (HLA-A, HLA-B, and HLA-C in humans), which are typically reserved for endogenous antigen [154]. Both murine and human pDCs are important contributors to antiviral immunity through their secretion of large amounts of type I interferon [155]. But while murine pDCs play a negligible role in antigen presentation, their human counterparts cross-present antigen effectively [152]. Given the diverse mechanisms through which they can interface with the adaptive immune system, dendritic cells are a highly desirable cellular target for a variety of applications in immunoengineering.

Adaptive immunity is the last layer of our defense system. Unlike innate immunity, which relies on the detection of broadly conserved PAMPs for the rapid identification and elimination of a variety of pathogens, adaptive immunity is highly specific, or “adapted,” for the specific pathogen that triggers its response [156]. The cellular components of the adaptive immune system include B lymphocytes and T lymphocytes. B lymphocytes, like the macrophages and dendritic cells of the innate immune system, are classified as professional APCs [157]. Although they exhibit a relatively low phagocytic capacity, B lymphocytes can endocytose antigen through a receptor mediated process [158]. Following the interaction of either soluble or membrane-bound antigen with its B cell receptor, B lymphocytes can internalize the

antigen-receptor complex and subsequently process and present the antigen on MHC class II molecules to recruit CD4⁺ T cells [157]. B lymphocytes are primarily recognized as the mediators of the humoral response. Through a multistep activation process, B lymphocytes can differentiate into either antibody-secreting plasma cells or long-lived memory B cells depending on the extracellular cues they encounter [159]. As such, B cells are of central importance to the development of vaccines [160].

T lymphocytes, or T cells, are responsible for several effector functions in adaptive immunity and are generally classified as helper T cells, cytotoxic T cells, and regulatory T cells [161]. Helper T cells, which are CD4⁺ T cells, can differentiate into several effector cell subsets following antigen binding by the T cell receptor (TCR) and activation [162]. CD4⁺ T cell subsets secrete variable cytokine profiles, which allow the different subsets to mediate an array of functions that shape both the adaptive and innate immune response [150]. Cytotoxic T cells, which are CD8⁺ T cells, provide protection from infected or malignant cells. Cytotoxic T cells are activated through TCR binding of antigen presented on MHC class I molecules (HLA-A, HLA-B, and HLA-C in humans) by APCs in the secondary lymphoid tissues [163]. Upon activation, CD8⁺ T cells undergo significant cellular expansion before migrating to their effector site. Upon reaching their effector sites, CD8⁺ T cells directly (i.e. cell-to-cell) eliminate infected or malignant cells in an antigen-specific fashion [163]. The specificity and direct nature through which they act make them highly desirable for the development of cancer immunotherapies [164]. Lastly, regulatory T cells, which are sometimes classified as an effector subset of CD4⁺ helper T cells [165], provide an additional level of control over a generated immune response. They are prominent mediators of antigen-specific immunological tolerance [166]. In doing so, regulatory T cells can prevent or mitigate the adverse effects that accompany an unintended or excessive immune response [166].

1.2.9. The Conundrum of Targeting Antigen Presenting Cells

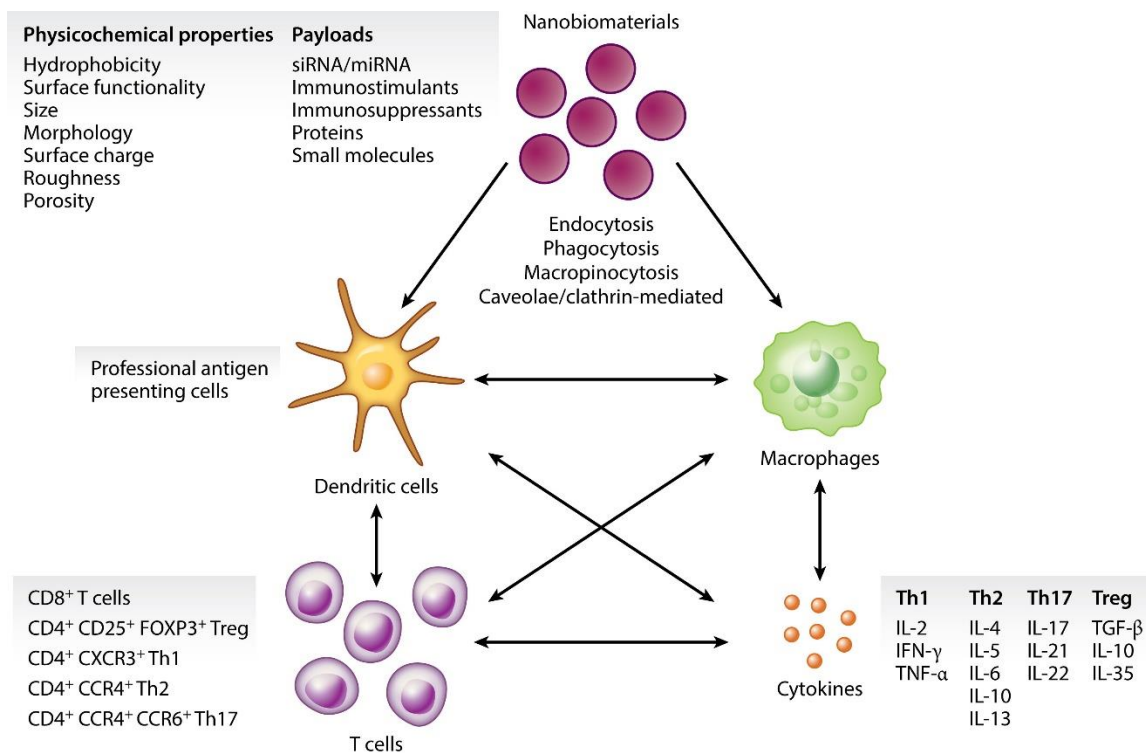
APCs, particularly those that constitute the MPS, are attractive candidates for immunomodulatory treatments involving nanocarriers. Their suitability in this role stems from how they interact with both foreign material and the functionally diverse cells in their environment. Humans are routinely exposed to a broad array of environmentally occurring nanoscale objects [3]. Whether these

objects be material or pathogenic in their nature, the cells of the MPS are tasked with their capture and elimination. As they have evolved to fulfill this function, monocytes, macrophages, and dendritic cells are all well-equipped to identify, interact with, and internalize nanocarriers. The internalization of macromolecules from the extracellular environment is formally known as endocytosis. The cells of the MPS routinely employ three distinct endocytic mechanisms: macropinocytosis, receptor mediated endocytosis, and phagocytosis. Macropinocytosis, which involves the engulfment and internalization of extracellular fluid, is a nonspecific mechanism [120]. This process can involve the formation of large endocytic vesicles known as macropinosomes, which range in size from 0.5 μm up to 10 μm [167]. Thus, macropinocytosis can be used to indiscriminately internalize nanocarriers exhibiting broad size characteristics. Both receptor mediated endocytosis and phagocytosis are induced through receptor specific interactions with cognate ligands. A variety of receptor ligands have been implicated in these processes. The ligands may exist on the nanocarrier surface through design or as a result of biomolecular adsorption. For example, receptor mediated endocytosis has been exploited for targeting APCs via serum-transport proteins, transferrin, and lipoproteins [168]. Phagocytosis is known to involve opsonins, like immunoglobulins and complement proteins [169, 170]. An important factor distinguishing these endocytic mechanisms are the size of the nanocarriers they can accommodate. Receptor mediated endocytosis is typically used to internalize particles that are less than 200 nm [168]. This limitation is imposed by the size of the clathrin-coated pits essential to this pathway [171]. Alternatively, phagocytosis is responsible for the internalization of particles that are typically greater than 500 nm [172].

In addition to their capacity to internalize nanocarriers of variable size, APCs are attractive cellular targets because of their ability to both promote and resolve inflammation. Inflammation-driven diseases, which include atherosclerosis, cancer, and those related to autoimmunity, are often the product of cytokine dysregulation [119]. Cytokines are integral for appropriate cellular function and can shift a given microenvironment toward either a pro- or anti-inflammatory state. For example, elevated levels of proinflammatory cytokines like TNF- α are hallmarks of rheumatoid arthritis [173]. But the microenvironment of solid tumors exhibits increased levels of anti-inflammatory IL-10 and transforming growth factor- β (TGF- β), which inhibits cytotoxic T cell function [174]. Given their functional diversity and phenotypic plasticity,

APCs can be influenced to secrete a variety of cytokines. As such, they are important cellular targets capable of dynamically altering the cytokine profiles at the center of inflammation-driven pathologies

(Figure 1-3).



AR Scott EA, et al. 2017.
Annu. Rev. Biomed. Eng. 19:57–84

Figure 1-3. Depiction of how nanocarrier physicochemical properties can indirectly influence T cell function. Physicochemical properties of nanocarriers can be designed to alter uptake within antigen presenting cells (APCs). These characteristics, along with the encapsulated active or payload, can influence T cell function through either cell-to-cell interactions or through APC secreted cytokines.. Abbreviations: IFN, interferon; IL, interleukin; miRNA, microRNA; siRNA, small interfering RNA; TGF, transforming growth factor; Th, helper T; TNF, tumor necrosis factor; Treg, regulatory T cells. Reprinted from [119]. Posted, with permission, from the Annual Review of Biomedical Engineering, Volume 19 © 2017 by Annual Reviews, <http://www.annualreviews.org>.

For strategies targeting APCs with nanocarriers to be effective, control over which cell type, and in some cases, which cell subset, internalizes the construct is imperative. And while the phagocytic capacity of APCs is an attractive characteristic, it simultaneously enhances the difficulty of achieving cell specific targeting. At the highest level, this task requires achieving delivery of a nanoscale object to a select number of cells. The dilemma stems from the fact that these targeted cells exist within a system where all cellular constituents have evolved to identify and eliminate nanoscale objects. Further adding to the complexity of this task are the functional differences that arise within a given cell type due to its tissue or microenvironment [175]. In some instances, functional differences can even be observed within different regions of the same organ. For example, the spleen contains several macrophage subsets, including red pulp macrophages and marginal metallophilic macrophages, that vary in where they reside. While both macrophages can phagocytose blood-borne particulates [176], red pulp macrophages are typically associated with directing tolerance [177] while marginal metallophilic macrophages have been implicated in the indirect activation of cytotoxic T cells [178]. Thus, the strategy of designing a nanocarrier to target a specific cell type, without considering the organ or tissue where it resides, is unlikely to be successful. In order to rationally design nanocarriers for targeting APCs, it is necessary to understand what nanocarrier physicochemical characteristics can be used to govern both their organ and cellular fate *in vivo*.

1.2.10. Nanocarrier Physicochemical Characteristics Influence Biological Identity

Upon preparation, nanocarriers are meticulously characterized to establish their synthetic identity. The nanocarrier synthetic identity refers to its specific combination of physicochemical characteristics upon formation and includes any post-preparative modifications that occur *in vitro* [179]. These physicochemical characteristics include the nanocarrier's morphology, size, surface chemistry (relative hydrophobicity, charge, and reactivity), elasticity, and display of ligands [180, 181]. While it is convenient to imagine these bare or pristine nanocarriers interacting with cells, the process is more complicated in practice. The introduction of nanocarriers into a complex environment, such as blood, results in the almost immediate adsorption of a variety of biomolecules onto the nanocarrier surface. Nucleic acids, carbohydrates [182], lipids [183], and proteins [184] are all believed to adsorb to the nanocarrier surface

and shape its biological identity. It is this biological identity that directly influences both the organ-level biodistribution and cellular interactions of administered nanocarriers [185].

Given the role that receptor mediated endocytic mechanisms play in nanocarrier internalization by APCs, the importance of the biological identity is clear. Efforts to understand the biological identity of nanocarriers has primarily focused on proteins due to their abundance in the most readily studied biological solution, the blood. As such, the biological identity of nanocarriers is often discussed under the guise of the protein corona (PC), a term coined by Dawson and Linse in 2007 [186]. Since its introduction, the PC has become a key design characteristic in nanocarrier platforms [187]. Concerted efforts have been made to elucidate how various physicochemical characteristics impact PC formation and cell uptake [188-190]. By understanding how both the nanocarrier influences the composition of the PC and how compositional changes in the PC influence cellular internalization, rational design can be used to shape the *in vivo* fate of the nanocarrier.

1.3. Scope of this Dissertation

PEG-*b*-PPS nanocarriers have proven to be useful constructs for a variety of applications centered around immunomodulation. Since it was first described in 2001, alterations to the design of PEG-*b*-PPS BCPs have been few and have focused on modifications to the PPS block. In this time, the surface characteristics of nanocarrier systems have been increasingly identified for their importance in governing cellular interactions. These interactions can be tailored through both passive and active targeting strategies. To further advance the utility of PEG-*b*-PPS nanocarriers within the immunomodulatory space, I developed functionally diverse PEG-*b*-PPS BCPs that could self-assemble into nanocarriers with variable surface characteristics. In this dissertation, I discuss my efforts to expand the library of functionalized PEG-*b*-PPS BCPs. From this pool of functionalized BCPs, I explore how certain PEG-*b*-PPS derivatives can be exploited for both passive targeting and applications in sustained delivery.

1.4. Publication Information

Portions of this chapter have been previously published. The published works correspond to the following citations:

Allen, S.D., Bobbala, S., **Karabin, N.B.**, Scott, E.A, *On the advancement of polymeric bicontinuous nanospheres toward biomedical applications*. *Nanoscale Horizons*, 2019. **4**: p. 258-272. **[40]**

Scott, E.A., **N.B. Karabin**, and P. Augsornworawat, *Overcoming Immune Dysregulation with Immunoengineered Nanobiomaterials*. *Annu Rev Biomed Eng*, 2017. **[119]**

CHAPTER 2

Synthesis of Functionally Diverse PEG-*b*-PPS BCPs

2.1. Abstract

A key determinant in the cellular fate of nanocarriers is the applied surface chemistry. By controlling the functional groups presented on nanocarrier surfaces, both active and passive targeting strategies may be implemented. The importance of surface chemistry for active targeting strategies, which require the nanocarrier surface to be decorated with reactive functional groups for the attachment of various ligands, is obvious. But, an evolving understanding of the importance of the PC has increased interest in passive targeting strategies, where nanocarrier surface chemistry is being employed as a means of controlling protein adsorption and, consequently, nanocarrier uptake. PEG-*b*-PPS is an established BCP that has been applied for the preparation of a variety of nanocarriers. Since first being described in 2001, limited efforts have been made to expand the potential functional groups displayed on PEG-*b*-PPS nanocarriers. In this chapter, I explore the synthesis of six previously undescribed PEG-*b*-PPS BCPs. The varying reactivities and charges exhibited by these BCPs permit their application in both active and passive targeting strategies.

2.2. Introduction

2.2.1. PEG-*b*-PPS: Innovations and Limitations

Since first being described by Napoli et al., PEG-*b*-PPS BCPs have typically been prepared through anionic ring-opening polymerization [30, 32-34, 52, 56, 57, 60, 81, 94, 191-202]. Anionic ring-opening polymerization is advantageous in this setting as it relies on the relatively mild thiolate anion to propagate the polymerization of PPS. In doing so, a diverse array of functional groups, including those that are biologically relevant, can be incorporated in the BCP [52]. While a number of nucleophiles could potentially be employed for initiation, sulfur-based species have been most effective [52, 203]. Out of the pool of sulfur-based moieties, Napoli et al. eschewed thioacid salts due to concerns over the stability of the

thioesters that would be formed during PPS initiation [52]. Instead, thiolates were utilized and continue to be the initiator of choice today.

As thiolate anions are generated from the deprotonation of thiols or the deprotection of thioacetates, a diverse pool of potential initiators can be used for the polymerization of propylene sulfide. In addition to the numerous small molecule initiators that exist, both thiol- and thioacetate-modified PEG can be used. Through the careful selection of initiating and end-capping species, the hydrophobic terminus of PPS can be modified to impart unique characteristics to PEG-*b*-PPS nanocarriers at the material level. This synthetic versatility has been explored for enhancing the diagnostic function of PEG-*b*-PPS nanocarriers through the covalent attachment of fluorescent dyes [95, 192, 195, 196, 202, 204]. It has also been investigated for enhancing the encapsulation of a variety of molecules. Modifications to the PPS block have permitted the stable complexation of nucleotides, including plasmid DNA [199] and small interfering RNA [198], through electrostatic interactions and have allowed for the covalent attachment of small molecule drugs [205, 206]. Furthermore, innovative strategies have been applied at the interface between the PEG and PPS blocks. Cerritelli et al. first described a PEG-*b*-PPS derivative that linked the respective blocks through a disulfide bond [194]. This linkage, which is reduction-sensitive, enhanced the intracellular destabilization of the nanocarriers and further demonstrated how nanocarrier function could be enhanced through innovative alterations of the BCP.

While numerous innovative strategies have been implemented on the hydrophobic block (a summary of which can be found in **Table 2-1**), fewer attempts have been made to explore the impact of alternative chemistries displayed on the PEG block. Most of the PEG-*b*-PPS BCPs described in the literature display a methyl group bound to the terminal oxygen of the PEG backbone. These BCPs typically use poly(ethylene glycol) monomethyl ether (mPEG) as a starting material. The presence of only a single terminal hydroxyl group simplifies syntheses that involve mPEG. But the convenience provided by mPEG comes at the expense of optionality, as the methoxy group that remains following the synthesis of the BCP is relatively inert [207].

Table 2-1. Summary of innovative PEG-*b*-PPS BCPs for enhanced nanocarrier function.

Block	Terminal Functional Group	Cognate Functional Group	Linkage	Attached Molecule	Purpose	Ref.
<u>Poly(propylene sulfide)</u>						
	Amine	NHS	NHS ester	Alexa Fluor™	Diagnostic	[195, 208]
	Amine	PTCDA	Imide	PBI	Diagnostic	[202]
	PDS	Sulfhydryl	Disulfide	Peptide	Encapsulation	[198]
	Thiolate	Maleimide	Thioether	BODIPY	Diagnostic	[192]
	Thiolate	Maleimide	Thioether	DyLight	Diagnostic	[95]
	Thiolate	PDS	Disulfide	PEOX	Encapsulation	[199]
	Thiolate	PDS	Disulfide	6-Tioguanine	Encapsulation	[205, 206]
<u>Block interface</u>						
	Thiolate	Thiolate	Disulfide	—	Cleavage	[194]
<u>Poly(ethylene glycol)</u>						
	Carboxylic Acid	Amine	Amide	ssDNA	Bioconjugation	[201]
	Carboxylic Acid	Amine	Amide	MMP-9 Cleavable Peptide	Stimuli Responsive Construct	[209]
	PDS	Sulfhydryl	Disulfide	Antigen	Bioconjugation	[208]

NHS = *N*-hydroxysuccinimide, PTCDA = perylene-3,4,9,10-tetracarboxylic dianhydride, PBI = perylene bisimide, BODIPY = boron-dipyrromethene, PDS = pyridyl disulfide, PEOX = poly(2-ethyl 2-oxazoline), ssDNA = single-stranded DNA, MMP = matrix metalloproteinase

Two strategies have been implemented to incorporate additional surface chemistries on PEG-*b*-PPS nanocarriers. First, the inert nature of mPEG can be circumvented by incorporating a secondary BCP to create a mixed system. Terminally-modified poloxamers have been added to PEG-*b*-PPS nanocarriers due to the chemical similarity exhibited by the two BCPs [197]. But the coassembly of chemically distinct BCPs is limited by the amount of secondary amphiphile that can be stably incorporated

into the self-assembled structure. Alternatively, heterobifunctional PEGs have been purchased and utilized for the preparation of PEG-*b*-PPS nanocarriers with alternative surface chemistries to the typically described methoxy. Both carboxylic acid- [200, 201] and pyridyl disulfide-functionalized [208] PEG-*b*-PPS BCPs have been described. But these constructs relied upon commercially available heterobifunctional PEG as a starting material, the cost of which could inhibit the investigation of a variety of functionalized PEG-*b*-PPS BCPs. Considering the limitations associated with currently utilized strategies, a safe, cost-effective, and efficient method of preparing heterotelechelic PEG materials is essential to the effective investigation of functionally diverse PEG-*b*-PPS BCPs.

2.2.2. Synthesis of Heterotelechelic PEG

As was discussed in Section 1.2.5., PEG has become ubiquitous within the field of biomaterials because of its ability to mitigate non-specific protein adsorption, enhance circulation time, and reduce immunogenicity. Its prevalence in BCPs and macromolecular conjugates has resulted in a broad exploration of the routes through which it can be synthesized. Heterotelechelic PEGs have conventionally been synthesized through two methods [210]. The most commonly employed strategy for preparing high-purity heterobifunctional PEGs is the anionic ring-opening polymerization of ethylene oxide. The functional diversity achieved through this strategy is the result of the initiator and end-capping agent selected [210]. While this polymerization is the most straightforward method, aspects of the synthesis limit its general adaptability. First, harsh reaction conditions, which include high temperatures and strong bases, limit the functional groups that can be incorporated [211]. Second, the anionic ring-opening polymerization of ethylene oxide is associated with several hazards [212], including monomer toxicity, monomer flammability, and toxic gas generation, that limit the broad adaptation of this method outside of classically trained polymer chemists. Alternatively, the partial functionalization of PEG (i.e. react PEG with one equivalent of the desired moiety) followed by the separation of the resulting un-, mono-, and bifunctional products has been explored [210]. But this strategy results in a 1:2:1 statistical mixture of the un-, mono-, and bifunctional products, respectively, thereby drastically decreasing overall yield across each synthetic step.

Mahou et al. described a method [213] to selectively increase the yield of the monofunctionalized PEG product by adapting a strategy originally implemented to modify small symmetric diols [214]. This synthesis uses silver (I) oxide to create a disparity in the reactivity of the terminal hydroxyls, which increases the probability of preparing the monotosyl product. The resulting α -tosyl- ω -hydroxyl PEG can subsequently be modified in stepwise fashion to produce a variety of heterobifunctional polymers. This synthesis (referred to as asymmetric activation) has several advantages over the previously described methods. In addition to being a considerably safer synthesis than the anionic ring-opening polymerization of ethylene oxide, this strategy drastically increases the yield of the monofunctionalized product [213]. Thus, asymmetric activation of commercial PEG can be used as a safe and cost-effective means of producing heterobifunctional PEGs for incorporation into PEG-*b*-PPS BCPs.

2.3. Materials and Methods

2.3.1. Chemicals

All chemical reagents were purchased from Sigma-Aldrich St. Louis, MO, USA unless stated otherwise.

2.3.2. Synthesis of Functionalized mPEGs

Linear poly(ethylene glycol) methyl ether (mPEG₄₅, Molecular Weight (MW) 2000; mPEG₁₇, MW 750) was dried via azeotropic distillation (For mPEG₄₅: 40.0 g, 20.0 mmol, 1 equivalent (EQ); For mPEG₁₇: 20 g, 26.67 mmol, 1 EQ) in toluene using a Dean-Stark trap. The dried solution was removed from heat and allowed to cool to room temperature under vacuum prior to purging the reaction vessel with nitrogen (N₂). Triethylamine (For mPEG₄₅: 16.72 mL, 120 mmol, 6 EQ; For mPEG₁₇: 18.58 mL, 133.35 mmol, 5 EQ) was added to the stirred solution. After cooling to 0°C, methanesulfonyl chloride (MsCl) (For mPEG₄₅: 17.74 mL, 100 mmol, 5 EQ; For mPEG₁₇: 10.32 mL, 133.35 mmol, 5 EQ) diluted in toluene (10 x Volume of MsCl) was added to the stirred solution dropwise. The reaction was stirred overnight at room temperature under N₂. Salt produced during the reaction was removed via vacuum filtration of the reaction mixture over a celite filter cake. Toluene was removed through rotary evaporation and the product was

precipitated in ice-cold diethyl ether. The precipitate was recovered via filtration, washed with cold diethyl ether, and dried under vacuum. The resulting mesylate-functionalized mPEG (mPEG-OMs) was stored under N₂ until further use. ¹H NMR (400 MHz, CDCl₃): δ 4.38 – 4.34 (m, 2H, -CH₂-O-SO₂), 3.65-3.60 (s, 180H, PEG backbone), 3.37 – 3.35 (s, 3H, O-CH₃), 3.07 – 3.05 (s, 3H, SO₂-CH₃).

Thioacetate-functionalized mPEG (mPEG-TA) was prepared from mPEG-OMs. In brief, mPEG-OMs (For mPEG₄₅-TA: 15.0 g, 7.5 mmol, 1 EQ; For mPEG₁₇-TA: 5.0 g, 6.67 mmol, 1 EQ) was dissolved in anhydrous dimethylformamide within a round bottom flask (RBF) that had been previously evacuated and purged with N₂. Potassium carbonate (For mPEG₄₅-TA: 5.18 g, 37.5 mmol, 5 EQ; For mPEG₁₇-TA: 3.69 g, 26.68 mmol, 4 EQ) and thioacetic acid (For mPEG₄₅-TA: 2.68 mL, 37.5 mmol, 5 EQ; For mPEG₁₇-TA: 1.90 mL, 26.68 mmol, 4 EQ) were added sequentially. The reaction was stirred overnight at room temperature. Salt produced during the reaction was removed via vacuum filtration of the reaction mixture over a celite filter cake. Dimethylformamide was removed through rotary evaporation. The product was dissolved in tetrahydrofuran and run on an aluminum oxide column. The collected product was concentrated by removing tetrahydrofuran via rotary evaporation and precipitated in ice cold diethyl ether. The precipitate was recovered via filtration, washed with cold diethyl ether, and dried under vacuum. The resulting mPEG-TA was stored under N₂ until further use. ¹H NMR (400 MHz, CDCl₃): δ 3.65-3.60 (s, 191H, PEG backbone), 3.37 – 3.35 (s, 3H, O-CH₃), 3.09 – 3.05 (t, 2H, CH₂-S-CO), 2.33 – 2.31 (s, 3H, CO-CH₃).

2.3.3. Synthesis of Bn-PPS-*b*-PEG-OMe BCPs

Bn-PPS-*b*-PEG₄₅-OMe was synthesized for FMs and MCs using a small molecule sulfhydryl initiator. Benzyl mercaptan (For FMs: 53.7 μL, 0.45 mmol, 1 EQ; For MCs: 98.7 μL, 0.83 mmol, 1 EQ), dissolved in anhydrous dimethylformamide, was deprotonated through the addition of sodium methoxide (0.5 M solution in methanol; For FMs: 0.50 mmol, 1.1 EQ; For MCs: 0.92 mmol, 1.1 Eq) to generate a thiolate anion. This thiolate anion was used to initiate the living anionic ring-opening polymerization of propylene sulfide (For FMs: 1.50 mL, 19.94 mmol, 44 EQ; For MCs: 1.50 mL, 18.37 mmol, 22 EQ). The terminal thiolate was endcapped through the addition of mPEG₄₅-OMs (For FMs: 1.57 g, 0.68 mmol, 1.5 EQ; For MCs: 2.00 g, 0.87 mmol, 1.05 EQ) and subsequently stirred overnight. Following the removal of dimethylformamide through rotary evaporation, the product was recovered through methanol precipitation

and cooled as needed. The resulting precipitate was recovered and dried under vacuum. ^1H NMR (400 MHz, CDCl_3): δ 7.36 - 7.32 (d, 4H, ArH), 3.68-3.63 (s, 180H, PEG backbone), 3.41 – 3.39 (s, 3H, O-CH₃), 3.00 - 2.85 (m, 89H, CH₂), 2.71 - 2.59 (m, 44H, CH), 1.44 - 1.37 (d, 132H, CH₃).

Bn-PPS-*b*-PEG₁₇-OMe was synthesized for the preparation of PSs via the stable macroinitiator mPEG₁₇-TA. mPEG₁₇-TA (0.50 g, 0.40 mmol, 1 EQ), deprotonated through the addition of sodium methoxide (0.5 M solution in methanol, 0.44 mmol, 1.1 EQ), was used to initiate the living anionic ring-opening polymerization of propylene sulfide (1.00 mL, 12.25 mmol, 30 EQ). The terminal thiolate was endcapped through the addition of benzyl bromide (1.44 mL, 2.0 mmol, 5 EQ) and subsequently stirred overnight. Following the removal of dimethylformamide through rotary evaporation, the product was recovered through methanol precipitation and cooled as needed. The resulting precipitate was recovered and dried under vacuum.

2.3.4. Synthesis of Heterobifunctional PEG

α -tosyl- ω -hydroxyl PEG₄₅ and PEG₂₃ were prepared by adapting a previously published protocol [213]. PEG (For HO-PEG₄₅-OTs: 30 g, 15 mmol, 1 EQ; For HO-PEG₂₃-OTs: 25 g, 25 mmol, 1 EQ) was dried via azeotropic distillation in toluene using a Dean-Stark trap. Following complete removal of toluene, the dry PEG was flushed with N₂ and dissolved in anhydrous dichloromethane before being placed on ice. Silver (I) oxide (For HO-PEG₄₅-OTs: 5.21 g, 22.5 mmol, 1.5 EQ; For HO-PEG₂₃-OTs: 8.69 g, 37.5 mmol, 1.5 EQ), potassium iodide (For HO-PEG₄₅-OTs: 1.79 g, 10.8 mmol, 0.72 EQ; For HO-PEG₂₃-OTs: 2.99 g, 18.0 mmol, 0.72 EQ), and *p*-Toluenesulfonyl chloride (For HO-PEG₄₅-OTs: 3.00 g, 15.75 mmol, 1.05 EQ; For HO-PEG₂₃-OTs: 5.00 g, 26.25 mmol, 1.05 EQ) were sequentially added to the vigorously stirring solution. After two hours, the sample was removed from its ice bath and was further allowed to react overnight at room temperature under N₂. Vacuum filtration over a celite filter cake removed generated salts and silver (I) oxide from the crude product. Dichloromethane was removed through rotary evaporation and the product was precipitated in ice cold diethyl ether. The precipitate was recovered via filtration, washed with cold diethyl ether, and dried under vacuum. The resulting tosylate-functionalized PEG (HO-PEG-OTs) was stored under N₂ until further use. ^1H NMR (400 MHz, DMSO-*d*₆): δ 7.78 - 7.72 (d, 2H), 7.47 - 7.43 (d,

2H), 4.55 - 4.49 (t, 1H, OH), 4.09 - 4.06 (t, 2H, CH₂-SO₂), 3.49 - 3.46 (s, 180H, PEG backbone), 2.40 - 2.38 (s, 3H, CH₃).

2.3.5. Synthesis of Bn-PPS-*b*-PEG-OH BCPs

Hydroxyl-terminated BCPs (Bn-PPS-*b*-PEG-OH) were prepared by endcapping PPS homopolymer with HO-PEG-OTs. Benzyl mercaptan (For FMs: 53.7 μ L, 0.61 mmol, 1 EQ; For MCs: 62.7 μ L, 0.53 mmol, 1 EQ), dissolved in anhydrous dimethylformamide and deprotonated through the addition of sodium methoxide (0.5 M solution in methanol; For FMs: 0.67 mmol, 1.1 EQ; For MCs: 0.58 mmol, 1.1 EQ), was used to initiate the living anionic ring-opening polymerization of propylene sulfide (For FMs: 2.00 mL, 26.58 mmol, 44 EQ; For MCs: 1.00 mL, 12.25 mmol, 23 EQ). The terminal thiolate was endcapped through the addition of HO-PEG₄₅-OTs (For FMs: 4.08 g, 1.69 mmol, 2.75 EQ; For MCs: 3.52 g, 1.45 mmol, 2.75 EQ) and subsequently stirred overnight. Following the removal of dimethylformamide through rotary evaporation, the product was recovered through precipitation in methanol and cooled as needed. Recovered precipitate was dried under vacuum. ¹H NMR (400 MHz, CDCl₃): δ 7.34 - 7.30 (d, 4H, ArH), 3.65 - 3.60 (s, 186H, PEG backbone), 3.00 - 2.85 (m, 89H, CH₂), 2.69 - 2.57 (m, 44H, CH), 1.42 - 1.35 (d, 130H, CH₃).

Benzyl mercaptan (42.0 μ L, 0.35 mmol, 1 EQ), dissolved in anhydrous dimethylformamide and deprotonated through the addition of sodium methoxide (0.5 M solution in methanol; 0.39 mmol, 1.1 EQ), was used to initiate the living anionic ring-opening polymerization of propylene sulfide (1.00 mL, 12.25 mmol, 35 EQ). The terminal thiolate was endcapped through the addition of HO-PEG₂₃-OTs (3.47 g, 2.65 mmol, 7.5 EQ) and subsequently stirred overnight. Following the removal of dimethylformamide through rotary evaporation, the product was recovered through precipitation in methanol and cooled as needed. Recovered precipitate was dried under vacuum. ¹H NMR (400 MHz, CDCl₃): δ 7.32 - 7.29 (d, 4H, ArH), 3.64 - 3.60 (s, 86H, PEG backbone), 2.96 - 2.81 (m, 80H, CH₂), 2.66 - 2.54 (m, 40H, CH), 1.40 - 1.33 (d, 119H, CH₃).

2.3.6. Synthesis of Bn-PPS-*b*-PEG-VS BCPs

The synthesis of vinyl sulfone-functionalized BCP (Bn-PPS-*b*-PEG-VS) was adapted from a previously published protocol [215]. Lyophilized PPS-*b*-PEG-OH (For PSs: 0.86 g, 0.22 mmol, 1 EQ; For FMs: 1.05 g, 0.20 mmol, 1 EQ) was dissolved in anhydrous dichloromethane and flushed with a N₂ atmosphere. Sodium hydride (For PSs: 0.26 g, 1.08 mmol, 50 EQ; For FMs: 0.24 g, 9.90 mmol, 50 EQ) was added to the stirring solution under N₂. Following hydrogen evolution, divinyl sulfone (For PSs: 1.09 mL, 1.08 mmol, 50 EQ; For FMs: 0.99 mL, 9.90 mmol, 50 EQ) was immediately added to the vigorously stirring solution. The solution was stirred under N₂ for a minimum of three days. Salt was removed from the crude product through vacuum filtration over a celite filter cake. Dichloromethane was removed through rotary evaporation and the resulting product was precipitated in methanol a minimum of three times. The recovered product was dried under vacuum. ¹H NMR (400 MHz, CDCl₃): δ 7.31 - 7.28 (d, 4H, ArH), 6.84 - 6.74 (dd, 1H, SO₂-CH=CH₂), 6.42 - 6.32 (d, 1H, =CH₂), 6.09 - 6.03 (d, 1H, =CH₂), 3.62 - 3.61 (s, 185H, PEG backbone), 2.95 - 2.80 (m, 86H, CH₂), 2.66 - 2.54 (m, 43H, CH), 1.40 - 1.33 (d, 129H, CH₃).

2.3.7. Synthesis of Bn-PPS-*b*-PEG-Phos BCPs

Phosphate-functionalized BCPs (Bn-PPS-*b*-PEG-Phos) were prepared directly from Bn-PPS-*b*-PEG-OH. Lyophilized Bn-PPS-*b*-PEG-OH (For PSs: 1.0 g, 0.29 mmol, 1 EQ; For FMs: 1.0 g, 0.19 mmol, 1 EQ; For MCs: 1.0 g, 0.28 mmol, 1 EQ) was massed into a previously evacuated and N₂ purged reaction vessel. The polymer was dissolved in 10 mL of anhydrous tetrahydrofuran and flushed with N₂ for one hour. After purging with N₂, the BCP solution was cooled to 0°C. Phosphorous (V) oxychloride (For PSs: 34.3 μL, 0.37 mmol, 1.27 EQ; For FMs: 22.5 μL, 0.24 mmol, 1.27 EQ; For MCs: 33.3 μL, 0.36 mmol, 1.27 EQ) was added dropwise to the vigorously stirred solution. Following the addition, the solution was removed from its ice bath and further allowed to react overnight at room temperature under N₂. The reaction was hydrolyzed through the addition of 5.0 mL of Milli-Q water and allowed to stir for five minutes. Subsequently, the product was extracted with dichloromethane, dried over sodium sulfate, and filtered. Dichloromethane was removed via rotary evaporation. The resulting product was recovered by precipitation and dried under vacuum overnight. ¹H NMR (400 MHz, CDCl₃): δ 7.24 - 7.22 (d, 4H, ArH), 3.58 - 3.54 (s, 71H, PEG backbone), 2.88 - 2.73 (m, 79H, CH₂), 2.59 - 2.47 (m, 40H, CH), 1.33 - 1.26 (d, 117H, CH₃). ³¹P NMR (162 MHz, CDCl₃): δ 0.2 ppm.

2.3.8. Synthesis of Bn-PPS-*b*-PEG-OMs BCPs

Mesylate-functionalized BCPs (Bn-PPS-*b*-PEG-OMs) were prepared directly from Bn-PPS-*b*-PEG-OH. Lyophilized Bn-PPS-*b*-PEG-OH (For PSs: 1.5 g, 0.39 mmol, 1 EQ; For FMs: 1.5 g, 0.26 mmol, 1 EQ; For MCs: 1.0 g, 0.25 mmol, 1 EQ) was massed into a previously evacuated and N₂ purged reaction vessel. The polymer was dissolved in 10 mL of anhydrous tetrahydrofuran and flushed with a N₂ atmosphere. After purging with N₂, triethylamine (For PSs: 327 μ L, 2.35 mmol, 6 EQ; For FMs: 215 μ L, 1.54 mmol, 6 EQ; For MCs: 212 μ L, 1.52 mmol, 6 EQ) was added to the stirred solution. After cooling to 0°C, MsCl (For PSs: 152 μ L, 1.96 mmol, 5 EQ; For FMs: 99 μ L, 1.28 mmol, 5 EQ; For MCs: 98 μ L, 1.27 mmol, 5 EQ) diluted in tetrahydrofuran (10 x Volume of MsCl) was added to the stirred solution dropwise. The reaction was stirred overnight at room temperature under N₂. Salt produced during the reaction was removed via vacuum filtration of the reaction mixture over a celite filter cake. Tetrahydrofuran was removed via rotary evaporation. The resulting product was recovered by precipitation in diethyl ether and dried under vacuum overnight. ¹H NMR (400 MHz, CDCl₃): δ 7.32 - 7.29 (d, 4H, ArH), 4.39 – 4.34 (m, 1H, -CH₂-O-SO₂), 3.64 - 3.60 (s, 80H, PEG backbone), 3.07 – 3.05 (s, 1.5, SO₂-CH₃), 2.95 - 2.80 (m, 73H, CH₂), 2.66 - 2.54 (m, 36H, CH), 1.40 - 1.33 (d, 110H, CH₃).

2.3.9. Synthesis of Bn-PPS-*b*-PEG-N₃ BCPs

Azide-functionalized BCPs (Bn-PPS-*b*-PEG-N₃) were prepared from mesylate-functionalized BCPs. Bn-PPS-*b*-PEG-OMs (For PSs: 1.0 g, 0.3 mmol, 1 EQ; For FMs: 1.1 g, 0.2 mmol, 1 EQ; For MCs: 1.37 g, 0.39 mmol, 1 EQ) was massed into a reaction vessel. After evacuating and then backfilling the reaction vessel with N₂, the polymer was dissolved in 50 mL of anhydrous dimethylformamide. Sodium azide (For PSs: 98 mg, 1.5 mmol, 5 EQ; For FMs: 65 mg, 1.0 mmol, 5 EQ; For MCs: 127 mg, 1.95 mmol, 5 EQ) was added to the stirred solution. After evacuating and backfilling with N₂, the reaction was heated to 90°C and refluxed overnight. Salt produced during the reaction was removed via vacuum filtration of the reaction mixture over a celite filter cake. Dimethylformamide was removed via rotary evaporation. The resulting product was dissolved in tetrahydrofuran and recovered by precipitation in methanol. The precipitate was collected and dried under vacuum overnight. ¹H NMR (400 MHz, CDCl₃): δ 7.32 - 7.29 (d,

4H, ArH), 3.64 - 3.60 (s, 73H, PEG backbone), 3.40 – 3.34 (s, 2, CH₂-N₃), 2.96 - 2.81 (m, 87H, CH₂), 2.66 - 2.54 (m, 42H, CH), 1.40 - 1.33 (d, 128H, CH₃). ¹³C NMR (126 MHz, CDCl₃): δ 138.2, 128.9, 128.5, 127.2, 70.6, 67.0, 50.7, 41.3, 38.4, 20.8.

2.3.10. Synthesis of Bn-PPS-*b*-PEG-NH₂ BCPs

Amine-functionalized BCPs (Bn-PPS-*b*-PEG-NH₂) were prepared from azide-functionalized BCPs. Bn-PPS-*b*-PEG-N₃ (For PSs: 0.5 g, 0.115 mmol, 1 EQ) was massed into a reaction vessel. After evacuating and then backfilling the reaction vessel with N₂, the polymer was dissolved in 5.0 mL of anhydrous tetrahydrofuran. Triphenylphosphine (For PSs: 36 mg, 0.139 mmol, 1.2 EQ) was added to the stirred solution. After two hours, 0.5 mL of Milli-Q water was added to the solution. The reaction vessel was evacuated, backfilled with N₂, and was permitted to stir at room temperature overnight. The tetrahydrofuran and water mixture was removed via rotary evaporation. The crude product was subsequently dissolved in dichloromethane and precipitated in methanol. The precipitate was cooled as needed, recovered, and lyophilized. ¹H NMR (400 MHz, CDCl₃): δ 7.34 - 7.31 (d, 4H, ArH), 3.67 - 3.63 (s, 69H, PEG backbone), 2.99 - 2.84 (m, 79H, CH₂), 2.66 - 2.54 (m, 40H, CH), 1.42 - 1.35 (d, 117H, CH₃). ¹³C NMR (126 MHz, CDCl₃): δ 138.2, 128.9, 128.5, 127.2, 70.6, 41.3, 38.4, 20.8.

2.3.11. Polymer Characterization

¹H, ¹³C, and ³¹P NMR spectra were acquired on either a 400 MHz Bruker Avance III HD Nanobay spectrometer or a 500 MHz Bruker Avance III spectrometer. Samples were prepared at a minimum concentration of 10 mg mL⁻¹ in either deuterated chloroform (CDCl₃) or dimethyl sulfoxide-d₆ (DMSO-d₆). NMR spectra were processed using the Mnova software (Mestrelab Research, Spain). Gel permeation chromatography (GPC) was completed using a Thermo Scientific Dionex UltiMate 3000 (Thermo Fisher Scientific, United States) fit with a manual injector, refractive index detector (ERC Refractomax 520, DataApex), and UV/Vis detector. The system was equipped with two TSKgel GMH_{xL}-L GPC columns (Tosoh Bioscience LLC, United States) assembled in series. Samples were dissolved in high performance liquid chromatography (HPLC)-grade tetrahydrofuran, manually injected, and eluted with an

HPLC-grade tetrahydrofuran mobile phase at a flow rate of 0.6 mL min⁻¹. Fourier transform infrared (FT-IR) spectra were acquired on a Nexus 870 spectrometer (Thermo Nicolet).

2.4. Results and Discussion

2.4.1. Synthesis of Bn-PPS-*b*-PEG-OMe BCPs

Since PEG-*b*-PPS was first synthesized in 2001, mPEG has been the most commonly used PEG derivative for this BCP system. The lone hydroxyl exhibited by mPEG is amenable to functionalization. But as hydroxide ions are strong bases, they are, in turn, poor leaving groups. To prepare functionalized derivatives of mPEG, the hydroxyl is initially converted into a better leaving group. For the purpose of preparing PEG-*b*-PPS, the hydroxyl of mPEG has been converted to sulfonate esters, such as tosylate or mesylate [52], or to alkyl halides [30, 57], which can both be easily displaced via nucleophilic substitution. These mPEG derivatives have been directly used to prepare PEG-*b*-PPS by reacting with the terminal thiolate of PPS, but alternatively, they can be used to prepare a sulfur-containing macroinitiator. To generate a protected mPEG initiator, thioacetic acid has been employed to generate mPEG-thioacetate (mPEG-TA) [30, 52, 57].

In my own work, I have prepared mPEG-mesylate (mPEG-OMs), as described by Scott et al. [192], for the preparation of methoxy (MeO)-functionalized BCPs. Similar to the tosylate-functionalized mPEG described by Napoli et al., mPEG-OMs can be readily converted into the stable macroinitiator mPEG-TA, which can initiate the polymerization of propylene sulfide [33, 95, 216]. Alternatively, mPEG-OMs can be used to endcap the polymerization of propylene sulfide, as the terminal thiolate of PPS can displace the mesylate through nucleophilic substitution [192]. I have employed both synthetic pathways, depicted in **Figure 2-1**, for the preparation of MeO-functionalized BCPs. Representative ¹H NMR spectra for mPEG₄₅-OMs and mPEG₄₅-TA can be found in **Figure 2-2** and **Figure 2-3**, respectively.

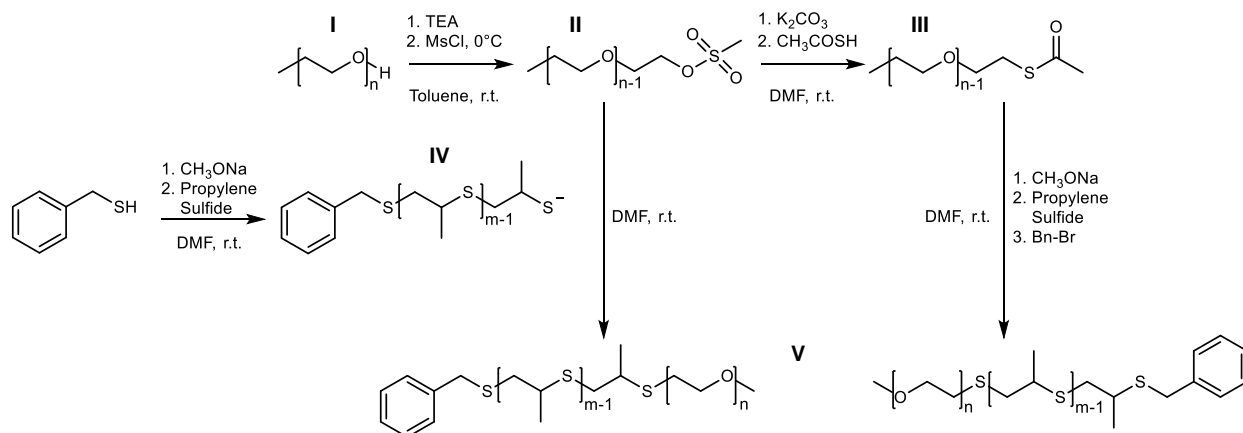


Figure 2-1. Synthetic pathways used to generate methoxy group terminated PEG-*b*-PPS BCPs.

Poly(ethylene glycol) monomethyl ether (mPEG) (I) is used to prepare mPEG-mesylate (II). II can be used as an intermediate to generate mPEG-thioacetate (III), which can subsequently be activated by base and employed to perform anionic ring-opening polymerization on propylene sulfide to produce Bn-PPS-*b*-PEG-OMe (V). Alternatively, II can be utilized directly to endcap poly(propylene sulfide) homopolymer (IV) that has been initiated with a sulfhydryl-containing small molecule, like benzyl mercaptan. Thus, V can be prepared utilizing an mPEG derivative as either an initiator or endcapping agent. TEA = triethylamine, MsCl = methanesulfonyl chloride, r.t. = room temperature, K₂CO₃ = potassium carbonate, CH₃COSH = thioacetic acid, DMF = dimethylformamide, CH₃ONa = sodium methoxide, Bn-Br = benzyl bromide.

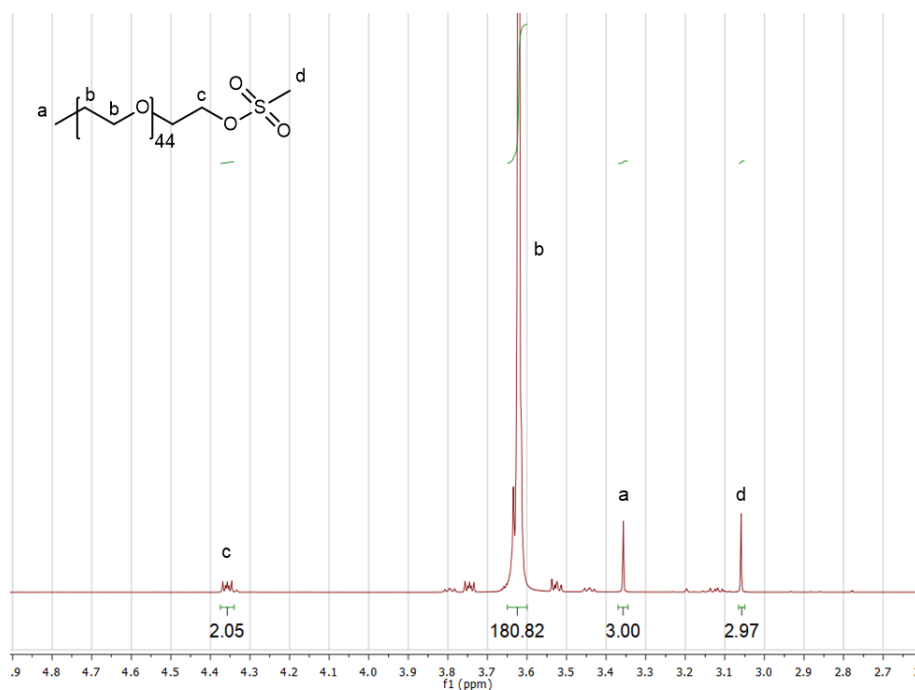


Figure 2-2. Representative ¹H NMR for mPEG₄₅-OMs in CDCl₃.

Figure 2-4 depicts overlays of the GPC chromatograms associated with the preparation of mPEG-OMs and mPEG-TA. A summary of PEG-derivatives generated for this dissertation can be found in **Table 2-2**. I have generally used mPEG₄₅-OMs as an endcapping agent for BCPs intended to self-assemble into FMs and MCs while I have used mPEG₁₇-TA as an initiator for PS-forming BCPs. A representative ¹H NMR spectrum and an overlay of the GPC chromatograms for PS-, FM-, and MC-forming Bn-PPS-*b*-PEG-OMe may be found in **Figure 2-5** and **Figure 2-6**, respectively. **Table 2-3** summarizes the characteristics of the syntheses and MeO-functionalized BCPs prepared in this dissertation.

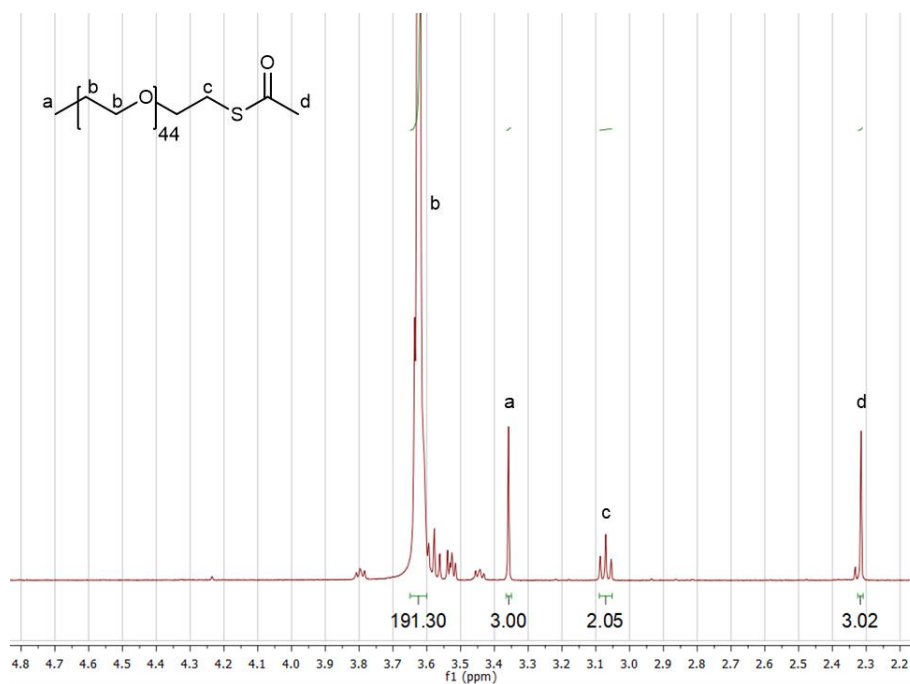


Figure 2-3. Representative ¹H NMR for mPEG₄₅-TA in CDCl₃.

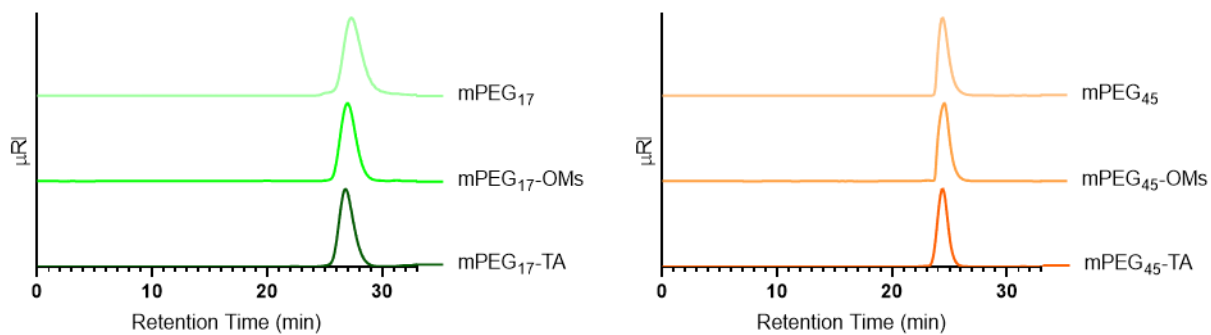


Figure 2-4. Gel permeation chromatography (GPC) chromatograms of mPEG derivatives. GPC chromatograms (refractive index versus retention time) for derivatives of mPEG₁₇ (left) and (b) mPEG₄₅ (right).

Table 2-2. Summary of PEG syntheses.

Polymer	Molecular Weight (g mol⁻¹)	Steps	Yield, Step (%)
mPEG ₁₇ -OMs	880	1	93.3
mPEG ₄₅ -OMs	2,078	1	94.3
mPEG ₁₇ -TA	863	2	30.7
mPEG ₄₅ -TA	2,196	2	76.0
PEG ₂₃ -OTs	1,147	1	88.0
PEG ₄₅ -OTs	2,140	1	91.9

mPEG = Poly(ethylene glycol) methyl ether, OMs = Mesylate,

TA = Thioacetate, PEG = Poly(ethylene glycol), OTs = Tosylate

Table 2-3. Summary of MeO-BCP syntheses used for nanocarrier formation.

Polymer	Molecular Weight (g mol⁻¹)	f_{PEG}	Steps	Yield, Step (%)
Bn-PPS ₂₈ - <i>b</i> -PEG ₄₅ -OMe	4,473	0.53	1	41.0
Bn-PPS ₄₄ - <i>b</i> -PEG ₄₅ -OMe	5,378	0.38	1	60.5
Bn-PPS ₂₈ - <i>b</i> -PEG ₁₇ -OMe	2,982	0.26	1	62.5

Bn = Benzyl, PPS = Poly(propylene sulfide), *b* = Block, PEG = Poly(ethylene glycol), OMe = Methoxy

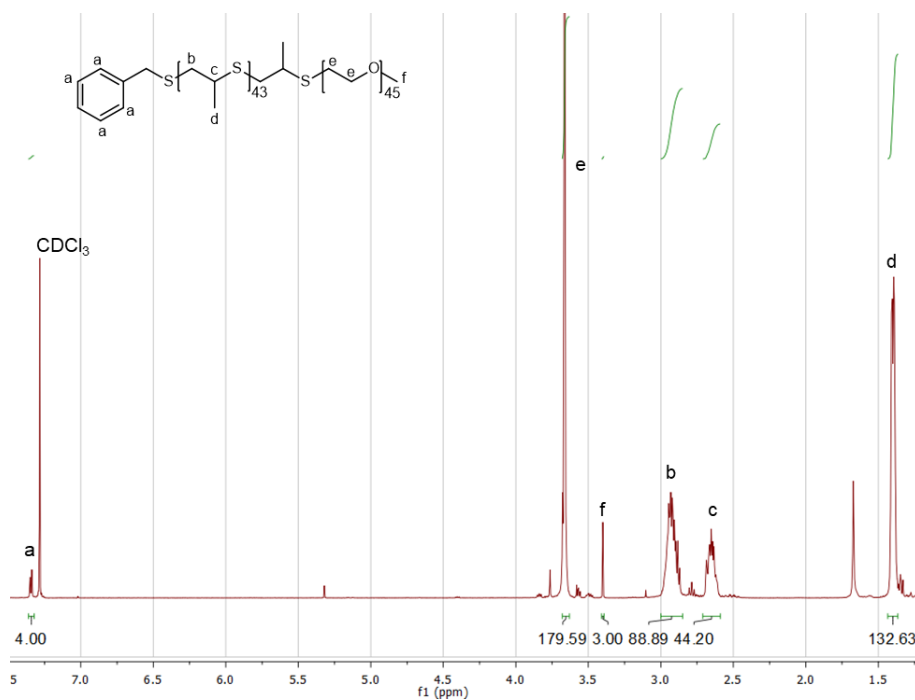


Figure 2-5. Representative ^1H NMR for Bn-PPS₄₄-b-PEG₄₅-OMe in CDCl_3 .

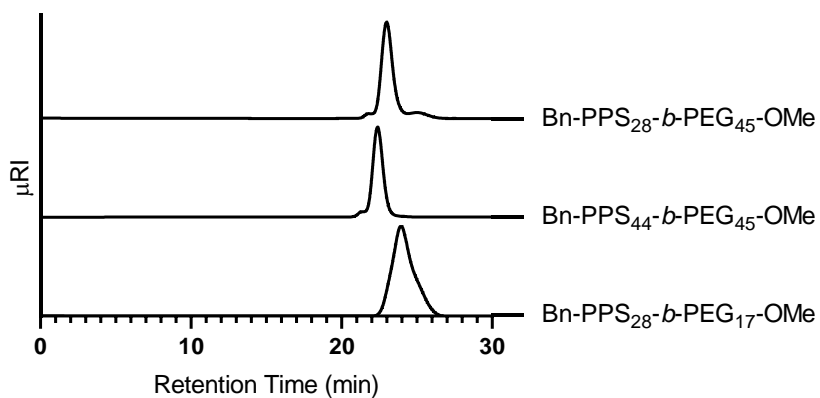


Figure 2-6. GPC chromatograms of methoxy group functionalized BCPs. GPC chromatograms (refractive index versus retention time) for Bn-PPS₂₈-b-PEG₄₅-OMe, Bn-PPS₄₄-b-PEG₄₅-OMe, and Bn-PPS₂₈-b-PEG₁₇-OMe used for the preparation of MCs, FMs, and PSs, respectively.

2.4.2. Synthesis of α -tosylate- ω -hydroxyl-PEG

As was discussed in Section 2.2., the relatively inert nature [217] of the terminal methoxy group on mPEG limits the application of Bn-PPS-*b*-PEG-OMe, particularly if the application entails the surface attachment of targeting ligands for active targeting strategies. One attempt at circumventing this limitation has been to incorporate a secondary amphiphile that is amenable to chemical modification [197]. But such strategies have their own limitations, as nanocarriers prepared through the coassembly of two or more BCPs can result in multiple nanocarrier populations that are segregated by BCP. As such, this strategy is limited in the percentage of secondary amphiphile that can be incorporated. To avoid this constraint, I sought to investigate how functionally diverse PEG-*b*-PPS BCPs could be prepared. By preparing BCPs that varied only in their PEG termini (equivalent f_{PEG} and choice of monomers), the amphiphile segregation observed in the mixed-amphiphile strategy could potentially be avoided. To successfully prepare such BCPs, I first synthesized heterobifunctional PEG.

Heterobifunctional PEGs, those exhibiting a different functional group at either terminus, have been investigated for the preparation of surface reactive PEG-*b*-PPS nanocarriers [201, 208, 209]. In these studies, heterotelechelic PEGs were purchased, which can limit both the scale and functional diversity of the subsequently generated BCPs due to cost. To avoid this limitation, I adapted a previously published synthesis for the monotosylation of PEG [213]. The resulting product, α -tosylate- ω -hydroxyl PEG, is an ideal starting material for the generation of chemically diverse PEG-*b*-PPS BCPs. The tosylate permits the use of this material to endcap the polymerization of propylene sulfide and the remaining hydroxyl is amenable to chemical functionalization. The described synthetic pathway is portrayed in **Figure 2-7**.

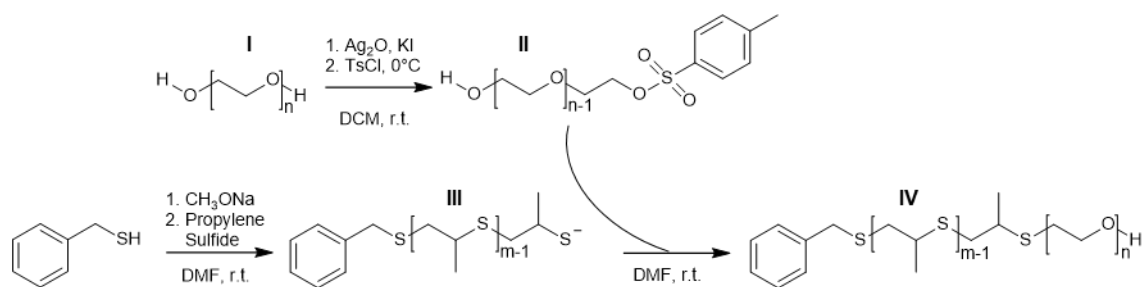


Figure 2-7. Synthetic pathway used to generate hydroxyl-terminated PEG-*b*-PPS BCPs.

Poly(ethylene glycol) (PEG) (**I**) is used to prepare PEG-tosylate (**II**). **II** can be used directly to endcap poly(propylene sulfide) homopolymer (**III**) that has been initiated with benzyl mercaptan following base-activation. Successful endcapping with **II** results in Bn-PPS-*b*-PEG-OH (**IV**). Ag₂O = silver (I) oxide, KI = potassium iodide, TsCl = p-toluenesulfonyl chloride, DCM = dichloromethane, r.t. = room temperature, CH₃ONa = sodium methoxide, DMF = dimethylformamide

The synthesis, originally described by Bouzide and Sauve for the selective monotosylation of small symmetric diols [214], involves silver (I) oxide and a catalytic amount of potassium iodide. Bouzide and Sauve attribute the monotosylation achieved through this synthesis to the formation of internal hydrogen bonds [214]. They theorized that as the oxygens of the PEG backbone complexed around the silver cations, there is an increased probability that one of the hydrogens from the two hydroxyls can achieve close enough proximity to form a hydrogen bond with an oxygen atom along the PEG backbone. With the formation of this internal hydrogen bond, the hydrogen atom becomes less acidic. Thus, the hydrogen of the hydroxyl group that is not involved in an internal hydrogen bond is more likely to be deprotonated by silver (I) oxide.

A representative ¹H NMR spectrum for α-tosylate-ω-hydroxyl-PEG₄₅ is depicted in **Figure 2-8**. The spectrum was acquired in DMSO-d₆. Unlike in CDCl₃, the hydrogen from the hydroxyl group is visible, appearing as a triplet from 4.55 – 4.49 ppm, and can be used to quantify the degree of PEG functionalization. Integration of the spectrum peaks indicated that ≈100% functionalization was achieved. Overlays of the chromatograms of PEG and PEG-OTs are depicted in **Figure 2-9**. Characteristics of the PEG-OTs synthesis can be found in **Table 2-2**.

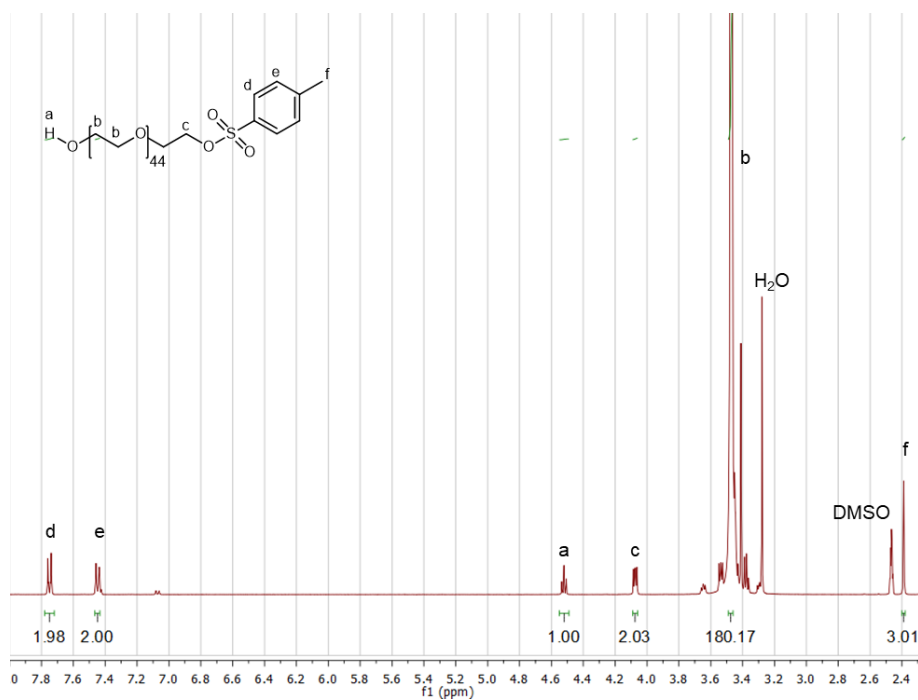


Figure 2-8. Representative ^1H NMR for PEG₄₅-OTs in DMSO- d_6 .

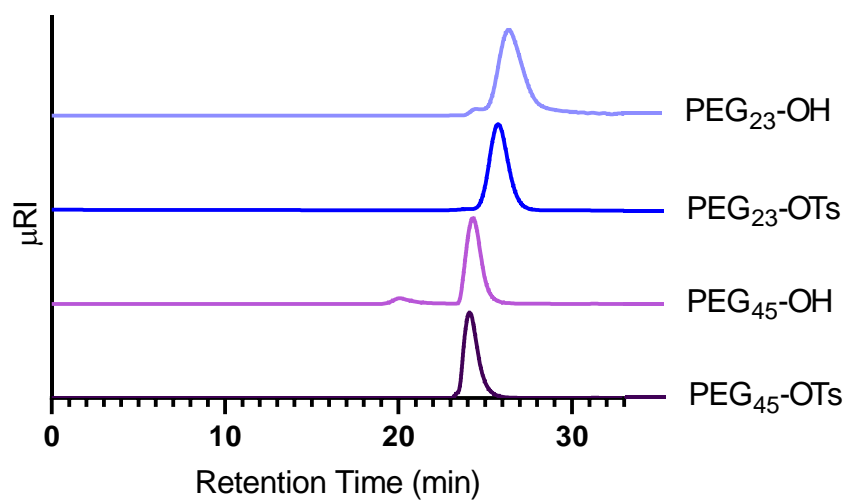


Figure 2-9. GPC chromatograms of tosylate-functionalized PEG. GPC chromatograms (refractive index versus retention time) for PEG₂₃-OTs and PEG₄₅-OTs overlaid with the chromatograms of PEG₂₃ and PEG₄₅.

^1H NMR does not distinguish between the mono- and ditosyl products. While Mahou et al. were able to achieve solely the monotosyl product from this synthesis, the crude product I synthesized was a mixture of un-, mono-, and difunctionalized PEG. An attempt at the quantitative functionalization of PEG would, in theory, result in a statistical distribution of un-, mono-, and difunctionalized PEG. Thus, 50% of the PEG product would be the monotosyl product. By using the asymmetric activation strategy described by Mahou et al., I was able to achieve up to $\approx 85\%$ of the monotosyl product (a value estimated from the degree of functionalization determined through ^1H NMR in subsequent syntheses). The increase in the fraction of monotosyl product and the scale this synthesis could be conducted allowed me to explore several functionalized derivatives of PEG-*b*-PPS.

2.4.3. Synthesis of Bn-PPS-*b*-PEG-OH BCPs

HO-PEG-OTs was used to endcap the polymerization of propylene sulfide. The terminal thiolate displaced the tosylate group exhibited by PEG through nucleophilic substitution, and in the process, covalently linked the two blocks to form Bn-PPS-*b*-PEG-OH. A representative ^1H NMR spectrum for Bn-PPS-*b*-PEG-OH is depicted in **Figure 2-10**.

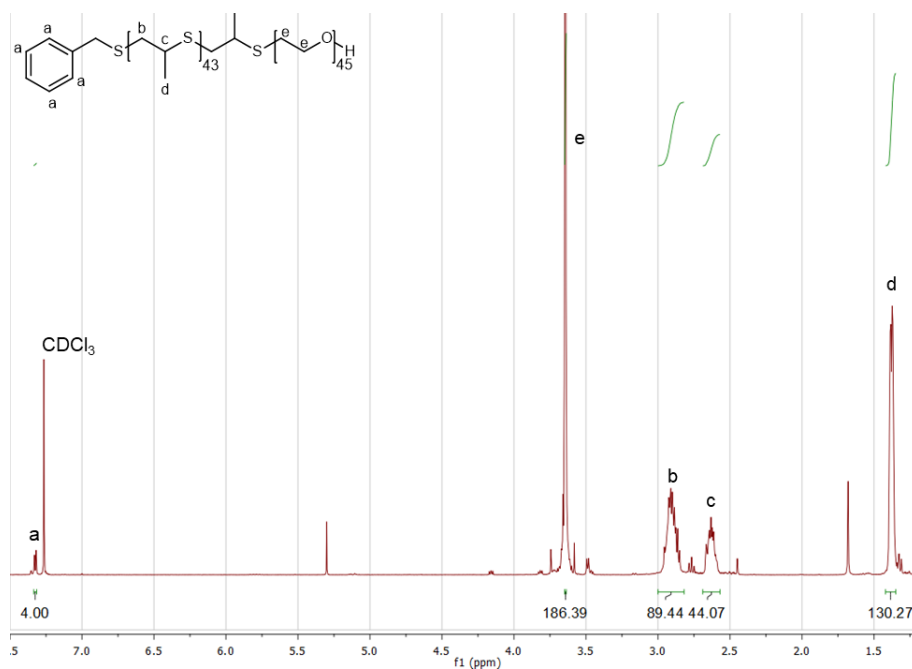


Figure 2-10. Representative ^1H NMR for Bn-PPS₄₄-*b*-PEG₄₅-OH in CDCl_3 .

The protons of the aromatic ring of the benzyl group were used to assess the degree of functionalization achieved by the α -tosylate- ω -hydroxyl-PEG endcap. As was observed in the functionalization of PEG, this remaining terminal hydroxyl group is amenable to chemical functionalization. As such, the synthesis of Bn-PPS-*b*-PEG-OH was key as it is the starting material for several additional syntheses, the products of which permit the preparation of PEG-*b*-PPS nanocarriers with diverse surface characteristics. The various BCPs synthesized for this dissertation are presented in the reaction scheme depicted in **Figure 2-11**.

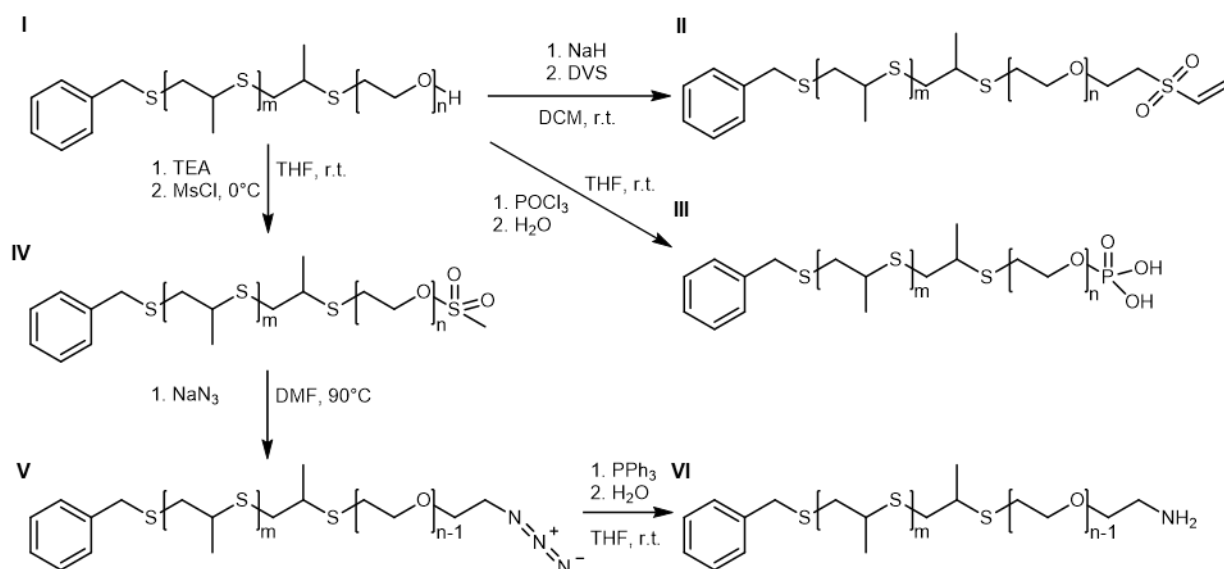


Figure 2-11. Synthetic pathways used to generate functionally diverse PEG-*b*-PPS BCPs. Bn-PPS-*b*-PEG-OH (**I**) can be used directly to prepare Bn-PPS-*b*-PEG-VS (**II**), Bn-PPS-*b*-PEG-Phos (**III**), and Bn-PPS-*b*-PEG-OMs (**IV**). The terminal mesylate group of **IV** can be displaced via nucleophilic substitution to prepare Bn-PPS-*b*-PEG-N₃ (**V**). **V** can subsequently be used to generate Bn-PPS-*b*-PEG-NH₂ via the Staudinger reduction. NaH = sodium hydride, DVS = divinyl sulfone, DCM = dichloromethane, r.t. = room temperature, POCl₃ = phosphorous (V) oxychloride, H₂O = water, THF = tetrahydrofuran, TEA = triethylamine, MsCl = methanesulfonyl chloride, NaN₃ = sodium azide, DMF = dimethylformamide, PPH₃ = Triphenylphosphine

2.4.4. Synthesis of Bn-PPS-*b*-PEG-VS BCPs

From Bn-PPS-*b*-PEG-OH, I sought to synthesize a BCP that would permit the preparation of surface reactive nanocarriers. The terminal functional group I first attempted to introduce onto PEG-*b*-PPS BCPs was vinyl sulfone (VS). VS groups are commonly utilized as bioconjugate linkers [218] given their ability to react quickly and reliably with both thiols and amines through a Michael-type addition. Amines and thiols are ubiquitous throughout living systems as they are integral parts of peptide backbones, amino acid side chains, and many other biological macromolecules. In turn, VS group functionalization on the hydrophilic portion of a BCP would allow for the incorporation of any variety of these components as targeting ligands, including those that are being studied for nanocarrier delivery to APCs [219, 220]. While both thiols and amines are strong Michael donors, reaction conditions can be skewed through changes in pH to favor the reaction of one group over the other [221]. Thiol Michael-type additions are favored under physiological conditions [222] and are advantageous because their mild reaction conditions mitigate the risk of denaturing the selected targeting ligand during conjugation. Furthermore, the resulting thioether sulfone linkage is resistant to hydrolytic degradation [223] which stands in contrast to commonly employed ester linkages that exhibit half-lives on the scale of minutes to hours [224]. As such, the stability afforded from this covalent bond could be beneficial for the attachment of both diagnostic and cell surface targeting moieties but may have limited use in applications where the attached molecule exhibits cleavage-induced activity. In addition to the nature of this chemistry, the preparation of VS-functionalized BCPs was attractive from a synthetic standpoint as the modification of the PEG hydroxyl to a VS group can be completed in a single step.

The preparation of Bn-PPS-*b*-PEG-VS was achieved by adapting a synthesis described by Lutolf and Hubbell for the modification of multiarm PEG [215]. This synthesis uses sodium hydride to deprotonate the terminal hydroxyl group and generate an alkoxide. The alkoxide is then reacted with a large molar excess (≥ 50 molar EQ) of divinyl sulfone. The rationale behind the large excess of divinyl sulfone is to reduce the likelihood of BCP crosslinking. A representative ^1H NMR spectrum for Bn-PPS-*b*-PEG-VS is depicted in **Figure 2-12**. The protons of the aromatic ring of the initiator, benzyl mercaptan, were used to assess the degree of VS-functionalization. By averaging the values of the three vinyl protons, I was able to determine that this synthesis could achieve a degree of VS-functionalization of $\approx 85\%$. GPC confirmed that

minimal BCP crosslinking occurred through this reaction (**Figure 2-13**). The use of this BCP will be explored in Chapter 4.

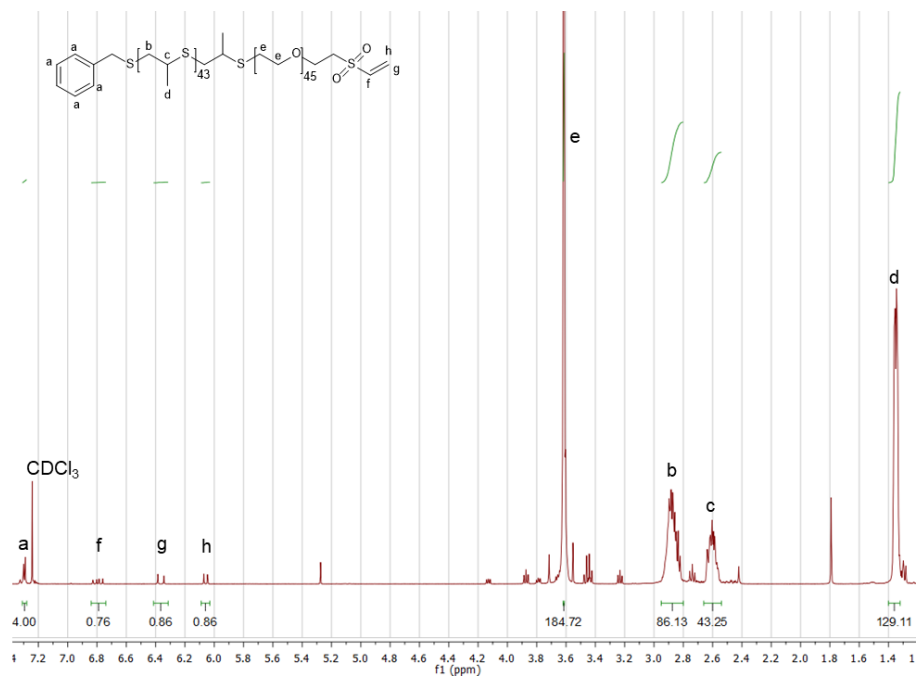


Figure 2-12. Representative ¹H NMR for Bn-PPS₄₃-b-PEG₄₅-VS in CDCl₃.

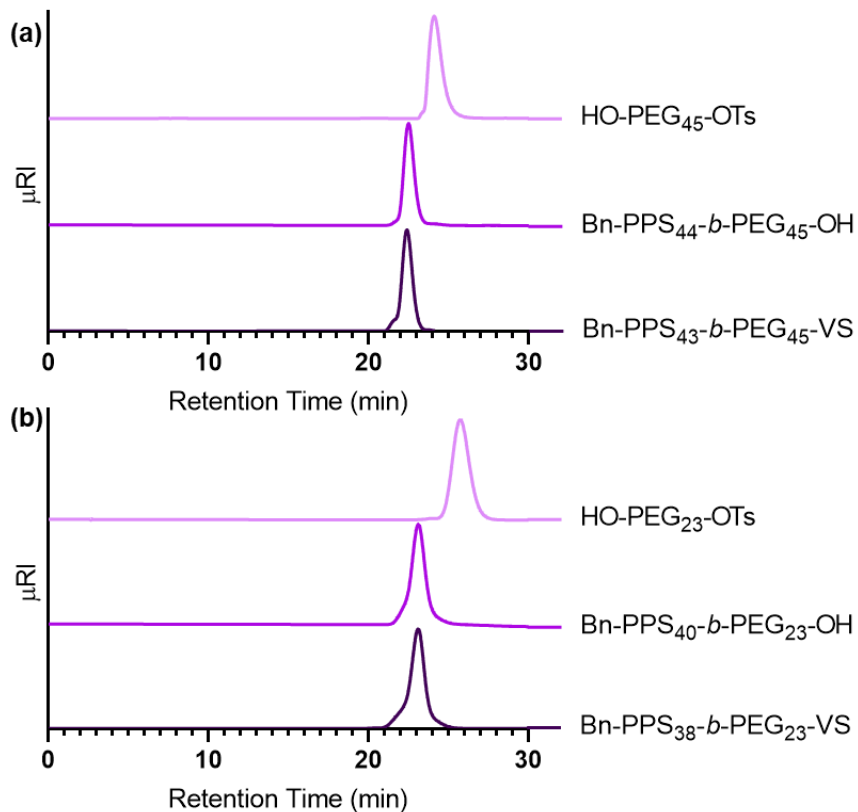


Figure 2-13. GPC chromatograms of vinyl sulfone-functionalized BCPs. GPC chromatograms (refractive index versus retention time) for (a) Bn-PPS₄₃-*b*-PEG₄₅-VS and (b) Bn-PPS₃₈-*b*-PEG₂₃-VS overlaid with the chromatograms of their respective precursors.

2.4.5. Synthesis of Bn-PPS-*b*-PEG-Phos BCPs

As was introduced in Section 1.2.10., nanocarrier surface charge is a characteristic that contributes to the cellular fate of the construct. Surface charge has been implicated in nanocarrier biodistribution [225], cellular internalization [226], and toxicity [227]. The broad impact this physicochemical characteristic imparts on nanocarrier behavior made investigating new functionalized BCPs worthwhile. Under physiologic conditions, nanocarriers composed of hydroxyl- and methoxy-functionalized BCPs will not exhibit a net charge. As such, I aimed to expand the pool of PEG-*b*-PPS BCPs to include derivatives that could permit the generation of nanocarriers with a negative or positive surface charge.

To prepare anionic PEG-*b*-PPS nanocarriers, I aimed to synthesize phosphate (Phos)-functionalized BCPs. Phosphates are an essential functional group for several biomacromolecules. They link nucleotides together through the formation of phosphate ester, or phosphoester, bonds and permit the post-translational modification of proteins through phosphorylation [228]. Their importance to these biological molecules stems from a few inherent characteristics. First, phosphoesters can be readily formed under physiologic conditions (i.e. in an aqueous environment at 37°C). In the absence of the appropriate enzyme, phosphoester bonds are hydrolytically stable. With an estimated half-life at 25°C of 10¹¹ years, the spontaneous hydrolysis of phosphate monoesters is insignificant [229]. But, several families of phosphatases, both non-specific and substrate specific, can efficiently catalyze phosphoester hydrolysis and, consequently, contribute to the dynamic nature of this functional group [230]. Additionally, the multiple sites of protonation expand the range of possible net charges [228] this functional group can achieve. At a minimum, phosphate monoesters exhibit a full negative charge at physiologic pH. From the perspective of nanocarrier design, the ability of phosphates to maintain a negative charge and potentially achieve a range of net charges made pursuing Phos-functionalized BCPs an attractive venture.

The preparation of Bn-PPS-*b*-PEG-Phos was achieved by adapting a synthesis described by Lu et al. for the functionalization of PEG [231]. Phosphorylation of Bn-PPS-*b*-PEG-OH was achieved through the addition of phosphorous (V) oxychloride. The resulting phosphonyl dichloride intermediate was hydrolyzed through the addition of water to generate Bn-PPS-*b*-PEG-Phos. Representative ¹H NMR and ³¹P NMR spectra for Bn-PPS-*b*-PEG-Phos are depicted in **Figure 2-14**. Overlaid in the ³¹P NMR spectrum are the characteristic peaks for phosphorous (V) oxychloride and phosphoric acid. The rightward shift of the phosphorous peak toward 0 ppm suggests the successful preparation of a monoester product [231] that is indicative of Bn-PPS-*b*-PEG-Phos. Furthermore, the unimodal peaks observed in the GPC chromatograms suggests that there was minimal BCP crosslinking (**Figure 2-15**). The use of this BCP will be investigated in Chapter 3.

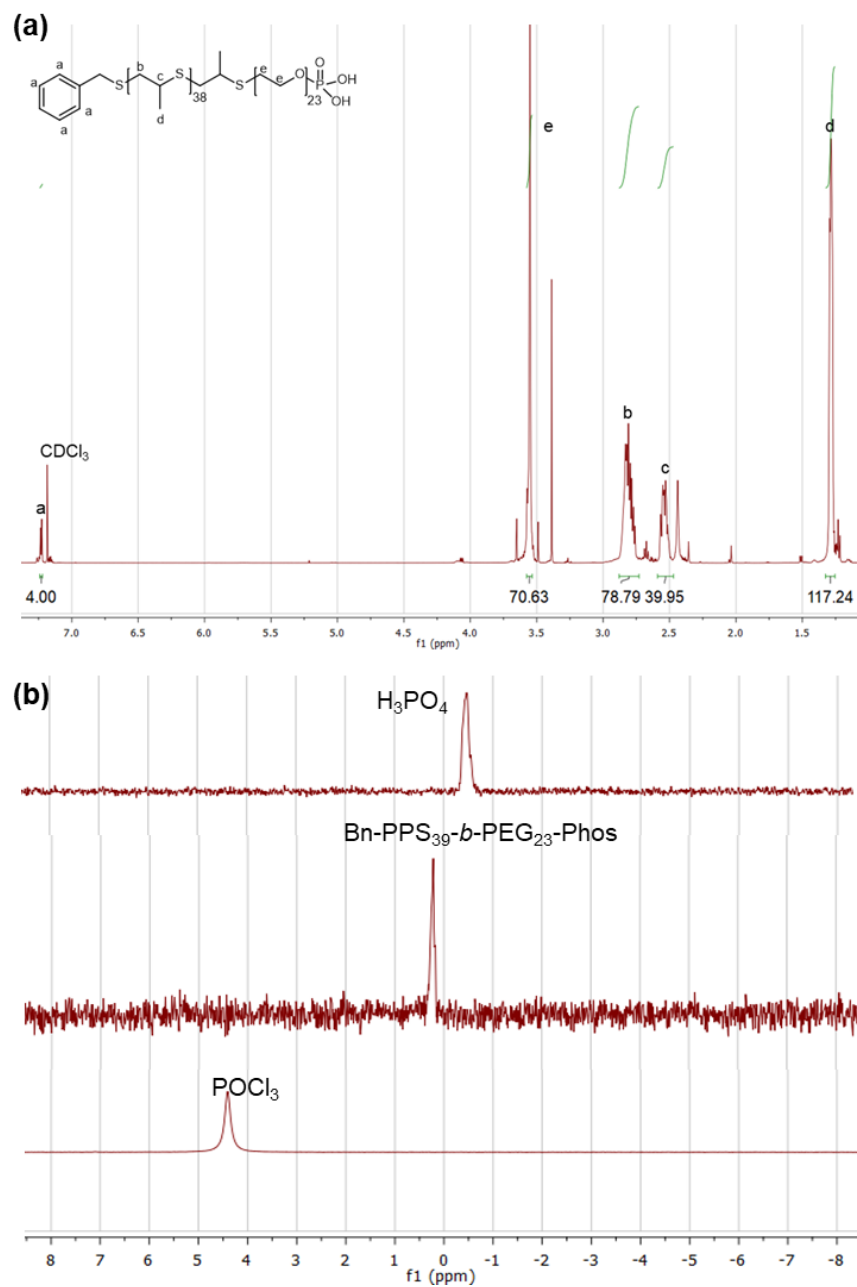


Figure 2-14. Representative NMR spectra of Bn-PPS₃₉-b-PEG₂₃-Phos in CDCl₃. (a) ¹H NMR spectrum for Bn-PPS₃₉-b-PEG₂₃-Phos. (b) ³¹P NMR spectrum for Bn-PPS₃₉-b-PEG₂₃-Phos.

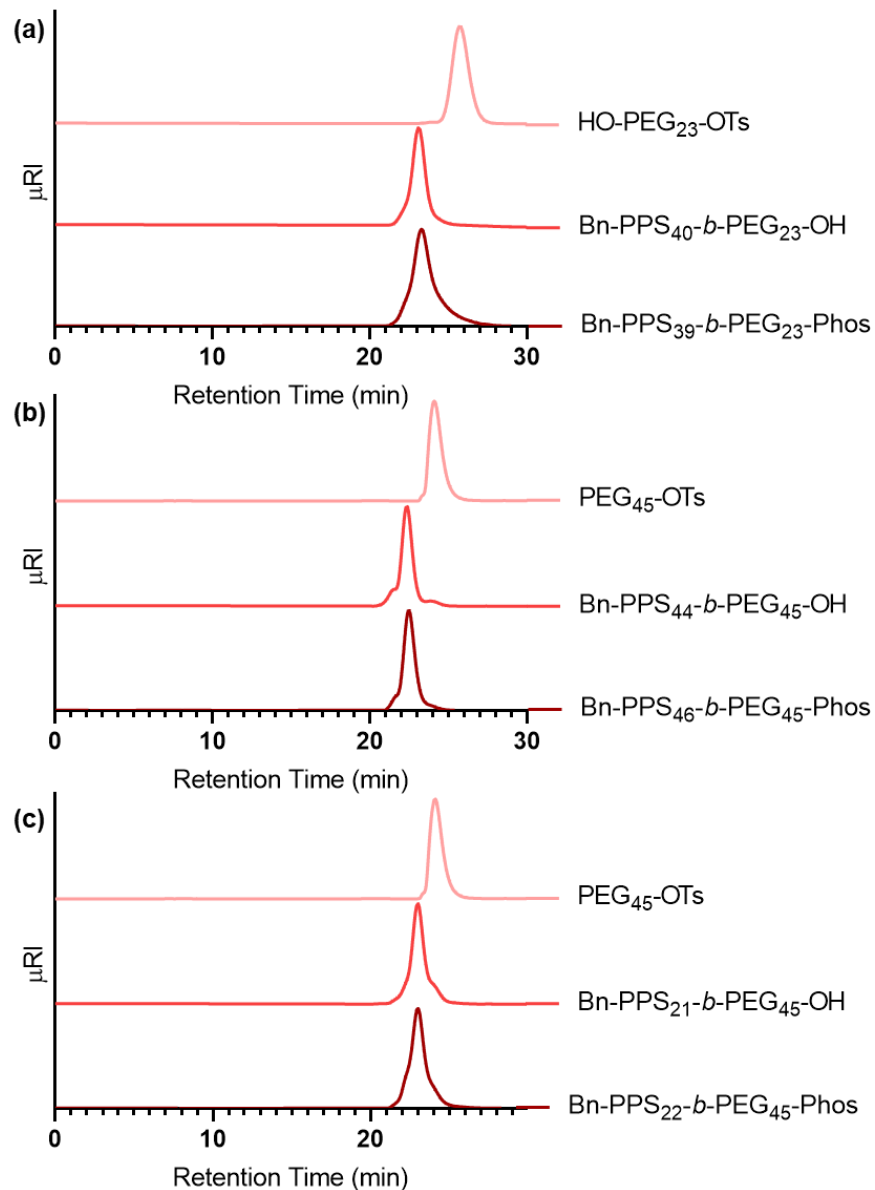


Figure 2-15. GPC chromatograms of phosphate-functionalized BCPs. GPC chromatograms (refractive index versus retention time) for (a) Bn-PPS₃₉-*b*-PEG₂₃-Phos, (b) Bn-PPS₄₆-*b*-PEG₄₅-Phos, and (c) Bn-PPS₂₂-*b*-PEG₄₅-Phos overlaid with the chromatograms of their respective precursors.

2.4.6. Synthesis of Bn-PPS-*b*-PEG-NH₂ BCPs

To prepare cationic PEG-*b*-PPS nanocarriers, I sought a means of preparing amine-functionalized BCP. Unlike the VS- or Phos-functionalized BCP syntheses, a multistep synthetic pathway was required. Following the general procedure described previously for mPEG, Bn-PPS-*b*-PEG-OH was functionalized with a mesylate leaving group to expand the range of nucleophiles able to successfully substitute at this position. A representative ¹H NMR spectrum for Bn-PPS-*b*-PEG-OMs is depicted in **Figure 2-16**. The appearance of a multiplet at 4.36 indicated the attachment of the mesylate group on the BCP. Integration of the singlet at 3.06 ppm, characteristic of the methyl protons of the mesylate group, was used to quantify the degree of functionalization.

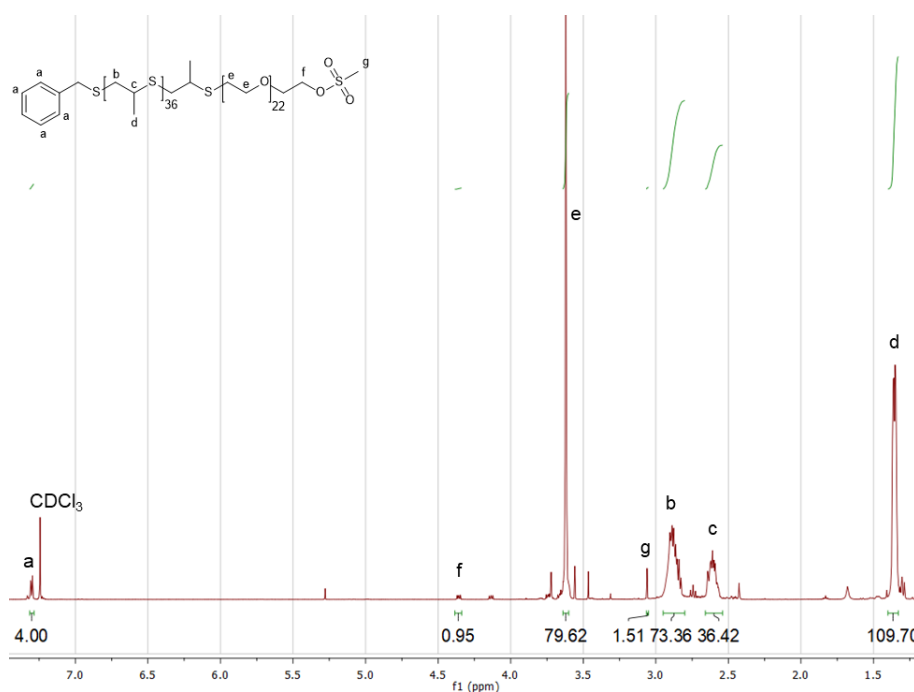


Figure 2-16. Representative ¹H NMR for Bn-PPS₃₇-*b*-PEG₂₃-OMs in CDCl₃.

Displacement of the terminal mesylate with sodium azide produced azide (N₃)-functionalized BCP (Bn-PPS-*b*-PEG-N₃). While this BCP was initially synthesized as an intermediate, azides exhibit several useful qualities that should be briefly introduced. Azides are bioorthogonal functional groups that

have been readily utilized within the biomaterials field for the surface attachment of ligands such as peptides [232]. The versatility of azides has permitted their use in a biological context via three reactions: the Staudinger ligation [233], Cu(I)-catalyzed azide-alkyne cycloaddition [234, 235], and strain-promoted azide-alkyne [3 + 2] cycloaddition [236]. The latter two reactions are considered “click chemistries” due to their high efficiency/yields, mild reaction conditions, and minimal purification requirements [237]. Due to the toxicity of the copper catalyst [238], the copper-free strain-promoted azide-alkyne [3 + 2] cycloaddition is particularly interesting for the post-formation modification of nanocarriers.

The introduction of the azide on Bn-PPS-*b*-PEG-N₃ was confirmed through ¹H NMR, ¹³C NMR, and FT-IR. In the ¹H NMR spectrum depicted in **Figure 2-17**, the loss of the ethyl peaks adjacent to and methyl proton peaks of the mesylate group (at 4.36 and 3.06 ppm, respectively) suggests the successful substitution of the mesylate group. The presence of peaks at 67.0 and 50.7 ppm depicted in the ¹³C NMR spectrum of **Figure 2-18** indicates the successful introduction of an azide. Additionally, the appearance of a peak on the FT-IR spectrum presented in **Figure 2-19** at 2,100 cm⁻¹, characteristic of N=N=N stretching, further suggests the successful preparation of Bn-PPS-*b*-PEG-N₃. To further confirm the presence of a functional azide on the BCP, I reacted Bn-PPS-*b*-PEG-N₃ with a dibenzocyclooctyne (DBCO)-modified PEG (DBCO-PEG₁₁₄). **Figure 2-20** depicts the GPC chromatograms of Bn-PPS-*b*-PEG-N₃, DBCO-PEG₁₁₄, and the Bn-PPS-*b*-PEG-Click-PEG₁₁₄. The leftward shift of the PEG conjugated BCP indicates an increase in molecular weight and further suggests the successful preparation of Bn-PPS-*b*-PEG-N₃.

In addition to being valuable functional groups for bioconjugation, azides can be reduced to primary amines via the Staudinger reduction. In this reaction, the nucleophilic addition of an aryl phosphine at the terminal nitrogen of an azide group results in the formation of an iminophosphorane, which can subsequently be hydrolyzed to an amine [239].

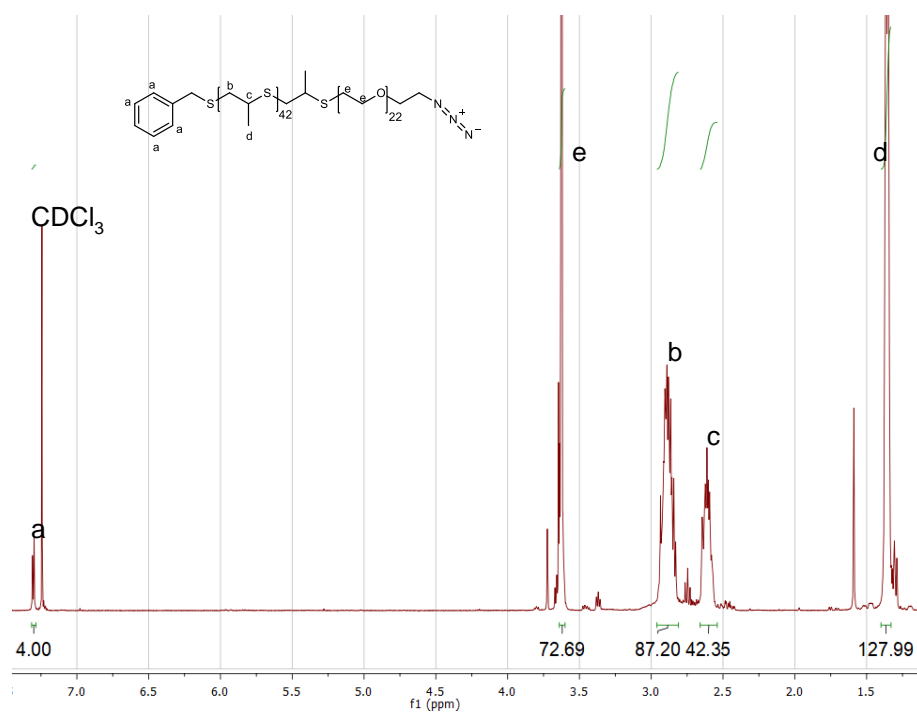


Figure 2-17. Representative ¹H NMR for Bn-PPS₄₃-b-PEG₂₃-N₃ in CDCl₃.

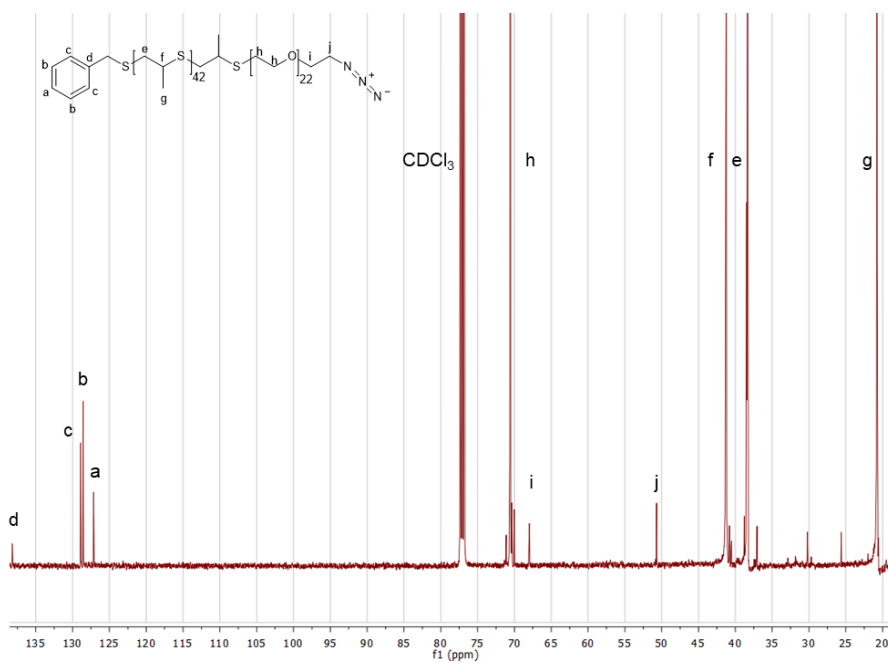


Figure 2-18. Representative ¹³C NMR for Bn-PPS₄₃-b-PEG₂₃-N₃ in CDCl₃.

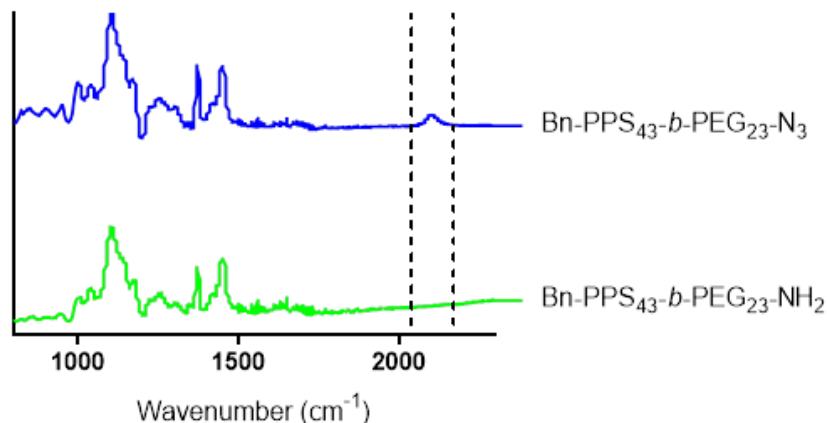


Figure 2-19. FT-IR spectra of azide- and amine-functionalized BCPs. FT-IR spectra of Bn-PPS₄₃-*b*-PEG₂₃-N₃ (top) and Bn-PPS₄₃-*b*-PEG₂₃-NH₂ (bottom). Dashed lines draw attention to the region where N=N=N stretching is expected. The lack of this peak in the bottom spectrum suggests the successful reduction of the azide.

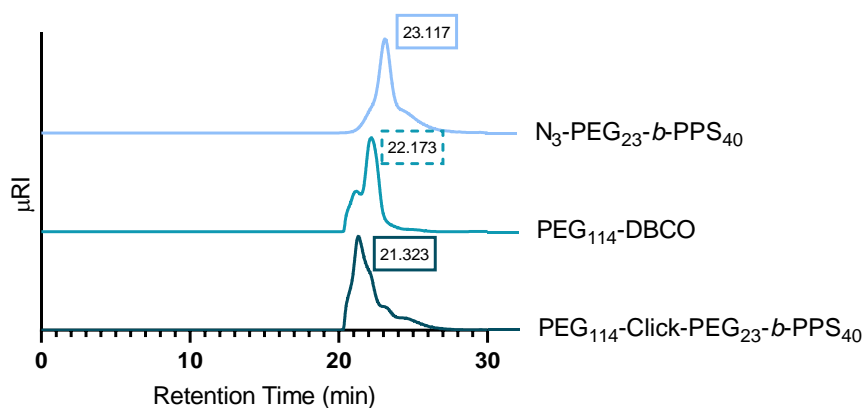


Figure 2-20. GPC confirmation of azide-functionalization. Overlay of GPC chromatograms (refractive index versus retention time) for Bn-PPS₄₀-*b*-PEG₂₃-N₃, PEG₁₁₄-DBCO, and the conjugated product of the two. The leftward shift in retention time for the conjugated product is indicative of an increase in molecular weight, which suggests the presence of a reactive azide on the BCP.

Bn-PPS-*b*-PEG-N₃, dissolved in tetrahydrofuran, was reacted with triphenylphosphine and hydrolyzed through the addition of water to prepare an amine-functionalized BCP (Bn-PPS-*b*-PEG-NH₂). Representative ¹H NMR and ¹³C NMR spectra for Bn-PPS-*b*-PEG-NH₂ are depicted in **Figure 2-21** and **Figure 2-22**, respectively. The loss of the peaks associated with azide functionalization in the ¹³C NMR spectra (at 67.0 and 50.7 ppm) of **Figure 2-22** and FT-IR spectra (at 2,100 cm⁻¹) of **Figure 2-19** suggest a successful reduction of the azide precursor. GPC chromatograms overlaying the OH-, MeO-, N₃-, and NH₂-BCPs for PSs can be found in **Figure 2-23**. An inability to successfully prepare this amine-functionalized BCP for the formation of MCs and FMs hindered further investigations into its potential applications. Although this material will not be discussed in further depth in this dissertation, it could be a useful BCP for the encapsulation or complexation of negatively charged payloads, such as nucleotides. As such, it permits future investigations of PEG-*b*-PPS nanocarriers as delivery vehicles for messenger RNA, small interfering RNA, and micro RNA.

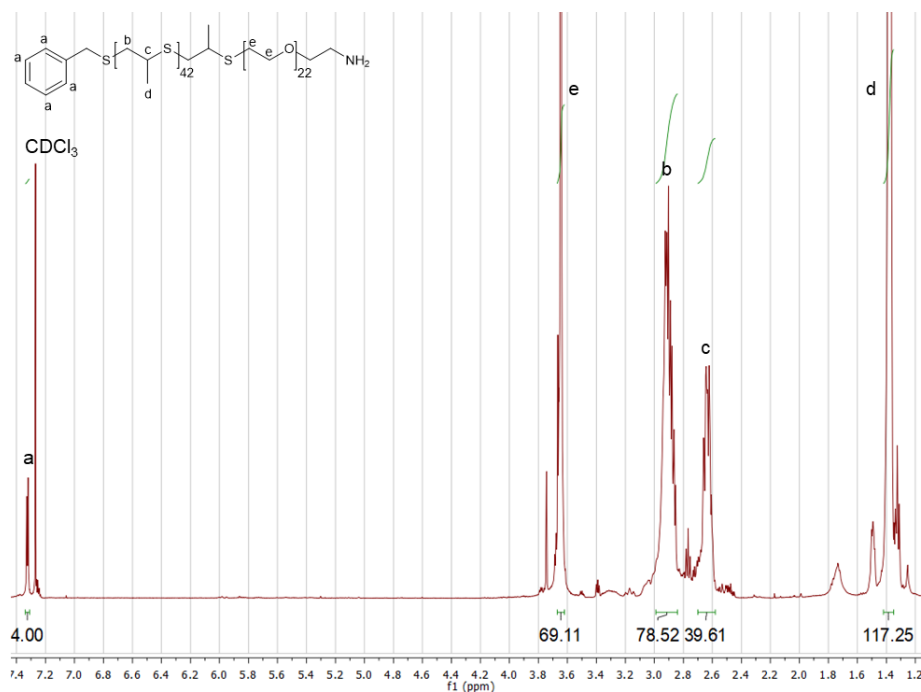


Figure 2-21. Representative ¹H NMR for Bn-PPS₄₃-*b*-PEG₂₃-NH₂ in CDCl₃.

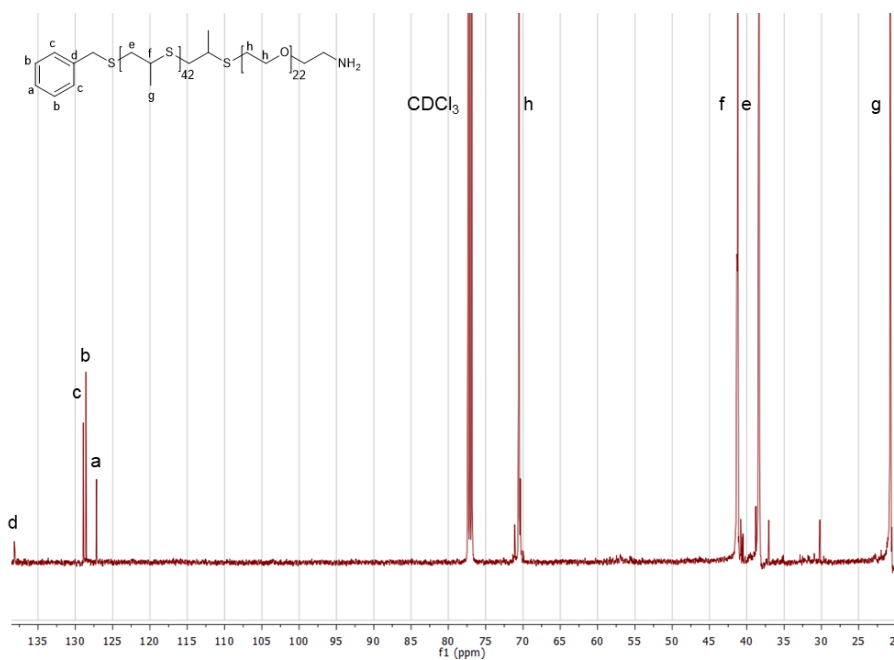


Figure 2-22. Representative ^{13}C NMR for $\text{Bn-PPS}_{43}\text{-}b\text{-PEG}_{23}\text{-NH}_2$ in CDCl_3 .

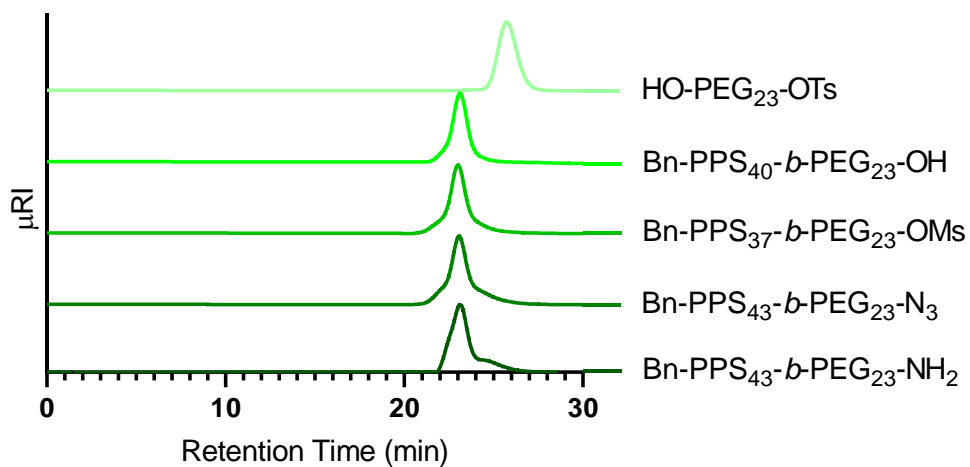


Figure 2-23. GPC chromatograms for the series of BCPs used to prepare $\text{Bn-PPS}_{43}\text{-}b\text{-PEG}_{23}\text{-NH}_2$.

GPC chromatograms (refractive index versus retention time) of $\text{HO-PEG}_{23}\text{-OTs}$, $\text{Bn-PPS}_{40}\text{-}b\text{-PEG}_{23}\text{-OH}$, $\text{Bn-PPS}_{37}\text{-}b\text{-PEG}_{23}\text{-OMs}$, $\text{Bn-PPS}_{43}\text{-}b\text{-PEG}_{23}\text{-N}_3$, and $\text{Bn-PPS}_{43}\text{-}b\text{-PEG}_{23}\text{-NH}_2$.

2.5. Conclusion

Tables 2-4, 2-5, and 2-6 present the BCP and synthesis characteristics for the functionalized-PEG-*b*-PPS BCPs used to prepare PSs, FMs, and MCs, respectively.

Table 2-4. Summary of BCP syntheses for polymersome formation.

BCP Label	Polymer	Molecular Weight (g mol ⁻¹)	f_{PEG}	Steps	Yield, Step (%)
1	Bn-PPS ₄₀ - <i>b</i> -PEG ₂₃ -OH	4,023	0.24	1	66.9
2	Bn-PPS ₃₈ - <i>b</i> -PEG ₂₃ -VS	3,918	0.23	2	58.0
3	Bn-PPS ₃₉ - <i>b</i> -PEG ₂₃ -Phos	3,911	0.21	2	62.8
4	Bn-PPS ₃₇ - <i>b</i> -PEG ₂₃ -OMs	3,790	0.24	2	78.3
5	Bn-PPS ₄₃ - <i>b</i> -PEG ₂₃ -N ₃	4,147	0.20	3	50.5
6	Bn-PPS ₄₃ - <i>b</i> -PEG ₂₃ -NH ₂	3,808	0.21	4	70.0

Bn = Benzyl, PPS = Poly(propylene sulfide), *b* = Block, PEG = Poly(ethylene glycol), OH = Hydroxyl, VS = Vinyl sulfone, Phos = Phosphate, OMs = Mesylate, N₃ = Azide, NH₂ = Amine

Table 2-5. Summary of BCP syntheses used for filomicelle formation.

BCP Label	Polymer	Molecular Weight (g mol ⁻¹)	f_{PEG}	Steps	Yield, Step (%)
1	Bn-PPS ₄₄ - <i>b</i> -PEG ₄₅ -OH	5,436	0.39	1	44.5
2	Bn-PPS ₄₃ - <i>b</i> -PEG ₄₅ -VS	5,469	0.39	2	87.3
3	Bn-PPS ₄₆ - <i>b</i> -PEG ₄₅ -Phos	5,619	0.38	2	61.0
4	Bn-PPS ₄₄ - <i>b</i> -PEG ₄₅ -OMs	5,462	0.37	2	69.5
5	Bn-PPS- <i>b</i> -PEG ₄₅ -N ₃	5,670	0.38	3	67.3

Bn = Benzyl, PPS = Poly(propylene sulfide), *b* = Block, PEG = Poly(ethylene glycol), OH = Hydroxyl, VS = Vinyl sulfone, Phos = Phosphate, OMs = Mesylate, N₃ = Azide

Table 2-6. Summary of BCP syntheses used for micelle formation.

BCP Label	Polymer	Molecular Weight (g mol ⁻¹)	f_{PEG}	Steps	Yield, Step (%)
1	Bn-PPS ₂₁ - <i>b</i> -PEG ₄₅ -OH	3,850	0.58	1	64.4
3	Bn-PPS ₂₂ - <i>b</i> -PEG ₄₅ -Phos	3,982	0.56	2	48.0
4	Bn-PPS ₃₈ - <i>b</i> -PEG ₄₅ -OMs	5,230	0.45	2	41.7
5	Bn-PPS ₃₄ - <i>b</i> -PEG ₄₅ -N ₃	4,860	0.46	3	47.6

Bn = Benzyl, PPS = Poly(propylene sulfide), *b* = Block, PEG = Poly(ethylene glycol), OH = Hydroxyl, Phos = Phosphate, OMs = Mesylate, N₃ = Azide

Through the synthesis of α -tosylate- ω -hydroxyl PEG, Bn-PPS-*b*-PEG-OH can be prepared. The hydroxyl of this BCP is amenable to functionalization and permits the preparation of several BCPs that differ in their PEG termini. The BCPs described in this chapter may be of use in the design of PEG-*b*-PPS nanocarriers relying on either passive or active targeting strategies. Nanocarriers that rely on passive targeting exploit one or several physicochemical characteristics in order to skew delivery to a specific tissue or cell type. Through the preparation of Bn-PPS-*b*-PEG-Phos and Bn-PPS-*b*-PEG-NH₂, nanocarriers exhibiting a negative or positive surface charge may be prepared. Surface charge, in addition to morphology, can now be more thoroughly investigated as a design characteristic in passive targeting strategies employing PEG-*b*-PPS nanocarriers. Furthermore, the synthesis of Bn-PPS-*b*-PEG-VS and Bn-PPS-*b*-PEG-N₃ may permit further investigation of PEG-*b*-PPS nanocarriers in active targeting strategies. While the inclusion of a secondary amphiphile has always allowed for PEG-*b*-PPS nanocarriers to be explored in active targeting, there are limitations concerning how much could be incorporated. The synthesis of these surface-functionalized BCPs directly addresses this limitation as it vastly expands the range of incorporated reactive groups for conjugation. Both the VS- and N₃-functionalized BCPs permit the efficient attachment of targeting ligands and diagnostic agents to the surface of PEG-*b*-PPS nanocarriers. While Bn-PPS-*b*-PEG-VS can conjugate either thiol or amine containing ligands depending on the conjugation conditions, Bn-PPS-*b*-PEG-N₃ presents the opportunity to explore bioorthogonal chemistries, such as the attachment of DBCO-

modified ligands. This latter strategy is particularly appealing as it eliminates the chemical promiscuity that the VS-functionalized BCP may experience when trying to conjugate a ligand with multiple thiols or amines.

Having demonstrated that PEG-*b*-PPS BCPs can be modified to exhibit a variety of different functional groups, my efforts shifted to trying to employ several of these BCPs for applications in passive targeting and sustained nanocarrier delivery.

2.6. Acknowledgements

This work made use of the IMSERC at Northwestern University, which has received support from the NSF (CHE-1048773); Soft and Hybrid Nanotechnology Experimental (SHyNE) Resource (NSF ECCS-1542205); the State of Illinois and International Institute for Nanotechnology (IIN).

I would also like to acknowledge the valuable advice I received from Dr. Fanfan Du. After several attempted synthetic pathways failed in the preparation Bn-PPS-*b*-PEG-NH₂, Fanfan suggested that I attempt the Staudinger reduction. I would also like to thank Yufan Yang. Yufan is an undergraduate researcher who has worked alongside me for the past few years. He has learned many of these syntheses along with me, and I would like to acknowledge his hard work in the generation of these materials.

2.7. Publication Information

Portions of this chapter have been previously published. The published works correspond to the following citations:

Karabin, N.B., et al., *Sustained micellar delivery via inducible transitions in nanostructure morphology.*

Nat Commun, 2018. 9(1): p. 624. [216]

CHAPTER 3

Exploring Combinations of Nanocarrier Surface Chemistry and Morphology for Passive Targeting

3.1. Abstract

Nanocarriers are of significant interest for applications within the immunomodulation space [119, 120, 240]. Due to their importance in both maintaining homeostasis and contributing to inflammation and autoimmunity, the cells of the MPS have garnered significant attention as cellular targets [117]. Efforts to increase the cellular specificity of nanocarriers have included both active [241] and passive [242, 243] targeting strategies, the former of which has been hindered by biological processes that screen the nanocarrier-presented targeting ligands upon their introduction into complex biological environments [244-246]. Previous studies have demonstrated that PEG-*b*-PPS nanocarrier morphology can be engineered to passively enhance the targeting specificity of the cells of the MPS. Building off this understanding, we demonstrate that morphology can be combined with nanocarrier surface chemistry to further influence cell associations within the MPS. Furthermore, we supplement previous studies by demonstrating how combinations of PEG-*b*-PPS nanocarrier morphology and surface chemistry achieve differential protein adsorption, a characteristic known to govern nanocarrier-cell interactions.

3.2. Introduction

3.2.1. Nanocarrier Synthetic versus Biological Identity

Introduced in Section 1.2.10. was the concept of the nanocarrier biological identity. Following the introduction of nanocarriers into the biological milieu, the once meticulously designed and characterized synthetic identity of the nanocarrier surface is immediately replaced by a new biological identity. This biological identity is the result of biomolecules, primarily proteins, adsorbing to the nanocarrier surface to reduce the high surface energy of the introduced system [181]. This dynamic shell of adsorbed biomolecules at the nanocarrier-fluid interface, dubbed the PC, is the actual surface that cells will directly interact and, as such, plays a central role in defining the cellular fate of the nanocarrier [247]. While the PC

was coined by Dawson and Linse in 2007 [186], the first studies that focused on identifying adsorbed plasma proteins on nanocarrier surfaces occurred about a decade earlier [248].

The PC is generally considered to consist of two separate layers: the hard and soft coronas. The hard corona consists of proteins exhibiting high-affinity interactions with the nanocarrier surface while the soft corona is composed of proteins that are involved in low-affinity interactions with the proteins of the hard corona [249]. The exchange rates associated with these layers vary significantly, with the hard corona exhibiting exchange rates on the scale of hours and the soft corona on the scale of seconds to minutes [250]. Due to the differences in the timescale of their interactions, some have suggested that the hard corona may be more critical in establishing the biological identity of a nanocarrier [181]. As such, much of the research conducted on the PC has focused on the hard corona and, for the remainder of this dissertation, any discussion of the PC will be restricted to the hard corona.

While the hard corona consists of high-affinity interactions between the nanocarrier and proteins, it is still considered a dynamic entity. Blood plasma is a complex solution that contains over 10,000 unique proteins [251]. The concentration of each of these proteins and their respective equilibrium binding constants for a given nanocarrier will determine the composition of the PC at a given time [252]. Several theories have been postulated to describe the process through which the PC achieves its equilibrium state. The “Vroman Effect,” which involves proteins of lower affinity desorbing from the material surface and being displaced by higher affinity proteins [253, 254], has often been discussed in the context of the PC. This process involves a series of adsorption and desorption events and suggests that the composition of the PC is highly dynamic. But a recent study has demonstrated the rapid formation of a PC that varies in the amount of each protein adsorbed over time but not in the diversity of adsorbed proteins [255]. Thus, alternative conceptualizations of the evolution of the PC have been put forth [256]. But given the broad complexity of nanocarrier systems that exist, it is possible, maybe even likely, that no single model perfectly describes this process.

A variety of physicochemical characteristics, including nanocarrier morphology [257], surface chemistry [258], surface charge [188], and porosity [259] govern how the PC forms and influence not only

the gross amount of protein absorbed but also the composition of the PC. These sometimes subtle compositional changes within the PC have been attributed to both promoting [260] and suppressing [261] nanocarrier internalization. As such, this suggests that rationally designing nanocarriers to govern the composition of the PC, rather than to prevent its formation, is a potential strategy for tailoring cellular uptake. The reliance on a nanocarrier's physicochemical properties to control its delivery to a specified cell population is known as passive targeting.

3.2.2. Passive Targeting with PEG-*b*-PPS Nanocarriers

As was introduced in Section 1.2.7., the conventional application of nanocarriers in passive targeting involves the somewhat controversial [115] EPR effect for the treatment of cancer [262]. For such an application, the goal is to enhance the nanocarrier circulation time (i.e. blood exposure) in order to drive accumulation within the tumor [263]. As such, the physicochemical characteristics of the nanocarrier are adjusted to minimize uptake within the MPS. But in immunomodulatory applications, where the cells of the MPS are the cellular targets, the nanocarrier physicochemical characteristics are tailored to shift uptake toward one cell over another. Size [264], shape [265], elasticity [266], and surface charge [267] are just a few of the characteristics that can be designed to skew colloidal uptake within the MPS. One characteristic often discussed in passive targeting is nanocarrier morphology [240], which realistically is defined by several individual physicochemical characteristics (i.e. size, elasticity, hydrophobicity, etc).

Recently, the Scott lab has demonstrated how the morphology of PEG-*b*-PPS nanocarriers can be exploited for passive targeting [33, 95, 204]. In these studies, nanocarriers sharing comparable chemical identities (Bn-PPS-*b*-PEG-OMe) but differing in their self-assembled morphologies were able to achieve varied organ- and cellular-level biodistributions. Yi et al. investigated the cellular fate of PEG-*b*-PPS PSs, FMs, and MCs following intravenous injection [95]. **Figure 3-1** depicts some of the flow cytometric analyses conducted in the study. Excluding the blood, most of the uptake observed within the spleen, lymph nodes, and liver occur via macrophages and dendritic cells. Within these populations, PSs and MCs tend to exhibit higher levels of uptake than the cylindrical FMs. But in the blood, uptake is dominated by neutrophils, monocytes, and dendritic cells. And unlike in the tissue resident cells of the spleen, lymph

nodes, and liver, FMs exhibited higher levels of cell association and internalization than their spherical counterparts.

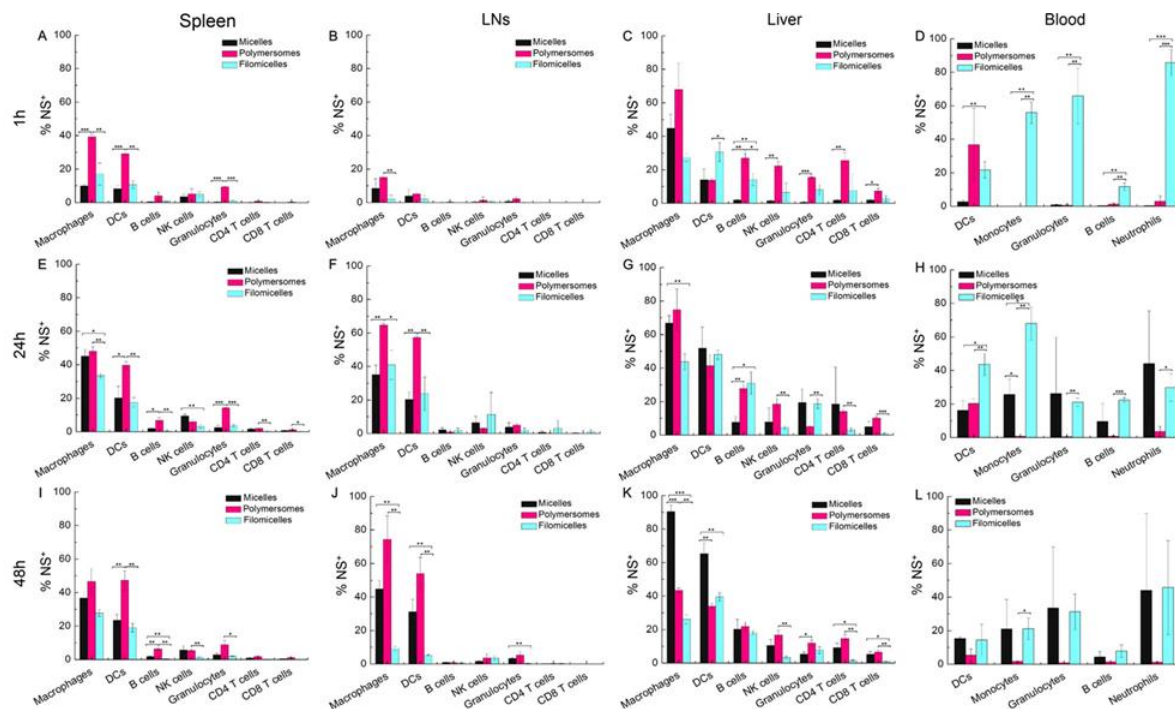


Figure 3-1. Cellular biodistributions of PEG-*b*-PPS nanocarriers following intravenous administration. Flow cytometric analysis of the association of MC, PS, and FM with immune cells isolated from spleen (A, E, I), lymph nodes (LNs) (B, F, J), liver (C, G, K), and blood (D, H, L) of C57BL/6 mice after time points of 1 h (A–D), 24 h (E–H), and 48 h (I–L) following tail vein injection. Histograms show the average percentages \pm standard deviation (SD) of nanostructure positive (NS+) cells for each indicated cell type in different tissue. Macrophages: CD11b+ F4/80+ ; dendritic cells (DCs): CD11c+ ; B cells: CD45+ CD19+ ; natural killer (NK) cells: CD45+ CD49b+ ; granulocytes: Gr-1+ CD11b+ ; CD4 T cells: CD45+ CD3+ CD4+ ; CD8 T cells: CD45+ CD3+ CD8+ ; monocytes: Ly6G–CD11c–CD11b+ ; and neutrophils: CD11b+ Ly6G+. Data were obtained from two independent experiments and contain N = 6–8 for each group. Statistical significance: * $p \leq 0.01$, ** $p \leq 0.005$, *** $p \leq 0.0001$. Reprinted with permission from [95]. © 2016 American Chemical Society.

Similar work stemming from the Hubbell and Levy labs has shown that, in addition to the physicochemical properties of the nanocarrier, route of administration can influence the cellular fate of the nanocarrier. Dowling et al. investigated the cellular biodistribution of PEG-*b*-PPS nanocarriers following subcutaneous administration [204]. **Figure 3-2** depicts the cellular biodistributions assessed via flow cytometry for PSs, FMs, and MCs within the spleen and lymph nodes.

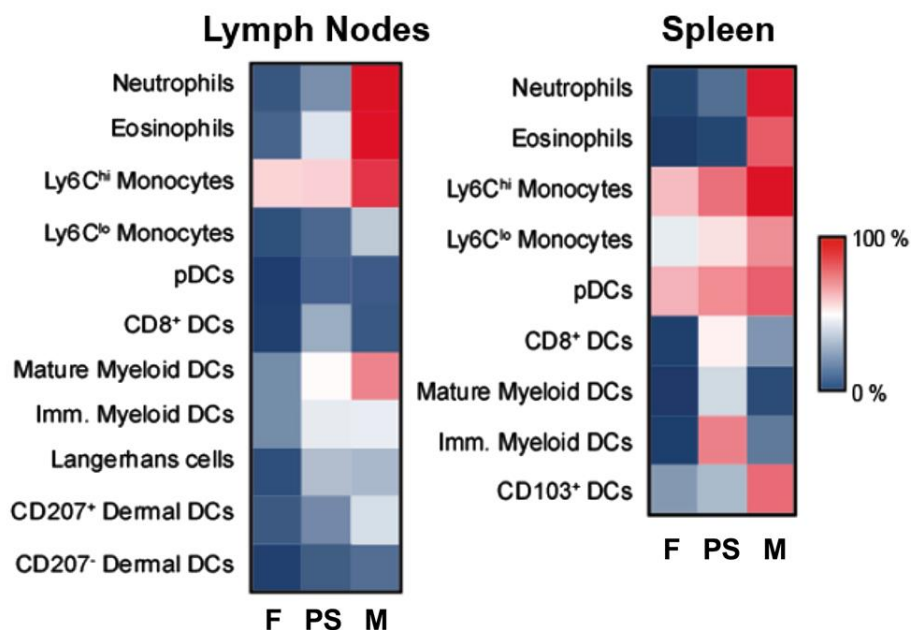


Figure 3-2. Cellular biodistributions of PEG-*b*-PPS nanocarriers following subcutaneous administration. Flow cytometric analysis of single-cell suspensions from mouse lymph nodes and spleens was conducted 24 hours after subcutaneous injection of fluorescent nanocarriers into the footpad ($n = 5-8$). A heat map demonstrates percentages of key phagocyte populations that associated with PEG-*b*-PPS filomicelles (F), vesicular polymersomes (PS), and spherical micelles (M). Amine-functionalized PEG₁₇-*b*-PPS₃₀ block copolymers were conjugated to fluorescent Dy647-N-hydroxysuccinimide and assembled in the presence of block copolymers engineered to generate filamentous, vesicular, or spherical morphologies. Adapted from [204] licensed under [Creative Commons By 4.0](#).

Overall, MCs exhibit the broadest uptake amongst the cell populations investigated, followed by PSs and, lastly, FMs. FMs only achieved greater than 50% uptake within monocytes and pDCs of the spleen and $ly6c^{hi}$ monocytes of the lymph nodes. Size may have been a significant factor in the observed cellular biodistributions as sub-100 nm structures are generally required for efficient drainage to the lymphatics following subcutaneous injection [268]. Though a valuable means of controlling nanocarrier fate, the route of administration will not be discussed further as a design characteristic in this dissertation.

Both works highlight how the physicochemical characteristics of PEG-*b*-PPS nanocarriers can be designed to achieve differential organ- and cellular-level biodistributions. Due to comparable chemical identities, the differences in uptake observed between PSs, FMs, and MCs are attributed to their differences in morphology. But, from our discussion in Section 3.2.1., we know that physicochemical characteristics, like morphology, can influence both the quantity and types of proteins that adsorb to the nanocarrier surface. As such, an opportunity exists to investigate how PEG-*b*-PPS nanocarriers interact with proteins and how (or if) the PC of PEG-*b*-PPS nanocarriers contributes to differences in uptake. The work encompassed in Chapter 3 strives to build off of previous studies to address whether: 1) surface chemistry can be exploited along with nanocarrier morphology to alter PEG-*b*-PPS nanocarrier uptake by the cells of the MPS and 2) the PC can be used to understand why these differences occur.

3.2.3. Combining Physicochemical Characteristics to Influence Cellular Interactions

Here, we investigate how combinations of surface chemistry and morphology can be used to influence PEG-*b*-PPS nanocarrier uptake within the primary cell subsets of the MPS. Previous studies involving PEG-*b*-PPS have largely utilized MeO-functionalized BCP. In addition to the MeO-functionalized BCPs, we use OH- and Phos-functionalized BCPs for the preparation of nine nanocarrier formulations that vary in their combination of morphology and surface chemistry (**Figure 3-3a,b**). We apply a holistic approach that assesses the inherent immunogenicity elicited by each formulation upon its introduction into human whole blood. We then explore how the various combinations of nanocarrier morphology and surface chemistry influence nanocarrier uptake within human monocytes, macrophages, and dendritic cells via flow cytometry. Finally, we examine whether the observed differential uptake of the nine formulations can be

further understood in the context of the PC (**Figure 3-3c,d**) by assessing bulk physicochemical changes to the nanocarriers following protein adsorption, and assessing formulation-specific differences in PC composition.

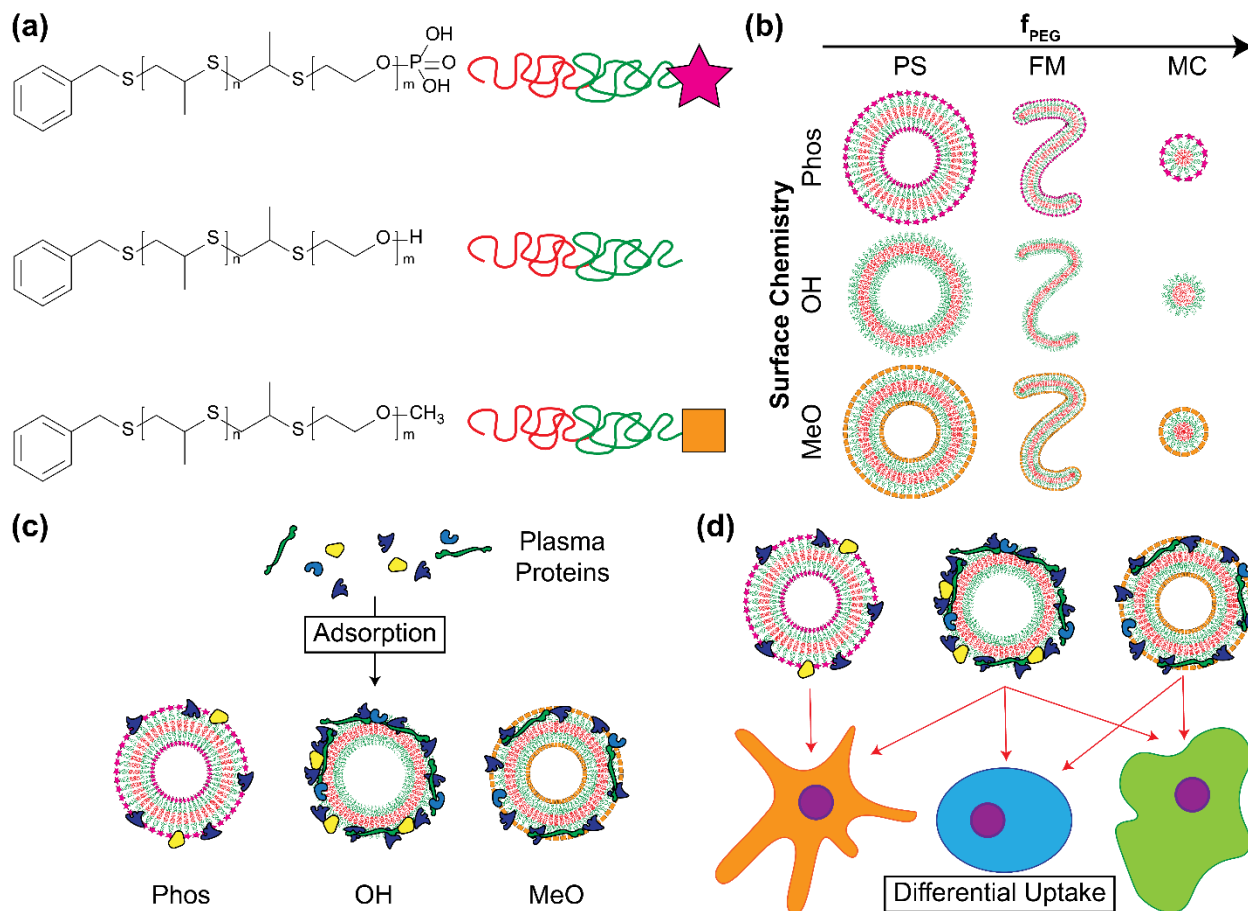


Figure 3-3. Schematic of PEG-*b*-PPS BCPs and the corresponding nanocarriers formed. (a) Schematic of the different functionalized BCPs. (b) Schematic of the nine nanocarrier formulations varying in surface chemistry and hydrophilic mass fraction (f_{PEG}). (c) Graphical depiction of how nanocarrier surface chemistry and morphology can lead to differential adsorption of plasma proteins. (d) Graphical depiction of how variations in the protein corona (PC) can influence nanocarrier uptake within the cells of the mononuclear phagocyte system (MPS).

3.3. Materials and Methods

3.3.1. Chemicals

All chemical reagents were purchased from Sigma-Aldrich St. Louis, MO, USA, unless stated otherwise. Fluorescent antibodies, Zombie Aqua fixable cell viability kit, IC cell fixation buffer, and LEGENDplex™ Human Inflammation Panel were acquired from BioLegend.

3.3.2. Preparation of FMs and MCs via Thin-Film Hydration

FMs and MCs were generated via thin-film hydration. BCP (either Bn-PPS-*b*-PEG-OMe, Bn-PPS-*b*-PEG-OH, or Bn-PPS-*b*-PEG-Phos) was dissolved in ~2 mL of dichloromethane (0.5 w/v%) within 2.0 mL clear glass vials (ThermoFisher Scientific). BCP films were formed on the inner surface of the vials by removing the dichloromethane under vacuum. The thin films were hydrated with 1 mL of Dulbecco's phosphate-buffered saline (1xDPBS) (ThermoFisher Scientific). FM assemblies were achieved through gentle agitation overnight at room temperature using a Stuart SB3 rotator. MC assemblies were achieved through vigorous agitation (1,500 rpm) overnight at room temperature using a Benchmark Scientific MultiTherm shaker.

3.3.3. Preparation of PSs via Flash Nanoprecipitation

PSs were formed using the confined impingement jets (CIJ) mixer described by Han et al. [269]. BCP (either PPS-*b*-PEG-OMe, PPS-*b*-PEG-OH, or PPS-*b*-PEG-Phos) were dissolved in 500 μ L of tetrahydrofuran (4.0% w/v) and aspirated via a 1 mL plastic disposable syringe. 500 μ L of 1xDPBS was aspirated via a second 1 mL syringe. Utilizing the multiple impingement process described by Allen et al. [94], the two solutions were hand impinged against one another within the CIJ mixer. The supersaturated solution exited the mixer into an empty 20 mL glass scintillation vial. The solution, consisting of 20 mg of BCP and a 1:1 mixture of tetrahydrofuran and 1xDPBS, was evenly split between the two syringes and once again hand impinged against one another within the CIJ mixer. The process was repeated an additional three times, the final of which concluded by exiting the mixer into a 1.5 mL reservoir of 1xDPBS. Tetrahydrofuran was removed by placing the samples under vacuum for a minimum of six hours.

3.3.4. Morphologic Confirmation via Cryogenic Transmission Electron Microscopy

Samples for cryogenic transmission electron microscopy (cryoTEM) were prepared by applying 3 μL of 10 mg ml^{-1} sample on pretreated lacey carbon 400 mesh TEM grids (Electron Microscopy Sciences). Following a 3 s blot, samples were plunge-frozen (Gatan Cryoplunge 3 freezer). Images of samples entrapped in vitreous ice were acquired using a field emission transmission electron microscope (JEOL 3200FS) operating at 300 keV with magnification ranging from 2,000 x to 12,000 x nominal magnification. Digital Micrograph software (Gatan) was used to align the individual frames of each micrograph to compensate for stage and beam-induced drift. Any further image processing conducted on the aligned frames was completed in ImageJ.

3.3.5. Confirmation of Nanocarrier Morphology via Small Angle X-ray Scattering

Small angle X-ray scattering (SAXS) studies were performed at the DuPont-Northwestern-Dow Collaborative Access Team (DND-CAT) beamline at Argonne National Laboratory's Advanced Photon Source (Argonne, IL, USA) with 10 keV (wavelength $\lambda = 1.24 \text{ \AA}$) collimated X-rays. All the samples were analyzed in the q -range ($0.001 - 0.5 \text{ \AA}^{-1}$), with a sample-to-detector distance of approximately 7.5 m and an exposure time of 3 s. The diffraction patterns of silver behenate were utilized to calibrate the q -range. The momentum transfer vector q is defined as $q = 4\pi \sin\theta/\lambda$, where θ is the scattering angle. Data reduction, consisting of the removal of solvent/buffer scattering from the acquired sample scattering, was completed using PRIMUS 2.8.2 software while model fitting was completed using SasView 4.0.1 software package. Nanocarrier morphology was confirmed by fitting the scattering profiles of PSs, FMs, and MCs with vesicle, flexible cylinder, and polymer micelle models, respectively.

3.3.6. Spherical Nanocarrier Characterization via Dynamic Light Scattering (DLS)

The hydrodynamic diameter of each of the six spherical nanocarriers was obtained via DLS measurements recorded using a Zetasizer Nano (Malvern Instruments) equipped with a 4mW He-Ne 633 laser. The nanocarrier size distributions and number average diameters were acquired from measurements recorded from three independently formed formulations ($n = 3$). Samples were analyzed in 0.1xDPBS prior to analysis.

3.3.7. Zeta Potential Assessment via Electrophoretic Light Scattering (ELS)

The zeta potential of each of the nine nanocarriers was obtained using a Zetasizer Nano (Malvern Instruments). The zeta potential of each nanocarrier was averaged using measurements recorded from three independently formed formulations ($n = 3$). Samples were analyzed in 0.1xDPBS prior to analysis.

3.3.8. Endotoxin Testing

Nanocarrier formulations were tested for endotoxin contamination using the QUANTI-Blue (InvivoGen) colorimetric enzyme assay. Raw-Blue cells (InvivoGen) were plated in 48 well plates (2.5×10^5 cells mL^{-1} , 400 μL). Subsequently, 40 μL of each nanocarrier formulation (5 mg mL^{-1}) was added per well and incubated for 24 h at 37°C with a 5% CO_2 atmosphere. Upon completion, 20 μL of cell supernatant was collected and added to 200 μL of the QUANTI-Blue detection media. Cell supernatants were incubated with the detection media for an additional 18 h at 37°C . SEAP activity was assessed by taking the optical density (OD) at 625 nm with a microplate reader (SpectraMax M3, Molecular Devices).

3.3.9. Assessment of Nanocarrier-Induced Cytokine Secretion

Whole blood samples containing ethylenediaminetetraacetic acid (EDTA) collected from three individual, healthy donors were acquired from Research Blood Components, LLC. Nanocarrier formulations (10 mg mL^{-1} , 8 μL) were added to 152 μL of human whole blood from each of the donors for 4 or 20 h at 37°C with a 5% CO_2 atmosphere. Lipopolysaccharide (LPS) (InvivoGen) and R848 (InvivoGen) were included in the analysis as positive controls and were tested at final concentrations of 1.0 and 10 $\mu\text{g mL}^{-1}$, respectively. After incubation, plasma was collected via centrifugation. Samples were subsequently prepared and analyzed following the manufacturer's protocol. Data acquisition was completed using a BD LSRFortessa. Acquired data was analyzed using the online Cytobank analysis suite.

3.3.10. Assessment of Nanocarrier-Induced Complement Activation

Nanocarrier formulations (10 mg mL^{-1} , 5 μL) were added to 95 μL of pooled complement human serum (Innovative Research) and incubated for 1 h at 37°C while being mixed at 200 rpm. Upon completion, samples were treated with 5 mM EDTA to stop the activation of complement and were placed on ice until further use. The concentrations of the human anaphylatoxins C3a, C4a, and C5a were

quantitatively assessed using a BD™ CBA Human Anaphylatoxin Kit. Generation of the C3a, C4a, and C5a standards and sample preparation were conducted following the manufacturer's protocol. Data acquisition was completed using a BD LSRFortessa. Acquired data was analyzed using the online Cytobank analysis suite.

3.3.11. THP-1 Culture Conditions

THP-1 cells (ATCC), a human leukemic monocyte cell line, were cultured in Roswell Park Memorial Institute (RPMI)-1640 medium (Gibco) supplemented with 10% fetal bovine serum (FBS) (Sigma-Aldrich), 1% GlutaMax (Gibco), and 1% penicillin–streptomycin (Gibco), hereafter referred to as complete RPMI. Culture conditions were maintained at 37°C with a 5% CO₂ atmosphere. Cells were subcultured as needed to insure cell concentration remained below 1.0 x 10⁶ cells mL⁻¹. Cells used for cytotoxicity or nanocarrier uptake studies were collected between passages 5 and 10.

3.3.12. THP-1 Differentiation to Macrophage-like Phenotype

THP-1 monocytes were differentiated toward a macrophage-like phenotype [270]. THP-1 cells, suspended in complete RPMI at a concentration of 2.0 x 10⁵ cells mL⁻¹, were treated with phorbol 12-myristate 13-acetate (PMA) at a final concentration of 25 nM upon dilution. Cells were plated in 48 well plates (2.0 x 10⁵ cells mL⁻¹, 500 μL) and incubated at 37°C with a 5% CO₂ atmosphere for 48 h. Following differentiation, PMA-containing media was removed and replaced with complete RPMI. THP-1 differentiated macrophages were given 24 h in PMA-free media prior to being washed and used for subsequent experiments.

3.3.13. Immature Dendritic Cell Differentiation from Human Monocytes

Monocyte derived immature dendritic cells were obtained by following a previously published protocol [271]. Negatively selected human monocytes (Astarte Biologics) were suspended in RPMI 1640 supplemented with 2% human AB serum (Sigma-Aldrich), 1% GlutaMax (Gibco), 1% penicillin–streptomycin (Gibco), 1000 U mL⁻¹ of Granulocyte-macrophage colony-stimulating factor (GM-CSF) (Shenandoah Biotechnology), and 500 U mL⁻¹ of IL-4 (Shenandoah Biotechnology), hereafter referred to as complete DC media. Monocytes were plated in 6 well plates (5.0 x 10⁵ cells mL⁻¹, 3.0 mL) and maintained

at 37°C with a 5% CO₂ atmosphere for 5 days. Three days after plating, half of the media volume was collected, centrifuged at 500xg for 5 min, and discarded. The cell pellet was resuspended in an equivalent volume of fresh complete DC media and redistributed among the wells.

3.3.14. Assessment of Nanocarrier Cytotoxicity

The 3-(4,5-Dimethylthiazol-2-yl)-2,5-Diphenyltetrazolium Bromide (MTT) assay was used to quantify the percentage of metabolically active cells as a readout of cell viability. THP-1 monocytes (5.0 × 10⁵ cells ml⁻¹, 200 μL) were plated in U-bottom 96-well plates. 20 μL of each nanocarrier formulation, at concentrations of 0, 1, 2, 5 and 10 mg ml⁻¹ in 1xDPBS, was added to the wells in quadruplicate and incubated for 24 h. 20 μL of MTT, at a concentration of 5 mg ml⁻¹ in 1xDPBS, was added to each well and incubated for an additional 6 h. Plates were centrifuged at 500xg for 5 min before the supernatant was removed from each well. Subsequently, 200 μL of dimethyl sulfoxide was added to each well to dissolve deposited formazan crystals. Absorbance measurements at 570 nm were acquired using a microplate reader (SpectraMax M3, Molecular Devices). Cell viability was assessed through the following formula:

$$\% \text{ Cell Viability} = \frac{OD_{Treat}}{OD_{Untreat}} \times 100\%$$

where OD_{Treat} is the optical density of a nanocarrier treated sample and OD_{Untreat} is the optical density of an untreated sample. The average percentage of viable cells was calculated from eight total measurements (n = 8) acquired through two independent experiments.

3.3.15. Cellular Uptake of Nanocarriers *in vitro*

All nanocarrier uptake studies were conducted utilizing a 4 h incubation period in serum-free media. Nanocarriers were tested under three conditions: (i) pristine (no exposure to pooled human plasma; BCP concentration of 5 mg mL⁻¹), (ii) following a 2-h incubation with pooled human plasma (1:1 volumetric ratio of nanocarrier formulation to human plasma; BCP concentration of 5 mg mL⁻¹), or (iii) following a 24-h incubation with human plasma (1:1 volumetric ratio of nanocarrier formulation to human plasma; BCP concentration of 5 mg mL⁻¹). Pooled human plasma was acquired from Zen-Bio Inc. and contained acid citrate dextrose (ACD) as an anti-coagulant.

THP-1 monocytes were collected via centrifugation (500xg for 5 min), washed with serum-free RPMI 1640, and recentrifuged. Pelleted cells were resuspended in serum-free RPMI 1640 to a final concentration of 2.5×10^5 cells mL⁻¹ and plated in 48 well plates (400 μ L). Cells were incubated for 1 h at 37°C with a 5% CO₂ atmosphere prior to the introduction of nanocarriers. After 1 h, 40 μ L (5 mg mL⁻¹) of each nanocarrier formulation for each defined condition were added to individual wells. Cells were incubated for 4 h at 37°C with a 5% CO₂ atmosphere following the addition of the nanocarrier formulations before being collected for uptake analysis via flow cytometry. Cells were stained with Zombie Aqua cell viability dye (BioLegend) for 15 min at a 1:200 dilution in cell staining buffer (BioLegend), washed with cell staining buffer, and briefly fixed with 2% paraformaldehyde prior to analysis on a BD LSRFortessa.

For THP-1 differentiated macrophages, complete RPMI was removed and the adherent cells were washed with serum-free RPMI 1640. Fresh serum-free RPMI (400 μ L) was added to each well. Cells were incubated for 1 h at 37°C with a 5% CO₂ atmosphere prior to the introduction of nanocarriers. After 1 h, 40 μ L (5 mg mL⁻¹) of each nanocarrier formulation for each defined condition were added to individual wells. Cells were incubated for 4 h at 37°C with a 5% CO₂ atmosphere following the addition of the nanocarrier formulations before being collected for uptake analysis via flow cytometry. Cells were stained with Zombie Aqua cell dye (BioLegend) for 15 min at a 1:200 dilution in cell staining buffer (BioLegend), washed with cell staining buffer, and briefly fixed with 2% paraformaldehyde prior to analysis on a BD LSRFortessa.

After 5 days of culture in complete DC media, differentiated immature dendritic cells were collected via centrifugation (500xg for 5 min), washed with serum-free RPMI 1640, and recentrifuged. Pelleted cells were resuspended in serum-free RPMI 1640 to a final concentration of 2.5×10^5 cells mL⁻¹ and plated in 48 well plates (300 μ L). Cells were incubated for 1 h at 37°C with a 5% CO₂ atmosphere prior to the introduction of nanocarriers. After 1 h, 30 μ L (5 mg mL⁻¹) of each nanocarrier formulation for each defined condition were added to individual wells. Cells were incubated for 4 h at 37°C with a 5% CO₂ atmosphere following the addition of the nanocarrier formulations before being collected for uptake analysis via flow cytometry. Cells were stained with Zombie Aqua cell viability dye (BioLegend) for 15 min at a 1:200 dilution in cell staining buffer (BioLegend) and subsequently stained with an antibody mixture containing

allophycocyanin (APC) anti-human CD209 (DC-SIGN) and fluorescein isothiocyanate (FITC) anti-human CD16 for 20 min. Cells were subsequently washed with cell staining buffer and fixed with 2% paraformaldehyde prior to analysis on a BD LSRFortessa. Acquired flow cytometry data for all cell types was analyzed using the online Cytobank analysis suite.

3.3.16. Nanocarrier Incubation with and Isolation from Human Plasma

Nanocarrier-protein isolation conditions were optimized by my lab mate Michael Vincent. Figures related to the optimization of this process can be found in Appendix A (**Figures A-1 – A-4**). Nanocarriers (BCP concentration of 5 mg mL⁻¹) of specified morphology and surface chemistry were incubated 1:1 with pooled human plasma at 37°C, 220 rpm. This nanocarrier:protein ratio was determined to yield the formation of PCs having a protein concentration within the dynamic range of the Pierce 660nm assay (**Figure A-1**). Compared against common assays for the determination of protein concentration, the Pierce 660nm assay was determined to have the greatest specificity for protein with minimal interference by PEG-*b*-PPS BCP (**Figure A-2**). The human plasma concentration was determined to be $\sim 21.9 \pm 5.2$ mg mL⁻¹ (mean \pm s.e.m.) using the Pierce 660nm assay (**Figure A-3**). Therefore, the working concentration of polymer and human plasma is 2.5 mg mL⁻¹ and ~ 11 mg mL⁻¹, respectively.

Nanocarrier-protein complexes were isolated by ultracentrifugation after incubation with human plasma for 2 and 24 hours. Images were obtained of each nanocarrier-protein mixture prior to ultracentrifugation to document any observed agglomeration. The array of sizes, and therefore masses, of the diverse polymeric nanocarrier morphologies analyzed in this study required ultracentrifugation for PC isolation. Ultracentrifugation was performed at 100,000 x g at 4°C for 45 min in an Optima MAX-XP ultracentrifuge (Beckman Coulter, Inc.). Supernatant was discarded, and nanocarrier-protein complexes were washed with sterile 1x phosphate buffered saline (PBS). This ultracentrifugation and washing process was repeated twice. Free (unadsorbed) plasma protein sediments minimally under these ultracentrifugation conditions (**Figure A-4**). After nanocarrier-protein complexes were isolated, the zeta potential was determined by ELS. The Zetasizer Nano (Malvern) was used to perform ELS.

3.3.17. Assessment of Total Protein Adsorption

The assessment of adsorbed protein was completed in collaboration with and following a protocol designed and optimized by my colleague Michael Vincent. Total adsorbed protein in a defined volume was determined by measuring protein concentration with the Pierce 660nm assay (ThermoFisher Scientific) using a Bovine Serum Albumin (BSA) concentration series as a calibration curve (0, 125, 250, 500, 750, 1000, 1500, and 2000 mg mL⁻¹) (**Figure A-2a**). Measurements were made in three replicates. The concentration of adsorbed proteins was determined by:

$$c = \frac{(A_{660,complex} - A_{660,NC}) - \beta_0}{\beta_1}$$

Where c is the determined protein concentration (in $\mu\text{g mL}^{-1}$), $A_{complex}$ is the absorbance of 660 nm light (A_{660}) measured in the nanocarrier-protein complex, A_{NC} is the A_{660} measured for the corresponding nanocarrier negative control lacking plasma, and β_0 and β_1 are the regression coefficients determined by simple linear regression using the aforementioned BSA calibration curve (**Figure A-2b,c**).

3.3.18. Quantification of Relative Protein Abundances via Densitometry

Quantification of protein abundances via densitometry was completed by my colleague Michael Vincent following a protocol he designed and optimized. He has permitted the inclusion of this work within this dissertation. The relative abundance of adsorbed proteins was determined by densitometry of silver-stained SDS-PAGE gels. All protein samples were prepared in Laemmli buffer containing 10% 2-mercaptoethanol. 1 μg of each protein sample was separated in one dimension using 4 - 20% tris-glycine gels (Mini-PROTEAN TGX, Bio-Rad Laboratories, Inc.). 10 μl of a 1:6 dilution of the PageRuler Plus pre-stained protein ladder was used as a molecular weight standard (ThermoFisher Scientific). 1 μg of 0.45 μm -filtered BSA was included on each gel to normalize band intensities and permit the comparison of protein relative abundance between gels. Electrophoresis proceeded at 110 V for 70 minutes. Gels were washed twice with Milli-Q water for five minutes, then subsequently fixed overnight in a 30% ethanol, 10% acetic acid solution (6:3:1 water:ethanol:acetic acid). On the following day, gels were washed twice in 10% ethanol for five minutes, followed by two washes in water for five minutes. The gels were subsequently silver stained in clean glass trays using the Pierce Silver Stain kit for mass spectrometry (ThermoFisher

Scientific), which is compatible with matrix assisted laser desorption ionization (MALDI) mass spectrometry. At the end of this procedure, each gel was developed for approximately 45 seconds. Staining was stopped by incubating the gels for 20 minutes in 5% acetic acid. The gels were washed in Milli-Q water prior to imaging.

Grayscale TIFF images (800 dpi) were obtained for each gel using an inexpensive Epson V39 scanner (Seiko Epson, Corp.). Inexpensive scanning systems reliably quantify band intensities [272]. Gel images were cropped and straightened in ImageJ [273]. To determine unknown molecular weights, the R_f was measured for each band and the molecular weight was calculated from a regression model computed for the molecular weight standards (**Figure A-5**). Densitometry was performed using GelAnalyzer software to quantify band intensities. Due to the large number of adsorbed proteins detected, band intensities of protein species were grouped in 10 kDa intervals in the 20 - 210 kDa range, and all intensities detected at a MW of >210 kDa were consolidated into a single group. The relative abundance of proteins in defined mass intervals was estimated using two different approaches. In the first approach, relative abundance of all proteins detected in a single lane was calculated as the MW-grouped band intensity divided by the total intensity computed for the lane. In the second approach, the MW-grouped band intensity was normalized against the intensity determined for 1 μ g of BSA run and stained on the same gel. The former approach is useful for assessing the relative abundances of protein species adsorbed to a given nanocarrier, whereas the latter approach provides a means for comparing protein abundances quantified for different nanocarrier formulations on the same gel, as well as estimated abundances between different gels that were stained separately under identical conditions. All relative abundance estimates were determined in three replicates.

3.4. Results and Discussion

3.4.1. Physicochemical Characterization of PEG-*b*-PPS Nanocarriers

Phos-, OH-, and MeO-functionalized BCPs were each synthesized with varying f_{PEG} to prepare PSs, FMs, and MCs exhibiting each of the three aforementioned surface chemistries (**Figure 3-3a**). **Figure 3-4** depicts a reaction scheme for the BCPs utilized in this chapter.

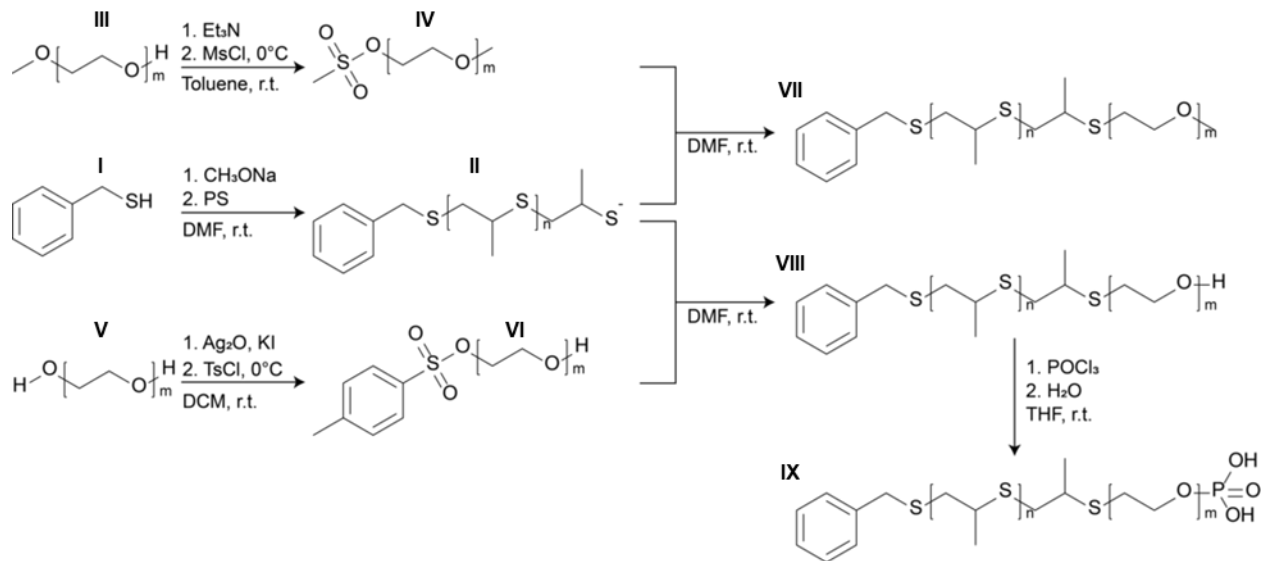


Figure 3-4. Synthetic pathway used to generate methoxy, hydroxyl, or phosphate terminated BCPs. Complete synthetic schema for PEG-*b*-PPS BCPs used in this chapter. Benzyl mercaptan (**I**) is base-activated and employed to perform anionic ring-opening polymerization on propylene sulfide to produce poly(propylene sulfide) homopolymer (**II**). To function as endcapping agents for **II**, mPEG (**III**) or PEG (**V**) are used to prepare mPEG-mesylate (**IV**) or HO-PEG-tosylate (**VI**). These two sulfonate PEG derivatives are used to endcap **II**, resulting in Bn-PPS-*b*-PEG-OMe (**VII**) and Bn-PPS-*b*-PEG-OH (**VIII**), respectively. The terminal hydroxyl on **VIII** is subsequently converted into a phosphate group to form Bn-PPS-*b*-PEG-Phos (**IX**).

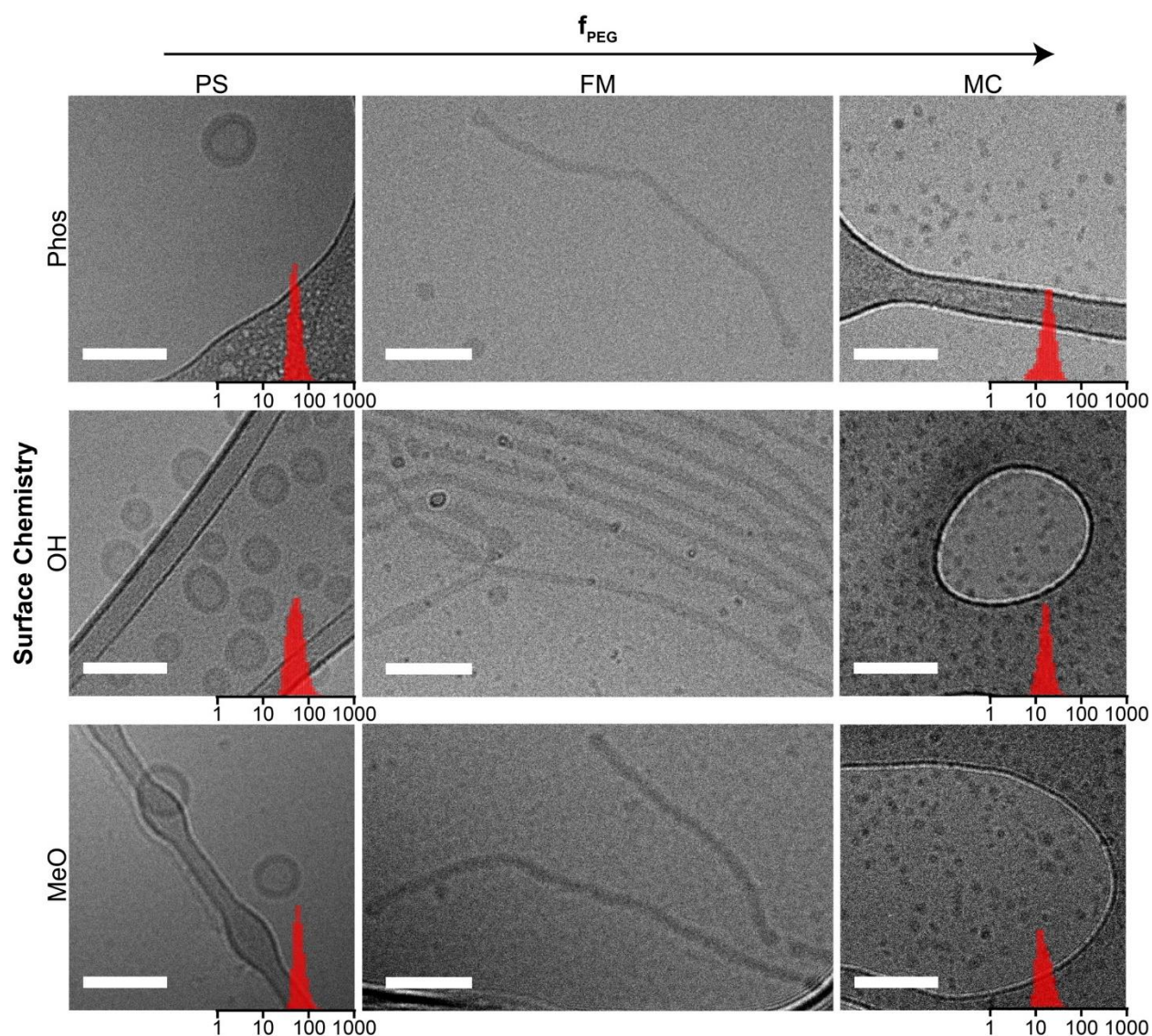


Figure 3-5. CryoTEM micrographs with overlaid histograms of particle hydrodynamic diameters for PSs and MCs. Cryogenic transmission electron micrographs of PSs (left), FMs (middle), and MCs (right) exhibiting either phosphate (top), hydroxyl (middle), or methoxyl (bottom) surface chemistries. Scale bar represents 100 nm. Overlaid on MC and PS images are histograms of their diameters acquired from DLS. X-axis is diameter in nanometers, y-axis is relative frequency.

PSs, FMs, and MCs exhibiting each of the three surface chemistries were successfully prepared and characterized by cryoTEM, DLS, SAXS, and ELS. CryoTEM micrographs (**Figure 3-5**) confirmed that each

BCP, irrespective of the terminal group extending off the PEG block, self-assembled into its anticipated morphology as predicted by its f_{PEG} . DLS and SAXS were completed to assess the size characteristics of each formulation (Figure 3-5, Figure 3-6).

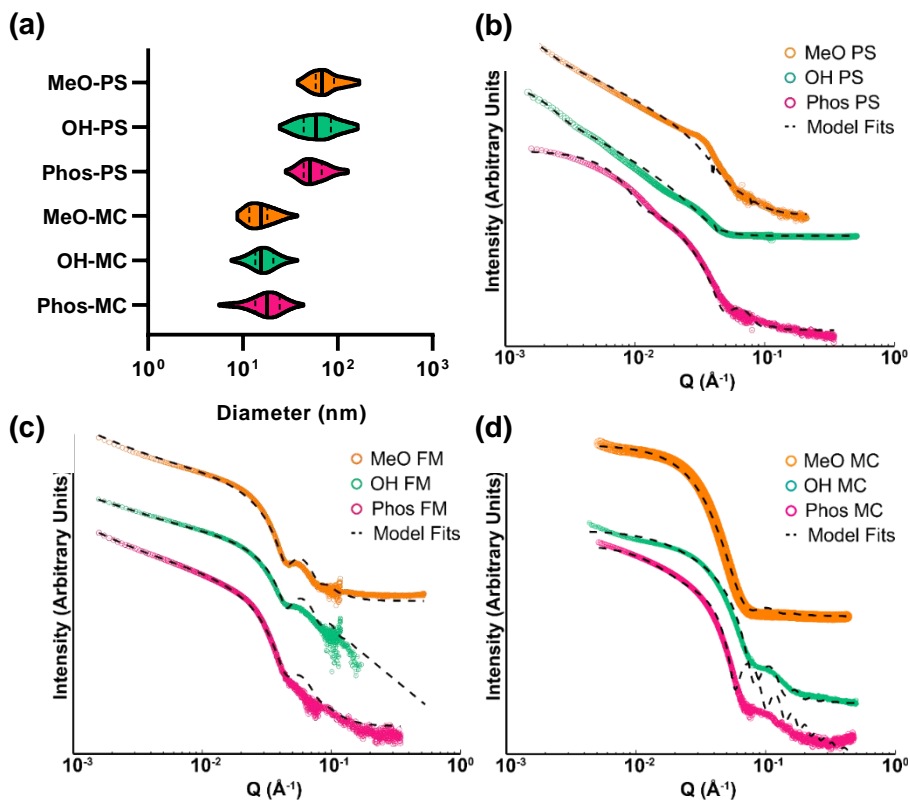


Figure 3-6. Morphologic characterization of PEG-*b*-PPS nanocarriers. (a) Violin plots depicting the number average diameter distributions for PSs and MCs obtained via DLS ($n = 3$). In addition to the distribution, each violin plot denotes the median (solid black line) and quartile values (dashed black lines) for the number average diameter of each formulation. (b) SAXS profiles of PEG-*b*-PPS PSs overlaid with corresponding fit for a vesicle model ($\chi^2 = 0.0645, 0.262, 0.555$ for MeO-, OH-, and Phos-PSs, respectively). (c) SAXS profiles of PEG-*b*-PPS FMs overlaid with corresponding fit for a flexible cylinder model ($\chi^2 = 0.777, 0.0439, 0.004$ for MeO-, OH-, and Phos-FMs, respectively). (d) SAXS profiles of PEG-*b*-PPS MCs overlaid with corresponding fit for a polymer micelle model ($\chi^2 = 0.0084, 0.0017, 0.0047$ for MeO-, OH-, and Phos-MCs, respectively).

DLS analysis of the spherical nanocarrier formulations (**Figure 3-6a**) indicated that PSs exhibited number average diameters ranging from 55 nm to 68 nm with number average polydispersity indices (PDIs) all below 0.150. MCs ranged in their number average diameters from 16 nm to 19 nm with number average PDIs below 0.120. The morphology of each nanocarrier was further confirmed through SAXS (**Figure 3-6b-d**). Due to the anisotropic nature of FMs, size characteristics were solely derived from SAXS analysis. The SAXS profile from each of the FM samples was fit utilizing a flexible cylinder model (**Figure 3-6c**). Model fitting indicated that FMs exhibited core radii of 17 nm – 18 nm and contour lengths extending into the micron range. Lastly, the zeta potential of each nanocarrier formulation was assessed via ELS (**Figure 3-7**).

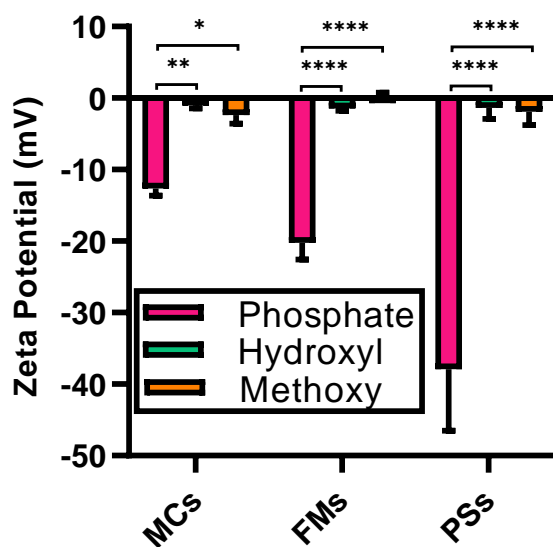


Figure 3-7. Zeta potential measurements of PEG-*b*-PPS nanocarriers. Average zeta potential of each nanocarrier formulation ($n = 3$). Significance was determined with Tukey's multiple comparison test. * $p < 0.05$, ** $p < 0.01$, **** $p < 0.0001$. Error bars represent s.d.

PSs, FMs, and MCs exhibiting either hydroxyl or methoxyl surface functionalities displayed zeta potentials ranging from -2 to 0 mV while those composed of Bn-PPS-*b*-PEG-Phos displayed zeta potentials ranging

from -38 to -13 mV. For nanocarriers composed of Phos-BCP, zeta potential measurements increased with the f_{PEG} of the BCPs (i.e. the smaller the f_{PEG} the more negative the zeta potential). There are several factors potentially contributing to these observed differences in the Phos-functionalized nanocarriers. First, differences in the molecular packing (Section 1.2.3.) exhibited by the three morphologies results in variations in the surface area per BCP [274], which would manifest as a difference in zeta potential between the nanocarriers. Additionally, morphological differences, pertaining to both size [275] and shape [276, 277], have been implicated in influencing the electrophoretic mobility of a particle in solution. This latter effect may contribute to the differences observed between Phos-MCs and Phos-FMs, as the orientation of high aspect ratio structures, like FMs, in the direction of the electric field can result in an increase in the observed electrophoretic mobility [276, 277]. Finally, previous studies have shown that the magnitude of the zeta potential can be influenced by particle concentration [278-281]. As the nanocarrier formulations in our studies are controlled on BCP concentration rather than particle concentration, the contribution of nanocarrier concentration to the observed differences in zeta potential cannot be excluded. Relevant physicochemical characteristics for both spherical and cylindrical nanocarriers can be found in **Table 3-1** and **Table 3-2**, respectively.

Table 3-1. Physicochemical characteristics of spherical nanocarriers.

Nanocarrier	Hydrodynamic Diameter [†] (nm)	PDI [‡]	Zeta Potential (mV)
Phos-PS	55 ± 4	0.10 ± 0.01	-38 ± 9
OH-PS	58 ± 17	0.13 ± 0.01	-1 ± 2
MeO-PS	68 ± 5	0.14 ± 0.02	-2 ± 2
Phos-MC	19 ± 5	0.11 ± 0.03	-13 ± 1
OH-MC	17 ± 3	0.08 ± 0.02	-1.1 ± 0.4
MeO-MC	16 ± 5	0.07 ± 0.01	-2 ± 1

[†]Number average value recorded via dynamic light scattering

[‡]Calculated from number average diameter distribution recorded via dynamic light scattering

Table 3-2. Physicochemical characteristics of cylindrical nanocarriers.

Nanocarrier	Cross Sectional Diameter [†] (nm)	Contour Length [†] (μm)	Zeta Potential (mV)
Phos-FM	34	2.5	-20 ± 2
OH-FM	36	1.2	-1.5 ± 0.3
MeO-FM	36	2.5	0.1 ± 0.6

[†]Values acquired from model fit of small angle X-ray scattering

3.4.2. Assessment of the Inherent Inflammatory Activity of PEG-*b*-PPS Nanocarriers

Nanocarrier characteristics including morphology [257], size [282], radius of curvature [283], surface charge [188], and surface chemistry [284] have been implicated in governing both the composition and amount of protein adsorbed to the nanocarrier surface following its introduction into a biological system. This new biological identity resulting from the PC will eventually dictate the effectiveness of the engineered construct at both reaching [262, 285] and interacting with its cellular target [286]. But along the way, the PC can potentially elicit deleterious immunologic effects [287]. As proteins adsorb onto the nanocarrier surface, there exists the potential for their denaturation [288-290] and subsequent exposure of previously buried antigenic epitopes [180]. While a more detailed mechanistic understanding of exactly how nanocarriers may inherently elicit these inflammatory responses is needed, a variety of both inorganic and organic nanocarriers have been shown to induce the secretion of proinflammatory cytokines [291]. As such, we sought to investigate whether PEG-*b*-PPS nanocarriers could inherently elicit an inflammatory response upon exposure to human blood samples. Furthermore, we explored how this immunogenicity is impacted by the nanocarrier morphology or surface chemistry.

We incubated each of the nine nanocarrier formulations, at a constant BCP concentration, with whole blood samples from three healthy individuals for either 4 or 20 hours. As protein adsorption/desorption processes on polymer surfaces have been observed to occur over tens of hours [292, 293], we selected the aforementioned time points to capture the early and late evolution of the PC. Plasma was collected following these incubation periods and was analyzed for a variety of proinflammatory cytokines, including IL-6, TNF-α, interferon (IFN)-γ, IFN-α, IL-1β, IL-12p70, IL-17A, IL-18, and IL-33,

proinflammatory chemokines monocyte chemoattractant protein (MCP)-1 and IL-8, and the anti-inflammatory cytokines IL-10 and IL-23. No obvious trends related to either nanocarrier morphology or surface chemistry materialized from the combined donor cytokine profiles observed following either 4 (Figure 3-8a) or 20 hours (Figure 3-8b) of incubation.

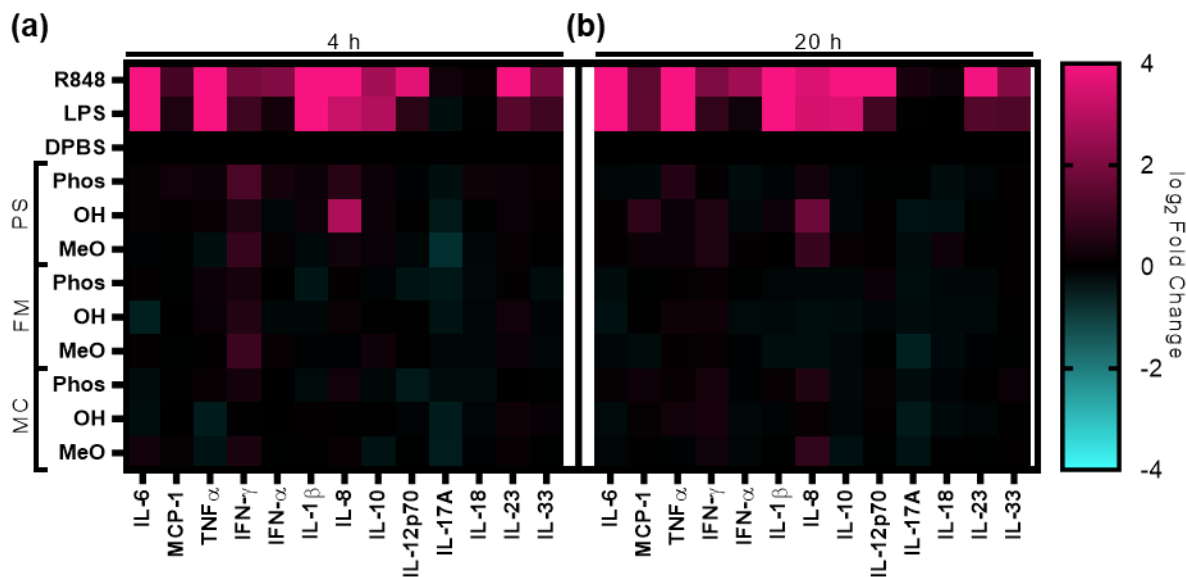


Figure 3-8. PEG-*b*-PPS nanocarrier-induced secretion of inflammatory cytokines. Heatmap depicting log₂ fold changes in cytokine secretion levels induced by nanocarrier incubation with whole blood for (a) 4 hours and (b) 20 hours (right) (n = 3).

PEG-*b*-PPS nanocarriers elicited cytokine profiles that differed from both the anti-bacterial and anti-viral cytokine profiles generated by LPS and R848, respectively. Irrespective of their unique combination of morphology and surface chemistry, PEG-*b*-PPS nanocarriers failed to induce a statistically significant alteration in the levels of secreted cytokines when compared to DPBS treatment. Although not statistically significant, the most dramatic response observed was the secretion of IL-8 following OH-functionalized PS treatment. In comparison to the DPBS control, OH-functionalized PSs induced 10-fold and 6-fold increases in IL-8 concentration following plasma incubation times of 4 and 20 hours, respectively. Further examination of the individual donor cytokine profiles (Figure 3-9) revealed that this increase was not the result of a

consistent uptick in chemokine secretion amongst all donors, but rather the result of a particularly strong response from one individual donor.

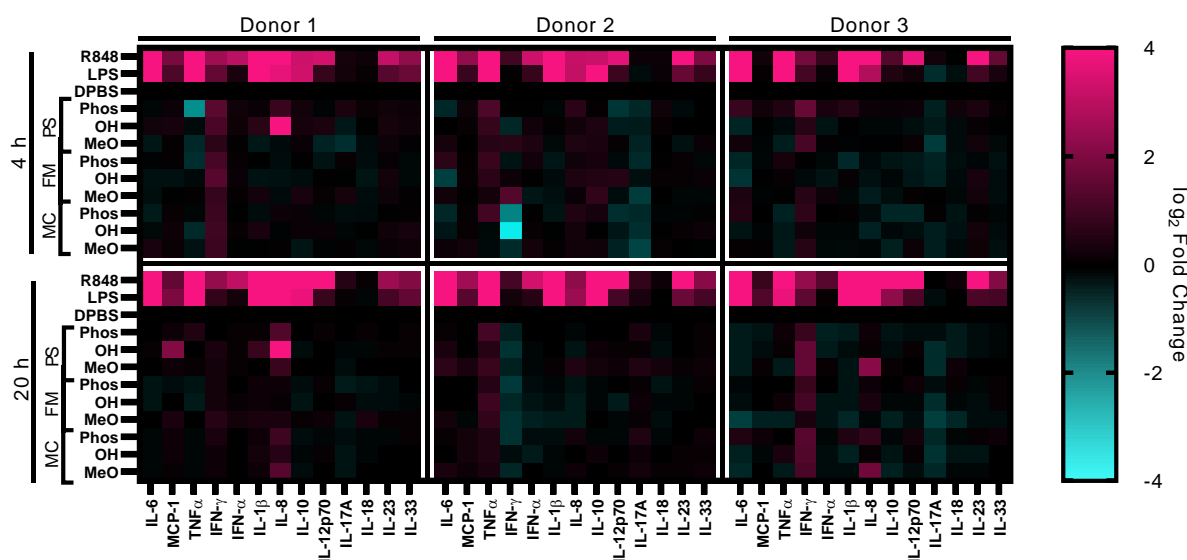


Figure 3-9. Individual donor cytokine profiles following 4 and 20 h incubations of nanocarrier formulations with whole blood. The upper row depicts the donor cytokine profiles following a 4-hour incubation of donor whole blood with the various nanocarrier formulations. The lower row depicts the donor cytokine profiles following a 20-hour incubation of donor whole blood with the various nanocarrier formulations. Individual donors ($n = 1$) are split into columns: Donor 1 (left), Donor 2 (middle), and Donor 3 (right).

Having observed an increase in IL-8 secretion following treatment with Bn-PPS-*b*-PEG-OH PSs, we sought to address whether a structural or material characteristic of this formulation could be culpable for this response. IL-8, also known as C-X-C Motif Chemokine Ligand 8 (CXCL8), is a chemokine secreted by monocytes, polymorphonuclear cells, and endothelial cells that is responsible for neutrophil recruitment during inflammation [294]. The amplification of IL-8 secretion by the human anaphylatoxin C5a has been observed in a variety of disease states [295-297]. C5a, which primarily functions as both a powerful chemotactic agent and neutrophil activator, is a byproduct of the complement cascade [298]. It is

well established that nanocarrier physicochemical properties, including surface chemistry, surface charge, size, and curvature, are capable of activating complement [298, 299]. Of these characteristics, nanocarrier surface functionality, particularly the presentation of hydroxyl groups, has been reported as a common feature for inducing complement activation [300, 301]. As such, we suspected that the increase in IL-8 secretion resulted from C5a production via the complement cascade. To investigate this potential mechanism, we incubated each of the nine nanocarriers with pooled human sera and quantified the amount of C3a, C4a, and C5a present (**Figure 3-10**).

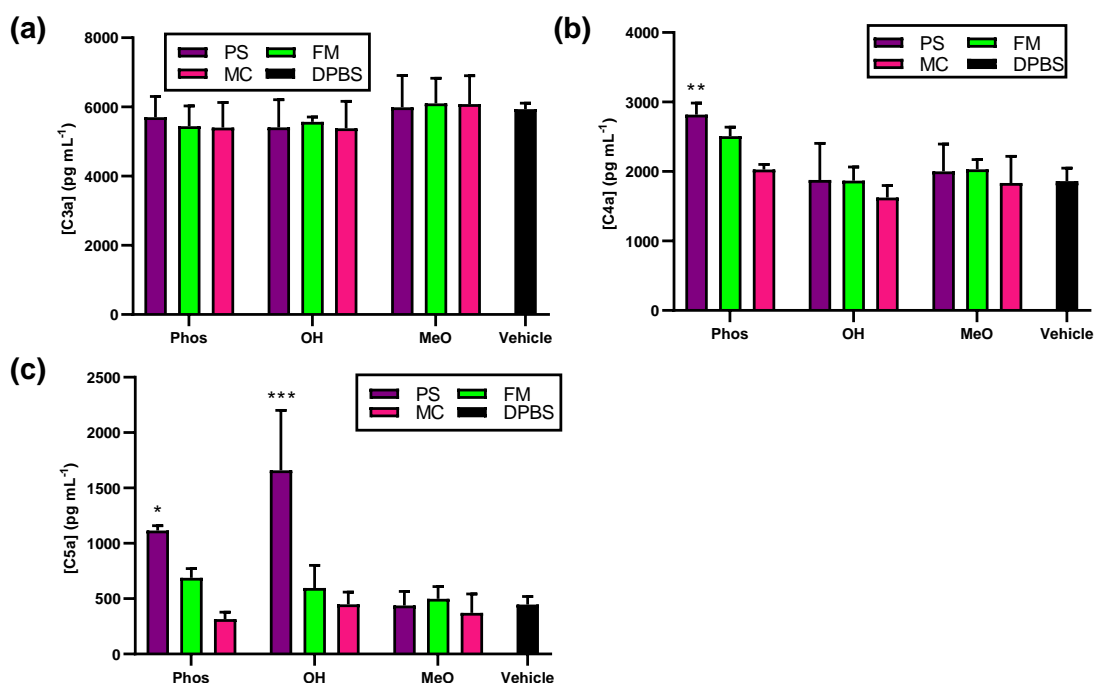


Figure 3-10. PEG-*b*-PPS nanocarrier-induced complement activation. Concentration of the anaphylatoxins (a) C3a, (b) C4a, and (c) C5a in human serum following nanocarrier treatment ($n = 3$). Significance was determined through 2-way ANOVA with Tukey's multiple comparison test. * $p < 0.05$, ** $p < 0.01$, *** $p < 0.001$. Error bars represent s.d. in all subfigures.

To our surprise, there were no statistically significant differences in the concentration of C3a for serum incubated with any nanocarrier formulation in comparison to DPBS treated serum (**Figure 3-10a**).

Previous studies have shown that both hydroxylated and negatively charged nanocarrier surfaces can activate complement through the alternative pathway [300, 302]. Polyhydroxylated nanocarrier surfaces are thought to contribute to the activation of the alternative pathway of complement by inducing a nucleophilic attack of the internal thioester bond exhibited by C3b [301], which can accelerate the alternative pathway through C3 tick-over [303]. Considering this, we expected the OH-functionalized and, potentially, the Phos-functionalized nanocarriers would activate complement via the alternative pathway. While no statistically significant differences were observed for the serum concentration of C3a, increases in C4a and C5a were observed (**Figure 3-10b,c**).

Phos-functionalized nanocarriers, specifically PSs and FMs, induced notable increases in C4a concentration, although only Phos-functionalized PSs induced a statistically significant increase with respect to DPBS treatment. Increases of approximately 50% and 35% were observed for the Phos-functionalized PSs and FMs, respectively (**Figure 3-10b**). The increase in C4a concentration by the Phos-functionalized PSs and FMs suggests activation of either the classical or lectin arms of the complement system. Charge has been identified as a contributing factor for activation of the classical pathway and may provide an explanation for the increase in C4a concentration observed following the treatment of serum with Phos-functionalized nanocarriers. Previous studies demonstrated that anionic lipid vesicles can activate the classical pathway through direct binding of C1q [304], an opsonin involved in the classical arm's initiation. C1q, which is composed of six subunits with globular cationic heads, is thought to interact directly with anionic surfaces through electrostatics [304]. This interaction has been proposed for vesicular structures, but whether it can be achieved in micellar structures, either cylindrical or spherical, remains unclear. Previous studies involving carboxylic acid-functionalized, anionic lipid MCs did not observe the direct interaction of C1q with the MC surface, potentially suggesting that the high curvature of MCs inhibits these structures from interacting with C1q [305]. But studies involving lipid vesicles have shown that nanocarrier-C1q interactions depend on the specific anionic functionality involved rather than simply the nanocarrier surface charge [306]. As such, direct interaction of C1q and Phos-functionalized FMs cannot be excluded from consideration.

The most potent of the anaphylatoxins, C5a, is a downstream product of all three arms of the complement cascade. C5a is involved in both the recruitment and activation of neutrophils [298] and is implicated in the amplification of IL-8 secretion. We assessed serum C5a concentrations following treatment with our nanocarrier formulations. Only Phos-functionalized and OH-functionalized PSs induced statistically significant increases in the concentration of C5a within serum when compared to DPBS treated controls (**Figure 3-10c**). Increases of approximately 150% and 270% were observed for the Phos-functionalized and OH-functionalized PSs, respectively. Interestingly, Phos- and OH-functionalized PSs induced the greatest levels of IL-8 secretion amongst the examined nanocarrier formulations following 4 hours of nanocarrier incubation with whole blood. While these results suggest the complement activating capabilities of Phos- and OH-functionalized PEG-*b*-PPS PSs influence additional inflammatory pathways, further studies are required to verify the interplay between the induced secretion of C5a and IL-8 in this BCP system.

3.4.3. Uptake of PEG-*b*-PPS Nanocarriers by the MPS

The MPS is the cellular surveillance system that has evolved to detect and eliminate foreign debris and pathogens. Comprised of monocytes, macrophages, and dendritic cells, the MPS is effective at sequestering and eliminating nanoscale structures, such as nanocarriers. As such, conventionally applied nanocarriers have often been designed to avoid detection from the MPS to increase circulation time. To reduce sequestration by the MPS, researchers have sought to mitigate opsonization, the process through which proteins adsorb to the surface of a foreign material to increase its visibility to the cells of the MPS [307]. But the recent focus on developing immunomodulatory nanocarriers has shifted how these constructs are designed. Rather than achieving complete avoidance of the MPS, nanocarriers are now designed to achieve tailored uptake within the MPS. Nanocarrier physicochemical characteristics, such as morphology [33, 95, 204], have been exploited for differential cell uptake. We sought to determine whether combinations of morphology and surface chemistry could be exploited to achieve differential uptake of PEG-*b*-PPS nanocarriers within monocytes, macrophages, and dendritic cells. Given the importance of protein adsorption in nanocarrier identification and uptake by the MPS, we assessed the uptake of our nine

nanocarrier formulations under three conditions in an attempt to understand how the physicochemical characteristics of PEG-*b*-PPS nanocarriers influence protein adsorption and, consequently, their internalization by the cells of the MPS.

Prior to assessing the influence of morphology and surface chemistry on the internalization of PEG-*b*-PPS nanocarriers, we first assessed the cytotoxicity of the various formulations. Monocyte-like THP-1 cells were incubated with each nanocarrier formulation at material concentrations ranging from 0.1 to 1.0 mg mL⁻¹ for 24 hours. Irrespective of the combination of nanocarrier morphology and surface chemistry, the viability of treated THP-1 cells exceeded 80% for all material concentrations tested (**Figure 3-11**). The concentration dependent differences in cell viability for a given nanocarrier were not significant within the range tested. The non-cytotoxic nature of PEG-*b*-PPS nanocarriers observed in this work was consistent with previously published studies [34, 95, 204, 308]. To ensure that cytotoxicity would not influence our ensuing cell uptake studies, we elected to use a BCP concentration of 0.5 mg mL⁻¹, a concentration where greater than 85% viability was observed for all formulations tested.

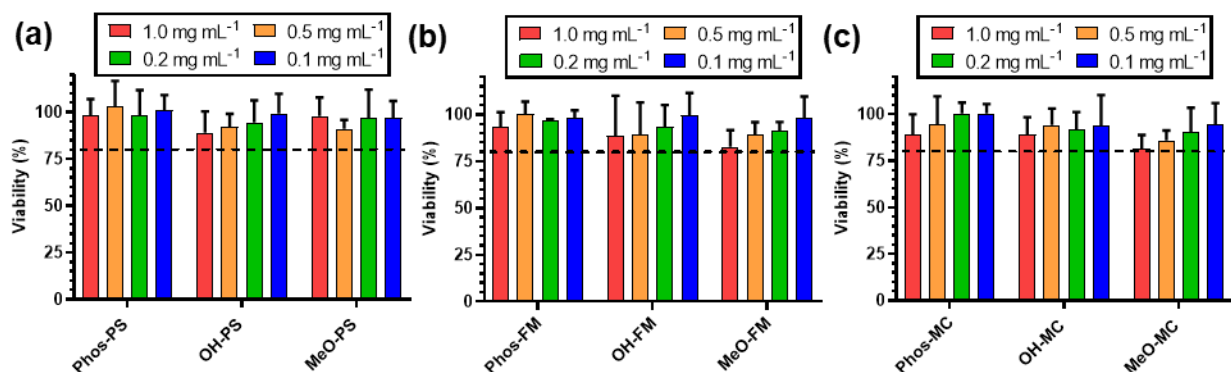


Figure 3-11. Cytotoxicity assessment of nanocarrier formulations with THP-1 monocytes. Impact on cell viability for Phos-, OH-, and MeO-functionalized a) PSs, b) FMs, and c) MCs ($n = 8$). Error bars represent s.d. The black dashed line denotes 80% viability.

The process utilized for the uptake studies within monocyte-like THP-1 cells, macrophage-like differentiated THP-1 cells, and immature dendritic cells is illustrated in **Figure 3-12**.

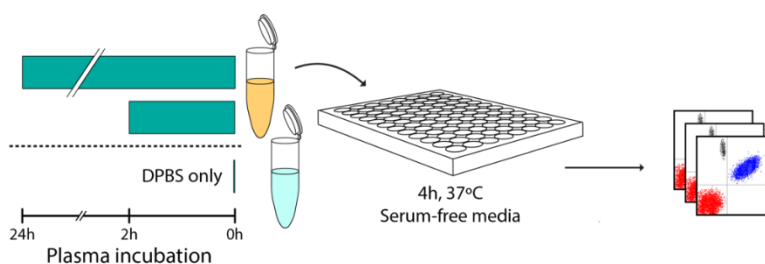


Figure 3-12. Conditions and process flow for *in vitro* uptake studies. Schematic depicting process flow for nanocarrier uptake studies. Dil-loaded nanocarriers under pristine conditions or following a 2-hour or 24-hour incubation with human plasma, are plated with cells in serum-free media. Following a 4-hour incubation, cells are recovered and prepared for flow cytometric analysis.

Cells, in serum-free media, were treated with each of the nanocarrier formulations. Each formulation was applied under three separate conditions: no protein exposure (i.e. pristine nanocarriers), following a two-hour incubation with human plasma, and following a 24-hour incubation with human plasma. Previous studies involving PEG-*b*-PPS nanocarriers have shown that circulation times on the scale of days can be achieved following intravenous administration [95]. Given the dynamic nature of the PC [309], which has been actively studied since the work of Vroman and Adams in the 1960s [254], we wanted to assess how changes to the PC that occur on the scale of hours up to a day influence the cellular interactions of PEG-*b*-PPS nanocarriers. For these studies, we utilized human plasma, rather than serum, to simulate how the PC might form on PEG-*b*-PPS nanocarriers *in vivo*. Previous studies have demonstrated that compositional changes in the PC can result from the choice of surrogate biological milieu [310]. These compositional changes, which include increased abundances of opsonins like complement proteins and fibrinogen in the nanocarrier PC [310], are of consequence for studies conducted using immune cells [287]. Therefore, we utilized plasma as it best recapitulates what nanocarriers may experience *in vivo*. To assess nanocarrier uptake via flow cytometry, the formulations prepared in these studies incorporate the hydrophobic dye Dil, which we have previously demonstrated can be stably encapsulated within PEG-*b*-PPS nanocarriers for weeks [216].

The influence of protein adsorption on nanocarrier agglomeration, specifically observed for the OH- and MeO-functionalized PSs, was apparent following both 2 hours and 24 hours of nanocarrier exposure to human plasma (**Figure 3-13**).

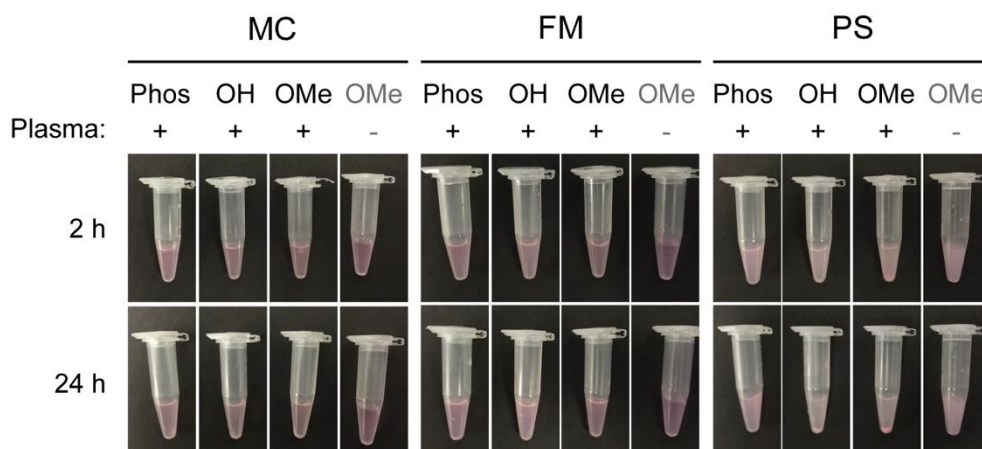


Figure 3-13. Assessment of nanocarrier agglomeration upon protein adsorption. Images of nanocarriers incubated for 2 hours or 24 hours in the presence or absence of plasma.

These macroscopic differences in colloidal stability suggested that surface chemistry was playing a role in the adsorption of protein on PEG-*b*-PPS nanocarriers, which we anticipated would influence their cellular interactions. Nanocarrier uptake was first assessed in monocyte-like THP-1 cells. Although these cells exhibit limitations in comparison to their physiologic counterparts, THP-1 cells are a valuable surrogate for human primary monocytes [311] and have been used extensively to investigate nanocarrier uptake [286, 312-315]. On the basis of morphology, MCs generally showed significantly less uptake than either PSs or FMs (**Figure 3-14a**). This trend was observed when comparing MCs to similarly functionalized PSs under all conditions tested and to FMs under the pristine and 2-hour plasma incubation conditions. FMs, under both the pristine and short plasma exposure conditions, exhibited high-levels of uptake irrespective of surface chemistry, suggesting a morphology-dependent characteristic may be influencing this interaction. This observation is consistent with the results of a previous *in vivo* study that observed elevated levels of association between PEG-*b*-PPS FMs and blood monocytes in comparison to PSs and MCs [95].

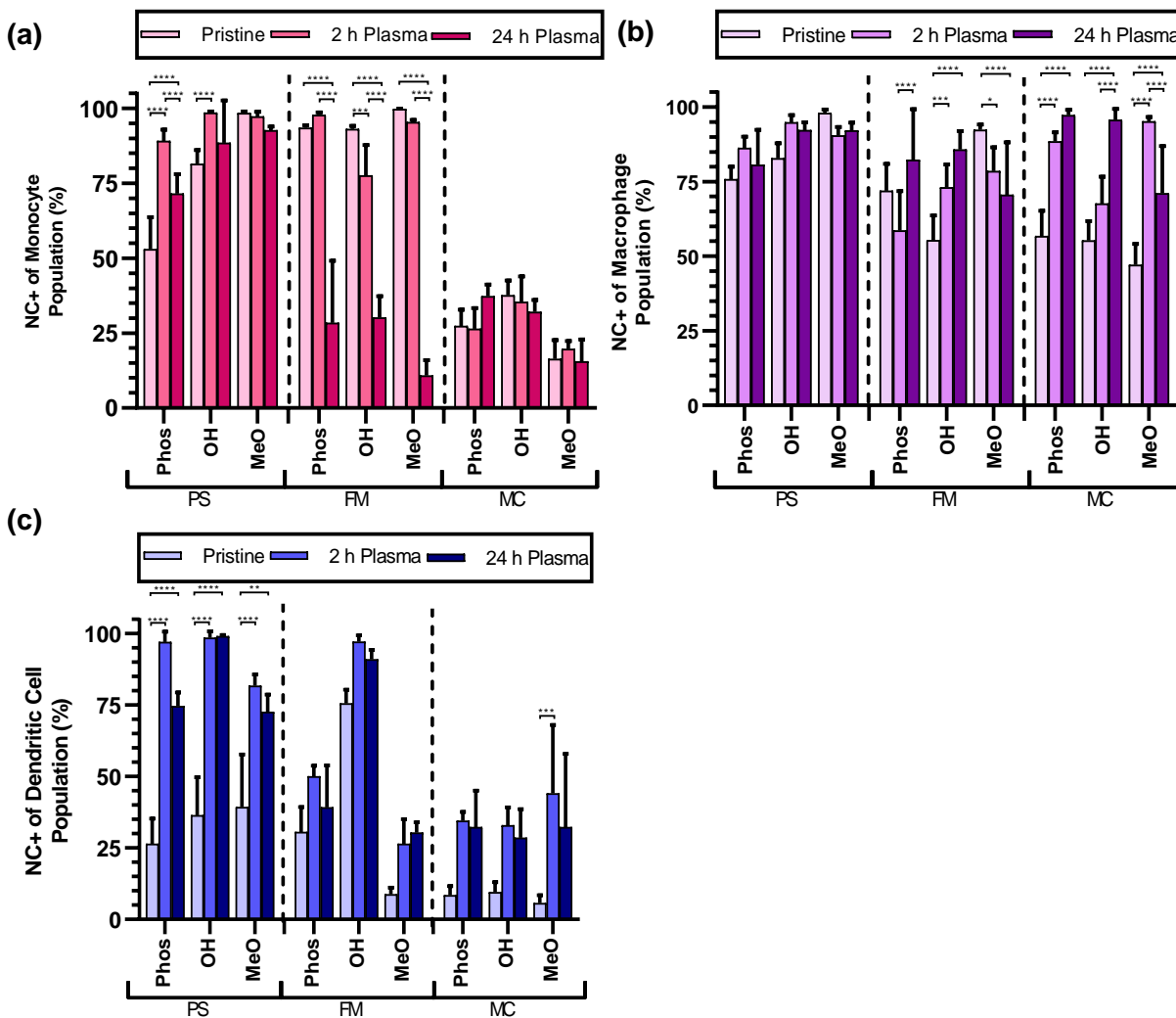


Figure 3-14. Cellular uptake of nanocarriers in the absence or presence of plasma proteins. Flow cytometric analysis of nanocarrier (DiI) uptake within: (a) monocyte-like THP-1 cells ($n = 10$; except OH-PSs with 24 h plasma incubation where $n = 9$), (b) macrophage-like dTHP-1 cells ($n = 10$), and (c) immature dendritic cells ($n = 4$). Significance was determined through 2-way ANOVA with Tukey's multiple comparison test. * $p < 0.05$, ** $p < 0.01$, *** $p < 0.001$, **** $p < 0.0001$. Error bars represent s.d. in all subfigures.

Plasma exposure induced varied responses in cell uptake for the different morphologies. In PSs, net uptake significantly increased with respect to the pristine condition following the 2-hour nanocarrier

exposure to plasma for both Phos- and OH-functionalized constructs but decreased for MeO-functionalized PSs (**Figure 3-14a**). FMs generally displayed a decrease in cell uptake with increased plasma exposure, irrespective of surface chemistry. Highly significant differences in FM cell uptake were observed between the pristine and 24-hour plasma incubation conditions as well as the 2-hour and 24-hour plasma incubation conditions (**Figure 3-14a**). MCs appeared to be the morphology least impacted by protein adsorption, as no statistically significant differences in cell uptake were observed between plasma incubation conditions. Overall, two thirds of the nanocarrier formulations experienced a net decrease in uptake with respect to the pristine condition following plasma exposure for either 2 hours or 24 hours (**Figure 3-14a**). Previous studies looking at the endocytosis of metallic and solid core nanoparticles in THP-1 cells have similarly observed decreases in nanocarrier internalization when serum proteins are present [286, 312, 313]. These studies suggested that the decreases in uptake were the result of decreases in nanocarrier zeta potential (more negative) upon protein adsorption. We will assess whether changes in zeta potential may have contributed to this net decrease in Section 3.4.4.

Next, we investigated the uptake of PEG-*b*-PPS nanocarriers in macrophage-like differentiated THP-1 cells. Like the THP-1 cells from which they are derived, macrophage-like differentiated THP-1 cells (dTHP-1 cells) are not perfect surrogates for primary human macrophages [316, 317]. But some have suggested that dTHP-1 cells are preferable to peripheral blood mononuclear cell (PBMC)-derived macrophages on the basis of their phagocytic capacity [316]. As such, dTHP-1 cells have been widely used for investigating nanocarrier uptake *in vitro* [286, 312, 318]. A variety of conditions involving PMA have been used to induce THP-1 cell differentiation toward a macrophage-like phenotype. For this study, we utilized a previously published protocol for the generation of naïve dTHP-1 cells [270]. As expected, dTHP-1 cells showed an overall increase in affinity for PEG-*b*-PPS nanocarriers in comparison to their monocyte-like counterparts (**Figure 3-14b**). General trends in nanocarrier association and uptake varied based on nanocarrier shape. In PSs and MCs, a net increase in nanocarrier uptake with respect to the pristine condition was observed for all spherical nanocarriers except for MeO-functionalized PSs upon plasma exposure (**Figure 3-14b**). Macrophage-like dTHP-1 cells differed from their monocyte-like counterparts with respect to the impact of condition on PS and MC uptake. Changes in PS uptake,

irrespective of surface chemistry, were not significantly different on the basis of nanocarrier condition, whereas the increases observed for MC internalization following plasma exposure were generally significant with respect to the pristine condition (**Figure 3-14b**). The overall increase in spherical nanocarrier uptake by dTHP-1 cells in comparison to their monocyte-like counterparts is most likely due to an increase in cell surface receptor expression [319]. Previous studies have observed increases in both scavenger and complement receptor expression following THP-1 cell differentiation [319], which most likely contributed to the significant changes observed in MC association/internalization by dTHP-1 cells following protein adsorption (**Figure 3-14b**). Cylindrical FMs displayed no overarching trends in uptake following plasma exposure. On the basis of surface chemistry, all Phos- and OH-functionalized nanocarriers, except Phos-functionalized FMs following 2-hour incubation with plasma, saw a net increase in percent uptake from the pristine condition upon plasma exposure. Interestingly, MeO-functionalized nanocarriers, except for spherical MCs, saw a net decrease in macrophage-like dTHP-1 cell uptake with respect to the pristine condition following plasma exposure (**Figure 3-14b**).

Lastly, we investigated the uptake of PEG-*b*-PPS nanocarriers in monocyte-derived immature dendritic cells. Their phagocytic capacity, ability to efficiently process and present antigen, and ability to initiate T cell immunity have made dendritic cells a desirable cellular target for biomaterial-based delivery systems designed for vaccination [320]. Under the pristine condition, PEG-*b*-PPS nanocarriers experienced lower levels of uptake within dendritic cells than within monocyte-like THP-1 or macrophage-like dTHP-1 cells (**Figure 3-14c**). Generally, nanocarrier internalization and association decreased with increasing BCP f_{PEG} (i.e. PSs exhibited increased uptake in comparison to FMs which exhibited increased uptake in comparison to MCs for a given surface chemistry) (**Figure 3-14c**). All nanocarrier formulations, irrespective of the combination of morphology and surface chemistry, saw an increase in dendritic cell uptake over the pristine condition following their incubation with plasma (**Figure 3-14c**). Though it should be noted that these increases in nanocarrier uptake were generally only significant for the PS morphology. While differences were observed within a given morphology and condition on the basis of surface chemistry, these differences were also generally not significant.

An interesting trend that was conserved regardless of cell type was the response of cell uptake to the nanocarrier condition (**Figure 3-14**). Rather than looking at each condition individually, the combination of the pristine, 2-hour plasma incubation, and 24-hour plasma incubation conditions can be viewed as the nanocarrier's conditional uptake profile. When looking at the conditional uptake profiles of the nanocarriers, the most common trend observed involved an increase in uptake from the pristine condition to the 2-hour plasma incubation condition followed by a decrease in uptake from the 2-hour to 24-hour plasma incubation condition. This trend was observed in approximately 60% of the conditional uptake profiles investigated. This result suggests that changes in the PC influence how PEG-*b*-PPS nanocarriers interact with cells of the MPS over time. To better understand how the PC influences PEG-*b*-PPS nanocarrier uptake, we assessed the total adsorption of protein to our nine nanocarrier formulations and investigated whether compositional changes could be detected within each formulation's PC.

3.4.4. Assessment of Total Protein Adsorption

Assessment of protein adsorption and changes to the physicochemical characteristics of PEG-*b*-PPS nanocarriers was completed in collaboration with my colleague Michael Vincent, who designed and optimized the protocols used in these studies. Nanocarrier surface chemistry induced significant changes in total adsorbed protein following both 2 hours (**Figure 3-15a**) and 24 hours (**Figure 3-15b**) of plasma incubation. Within each morphology, MeO-functionalization resulted in the lowest total amount of adsorbed protein following 2 hours of nanocarrier incubation with human plasma (**Figure 3-15a**). A similar trend was observed for MCs and FMs following 24 hours of plasma incubation but not for PSs (**Figure 3-15b**). Within PSs, divergent responses from the two neutral nanocarriers with respect to the total protein adsorbed at the 2-hour timepoint, specifically an increase in protein adsorption for the MeO-PSs and a decrease in protein adsorption for OH-PSs, resulted in the OH-PSs exhibiting the lowest total amount of adsorbed protein at the 24-hour timepoint (**Figure 3-15b**). Within a given morphology, Phos-functionalized PEG-*b*-PPS nanocarriers exhibited the greatest total amount of protein adsorption. These results support previous observations that increasing the negative charge density increases protein adsorption to nanocarrier surfaces [321].

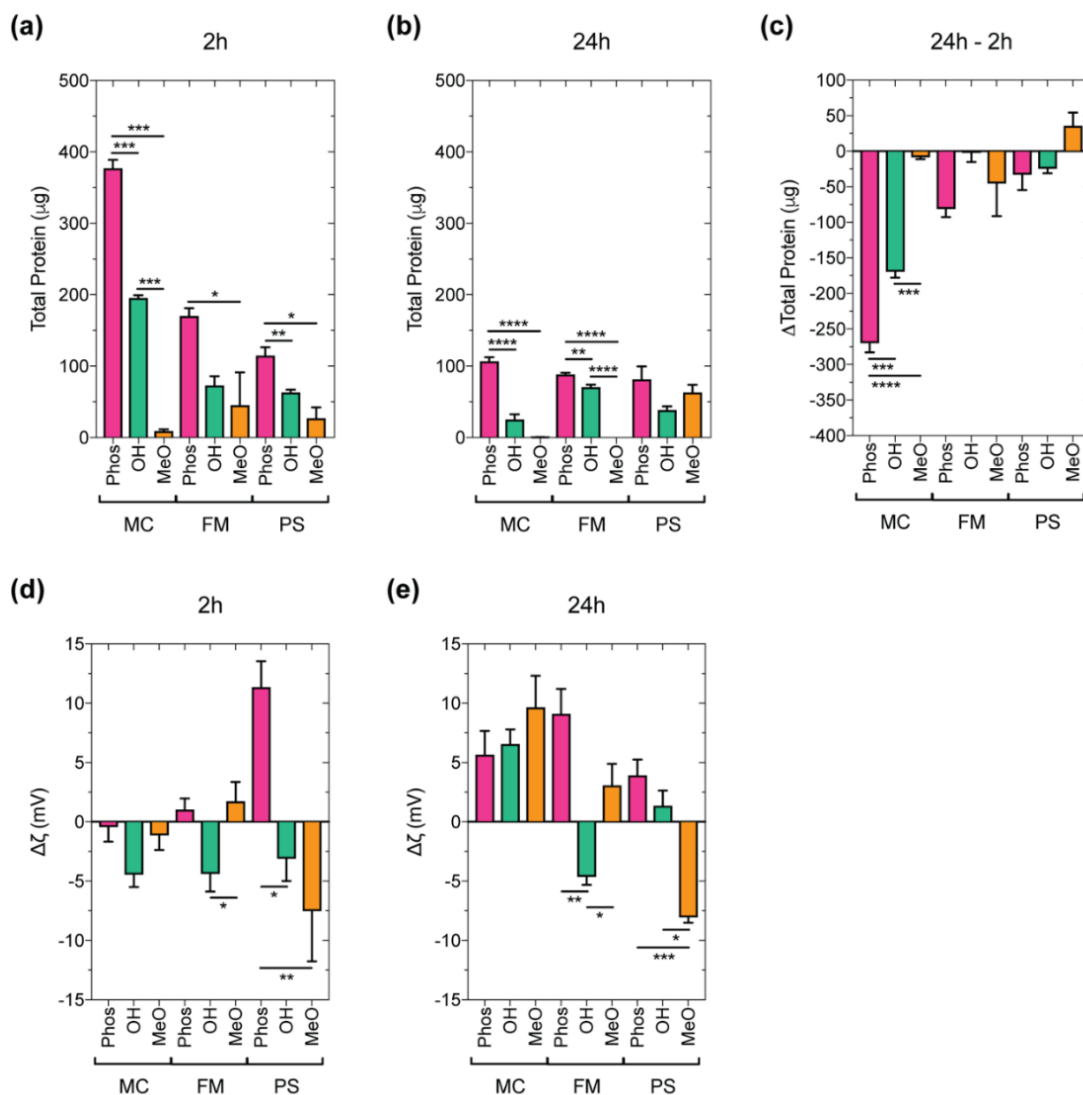


Figure 3-15. Quantification of total adsorbed protein and zeta potential changes following plasma incubation. Total amount of protein adsorbed to PEG-*b*-PPS nanocarriers isolated from human plasma following (a) 2 hours and (b) 24 hours of incubation. (c) Difference in total adsorbed protein between the 24-hour and 2-hour timepoints. Changes in nanocarrier zeta potential following incubation with human plasma for (d) 2 hours and (e) 24 hours. Statistical analysis was completed within each morphology separately. Significance was determined through one-way ANOVA with Tukey's multiple comparison test. For all cases, error bars represent s.e.m., $n = 3$. * $p < 0.05$, ** $p < 0.01$, *** $p < 0.001$, and **** $p < 0.0005$.

Interestingly, MeO-PSs were the only PEG-*b*-PPS nanocarrier formulation that experienced an increase in protein adsorption between the 2-hour and 24-hour timepoints (**Figure 3-15c**). The general decrease in total adsorbed protein observed in the remaining eight nanocarrier formulations suggests that the introduction of PEG-*b*-PPS nanocarriers into plasma results in an initial surge in adsorption that equilibrates with time as equilibrium is reached between the free and adsorbed protein during the incubation period (**Figure 3-15c**). Within a given morphology, the relative change in total adsorbed protein elicited by nanocarrier surface chemistry was only significant for MCs (**Figure 3-15c**).

Protein adsorption resulted in significant changes to nanocarrier zeta potential at both timepoints examined. Following 2 hours of plasma incubation (**Figure 3-15d**), protein adsorption induced a decrease in nanocarrier zeta potential (more negative) for six of the nine formulations. But, seven of the nine nanocarrier formulations isolated from plasma following 24 hours of incubation experienced increases in their zeta potential (more positive) (**Figure 3-15e**). The general decrease in zeta potential observed following the 2-hour plasma incubation is expected as most plasma proteins exhibit an overall negative charge at physiologic pH. Thus, adsorption of these anionic proteins should reduce the measured zeta potential of the nanocarrier. The increase in zeta potential observed following 24 hours of plasma incubation can be understood in the context of the protein desorption depicted in **Figure 3-15c**. As negatively charged species desorb from a given nanocarrier, the observed zeta potential should increase (become more positive).

There are several morphology-specific observations concerning the influence of protein adsorption on zeta potential worth noting. For MCs, highly significant ($***p < 0.001$ and $****p < 0.0005$) differences in total adsorbed protein were observed between the two timepoints (**Figure 3-15c**), yet no significant changes in zeta potential were observed within any micellar formulation following protein adsorption (**Figure 3-15d,e**). The lack of significant changes in zeta potential for MeO-MCs following plasma incubation makes sense given the limited protein adsorption observed at either time point (**Figure 3-15a,b**). Phos- and OH-MCs experienced significant protein adsorption in comparison to MeO-MCs (**Figure 3-15a-c**), yet the resulting protein-induced changes in zeta potential were not significantly different

from the changes observed for MeO-MCs (**Figure 3-15d,e**). Given the differences in total protein adsorbed and the variable impact this adsorption had on the zeta potential of the MC formulations, this result suggested that MC surface chemistry may induce compositional changes within the PC.

Protein adsorption led to interesting changes in zeta potential for the cylindrical nanocarriers. Phos-FMs experienced a net increase in zeta potential (more positive) in response to protein adsorption, but OH-functionalized FMs experienced a net decrease in zeta potential (more negative) following adsorption (**Figure 3-15d,e**). Both surface functionalities are more hydrophilic than the MeO surface chemistry and induced greater amounts of protein adsorption. Yet protein adsorption induced an inverse response in the directionality of their respective zeta potentials. When considering the magnitude of each construct's average zeta potential in comparison to the average plasma protein, this response is as expected. In the pristine condition, Phos-functionalized FMs have a negative zeta potential that is much greater in magnitude than the average protein, whereas the OH-FM zeta potential is more comparable to the slightly negative charge expected of the average plasma protein (**Table 3-2**). In the context of adsorption, the deposition of negatively charged plasma proteins on Phos-FMs is expected to increase the average zeta potential toward 0 mV, while the adsorption of plasma proteins to OH-FMs should shift the zeta potential of these nanocarriers further from 0 mV. Another interesting observation was made concerning the two neutral surface chemistries (OH- and MeO-functionalized FMs). A significant difference in zeta potential was observed between the neutral surface chemistries at both timepoints (**Figure 3-15d,e**). Following 2 hours of plasma incubation, both the OH- and MeO-functionalized FMs exhibited comparable amounts of protein adsorption (**Figure 3-15a**). Yet, the neutral FMs experienced inverse responses in their zeta potentials following protein adsorption over the same incubation period (**Figure 3-15d**). As was noted for the MC formulation, this result may suggest that surface chemistry is responsible for compositional changes within the PEG-*b*-PPS FM-PC.

PSs exhibited similar trends to what was described for FMs with regards to the influence of protein adsorption on zeta potential. Phos-PSs experienced a net increase in zeta potential (more positive) following protein adsorption, while MeO-functionalized PSs experienced a net decrease in zeta potential

(more negative) following both 2 and 24 hours of plasma exposure (**Figure 3-15d,e**). Unlike the OH-functionalized FMs, opposing responses were observed for the zeta potential of OH-PSs at the 2-hour and 24-hour timepoints. Protein adsorption at the 2-hour timepoint resulted in a negative shift in zeta potential (**Figure 3-15d**), but after an observed decrease in the total quantity of adsorbed protein at the 24-hour timepoint (**Figure 3-15c**), OH-PSs experienced a positive shift in zeta potential (**Figure 3-15e**).

3.4.5. Relative Abundances of Proteins Adsorbed to PEG-*b*-PPS Nanocarriers

Determination of the relative abundances of proteins in the PCs of PEG-*b*-PPS nanocarriers was completed in collaboration with my colleague Michael Vincent, who optimized the protocols and analyzed the data described in this section. Having quantified bulk protein adsorption and its impact on the zeta potential of the nine nanocarrier formulations, we investigated whether the relative abundances of adsorbed proteins was significantly different as a result of nanocarrier morphology, surface chemistry, or plasma incubation time. For this analysis, 1 μg of protein from each formulation was separated via SDS-PAGE (**Figure 3-16a-c**). The separated protein subpopulations were stained using a mass spectrometry-compatible silver staining technique and their relative abundances ($n = 3$) were quantified with respect to a known quantity of albumin (**Figure 3-16d-f**). To simplify the analysis, protein abundances were quantified for molecular weight ranges (10 kDa per grouping). Due to constraints imposed by the maximum gel loading volume, 1 μg of protein could not be loaded into the gel for three samples (MeO-MCs for both the 2-hour plasma incubation and 24-hour plasma incubation; MeO-FMs for the 24-hour plasma incubation) due to their limited levels of protein adsorption (**Figure 3-15a,b**). For these samples, gel lanes were loaded with the maximum volume of sample at its recovered concentration. For clarity, the lanes corresponding to these samples have been denoted with an asterisk on the MC (**Figure 3-16a**) and FM (**Figure 3-16b**) gels. Due to variations in the total protein present within these three samples, only the relative abundances of proteins within each individual formulation may be compared.

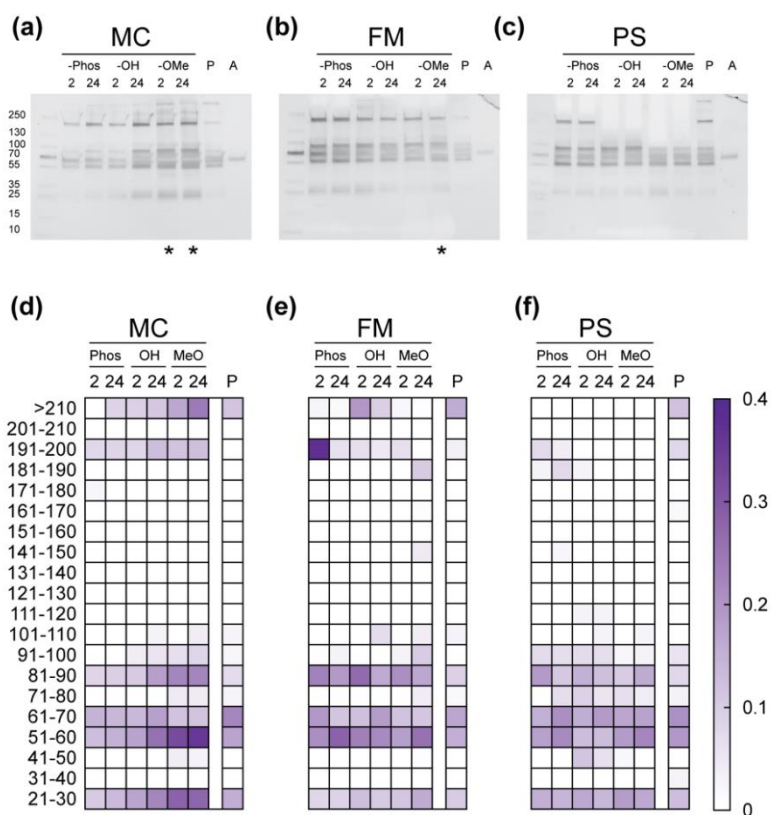


Figure 3-16. Quantification and identification of adsorbed protein following plasma incubation.

Silver stained adsorbed proteins separated by SDS-PAGE grouped by (a) MC, (b) FM, and (c) PS morphologies. One microgram of total protein was run per lane for each sample. Albumin-normalized relative abundance of adsorbed proteins determined by densitometry for (d) MCs, (e) FMs, and (f) PSs ($n = 3$). Molecular weights were determined by non-linear regression against migration distance of known MW standards. Quantified band intensities were combined into groups of 10 kDa intervals (displayed to the left of heat map (d)).

Observable differences in both the intensity and number of bands were apparent amongst the various formulations via visual inspection (**Figure 3-16a-c**). It should be noted that for protein electrophoresis along a single dimension, a single band may encompass several protein subpopulations exhibiting similar molecular weights that are not resolved by density of the polyacrylamide matrix used in the experiment. Within a single formulation, the time-dependent comparison of the relative abundance of a

protein subpopulation between the 2-hour and 24-hour timepoint revealed that most proteins (grouped by their molecular weight interval) maintain a constant or experience an increase in their relative abundance at the 24-hour timepoint (**Figure 3-16d-f**). Decreases in relative abundance were only observed for five molecular weight groups among the 18 formulations/conditions tested. These decreases in relative abundance were observed for the 191 - 200 kDa protein(s) in Phos-FMs, the > 210 kDa protein(s) and 81 - 90 kDa protein(s) for OH-FMs, the 81 - 90 kDa protein(s) for MeO-FMs, and the 81 - 90 kDa protein(s) of the Phos- PSs (**Figure 3-16d-f**). It should be noted that due to potential migration differences that may occur for proteins exhibiting molecular weights near an interval bound, observed differences between adjacent molecular weight groupings were excluded from analysis. For clarity, an example of an ignored difference is observed for the MeO-functionalized PSs (**Figure 3-16f**), where there is an apparent loss of the 191 - 200 kDa protein(s) detected at 2-hours and an apparent gain of a lower molecular weight 181 - 190 kDa protein(s) at the 24-hour timepoint.

Some interesting observations were made on the basis of morphology and surface chemistry. Neutral PSs experienced insignificant adsorption of high molecular weight proteins (> 150 kDa). For the vesicular structures investigated, only the Phos-functionalized PSs experienced adsorption of high molecular weight species, but this was limited to a relatively low abundance of 181 – 200 kDa protein(s) (**Figure 3-16f**). On the other hand, MCs and FMs exhibited adsorption of proteins with molecular weights > 190 kDa (**Figure 3-16d-e**), irrespective of the surface chemistry displayed. Interestingly, the 191- 200 kDa protein(s) adsorbed to Phos-functionalized FMs at the 2-hour timepoint had the greatest relative abundance quantified in our study (**Figure 3-16e**). However, a substantial decrease in the abundance of this protein population was observed at the 24-hour timepoint. The 51 - 60 kDa protein(s) exhibited the sole increase in abundance in this formulation (**Figure 3-16e**). These results suggest the possible displacement of the high molecular weight proteins with proteins in 51-60 kDa range as the PC formed on Phos-functionalized FMs evolves with time. While the general changes in PC composition have been investigated, further identification of the individual proteins present are underway.

3.5. Conclusion

Utilizing the BCPs described in Chapter 2, we were able to prepare nine nanocarrier formulations that varied in their combination of morphology and surface chemistry. The introduction of the Phos- and OH-functionalities did not alter the expected aggregate morphology as predicted by f_{PEG} . Nanocarriers were investigated for their ability to induce cytokine secretion and their ability to activate complement. PEG-*b*-PPS nanocarriers elicited cytokine secretion profiles that differed from those induced by either toll-like receptor (TLR) 4 or TLR7/8 following incubation with human whole blood. No significant changes in cytokine secretion were observed following nanocarrier incubation in comparison to the DPBS control, although the elevated levels of IL-8 observed in response to OH-PS treatment spurred further investigation. We hypothesized that the IL-8 secretion observed may be linked to elevated C5a present due to complement activation, a process where polyhydroxylated particles have previously been implicated. To test this hypothesis, we assessed the concentration of the human anaphylatoxins C3a, C4a, and C5a in serum following nanocarrier treatment. We observed statistically significant increases in C4a and C5a concentration following Phos-PS treatment and a statistically significant increase in C5a concentration in response to OH-PS treatment in comparison to the DPBS control. The results demonstrate the potential for both charged and hydroxylated PEG-*b*-PPS nanocarriers to activate complement. Furthermore, it suggests a potential link between C5a and IL-8 secretion, but a more rigorous set of investigations is required to establish this relationship.

Lastly, we investigated the impact of PEG-*b*-PPS nanocarrier morphology and surface chemistry on cell uptake and protein adsorption. While morphology was the primary determinant of nanocarrier uptake within a given cell type, surface chemistry-associated differences were observed. One interesting observation pertained to the interaction of Phos-PSs with immature dendritic cells. When comparing the percent uptake within monocyte- and macrophage-like cells, MeO-PSs exhibit increased levels of uptake for all conditions tested in comparison to its Phos-functionalized counterpart. But within immature dendritic cells, Phos-PSs exhibit elevated, though not statistically significant, levels of uptake in comparison to MeO-PSs following plasma incubation. One of the most interesting observations pertained

to the impact of plasma incubation on nanocarrier uptake. The most common trend observed involved an increase in uptake from the pristine condition to the 2-hour plasma incubation condition followed by a decrease in uptake from the 2-hour to 24-hour plasma incubation condition.

Both the bulk protein adsorption and differences in the protein species (defined by MW ranges) were investigated for the nine nanocarrier formulations. In the context of bulk protein adsorption, differences were observed across timepoints, morphologies, and surface chemistries. To our surprise, a decrease in protein adsorption was observed across timepoints for all formulations except for MeO-functionalized PSs. Within a given surface chemistry, the total amount of adsorbed protein at the 2-hour timepoint decreased with decreasing f_{PEG} , but this trend was lost at 24-hours. Within a given morphology, protein adsorption decreased with the polarity of the surface functionality (i.e. Phos > OH > MeO). The propensity of Phos-functionalized nanocarriers to increase protein adsorption aligns with what has been reported in the literature, where surface charge induced increases in protein adsorption have been observed for both cationic as well as anionic nanocarriers. In addition to the changes in bulk protein adsorption, differences in the MW species that comprise the PC were also observed. On the basis of morphology, the contribution of high MW species to the PC decreased with a decreasing f_{PEG} . General trends across morphology based on surface chemistry were less apparent, though the presence of 181- 200 kDa protein(s) across all three morphologies was only observed for the Phos-functionalized nanocarriers. While the identification of these compositional differences are a start, more thorough analysis attempting to identify the individual proteins that comprise the PC for each formulation are currently underway.

3.6. Acknowledgments

We acknowledge staff and instrumentation support from the Structural Biology Facility at Northwestern University, the Robert H. Lurie Comprehensive Cancer Center of Northwestern University and NCI CCSG P30 CA060553. The Gatan K2 direct electron detector was purchased with funds provided by the Chicago Biomedical Consortium with support from the Searle Funds at The Chicago Community Trust. SAXS experiments were performed at the DuPont-Northwestern-Dow Collaborative Access Team (DND-CAT) located at Sector 5 of the Advanced Photon Source (APS). DND-CAT is supported by

Northwestern University, E.I. DuPont de Nemours & Co., and The Dow Chemical Company. This research used resources of the Advanced Photon Source, a U.S. Department of Energy (DOE) Office of Science User Facility operated for the DOE Office of Science by Argonne National Laboratory under Contract No. DE-AC02-06CH11357. This work made use of the EPIC facility of Northwestern University's NUANCE Center, which has received support from the Soft and Hybrid Nanotechnology Experimental (SHyNE) Resource (NSF ECCS-1542205); the MRSEC program (NSF DMR-1720139) at the Materials Research Center; the International Institute for Nanotechnology (IIN); the Keck Foundation; and the State of Illinois, through the IIN. This work was supported by the Northwestern University – Flow Cytometry Core Facility supported by Cancer Center Support Grant (NCI CA060553).

I would like to acknowledge all the researchers who were instrumental in these experiments. Jonathan Remis acquired the cryoTEM micrographs for this work. Dr. Sharan Bobbala modeled the SAXS data presented here. Dr. Sean Allen acquired and helped analyze much of the flow cytometry data. He and Molly Frey are responsible for the illustrations presented in this chapter. I would also like to acknowledge Dr. Matt Clutter (High Throughput Analysis Laboratory, NU) for conducting the assessment of nanocarrier immunogenicity and for acquiring the complement activation data. Lastly, I would like to thank both Molly Frey and Mike Vincent. Molly was the first student in the Scott lab to begin questioning the impact of PEG-*b*-PPS nanocarrier chemistry on protein adsorption. Her suggestion/influence helped drive this project to where it is now. Mike is responsible for the design, development, optimization, and execution of the protein analysis pipeline relied on for this work. The data presented in Appendix A is Mike's own, and I thank him for allowing me to present it here to explain our rationale for how we chose to analyze the protein-nanocarrier complexes. He made the PC analysis his own and was central to the success of this project.

3.7. Publication Information

Portions of this chapter are in preparation for publication. The working manuscript title encompassing the experiments discussed in this chapter is:

Karabin, N.B.; Vincent, M.P.; Allen, S.D.; Frey, M.; Bobbala, S.; Yi, S.; Yang, Y.; Scott, E.A. Achieving differential protein adsorption and cellular uptake through combinations of nanocarrier morphology and surface chemistry. 2019.

CHAPTER 4

Leveraging BCP Functionality for Sustained Nanocarrier Delivery

4.1. Abstract

Nanocarrier administration has primarily been restricted to intermittent bolus injections with limited available options for sustained delivery *in vivo*. Here, we demonstrate that cylinder-to-sphere transitions of self-assembled FM-scaffolds can be employed for sustained delivery of monodisperse micellar nanocarriers with improved bioresorptive capacity and modularity for customization. Modular assembly of FMs from diverse BCP chemistries allows *in situ* gelation into hydrogel scaffolds following subcutaneous injection into mice. Upon photo- or physiological oxidation, molecular payloads within FMs transfer to micellar vehicles during the morphological transition, as verified *in vitro* by electron microscopy and *in vivo* by flow cytometry. FMs composed of multiple distinct BCP fluorescent conjugates permit multimodal analysis of the scaffold's non-inflammatory bioresorption and micellar delivery to immune cell populations for one month. These scaffolds exhibit highly efficient bioresorption wherein all components participate in retention and transport of therapeutics, presenting previously unexplored mechanisms for controlled nanocarrier delivery.

4.2. Introduction

4.2.1. The Case for Sustained Nanocarrier Delivery

Nanocarriers present a versatile means of delivering therapeutic and diagnostic agents to specific cells and tissues [120, 308, 313, 322, 323]. Targeted nanocarrier delivery systems are primarily administered by bolus intermittent injections and infusions, with few options available for sustained delivery [324]. Sustained delivery platforms have proven highly advantageous for drug administration, particularly for long-term processes such as wound healing [325, 326], hormone therapy [327, 328], and transplant tolerance [329, 330], and incorporation of nanocarriers may further improve the efficacy and flexibility of these applications [331, 332]. Due to the physicochemical similarities and cellular biodistributions between nanoscale materials and viruses, nanocarriers have demonstrated considerable advantages for the

targeting and modulation of phagocytic APCs that are critical for eliciting immune responses during vaccination and immunotherapy [119, 120, 333-335]. As a result, controlled long term delivery of nanocarriers may present avenues for immunization and the treatment of diseases characterized by severe immune dysregulation, such as cancer, cardiovascular disease, and diabetes [119, 120].

4.2.2. Limitations of Current Sustained Delivery Platforms for Nanocarriers

The most common sustained nanocarrier delivery platforms are composite systems that rely on implanted or injected hydrogel networks to entrap nanoparticulate delivery vehicles [153, 336-339].

Figure 4-1 provides a graphical depiction of a composite system for sustained nanocarrier delivery.

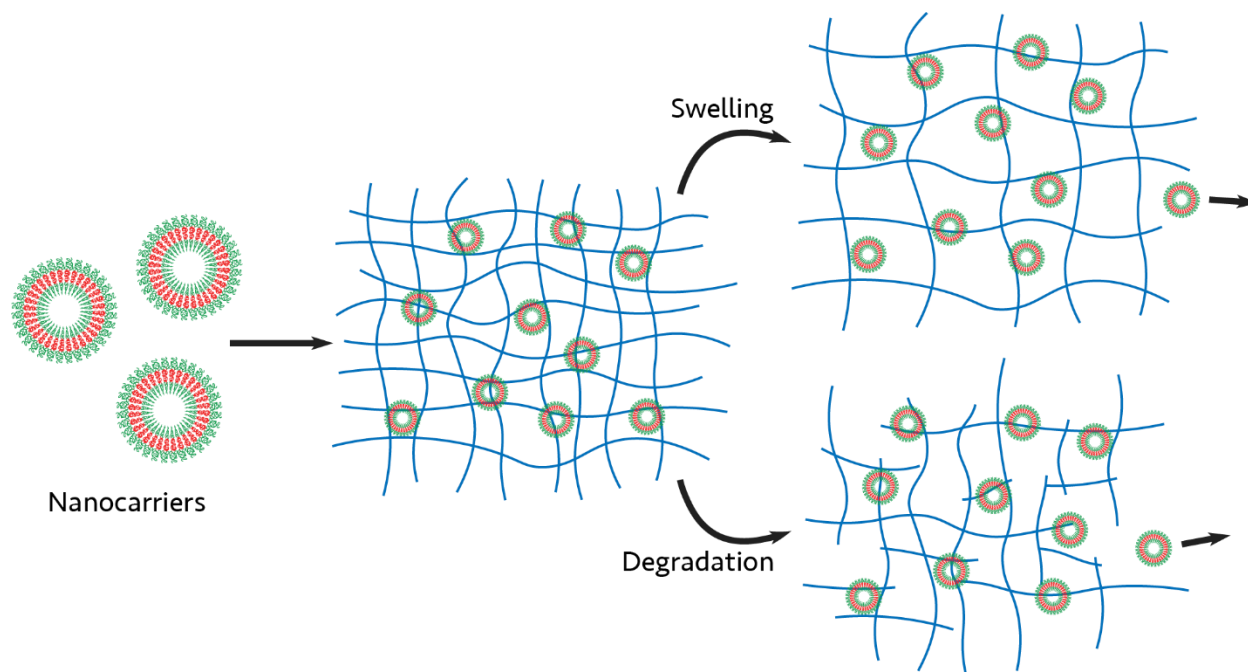


Figure 4-1. Graphical depiction of a composite nanocarrier-hydrogel system. Conventional sustained nanocarrier platforms rely on composite systems. In these systems, nanocarriers are mixed into the polymer solution prior to crosslinking. Upon gelation, the nanocarriers become entrapped within the hydrogel. Nanocarrier release is controlled by the rate/degree of hydrogel swelling or degradation.

Such systems employ either crosslinked synthetic or natural biopolymers to modulate the diffusive release of entrapped nanocarriers, but given the structural role of the polymer network, only a fraction of the total

material present in the construct plays a direct role in delivery of the therapeutic molecule. Therefore, the bulk of the hydrogel material serves no direct therapeutic purpose and may instead elicit chronic inflammatory responses with or without controlled degradation [340, 341]. The primary disadvantage of these hydrogels is the foreign body response, which eventually leads to isolation of the implant through formation of a fibrous capsule that can induce patient discomfort and disruption of nanocarrier release kinetics [340, 342]. To enhance tolerability of nanocarrier-loaded hydrogels, alternative strategies have emerged that include hydrogels composed of non-covalently linked nanocarriers themselves without polymer matrices [343], as well as hydrogels composed of polymers with reduced inflammatory potential [341, 344]. We sought to combine and improve upon both these strategies by developing a synthetic macromolecular hydrogel network that could dynamically restructure into monodisperse nanoscale vehicles for non-inflammatory bioresorption and sustained nanocarrier delivery.

4.2.3. Dynamic Self-assembly Behavior of BCPs

Depending on the method of preparation and solution conditions, BCP systems can controllably self-assemble into nonequilibrium structures that can be induced to further transition into different thermodynamically stable morphologies upon appropriate stimulation [94, 345-347]. For example, BCPs can assemble into high aspect ratio cylindrical FMs that can transition to spherical MCs under a variety of conditions [346-351]. CryoTEM has been used to capture various snapshots of these processes [346, 349-351]. Surface tension-dependent mechanisms at the solvent/BCP interface for these cylinder-to-sphere (i.e. FM-to-MC) transitions have been investigated both empirically and theoretically [346, 347, 349-351]. Since BCPs have been employed for the formation of hydrogels [352-354], we hypothesized that a hydrogel composed of FMs that are susceptible to inducible or continuous changes in surface tension may be employed for sustained micellar delivery. As the cylindrical FMs transition to their spherical counterparts, the primary structural component of the hydrogel depot would become an active participant in delivery of therapeutic or diagnostic payloads.

4.2.4. Oxidation Sensitivity of PEG-*b*-PPS Permits Morphological Transitions

As was introduced in Sections 1.2.5. and 1.2.6., PEG-*b*-PPS is a versatile BCP system that has been utilized to produce a variety of self-assembled nanocarriers, many of which can undergo oxidation-dependent changes in nanostructure morphology [32, 60, 82]. The assembled nanostructure is a function of the PEG-*b*-PPS hydrophilic mass fraction (molecular weight ratio of the hydrophilic block to the total BCP) [60, 82, 95, 204]. By controlling the block lengths of PEG-*b*-PPS, monodisperse populations of spherical MCs, vesicular PSs, and cylindrical FMs have been produced for the delivery of both hydrophilic and lipophilic payloads [30, 94, 192, 204]. The ability to form diverse nanostructure morphologies can be partially attributed to the low T_g (227 K) and resulting high chain flexibility of the hydrophobic PPS block that permits rapid transitions between metastable aggregate morphologies [94, 355, 356]. Importantly, PEG-*b*-PPS oxidizes to more hydrophilic poly(propylene sulfoxide) or poly(propylene sulfone) copolymers (**Figure 4-2**), which allows rapid and controlled oxidation-triggered transitions of PEG-*b*-PPS nanostructure morphologies [60, 82]. Oxidation has been previously employed to induce payload release from the aqueous interiors of PEG-*b*-PPS PSs [82, 192, 193], but has not been used to induce cylinder-to-sphere transitions for sustained delivery.

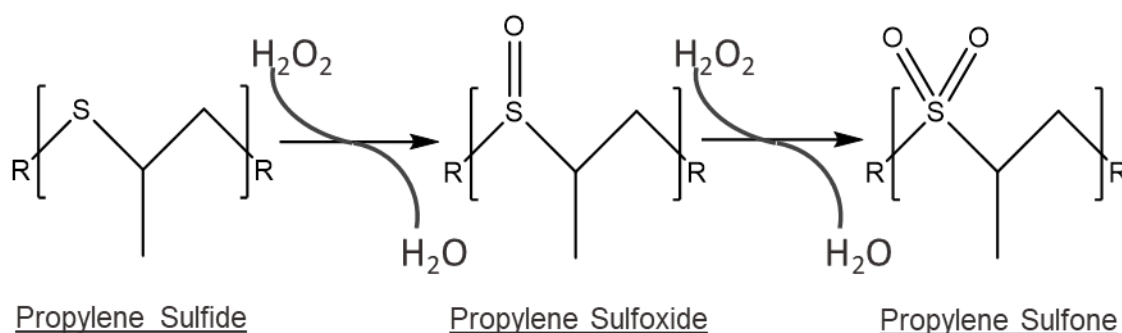


Figure 4-2. Schematic of propylene sulfide oxidation. Propylene sulfide, in the presence of reactive oxygen species such as hydrogen peroxide (H_2O_2), is converted to propylene sulfoxide and, eventually, propylene sulfone. The oxidation of propylene sulfide results in an increase in hydrophilicity, which can influence the preferred aggregate morphology of PEG-*b*-PPS.

We hypothesized that cylinder-to-sphere transitions may occur for PEG-*b*-PPS FMs due to changes in surface tension that occur under oxidative conditions as propylene sulfide converts to more hydrophilic derivatives. After characterizing FMs in solution via cryoTEM and SAXS, we captured these morphologic transitions via cryoTEM. Thermodynamic modelling was subsequently used to verify the potential driving force for the cylinder-to-sphere transition. Modification of the PEG-*b*-PPS synthesis allowed for the generation of surface reactive FMs that could be covalently crosslinked together to form a macroscopic scaffold. The transition of FM-scaffolds to micellar delivery vehicles in response to either photooxidation or physiologic oxidation was studied both *in vitro* and *in vivo*, respectively. Studies were conducted to characterize the released micelles and confirm their presence *in vivo*. Lastly, the sustained release of micellar vehicles was explored *in vivo*. Nanostructure uptake by APCs within various lymphoid tissues and histological analysis of the tissue surrounding the injection site were assessed to highlight the platform's potential for future *in vivo* applications.

4.3. Materials and Methods

4.3.1. Chemicals

All chemical reagents were purchased from Sigma-Aldrich St. Louis, MO, USA, unless stated otherwise. Fluorescent antibodies, Zombie Aqua fixable cell viability kit, cell staining buffer, and IC cell fixation buffer were acquired from BioLegend.

4.3.2. Preparation of FM Assemblies

FMs were generated via thin-film rehydration. PEG-*b*-PPS was dissolved in ~2 mL of dichloromethane (0.5 w/v%) within 2.0 mL clear glass vials (ThermoFisher Scientific). Following the removal of dichloromethane with desiccation, the thin polymer films were hydrated with 1 mL of either DPBS (ThermoFisher Scientific) or Milli-Q water and gently agitated overnight using a Stuart SB3 rotator.

4.3.3. Cryogenic Transmission Electron Microscopy (CryoTEM)

Samples for cryoTEM were prepared by applying 3 μL of 10 $\text{mg}\cdot\text{mL}^{-1}$ sample on pretreated holey or lacey carbon 400 mesh TEM copper grids (Electron Microscopy Sciences). Following a 3 s blot, samples were plunge-frozen (Gatan Cryoplunge 3 freezer). Images of samples entrapped in vitreous ice were acquired using a field emission transmission electron microscope (JEOL 3200FS) operating at 300

keV with magnification ranging from 2,000 x to 12,000 x nominal magnification. Digital Micrograph software (Gatan) was used to align the individual frames of each micrograph to compensate for stage and beam-induced drift. Any further image processing conducted on the aligned frames was completed in ImageJ.

For cryogenic electron tomography studies, FM solutions were mixed with hydrogen peroxide (H_2O_2) for a final H_2O_2 concentration of 0.01% by weight 30 minutes prior to freezing following the protocol described above. Tomographs were acquired at 12,000 x nominal magnification, corresponding to a 3.4 Å pixel spacing, and a total electron dose of $\sim 50 \text{ e}^- \text{ \AA}^{-2}$. Data was collected using SerialEM. An asymmetric tilt range spanning 83° was acquired with individual images captured every 2° . The collected image series was processed using the IMOD 4.9.5 package, saved as an individual stack of images, and converted into a movie via ImageJ.

4.3.4. Graphene Liquid Cell Transmission Electron Microscopy (GLC-TEM)

FMs were mixed with concentrated H_2O_2 and immediately imaged (within 5 minutes post-mixing) via GLC-TEM. Final concentrations of polymer and H_2O_2 were 8 mg mL^{-1} and 5% w/w, respectively. For GLC-TEM sample preparation, 2000-mesh graphene coated TEM grids were obtained from Graphene Supermarket (Graphene Laboratories Inc., NY, USA) and APS copper etchant 100 was purchased from Transene Company (MA, USA). Graphene liquid cells were prepared as previously described [357]. Imaging was conducted on a Hitachi HT7700 TEM operated at 80 kV. Electron doses of $0.1 - 2 \text{ e nm}^{-2} \text{ s}$ were utilized during micrograph acquisition. Image processing was completed in ImageJ.

4.3.5. Small Angle X-ray Scattering (SAXS)

SAXS studies were performed at the DuPont-Northwestern-Dow Collaborative Access Team (DND-CAT) beamline at Argonne National Laboratory's Advanced Photon Source (Argonne, IL, USA) with 10 keV (wavelength $\lambda = 1.24 \text{ \AA}$) collimated X-rays. The scattering profile of FMs was assessed both in DPBS and in 15% w/w H_2O_2 . All the samples were analyzed in the q-range (0.001 to 0.5 \AA^{-1}), with a sample-to-detector distance of approximately 7.5 m and an exposure time of 1 s. The diffraction patterns of silver behenate were utilized to calibrate the q-range. The momentum transfer vector q is defined as $q=4\pi \sin\theta/\lambda$, where θ is the scattering angle. Data reduction, consisting of the removal of solvent/buffer scattering from

the acquired sample scattering, was completed using PRIMUS 2.8.2 software while model fitting was completed using SasView 4.0.1 software package.

4.3.6. Preparation of Ethyl Eosin- and Dil-loaded FM-scaffolds

FMs were generated via thin-film rehydration. Mixtures of PEG-*b*-PPS and VS-PEG-*b*-PPS consisting of 0%, 10%, 20%, and 30% by mass of the VS-functionalized BCP were dissolved in ~2.0 mL of dichloromethane (2.5 w/v%) within 2.0 mL clear glass vials (ThermoFisher Scientific). For the preparation of ethyl eosin-loaded FM-scaffolds, ethanol containing ethyl eosin was added to the vials for a final fluorophore concentration of 0.75% w/w with respect to polymer mass. For the preparation of Dil-loaded FM-scaffolds, ethanol containing Dil (ThermoFisher Scientific) was added to the vials for a final Dil concentration, with regard to polymer mass, of 0.067% w/w. Following the removal of dichloromethane and ethanol via desiccation, the thin polymer films were hydrated with 493 μ L of DPBS and gently agitated for a minimum of 36 hours using a Stuart SB3 rotator resulting in 10% w/v solutions of ethyl eosin- or Dil-encapsulating FMs. Ethyl eosin loading efficiency was quantified as described previously [82].

For scaffold formation, 8-arm PEG-thiol (Creative PEGWorks) was dissolved in DPBS to produce a 10% w/v solution. The 8-arm PEG-thiol solution was added to the 10% w/v FM solution corresponding to a 1.1:1 molar ratio of thiol:vinyl sulfone. The mixture was briefly vortexed before 55.0 μ L aliquots were plated in 6 mm Teflon molds and cured at 37°C for 30 minutes in a humidified environment to prevent evaporative loss. Following the curing procedure, scaffolds were carefully recovered and washed for 1 hour in 2.0 mL reservoirs of Milli-Q water.

4.3.7. Cryogenic Scanning Electron Microscopy (CryoSEM)

Swollen scaffolds were quartered. Sections exhibiting a thickness of approximately 200 μ m were further trimmed and placed in aluminum sample carriers (TECHNOTRADE International) with a 3 mm outer diameter and cavity depth of 200 μ m. High-pressure freezing (HPM100, Leica) was used to preserve the internal structure of the scaffolds as seen in the wet state through vitrification. A pressure exceeding 2,100 bar was applied to the samples prior to cryogenic immobilization. Vitrified samples were recovered and stored in liquid nitrogen until further processing.

Cryo-planing (UC7/FC7 Cryo-Ultramicrotome, Leica) was performed to provide a flat internal plane for imaging. While maintaining an ambient temperature of -170°C , between 60 and 120 μm were removed from the sample surface. Planed samples were recovered from the dry nitrogen atmosphere and transferred in liquid nitrogen for freeze-etching and coating. After loading in a VCT shuttle, freshly planed samples were transferred into a freeze-etching instrument (ACE600 High Vacuum Coater, Leica) precooled to -120°C under high vacuum. To sublimate water from the surface, the temperature was raised to -105°C and held for 9 minutes. After etching the surface, the temperature was again lowered to -120°C and the sample surface was coated with 4.0 nm of platinum and 4.0 nm of carbon to minimize charging effects. Etched and coated samples were subsequently transported via the VCT shuttle to the pre-cooled cryo-stage set at -120°C in a field emission scanning electron microscope (S4800-II FE-SEM, Hitachi). Images were obtained at -110°C with an accelerating voltage of 2.0 kV.

4.3.8. Rheological Analysis of FM-scaffolds

Rheological analysis was conducted at 37°C in a humidified atmosphere using a dynamic oscillatory rheometer (HR-2 DHR, TA Instruments) equipped with an 8 mm parallel plate geometry. Scaffolds were crosslinked within the rheometer gap, initially set to 0.5 mm, and allowed to cure for 30 minutes before being compressed to the final gap height of 0.3 mm just prior to analysis. An amplitude sweep was completed to verify that analysis was conducted within the linear viscoelastic region. Frequency dependence of the storage and loss moduli was analyzed in oscillatory mode with 0.5% applied strain ($n = 3$).

4.3.9. Photoinduced Oxidation of FM-scaffolds *in vitro*

Visible light was used to generate singlet oxygen to induce FM oxidation and transition to spherical MCs. FM-scaffolds encapsulating ethyl eosin were incubated in 1 mL of Milli-Q water within 3.5 mL glass vials (ThermoFisher Scientific). Scaffolds were exposed to white light (Max-303 Xenon Light Source, Asahi Spectra) at an intensity of $3.4 - 3.5 \text{ mW cm}^{-2}$ for 6 to 24 hours. Following irradiation, the 1.0 mL supernatant was removed and the remaining monolithic scaffold was lyophilized. Masses of the lyophilized scaffolds were used to assess scaffold degradation ($n = 3$ for non-irradiated control scaffolds; n

= 3 for control scaffolds confirming average initial mass; n = 6 for 10% VS-BCP scaffolds irradiated for 18 h; n = 7 for all other treatment groups).

4.3.10. Accelerated Degradation of FM-scaffolds *in vitro*

Accelerated degradation studies were conducted with Dil-loaded FM-scaffolds. Scaffolds were incubated in supraphysiologic solutions of H₂O₂, exhibiting concentrations of 0 mM, 100 mM, and 500 mM, at 37°C for up to one week. Reservoir volumes of 1 mL were maintained within 3.5 mL glass vials (ThermoFisher Scientific). To assess the cumulative release from FM-scaffolds in response to oxidation, 100 µL aliquots of sample were collected at various timepoints and added to black-walled 96 well plates to measure Dil fluorescence (excitation/emission 549/565 nm) on a SpectraMax M3 (Molecular Devices) plate reader (n = 3).

4.3.11. Characterization of Released MC

From the recovered supernatant, 0.5 mL aliquots were diluted in 1.5 mL of Milli-Q water and analyzed for absorbance at 270 nm (SpectraMax M3, Molecular Devices) (n = 6 for 10% VS-BCP and 20% VS-BCP irradiated for 18 h; n = 7 for all other treatment groups). The size distribution of released nanostructures was obtained using a Zetasizer Nano (Malvern Instruments) equipped with a 4mW He-Ne 633 laser (n = 3).

Nanostructure morphology was observed through cryoTEM, with sample preparation mimicking the protocol described above. CryoTEM was also used to confirm nanostructure size characterization provided by DLS. In brief, micrographs of MCs in the supernatants of scaffolds irradiated for 6 and 24 hours were acquired at 4,000 x nominal magnification. A total of 500 individual MCs, pooled from three separate micrographs for each sample, were manually sized via ImageJ to assess micellar size distributions for each formulation at both the 6 and 24 hour timepoints. Binning and histogram generation were completed in GraphPad Prism 7.03.

4.3.12. Animals

A/J female mice, 6-8 weeks old, were purchased from Jackson Laboratories. All mice were housed and maintained in the Center for Comparative Medicine at Northwestern University. All animal experimental procedures were performed according to protocols approved by the Northwestern University

Institutional Animal Care and Use Committee (IACUC). A power analysis was performed to estimate the number of animals required for each experimental group. No randomization or blinding method was used to assign animals to specific groups. Statistical significance between animal groups was assessed by Mann-Whitney U test.

4.3.13. *In vivo* MC Release from Subcutaneously Injected FM-scaffolds

FMs were generated via thin-film rehydration. Mixtures of PEG-*b*-PPS, PEG-*b*-PPS-DyLight, and VS- PEG-*b*-PPS consisting of 20% by mass of the VS-functionalized polymer were dissolved in ~2.0 mL of dichloromethane (2.5 w/v%) within 2.0 mL clear glass vials (ThermoFisher Scientific). Ethanol containing Dil (ThermoFisher Scientific) was added to the vials for a final Dil concentration, with regard to polymer mass, of 0.067% w/w. Following the removal of dichloromethane and ethanol via desiccation, the thin polymer films were hydrated with 493 μ L of DPBS and gently agitated for a minimum of 36 hours using a Stuart SB3 rotator resulting in 10% w/v solutions of Dil-encapsulating, DyLight-conjugated FMs.

For scaffold formation, 8-arm PEG-thiol (Creative PEGWorks) was dissolved in DPBS to produce a 10% w/v solution. A volume of the 8-arm PEG-thiol solution was added to the 10% w/v FM solution corresponding to a 1.1:1 molar ratio of thiol:vinyl sulfone. The mixture was briefly vortexed before 50 μ L were injected subcutaneously into the scapular region of isoflurane anesthetized A/J mice for in situ crosslinking using a 28G syringe (n = 4). As a control, Dil solubilized in ethanol was added to DPBS with a final concentration equal to that loaded into the FMs. 50 μ L of the Dil solution were injected in the same manner as the scaffold solution into separate A/J mice, 24 hours before the mice were euthanized for flow cytometry (n = 4).

4.3.14. *In vivo* Degradation of Subcutaneously Injected FM-scaffolds

FMs composed of either PEG-*b*-PPS, PEG-*b*-PPS-DyLight, and VS-PEG-*b*-PPS (as described above) or simply PEG-*b*-PPS and PEG-*b*-PPS-DyLight were generated via thin-film rehydration. BCP mixtures were dissolved in ~2.0 mL of dichloromethane (2.5 w/v%) within 2.0 mL clear glass vials (ThermoFisher Scientific). Following the removal of dichloromethane via desiccation, the thin polymer films were hydrated with 493 μ L of DPBS and gently agitated for a minimum of 36 hours using a Stuart SB3 rotator resulting in 10% w/v solutions of DyLight-conjugated FMs.

50 μL of either a mixture of free DyLight 755 maleimide (0.03 mg) and free DyLight 633 maleimide (0.03 mg) in DPBS ($n = 5$), free FMs ($n = 4$), or VS-functionalized FMs ($n = 4$) were injected subcutaneously into the scapular region of isoflurane anesthetized A/J mice using a 28G syringe. For scaffold formation, 8-arm PEG-thiol (Creative PEGWorks) was dissolved in DPBS to produce a 10% w/v solution. A volume of the 8-arm PEG-thiol solution was added to the 10% w/v FM solution corresponding to a 1.1:1 molar ratio of thiol:vinyl sulfone. The mixture was briefly vortexed prior to injection and subsequent *in situ* crosslinking. For consistency, free FM solutions also received an equivalent volume of the 8-arm PEG-thiol solution prior to injection.

An IVIS Spectrum *in vivo* imaging system with a heated stage and an inhaled isoflurane manifold was used to capture intravital fluorescence images. Images were collected over the course of 28 days using filter sets of 640/745 (AF-633) and 680/800 (AF-750) with a 1.5-cm subject height. To process images, all timepoints corresponding to a single treatment group were simultaneously loaded into Living Image software. Visualization of DyLight signal was scaled per treatment rather than individual mouse. The minimum threshold value for signal visualization was increased until signal depicted on the feet and tails of all mice in the analysis was removed. Circular regions of interest (ROIs) were applied for each mouse in the treatment group and adjusted to an area that encompassed all visible signal. Size adjusted ROIs were generated across timepoints for individual mice allowing for equivalent ROIs to be applied across all timepoints within the study. Total radiant efficiency was measured and recorded. The average background signal, recorded in an untreated A/J mouse, was used to calculate the total background radiant efficiency for each ROI. The total radiant efficiency associated with only the presence of DyLight-755 was calculated by subtracting the background radiant efficiency from the total radiant efficiency as measured in Living Image software.

4.3.15. Assessment of Immune Cell Biodistributions of Released MCs

For all the flow cytometry studies, mice were euthanized by CO_2 inhalation and cervical dislocation. Draining lymph nodes (brachial and axillary), non-draining lymph nodes (inguinal), spleen, and liver were collected from all mice. Liver was incubated in a collagenase solution (0.4 $\text{mg}\cdot\text{mL}^{-1}$ DNase I, 1.5 $\text{mg}\cdot\text{mL}^{-1}$ collagenase A, 5% FBS, 10 mM HEPES, in Hank's Balanced Salt Solution (HBSS)) for 45 minutes

at 37 °C, as described previously [358], and then was processed as described for the other organs. All other organs were homogenized by mechanical disruption before being passed through a 70 µm nylon filter and washed with RPMI. Cells were resuspended in cell staining buffer, separated into flow tubes, and were blocked with anti-CD16/CD32 and stained for cell viability using Zombie Aqua for 15 minutes. Cells were then stained with an antibody cocktail for 30 minutes. Cells were fixed overnight in a 1:1 solution of cell staining buffer and IC fixation buffer prior to flow cytometric analysis.

For the Dil-DyLight 633 colocalization studies, mice were euthanized one week after scaffold-FM injection (and 24 hours after free Dil injection). The antibody cocktail used for this experiment was: PerCP/Cy5.5 anti-mouse CD45, Pacific Blue anti-mouse CD19, FITC anti-mouse CD11c, APC/Cy7 anti-mouse CD11b, PE/Cy7 anti-mouse F4/80). Dil was detected using the PE channel and DyLight 633 was detected using the APC channel.

For the one-month release studies, mice were euthanized 28 days after subcutaneous injection of free DyLight, uncrosslinked (i.e. free) FMs, and FM-scaffold solution. The antibody cocktails used for these studies were as follows: panel 1 – Pacific Blue anti-mouse CD11c, FITC anti-mouse MHCII I-A/I-E, PerCP/Cy5.5 anti-mouse CD45, PE anti-mouse B220, PE/Cy7 anti-mouse CD8a, and APC/Cy7 anti-mouse Gr-1; panel 2 – Pacific Blue anti-mouse CD11c, FITC anti-mouse F4/80, PerCP/Cy5.5 anti-mouse CD11b, PE anti-mouse CD169, PE-Cy7 anti-mouse Ly-6G, APC-Cy7 anti-mouse CD45. DyLight 633 was detected using the APC channel for both panels. Flow cytometry was performed on a BD LSRII, and data was analyzed using the CytoBank online software [359].

4.3.16. Histological Analysis

At 28 days following the subcutaneous injection of free DyLight 755 maleimide, free FMs, or FM-scaffolds, mice were sacrificed via carbon dioxide asphyxiation and cervical dislocation. Skin samples and surrounding injection site tissues were harvested (n = 3 for each treatment group) and subsequently fixed in 10% neutral buffered formalin for 96 hours. Following tissue dehydration in ethanol, samples were embedded in paraffin, sectioned, and stained with haematoxylin and eosin (H&E) or Masson's trichrome.

4.4. Results and Discussion

4.4.1. Characterization of PEG-*b*-PPS FM and their Transition to MC

Figure 4-3 depicts the synthetic pathways used to prepare the BCPs utilized in this chapter.

The details pertaining to these syntheses can be found in Chapter 2.

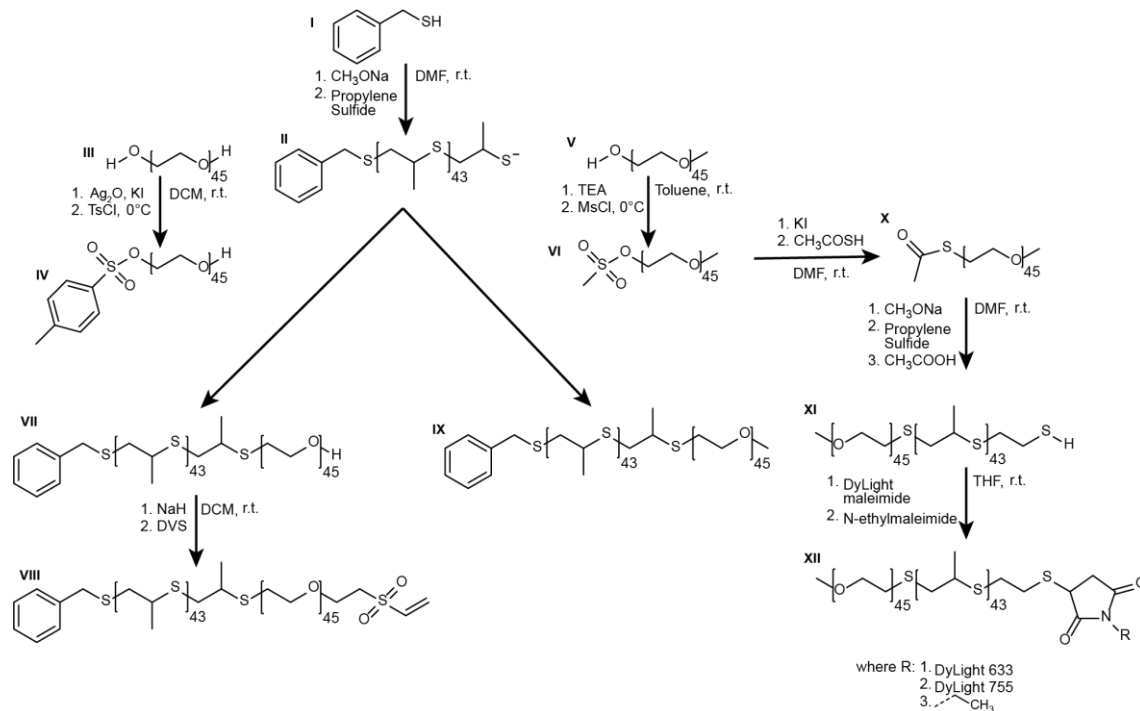


Figure 4-3. Synthetic pathway used to generate PEG-*b*-PPS BCPs used in Chapter 4. Benzyl mercaptan (I) is used to perform ring-opening polymerization on propylene sulfide to produce PPS homopolymer (II). To be used as an end capping agent for II, hydroxyl PEG (III) or mPEG (V) must first be functionalized with a leaving group, such as a tosylate or mesylate group to form hydroxyl PEG monotosylate (IV) or methyl ether PEG mesylate (VI). These two PEG derivatives are used to end cap II, resulting in products VII and IX, respectively. The available hydroxyl on VII is subsequently converted into a vinyl sulfone group to form Bn-PPS-*b*-PEG-VS (VIII). To synthesize the DyLight-conjugated polymer, mPEG-OMs (VI) must first be converted into a thiol-containing compound, through reaction with thioacetic acid, to form mPEG-TA (X). This is reacted in the same manner as the synthesis of compound II, to form PEG-*b*-PPS-Thiol (XI). This thiol group is available for covalent conjugation with maleimide groups to afford a number of conjugated PEG-*b*-PPS compounds (XII). Reproduced from [216] licensed under [Creative Commons By 4.0](https://creativecommons.org/licenses/by/4.0/).

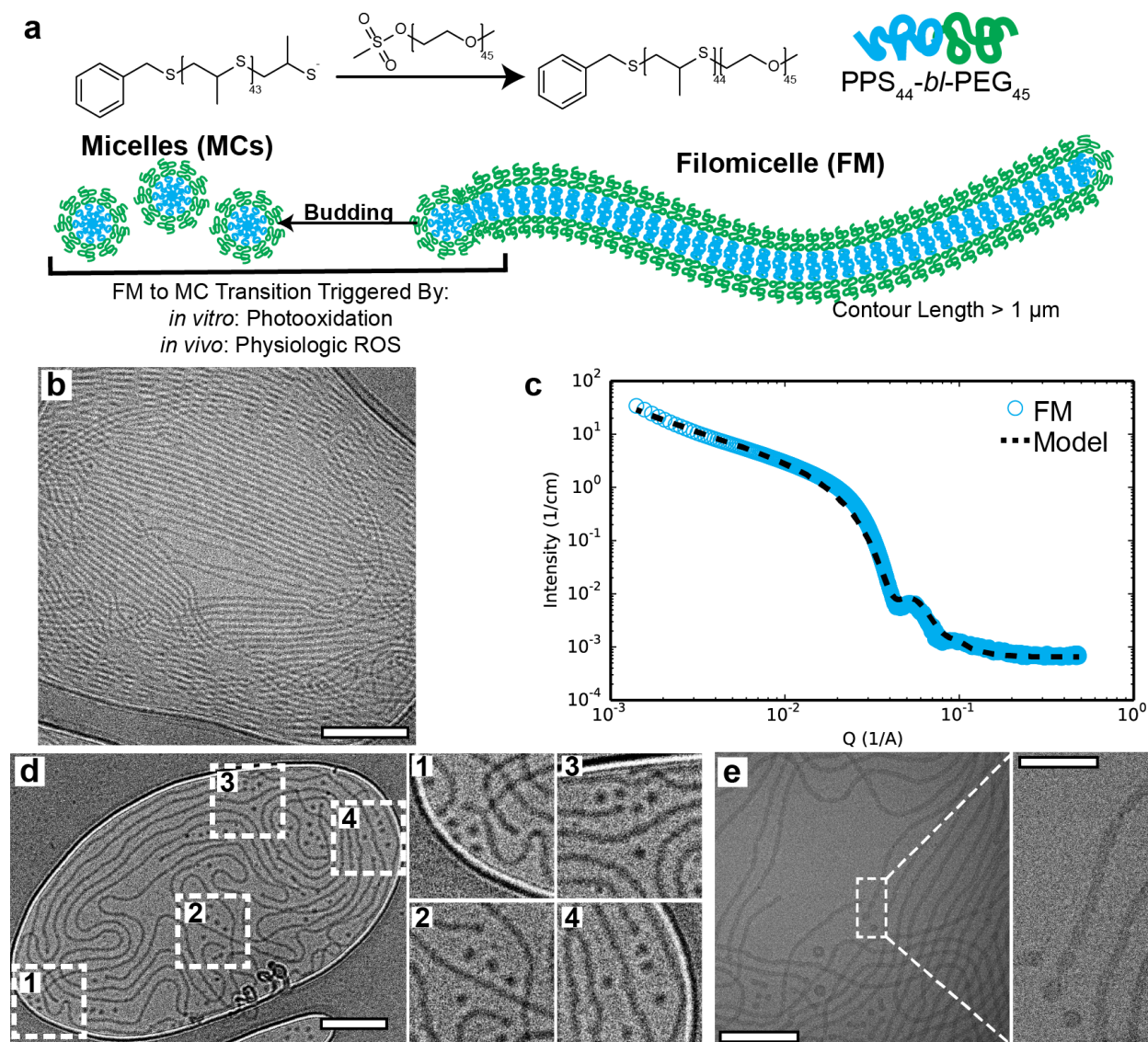


Figure 4-4. Characterization of PEG-*b*-PPS FMs and visualization of micelle budding. (a) Schematic of PEG-*b*-PPS BCP and diagram of a self-assembled filomicelle (FM) transitioning to a micellar vehicle. (b) CryoTEM micrograph of filomicelles. Scale bar represents 200 nm. (c) Small angle X-ray scattering of a filomicelle solution and corresponding model fit (flexible cylinder model). (d) and (e) CryoTEM micrographs demonstrate that cylinder-to-sphere transitions occur through a budding mechanism at the ends of filomicelles. Scale bars, left to right, 250 nm, 200 nm, 50 nm. Reproduced from [216] licensed under [Creative Commons By 4.0](https://creativecommons.org/licenses/by/4.0/).

FMs were prepared from methoxy-functionalized PEG₄₄-*b*-PPS₄₅ BCPs (MeO-BCP) (**Figure 4-4a**). CryoTEM confirmed that PEG-*b*-PPS BCPs with a hydrophilic mass fraction of 0.38 formed stable FMs exhibiting PPS core radii estimated between 8-10 nm and lengths in excess of a micron (**Figure 4-4b**). SAXS analysis of FM characteristics was achieved by fitting the FM scattering profile with a flexible cylinder model [360] ($\chi^2 = 0.068$) using a cylinder length of 2 μm , a persistence length of 150 nm and a PPS core radius of 8 nm (**Figure 4-4c**), which corresponded well with the observed cryoTEM. We further employed cryoTEM to capture morphologic transitions at the high curvature ends of FMs assembled from MeO-BCPs. Clusters of micelles were visually confirmed to concentrate primarily at the ends of FMs and were suggestive of sequential release (**Figure 4-4d,e**). Additional cryoTEM micrographs appear to capture the semi-spherical endcaps of FMs budding from the nanocarrier's cylindrical body (**Figure 4-5a, b, c**).

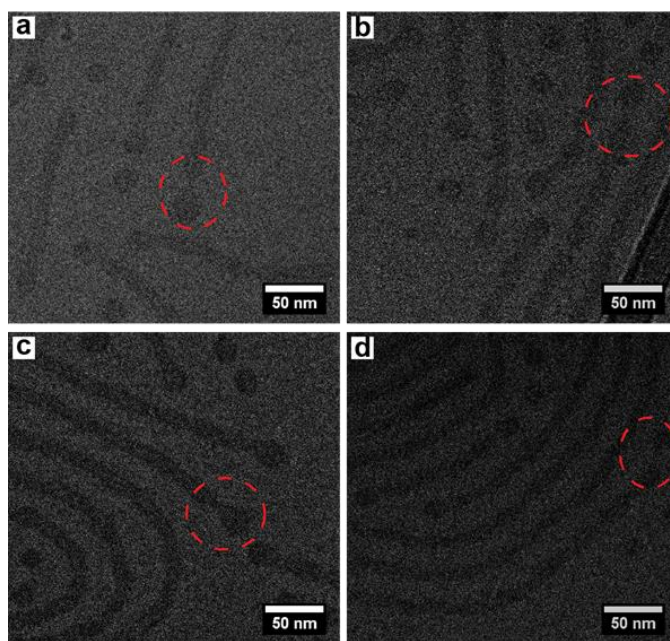


Figure 4-5. Additional cryoTEM micrographs of micelle budding. (a) – (c) CryoTEM micrographs of micellar budding from PEG-*b*-PPS filomicelles and (d) DyLight conjugated PEG-*b*-PPS filomicelles, with dotted red circles highlighting examples of budding. Scale bar represents 50 nm. Reproduced from [216] licensed under [Creative Commons By 4.0](https://creativecommons.org/licenses/by/4.0/).

Three-dimensional cryoTEM tomography verified that the depicted MCs were not the result of FMs oriented perpendicularly to the sample grid but were in fact a separate morphology (**Supplementary Movie 1**). The resulting micrographs exhibit similarities to previously described FM end-associated transitions [349, 350].

As cryoTEM requires vitrification of the sample, the acquired micrographs provide only snapshots of specific moments in time and, therefore, only limited information about this dynamic process. To capture the FM-to-MC transition in real-time, we utilized biocompatible graphene liquid cell transmission electron microscopy (GLC-TEM). This technique involves encapsulation of colloidal liquid samples between two monolayers of graphene, minimizing sample thickness for liquid imaging in a transmission electron microscope [357]. Graphene monolayers are electron transparent [361, 362] and permit monitoring dynamic processes within a liquid environment with atomic resolution [357]. We utilized this technique to capture the FM-to-MC transition in real-time. FMs were incubated with 5% w/w H_2O_2 and segments of three FMs were observed for several minutes. **Figure 4-6** shows three images captured during the three-minute time course.

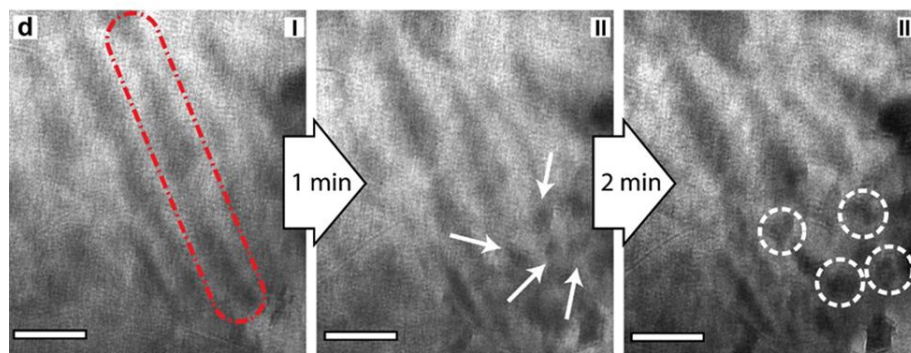


Figure 4-6. Graphene liquid cell (GLC)-TEM micrographs capture FM-to-MC budding in real time.

GLC-TEM micrographs at $t = 0$ min (I), $t = 1$ min (II), and $t = 3$ min (III). The dotted red cylinder in (I) highlights one of three visible structures (FMs) oriented diagonally across the micrograph. The white arrows in (II) point to dark globular structures that appear along the lower length of the two rightmost FMs. The dotted white circles in (III) highlight individual spherical structures that are discontinuous from the FMs. Scale bars, 50 nm.

We observed what appeared to be the end-localized formation of spherical structures (**Figure 4-6-II**) that were discontinuous from the FM from which they formed (**Figure 4-6-III**). Like the cryoTEM micrographs previously described, this experiment suggested that the PEG-*b*-PPS FM-to-MC transition occurs through an end-localized sphero-cylinder mediated mechanism.

To further investigate the PEG-*b*-PPS FM-to-MC transition, SAXS studies were conducted on FMs under oxidative conditions. Both SAXS and small angle neutron scattering have been employed to characterize the kinetics of the FM-to-MC transition in BCP systems [347]. The kinetics of this morphologic transition can provide insight as to whether the transition occurs through a Rayleigh instability-induced mechanism, where undulations along the length of the cylinder precede the complete disassembly of the cylindrical structure, or a sphero-cylinder mediated transition mechanism, where spherical MCs bud from the ends of the cylinders. **Figure 4-7** depicts the SAXS profiles of PEG-*b*-PPS FMs incubated in 15% w/w H₂O₂ (4.9 M) for up to two hours.

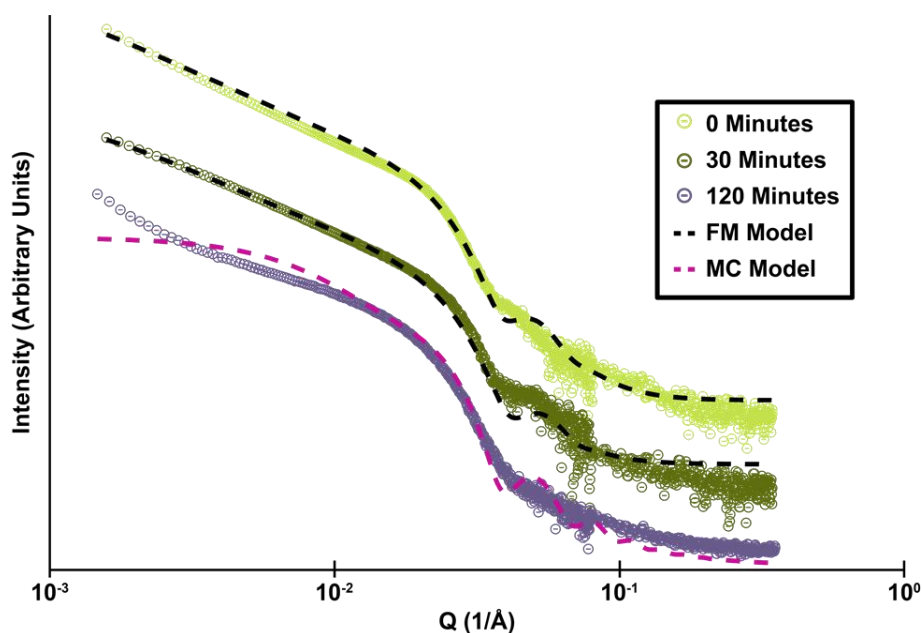


Figure 4-7. Confirmation of the FM-to-MC transition through small angle X-ray scattering (SAXS).

SAXS profiles of PEG-*b*-PPS FMs in a 4.9 M solution of H₂O₂. SAXS acquired following 0, 30, and 120 min of oxidation and fit with either a flexible cylinder or polymer micelle model.

Modeling of the SAXS profiles was used to determine the FM characteristics. Initially, the FMs exhibit a length of several microns (2.2 μm) and are well-fit by the flexible cylinder model ($\chi^2 = 0.089$). After being maintained in oxidative conditions for 30 minutes, the FMs, while still well-fit by the flexible cylinder model ($\chi^2 = 0.0014$), exhibit a length of approximately 900 nm. Following two hours of incubation in the oxidative solution, the SAXS profile of the sample is more consistent with polymer MC with a diameter ≈ 40 nm (i.e. fit with polymer micelle model; $\chi^2 = 0.0107$). This preliminary study demonstrated that the induced transition of PEG-*b*-PPS FMs to spherical MCs in a highly oxidative solution (49,000 times more concentrated than physiologic levels of H_2O_2) occurs on a timescale of tens of minutes to hours. The timescale of this transition, coupled with the observations made through cryoTEM and GLC-TEM, suggests that the PEG-*b*-PPS FM-to-MC transition proceeds through a sphero-cylinder mediated transition mechanism as opposed to a Rayleigh instability-induced mechanism.

4.4.2. Thermodynamic Modelling of FM-to-MC Transition

Given the oxidation sensitivity of the hydrophobic block and the impact that this oxidation has on overall BCP hydrophilicity, we hypothesized that oxidizing agents within the immediate FM environment could provide sufficient stimuli to trigger the cylinder-to-sphere transition within the PEG-*b*-PPS BCP system. Previous research in amphiphilic BCP micelles has shown that the cylinder-to-sphere morphologic transition can be driven by interfacial tension [348, 363, 364]. Using a thermodynamic model and interfacial measurements obtained via drop shape apparatus (DSA), we show that the transition in PEG-*b*-PPS can be understood by the reduction of interfacial energy upon oxidation of the sulfide group which is balanced by the chain stretching of core and corona blocks. Our thermodynamic analysis of PEG-*b*-PPS in solution follows the framework outlined in theoretical work by Zhulina et al. and Lund et al. [348, 363]. In this model, the total free energy of a BCP micelle is written as a sum of three components: the interfacial energy between core and solvent, F_{int} ; the elastic energy of stretching chains in the core, F_{core} ; and the energy associated with the chains in the corona, F_{corona} [364]. Each contribution can be broken down for cylindrical and spherical morphologies:

$$F_{int} = \frac{A_j \gamma}{P k_B T} \begin{cases} A_j = 4\pi R_c^2 & \text{Spheres} \\ A_j = 2\pi R_c L & \text{Cylinders} \end{cases} \quad (1)$$

Here, γ is the interfacial tension, R_c the core radius, P the aggregation number assuming a compact core: $P = 4\pi R_c^3 N_{avo} / (3V_{PPS})$ and $P = \pi R_c^2 L N_{avo} / V_{PPS}$ for spheres and cylinders, respectively. V_{PPS} is the molar volume of PPS block and N_{avo} is Avogadro's number.

$$F_{core} = k_j \frac{R_c^2}{R_{ee}^2} \begin{cases} k_j = \frac{\pi^2}{16} & \text{Spheres} \\ k_j = \frac{3\pi^2}{30} & \text{Cylinders} \end{cases} \quad (2)$$

Where $R_{ee} = N_{PPS}^{1/2} l_{PPS}$ is the unperturbed end-to-end radius of gyration of PPS, the core-forming block. N_{PPS} denotes the number of propylene sulfide monomers in the PPS block and l_{PPS} the effective segment length of PPS.

$$F_{corona} = \begin{cases} \frac{\nu C_F R_c}{\sqrt{s}} \ln \left(1 + \frac{l_{PEG} C_H N_{PEG} \left(\frac{s}{l_{PEG}^2} \right)^{(v-1)/2\nu}}{\nu R_c} \right) & \text{Spheres} \\ \frac{2C_F R_c}{\sqrt{s}} \left[\left(1 + \frac{(1+\nu) l_{PEG} C_H N_{PEG} \left(\frac{s}{l_{PEG}^2} \right)^{\frac{\nu-1}{2\nu}}}{2\nu R_c} \right)^{\nu/(\nu+1)} - 1 \right] & \text{Cylinders} \end{cases} \quad (3)$$

Where ν is the excluded volume parameter, s is the area available per BCP chain. N_{PEG} denotes the number of ethylene oxide monomers in the PEG block, and l_{PEG} the effective segment length of PEG. The total free energy of a micelle, $F_{micelle} = F_{int} + F_{core} + F_{corona}$, is minimized with respect to the core radius, R_c . The calculations were performed with all molecular parameters fixed. This included the compositions and molecular weights known from characterizations, while radii of gyration and segment lengths (l_{PEG} and l_{PPS}) were estimated from previous works [348]. Numerical prefactor parameters, C_F and C_H , were taken from

the literature [348, 363]. The equilibrium core radius R_c corresponding to free energy minima for spherical and cylindrical micelles is shown in **Figure 4-8a** while the micelle free energy calculated at the equilibrium core radius is shown in **Figure 4-8b**.

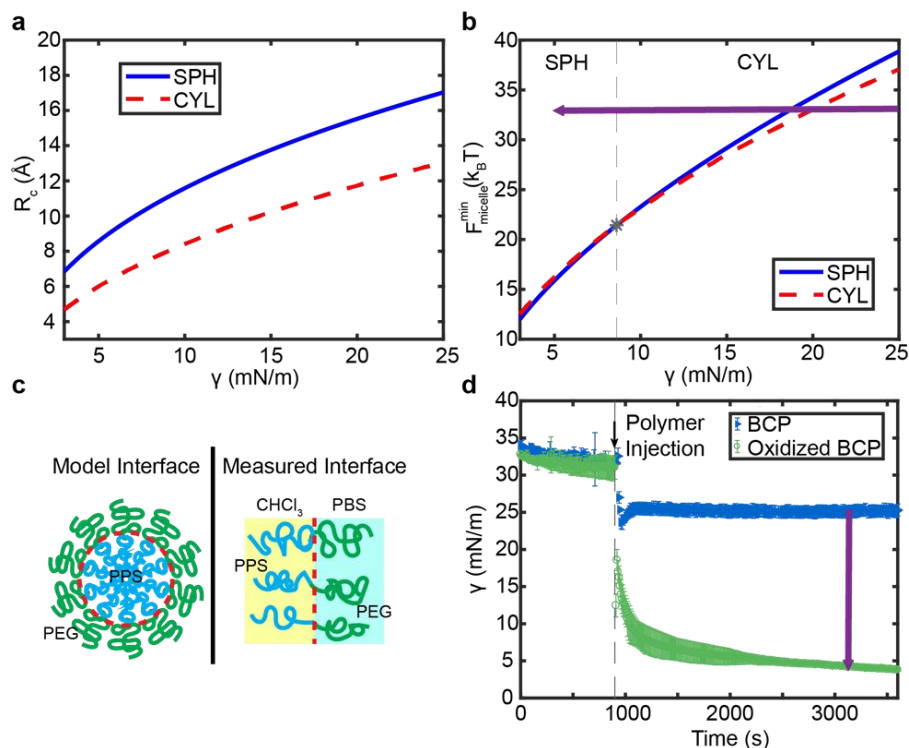


Figure 4-8. Thermodynamic modeling and interfacial measurements of oxidation based cylinder-to-sphere transitions. (a) Equilibrium core radii corresponding to the free energy minima for spherical micelles (SPH) and cylindrical filomicelles (CYL) and (b) Total free energy of SPH and CYL calculated at the equilibrium core radii. Star represents the interfacial tension at which cylinder-to-sphere transition occurs ($\gamma \approx 8$). Above this interfacial tension, structures prefer a CYL morphology; below this energy, SPH are formed. As BCP is oxidized, it moves across the map as indicated by the purple arrow. (c) Schematic highlighting differences between the modeled and measured systems. (d) Interfacial tension measurements with 2 mg mL^{-1} of BCP injected into the chloroform embedding phase at 900 seconds. Oxidizing BCP reduces the interfacial tension as indicated by the purple arrow. Reproduced from [216] licensed under [Creative Commons By 4.0](https://creativecommons.org/licenses/by/4.0/).

At high interfacial tension, cylindrical micelles are favored. Cylindrical micelles have a smaller core radius at the same interfacial energy, which reduces the elastic energy of the chains in the core. At lower interfacial tension, the system can accommodate a larger interfacial area, which leads to the formation of spherical micelles that minimize the interchain repulsion in the corona. From the thermodynamic model, we predict the transition to occur at $\gamma \cong 8 \text{ mN m}^{-1}$.

Experimentally measured values of the interfacial tension at the aqueous and organic solvent interface (**Figure 4-8c**) are shown in **Figure 4-8d** for PEG-*b*-PPS prior to and post oxidation in DPBS. Oxidation of the BCP was confirmed via ^1H NMR (**Figure 4-9**) as has been previously reported [82]. Interfacial tension measurements were collected using DSA following a previously published procedure [365]. We show that the oxidation of the PPS block leads to a substantial decrease in the interfacial tension. The final interfacial tension ($\gamma \cong 5 \text{ mN m}^{-1}$) of the oxidized polymer is below our calculated transition point, indicating that the decrease in γ can trigger the transition from cylinders to spheres in PEG-*b*-PPS micelles as the PPS block is oxidized.

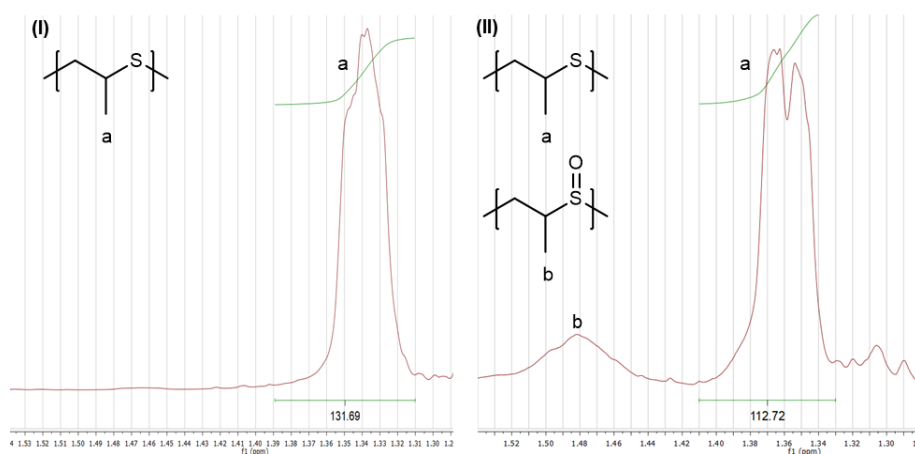


Figure 4-9. ^1H NMR confirmation of PEG-*b*-PPS oxidation for DSA experiments. MeO-functionalized PEG-*b*-PPS was used to form FMs and was subsequently oxidized through the addition of H_2O_2 . ^1H NMR spectra depicting the CH_3 protons of propylene sulfide for BCP prior to (I) and post-oxidation (II). The peak at 1.48 ppm in II indicates the presence of propylene sulfoxide.

This model provides qualitative confirmation of interfacial tension-driven cylinder-to-sphere transitions in PEG-*b*-PPS assembled morphologies. However, a quantitative comparison is not straightforward for several reasons. First, the measured interfacial tension in DSA represents the energy between PPS and PEG blocks across the chloroform-DPBS interface (**Figure 4-8c**). This interface contains a lower concentration of polymer than the model interface between the core and the corona block. Second, the thermodynamic model relies on numerical prefactors and long chain statistics, which are not necessarily applicable in the present system of only 44 propylene sulfide and 45 ethylene oxide repeat units. Further theoretical work would be necessary to more appropriately capture the description of the present system, but this is beyond the scope of our work presented here.

4.4.3. FM-scaffold Preparation and Characterization

To achieve rapid controllable crosslinking of FMs under physiologic conditions, we synthesized VS-functionalized PEG-*b*-PPS BCP modules (VS-BCP) (**Figure 4-10a**) [213]. VS-BCPs were co-assembled with non-reactive MeO-BCP at different ratios to achieve FMs with controllable levels of VS surface functionalization for subsequent crosslinking. Having experimentally observed the FM-to-MC transition and theoretically examined how this transition could be driven through oxidation for individual FMs in solution, we proceeded to assess whether this transition could be exploited when FMs were crosslinked into a macroscopic construct. To investigate sustained micellar release from FM scaffolds, we employed both VS-BCP and MeO-BCP to form modular FMs capable of being crosslinked into filamentous hydrogels (**Figure 4-10b**). At concentrations of 100 mg·mL⁻¹, these FMs formed viscous solutions that crosslinked into stable hydrogels within minutes in the presence of an 8-arm PEG-thiol crosslinker following injection into molds (**Figure 4-10c**).

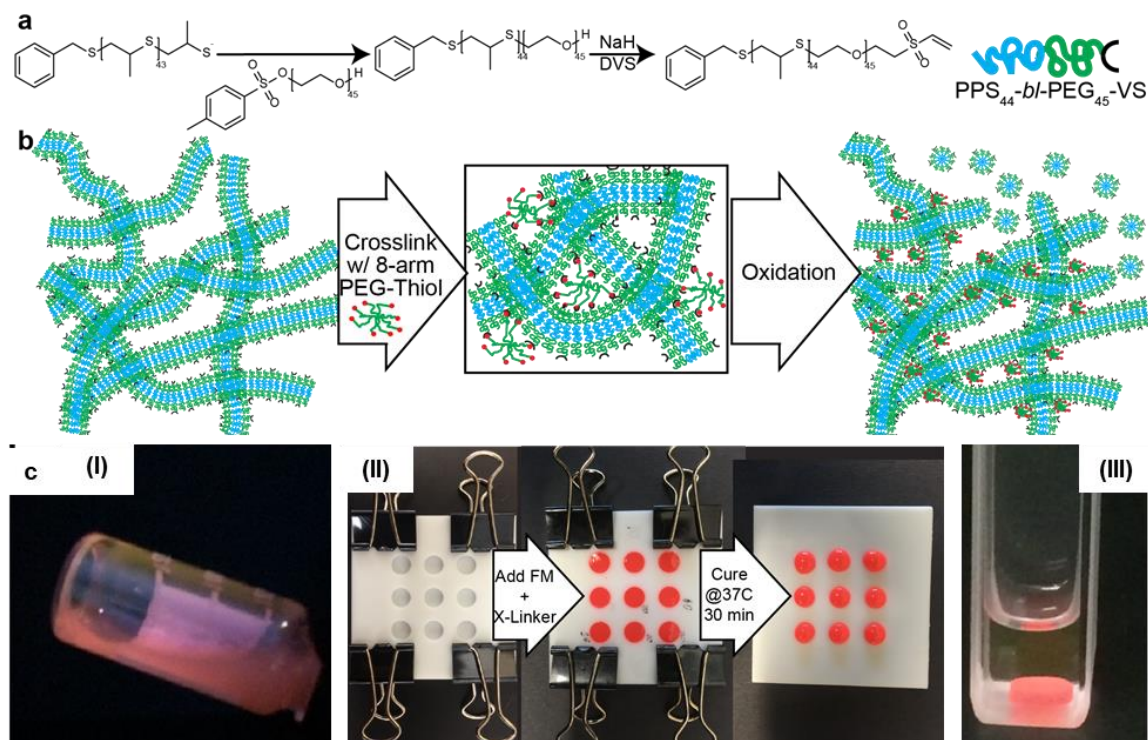


Figure 4-10. Graphical representation of crosslinked FM-scaffolds. (a) Schematic of vinyl sulfone (VS-BCP) PEG-*b*-PPS block copolymer synthesis. (b) Graphical depiction of an FM-scaffold crosslinking with 8-arm PEG-thiol and subsequent oxidation-triggered induction of the cylinder-to-sphere transition for release of micelles (MCs). FMs with PPS cores (blue) and PEG outer coronas (green) are shown as networks that can be crosslinked into stable porous scaffolds through modular incorporation of thiol (red) reactive BCP end-functionalized with VS (black) moieties. Oxidation *via* photo-oxidation (*in vitro*) or through physiologic levels of ROS (*in vivo*) induced cylinder-to-sphere (FM-to-MC) transitions for the release of monodisperse micelles. (c) Images depicting the formation of FM-scaffolds for *in vitro* studies. (I) A 100 mg mL⁻¹ (10 wt%) modular VS-BCP/MeO-BCP FM solution comprised of 20% w/w VS-BCP before crosslinking. (II) Teflon molds were filled with the 10 wt% solution of ethyl eosin-loaded FMs along with corresponding volumes of the 8-arm PEG-SH crosslinker. Plated FM solutions were cured for 30 minutes at 37°C in a humidified environment to produce the FM-scaffolds. (III) Crosslinked FM-scaffolds maintain their cylindrical structure in DPBS. Adapted from [216] licensed under [Creative Commons By 4.0](https://creativecommons.org/licenses/by/4.0/).

Differing the ratios of VS-BCP and MeO-BCP allowed tuning of the rheological properties of the crosslinked hydrogels (**Figure 4-11**). Oscillatory mode rheological analysis of the crosslinked scaffolds composed of 10%, 20%, and 30% w/w of the VS-BCP revealed increases in the elastic modulus over the tested frequency range, as well as a decrease in frequency dependence at low to moderate frequencies (**Figure 4-11b**). Scaffolds exhibited frequency dependence in both their storage and loss moduli at higher frequencies, and the inverse linear dependence of complex viscosity with regard to frequency was indicative of a solid-to-liquid transition (**Figure 4-11b-d**). Crosslinked FM-scaffolds demonstrated similar rheological behavior to the physically crosslinked PEG-*b*-oligo(ethylene sulfide) constructs described previously [366].

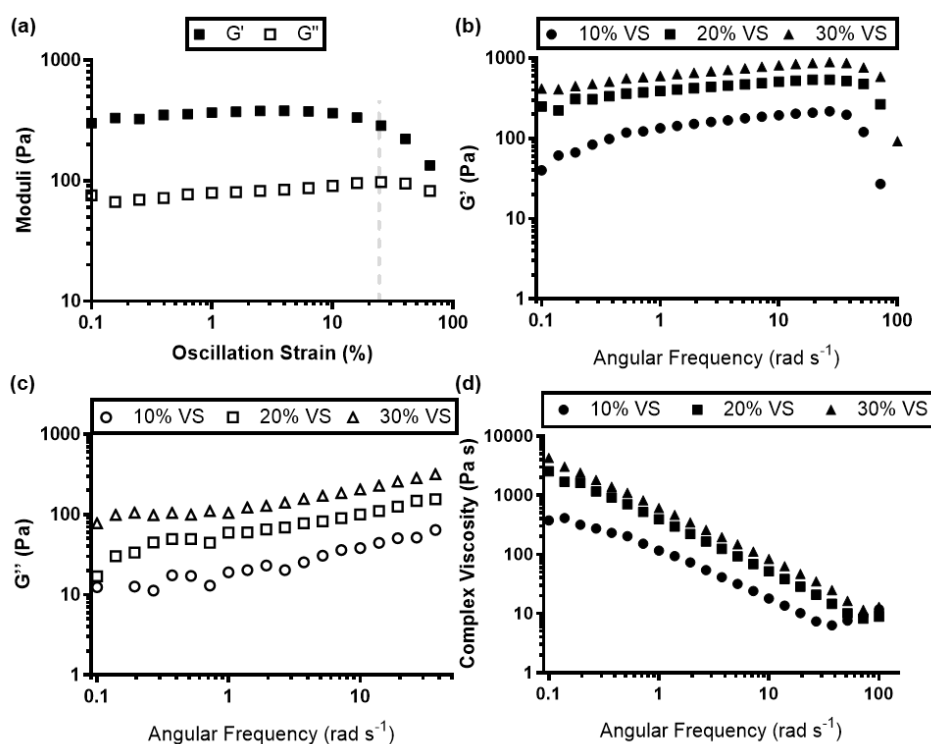


Figure 4-11. Rheological characterization of PEG-*b*-PPS FM-scaffolds. (a) Strain-dependent oscillatory rheology of FM-scaffolds (10 wt%) incorporating 20% VS-BCP (Angular frequency = 6.28 rad s^{-1} , 37°C). Frequency-dependent oscillatory rheology of (b) storage moduli (G'), (c) loss moduli (G''), and (d) complex viscosities for FM-scaffolds (10 wt%) exhibiting varying percentages of VS-BCP (Strain = 0.5%, 37°C). Adapted from [216] licensed under [Creative Commons By 4.0](https://creativecommons.org/licenses/by/4.0/).

Analysis of scaffolds by cryoSEM (**Figure 4-12**) revealed an underlying nanoporous architecture with mesh sizes ranging from tens to hundreds of nanometers, reminiscent of collagen matrices and previously reported surfactant and BCP molecular gels [367, 368].

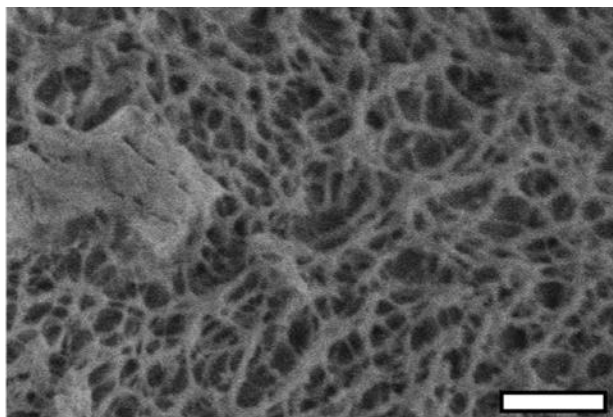


Figure 4-12. CryoSEM confirms FMs maintain their cylindrical structure upon crosslinking.

CryoSEM micrograph of the underlying fibrous architecture of a FM-scaffold containing 20% w/w VS-BCP. Scale bar, 1 μm . Adapted from [216] licensed under [Creative Commons By 4.0](https://creativecommons.org/licenses/by/4.0/).

4.4.4. Oxidation of FM-scaffolds for Induced Release of MCs *in vitro*

While we had established that oxidation could drive the FM-to-MC transition in individual nanocarriers, we had yet to confirm that oxidation could induce the degradation of macroscopic FM-scaffolds. To assess whether FM-scaffolds transitioned to and released spherical MCs, we loaded VS-BCP/MeO-BCP FMs with the photo-oxidizer ethyl eosin to hasten the oxidation process through exposure to white light and rapidly induce scaffold degradation *in vitro* (**Figure 4-13**).

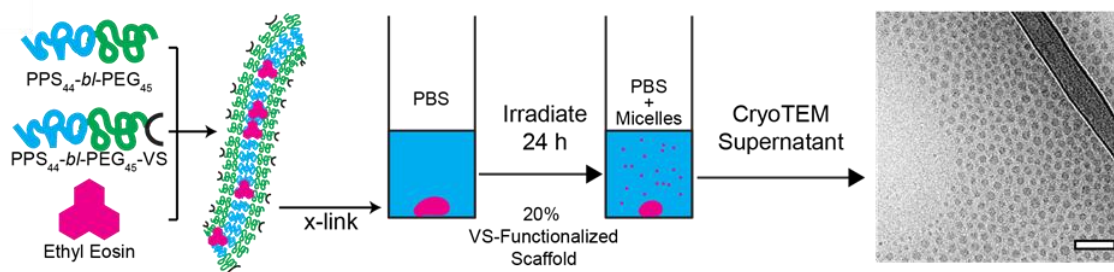


Figure 4-13. Graphical depiction of the *in vitro* photo-oxidation of ethyl eosin-loaded FM-scaffolds. Schematic portraying photo-oxidation of ethyl eosin-loaded FM-scaffolds, with representative cryoTEM micrograph of released PEG-*b*-PPS MCs. Adapted from [216] licensed under [Creative Commons By 4.0](https://creativecommons.org/licenses/by/4.0/).

Photo-oxidation has been previously demonstrated to provide precise spatio-temporal control over transitions in PEG-*b*-PPS nanostructure morphology [82]. Ethyl eosin was selected due to its hydrophobic nature (logP of 7.497) [369], which allowed partitioning within the PPS core for rapid and reproducible localized oxidation [82]. Scaffolds incorporating 10%, 20%, or 30% w/w of VS-BCP and loaded with 0.75% ethyl eosin by mass were exposed to white light for varying durations of time at room temperature. Ethyl eosin loading efficiency within the FM core at 0.75% by mass was determined to be approximately 83% (**Figure 4-14**), consistent with previous studies loading ethyl eosin within PEG-*b*-PPS nanostructures [82].

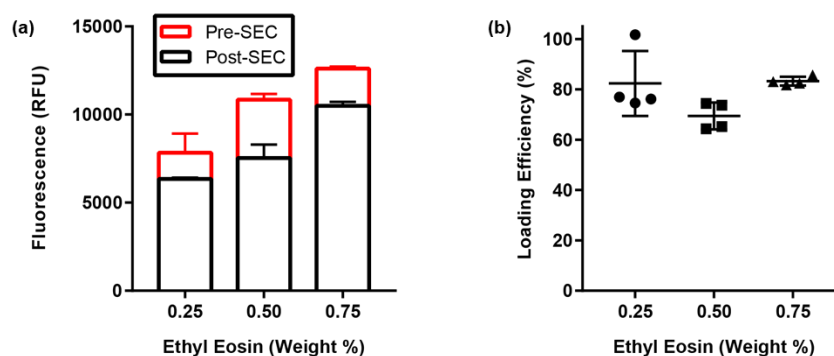


Figure 4-14. Loading efficiency of ethyl eosin within FMs. (a) Fluorescence intensity readings of loaded ethyl eosin within FM before and after gravity size exclusion on a sepharose 6B column and (b) loading efficiency derived from a single SEC purification with four measurement replicates ($n = 4$). Error bars represent the s.d. Adapted from [216] licensed under [Creative Commons By 4.0](https://creativecommons.org/licenses/by/4.0/).

CryoTEM and DLS were conducted on the supernatant surrounding the irradiated scaffolds, revealing monodisperse populations of spherical micelles despite varying percentages of VS-BCP (**Figure 4-15**).

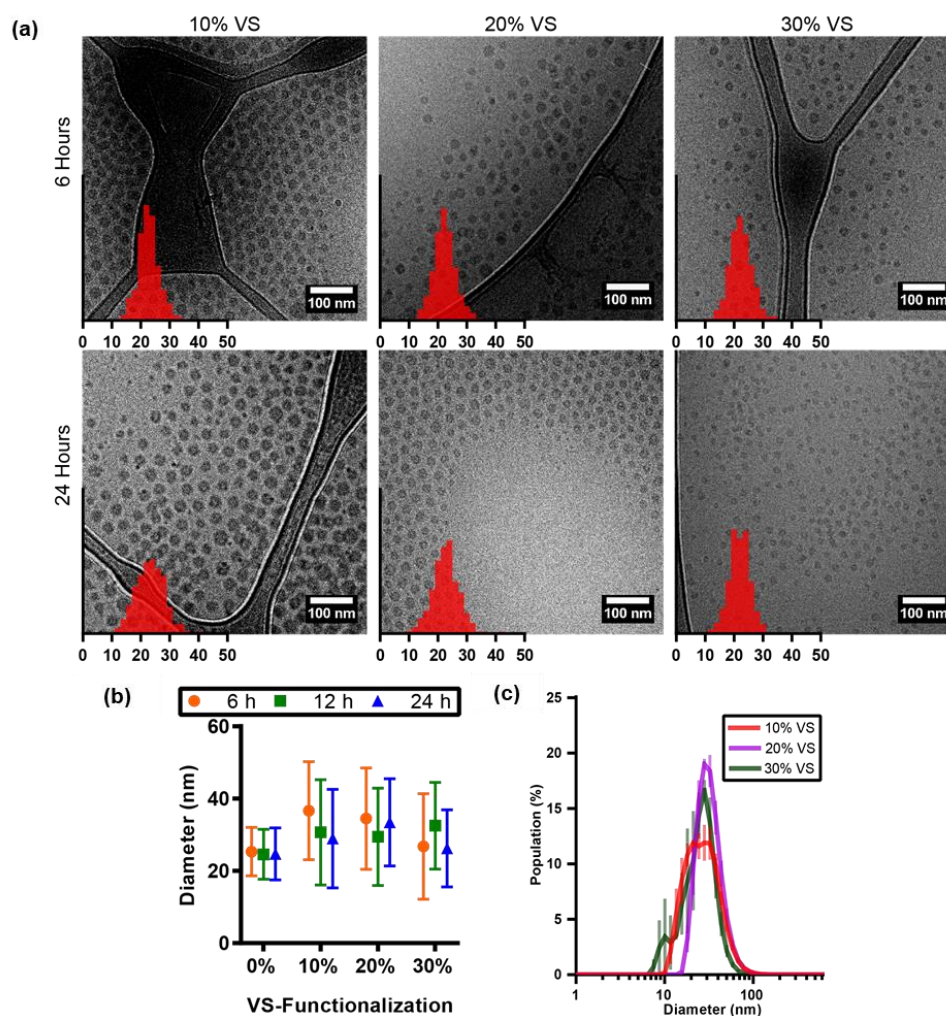


Figure 4-15. Characterization of MCs released from ethyl eosin-loaded PEG-*b*-PPS FM-scaffolds *in vitro*. (a) Representative cryoTEM images of micelles released into the supernatant after photodegradation of FM-scaffolds incorporating 10%, 20%, or 30% w/w VS-BCP, irradiated for 6h or 24h. Overlaid on images are histograms of MC diameters ($n = 500$) measured from cryoTEM images. X-axis is diameter in nanometers, y-axis is relative frequency. (b) Diameters of PEG-*b*-PPS MCs released from irradiated scaffolds into supernatant ($n = 3$). Error bars represent s.e.m. (c) DLS size distribution of nanocarriers released from scaffolds irradiated for 24 h ($n = 3$). Error bars represent s.d. Reproduced from [216] licensed under [Creative Commons By 4.0](https://creativecommons.org/licenses/by/4.0/).

CryoTEM confirmed that the released nanocarriers exhibited comparable size characteristics, with estimated average diameters ranging from 22 to 25 nm in ImageJ and maintained a spherical morphology regardless of the duration of time the scaffolds were exposed to oxidizing conditions (**Figure 4-15a**). DLS analysis determined that the spherical MCs displayed number average diameters that ranged from 25 to 37 nm, and no statistically significant difference was detected between scaffolds irrespective of irradiation time or crosslinking density (**Figure 4-15b,c**). While the ImageJ and DLS determined diameters were comparable, the variation between the two measurement techniques can largely be attributed to the lack of contrast provided by the PEG corona in the cryoTEM micrographs. Due to hydration and swelling of the PEG corona when the sample is frozen in vitreous ice, there is little to no contrast with the surrounding aqueous environment [370]. As such, the ImageJ analysis of MC hydrodynamic diameter accounts for only the hydrophobic PPS core of the nanostructures. Following 24 h of irradiation, MCs released from scaffolds incorporating 10%, 20%, and 30% of the VS-BCP exhibited number average PDIs of 0.226, 0.131, and 0.168 respectively (**Figure 4-15b**). These results verify that monodisperse MCs with sub-40 nm diameters were released from PEG-*b*-PPS FM-scaffolds regardless of the crosslinking density and exposure time to oxidizing conditions. The size characteristics of the released nanostructures are particularly noteworthy as they fall within a range optimal for lymphatic transport following subcutaneous injection [268, 301, 371]. As such, MCs released from subcutaneously injected FM-scaffolds are expected to efficiently drain from the interstitial space into lymphatics, permitting delivery to lymphoid tissues such as the draining lymph nodes and spleen.

In addition to characterizing the surrounding supernatant, the remaining scaffolds were also analyzed following irradiation. **Figure 4-16a** compares the percentage of scaffold mass remaining for irradiated scaffolds and non-irradiated controls. In the absence of irradiation, FM-scaffolds incorporating 10%, 20%, or 30% w/w of the VS-BCP lost approximately 21%, 9%, and 5%, respectively, of their average initial mass over 24 h. But following 24 h of exposure to white light at 3.4 – 3.5 mW cm⁻², these percentages increased to approximately 84%, 46%, and 27%, respectively.

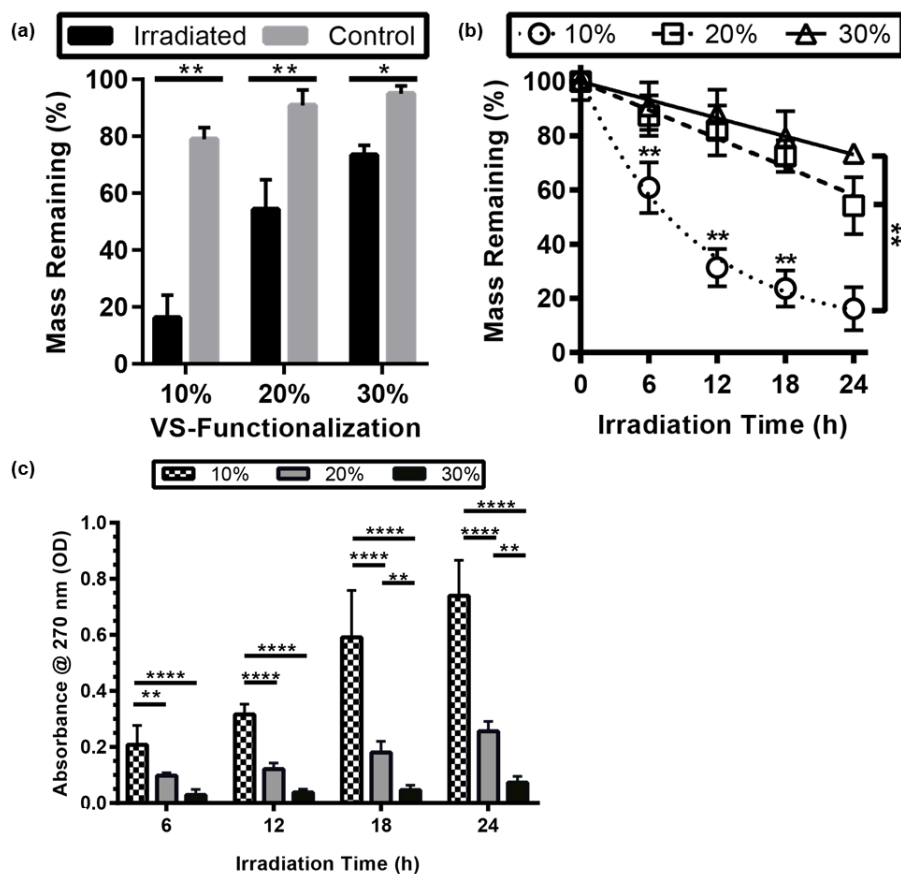


Figure 4-16. Light-induced degradation of ethyl eosin-loaded PEG-*b*-PPS FM-scaffolds *in vitro*.

(a) Percent mass remaining of scaffolds irradiated for 24 h in comparison to non-irradiated controls ($n = 3$ for the control samples and $n = 7$ for the irradiated samples). (b) Modular incorporation of VS-BCP influences light induced scaffold degradation over 24 h ($n = 7$ for all samples except for $t = 0$ h, where $n = 3$, and scaffolds incorporating 20% VS-BCP for $t = 18$ h, where $n = 6$). (c) Absorbance measurements at 270 nm of released PEG-*b*-PPS in supernatant following scaffold irradiation for 6, 12, 18, and 24 h ($n = 7$ for all groups except scaffolds incorporating 10% and 20% VS-BCP irradiated for 18 h where $n = 6$). Significance for (a) and (b) were determined with the Sidak's and Tukey's multiple comparison tests, respectively. In both cases, * $p < 0.001$, ** $p < 0.0001$. Significance between groups for (c) assessed by 2-way RM ANOVA with Tukey's multiple comparison, * $p < 0.05$, ** $p < 0.01$, *** $p < 0.001$, and **** $p < 0.0001$. Error bars represent s.d. Adapted from [216] licensed under [Creative Commons By 4.0](https://creativecommons.org/licenses/by/4.0/).

Furthermore, mass differences between scaffolds containing 10% and either 20% or 30% of the VS-BCP were statistically significant at all time points tested from 6 hours of irradiation onward, while those between scaffolds containing 20% and 30% of the VS-BCP were significant only after 24 h of irradiation (**Figure 4-16b**). These trends in scaffold mass loss were corroborated by an increasing presence of monodisperse PEG-*b*-PPS MCs in the supernatant (**Figure 4-16c**).

While the photo-oxidation of FM-scaffolds demonstrated that oxidation could drive the micellization of these constructs, the *in situ* generation of oxidant at or very near to the PPS core may have increased the probability that sulfide oxidation occurred. When applied *in vivo*, FM-scaffold oxidation will rely on the diffusion of ROS, present in the surrounding environment, to the PPS core. Physiological ROS, such as singlet oxygen, peroxynitrite, and H₂O₂, vary in their estimated diffusion lengths, which range from 50 nm for singlet oxygen [372] to over 1 mm for H₂O₂ [373]. To assess whether ROS present in the surrounding environment can induce FM-scaffolds to transition into spherical MCs, we conducted an accelerated degradation study using supraphysiologic concentrations of ROS. FM-scaffolds incorporating 20% of the VS-BCP and loaded with the hydrophobic dye Dil were incubated at 37°C in H₂O₂ solutions ranging from 0 mM up to 500 mM. H₂O₂ solutions of 100 mM and 500 mM induced complete scaffold micellization in approximately 4 and 1 day(s), respectively (**Figure 4-17a**). Similarly to what was observed via photo-oxidation, MCs released into the supernatant were monodisperse and exhibited hydrodynamic diameters less than 30 nm and PDI values below 0.200 (**Figure 4-17b**). These studies confirmed that ROS, either generated within the FM-scaffold or present in the surrounding environment, can induce the micellization of FM-scaffolds.

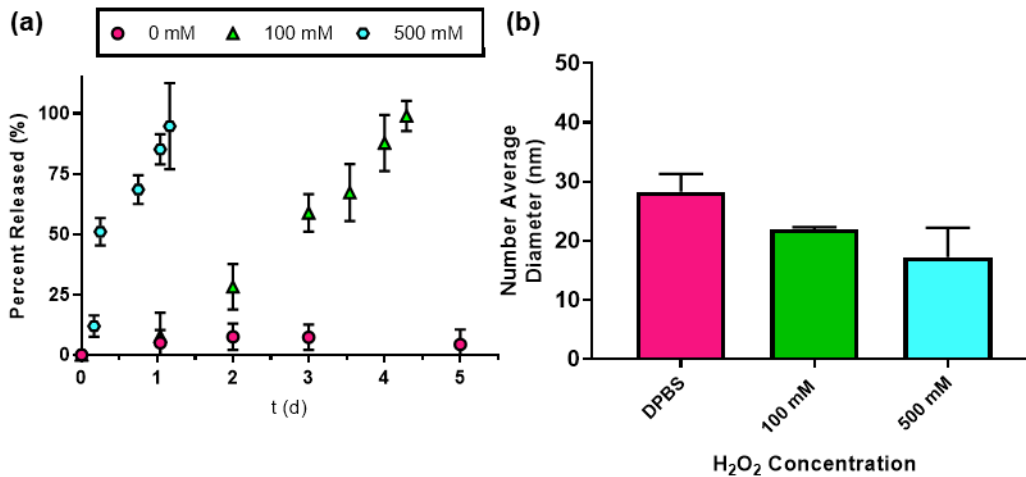


Figure 4-17. H₂O₂ induced degradation of Dil-loaded PEG-*b*-PPS FM-scaffolds *in vitro*. FM-scaffolds incorporating 20% of the VS-BCP were incubated with 0 mM, 100 mM, and 500 mM solutions of H₂O₂. (a) FM-scaffold degradation was monitored over the course of 5 days through the increase in Dil fluorescence in the supernatant ($n = 3$). (b) Diameters of PEG-*b*-PPS MCs released from degraded scaffolds into supernatant ($n = 3$). MC characterization was conducted on the supernatant from the final timepoint of each condition. Differences in MC diameter were not found to be statistically significant. Error bars represent s.d.

4.4.5. Release of Intact MCs from FM-scaffold *in vivo*

Having produced FM-based scaffolds and demonstrated their unique degradation mechanism *in vitro*, we aimed to investigate their ability to release MCs *in vivo*. While difficult to quantify, biologically relevant concentrations of ROS have been estimated to range from 50 – 100 μM [374], and we have previously demonstrated that H₂O₂ at as low as 5 μM can induce changes in PEG-*b*-PPS nanocarrier morphology [308]. We therefore hypothesized that continuous exposure of FM-scaffolds to physiologic levels of oxidation could be sufficient to induce sustained FM-to-MC transitions *in vivo* following subcutaneous injection in mice. Due to their stability and moderate degradation rate while releasing monodisperse micelles (**Figures 4-16** and **4-17**), modular FM-scaffolds incorporating 20% VS-BCP were selected for further *in vivo* degradation studies. To assess the release rate, stability and cell uptake of MC

from the scaffolds, we synthesized a modular system with four BCP components to permit stable *in situ* gelation following subcutaneous injection and multimodal imaging of MC release: MeO-BCP that comprises the majority of the FM, VS-BCP for crosslinking, DyLight 633 conjugated BCP (633-BCP) for flow cytometric analysis of MC uptake by cells, and DyLight 755 conjugated BCP (755-BCP) for near infrared whole mouse imaging of MC release (**Figure 4-18**). CryoTEM confirmed that incorporation of the DyLight-conjugated BCPs into the FMs did not alter FM morphology (**Figure 4-19**) or their ability to transition to spherical MCs (**Figure 4-5d**).

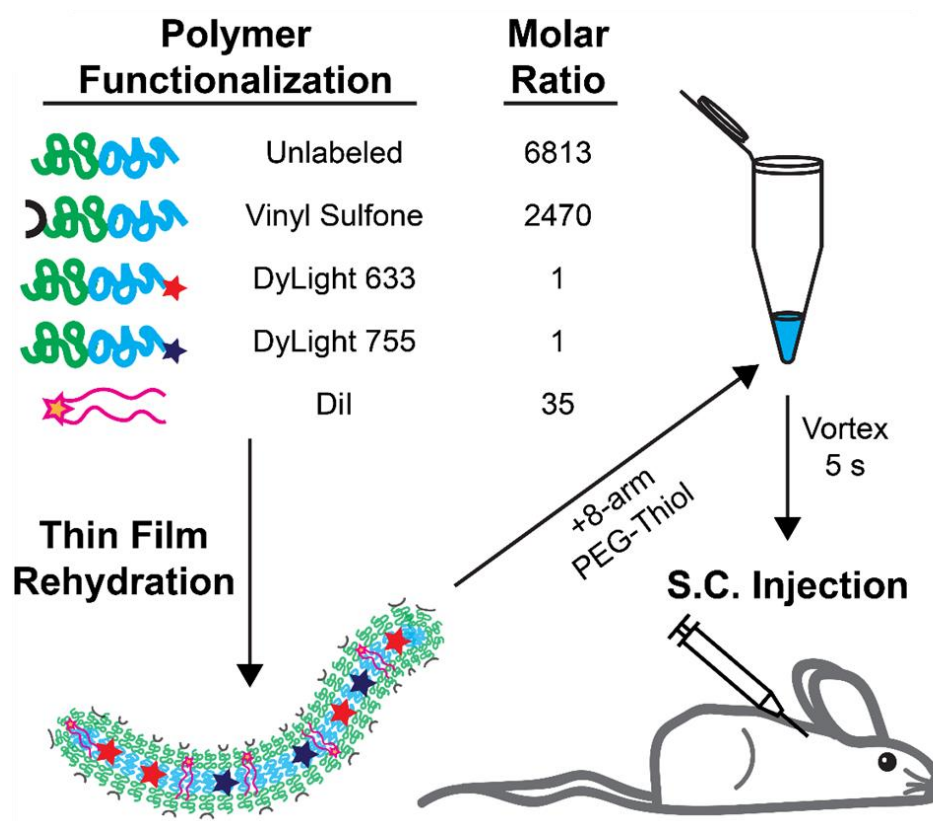


Figure 4-18. Graphical depiction of modular PEG-*b*-PPS FM-scaffold preparation for *in situ* scaffold crosslinking and *in vivo* delivery. Schematic of Dil-loaded PEG-*b*-PPS FM modularly assembled from four separate BCPs for *in situ* crosslinking into FM-scaffolds and multimodal analysis following subcutaneous (S.C.) injection. Adapted from [216] licensed under [Creative Commons By 4.0](https://creativecommons.org/licenses/by/4.0/).

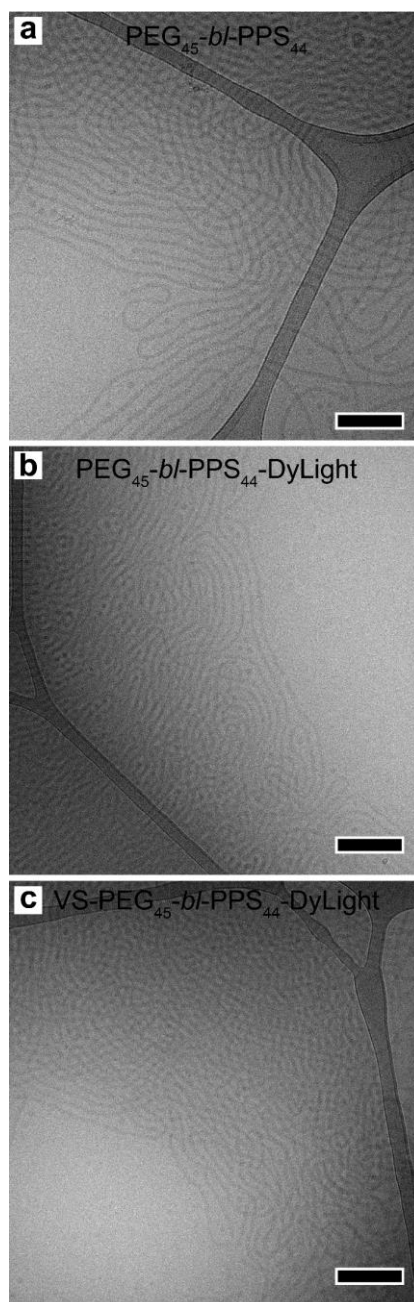


Figure 4-19. CryoTEM confirmation of FM morphology for DyLight incorporating structures. CryoTEM micrographs comparing FMs prepared from (a) MeO-BCP, (b) MeO-BCP, 633-BCP, and 755-BCP, and (c) MeO-BCP, VS-BCP, 633-BCP, and 755-BCP. Scale bar, 200 nm. Reproduced from [216] licensed under [Creative Commons By 4.0](https://creativecommons.org/licenses/by/4.0/).

To verify that hydrophobic payloads and BCPs within FM-scaffolds can transfer to intact MC vehicles, as opposed to associating with lipid carrier proteins in biological fluids, we loaded the lipophilic dye Dil into the four-component modular FM-scaffolds and assessed cellular uptake of released MCs *in vivo* (**Figure 4-18**). Cellular colocalization of Dil fluorescence with that of 633-BCP by flow cytometry would indicate the uptake of intact MCs, while separate signals would be indicative of separate release and cellular uptake of free form and/or protein complexed 633-BCP and Dil. Dil-loaded FMs were mixed with 8-arm PEG-thiol and injected subcutaneously into the scapular region of adult A/J mice for *in situ* crosslinking and stable adherence to surrounding tissue via VS-BCP Michael addition reactions (**Figure 4-18**) [335]. Intravital fluorescence imaging of the 755-BCP signal was used to monitor the release of material from the injection site over the course of 7 days (**Figure 4-20**).

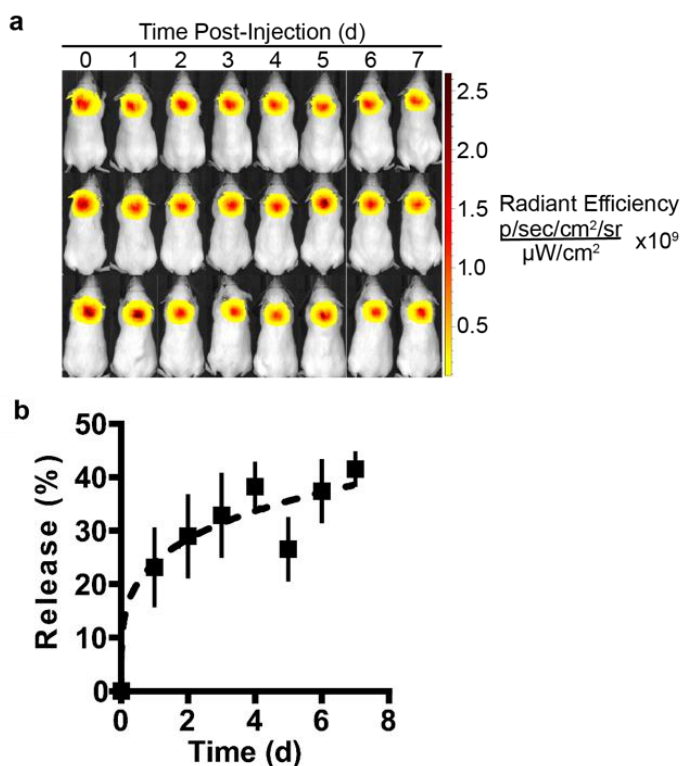


Figure 4-20. Intravital fluorescence imaging (IVIS) of cumulative MC release over 7 days. (a) Complete IVIS image set for 7 day colocalization study. (b) Cumulative MC release (loss of DyLight 755 fluorescence) from *in situ* crosslinked FM-scaffolds containing 20% w/w VS-BCP over 7 days (n = 3). Error bars represent s.e.m. Adapted from [216] licensed under [Creative Commons By 4.0](https://creativecommons.org/licenses/by/4.0/).

As a control, the same volume and concentration of free form Dil in a DPBS solution was administered as a bolus injection and assessed after 24 h. Mice were subsequently sacrificed to assess MC uptake by cells within the spleen and draining lymph nodes. Recovery of the remaining hydrogel scaffold and its *ex vivo* manipulation verified successful *in situ* crosslinking and scaffold stability (**Figure 4-21**).

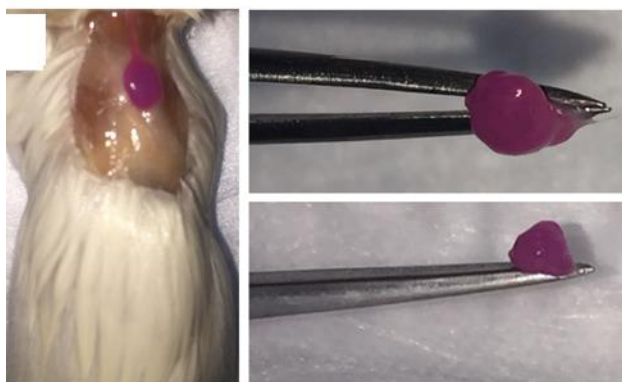


Figure 4-21. *Ex vivo* manipulation of an *in situ* crosslinked FM-scaffold. Excised crosslinked scaffold one week after subcutaneous injection. Adapted from [216] licensed under [Creative Commons By 4.0](#).

For control mice, flow cytometry revealed that approximately 1.6% of extracted CD45+ splenocytes exhibited Dil fluorescence while effectively no cells were found to be double positive for Dil and 633-BCP in the spleen (**Figure 4-22a,b; Figure 4-23**). In contrast, cells were primarily found to be either double negative or double positive (1.6% of CD45+ splenocytes) in the FM-scaffold group, indicative of stable retention and colocalization of Dil within modular MCs containing 633-BCP during cellular uptake. The linear correlation between Dil and 633-BCP fluorescence intensity (adjusted $r^2 = 0.9773$ from Pearson's correlation coefficient) demonstrates a constant ratio of fluorescence in cells with both low and high levels of MC uptake, further confirming delivery of intact MCs containing a consistent distribution of the BCPs and loaded Dil (**Figure 4-22a**). We calculated the percentages of Dil-positive CD45+ and F4/80+ (phagocytic monocyte and macrophage populations) splenocytes that exhibited colocalized DyLight 633 fluorescence in spleen and draining lymph nodes (axillary and brachial), which revealed statistically significant differences between the FM-scaffolds and the control for both cell populations (**Figure 4-22b, Figure 4-23**). The association of Dil fluorescence with released MCs combined with continuous loss of 755-BCP

signal verify transfer of hydrophobic payloads from a scaffold depot to a nanocarrier delivery system and suggests that the cylinder-to-sphere transition can be exploited for the release of micellar delivery vehicles in a biological setting.

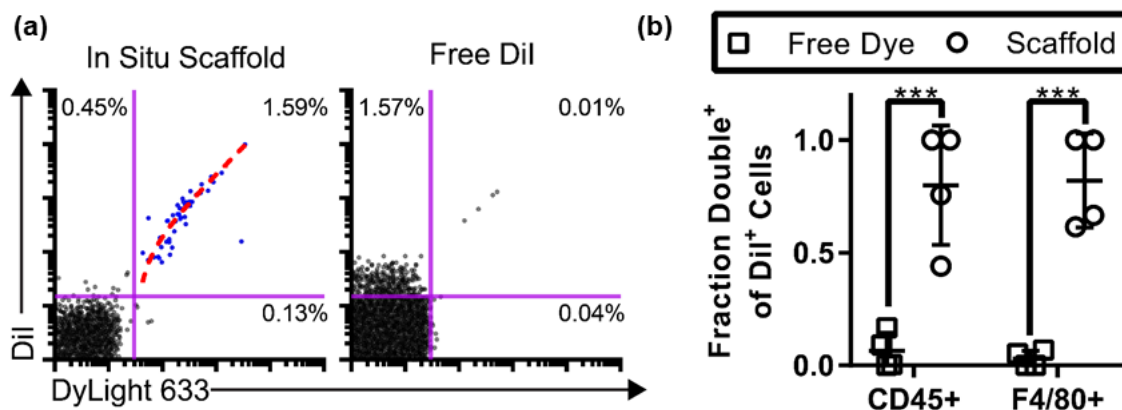


Figure 4-22. Cellular colocalization of encapsulated and covalently attached dyes suggest intact MC release *in vivo*. (a) Representative flow cytometric dot plots displaying uptake of intact (double positive Dil⁺ DyLight 633⁺) released MCs by CD45⁺ cells recovered from the spleens of mice receiving injections of either Dil-loaded *in situ* crosslinked modular FM-scaffolds or free solubilized Dil in DPBS. Percentages of events within the quadrant gates out of all events in the graph are shown. Linear fit (dotted, red) is overlaid upon the Dil⁺ DyLight 633⁺ events (blue dots), adjusted $r^2 = 0.9773$ from Pearson's correlation coefficient. Both axes are on a logarithmic scale. (b) Quantification of MC (DyLight 633) and Dil uptake by CD45⁺ or F4/80⁺ cells recovered from the spleen of mice receiving either Dil-loaded *in situ* crosslinked FM-scaffolds or free Dil. The y-axis represents the fraction of all Dil⁺ cells that were also Dil⁺ DyLight 633⁺ double positive. Lower fractions suggest separate uptake of solubilized Dil alone while higher fractions received intact MCs and thus both Dil and DyLight 633 simultaneously (n = 4 for both groups). Error bars represent s.d., Significance between groups assessed by Mann-Whitney U test, *** p < 0.001. Adapted from [216] licensed under [Creative Commons By 4.0](https://creativecommons.org/licenses/by/4.0/).

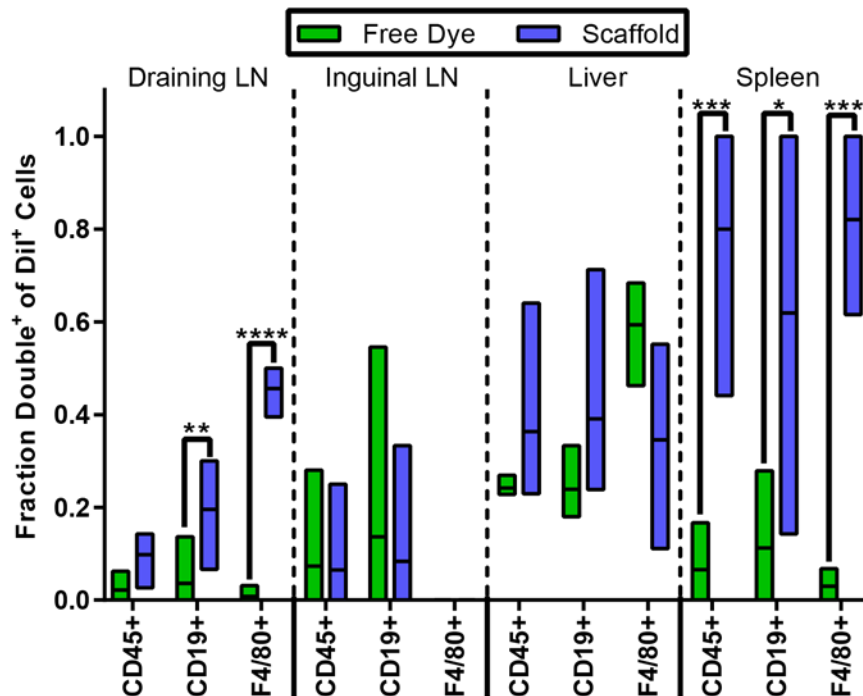


Figure 4-23. Additional flow cytometric analysis from the colocalization experiment. Additional flow cytometric analysis of Dil and 633-BCP uptake by immune cell populations *in vivo*. The y-axis represents the fraction of Dil⁺ cells that were also positive for 633-BCP (n = 4). Floating columns represent min, mean, and max. Significance was determined by Mann-Whitney U Test, two-tailed. * p<0.05, ** p<0.01, *** p<0.001, **** p<0.0001. Reproduced from [216] licensed under [Creative Commons By 4.0](#).

4.4.6. Sustained FM-scaffold Release of MCs for Immune Cell Uptake

Upon confirming that FM-scaffold degradation *in vivo* releases intact micellar nanocarriers, we next investigated sustained MC release and biocompatibility during bioresorption. We again employed the four-component modular FMs containing both 755-BCP and 633-BCP for a multimodal analysis via near infrared fluorescence whole mouse imaging and flow cytometry. The time course of the dissipation of the DyLight 755 signal was monitored for 28 days following subcutaneous injection of the *in situ* crosslinked scaffold (20%VS/MeO/633/755-BCP FMs with 8-arm PEG-thiol), non-crosslinked FMs (MeO/633/755-BCP FMs with 8-arm PEG-thiol), or bolus DyLight 755 in DPBS (**Figure 4-24**, **Figure 4-25a**).

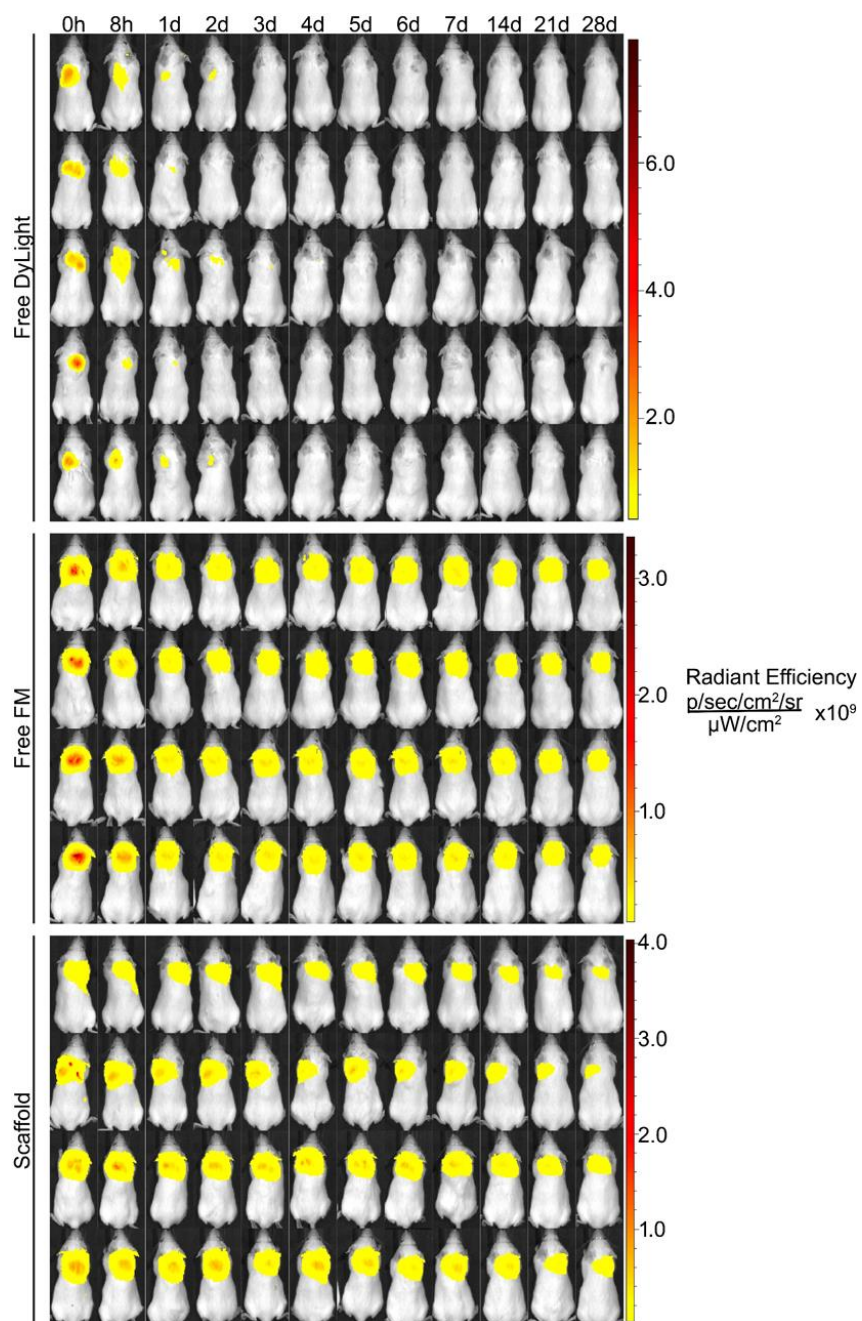


Figure 4-24. Complete IVIS image set for 28-day *in vivo* degradation study. IVIS images for all mice injected with DyLight 755 as: free solubilized dye, conjugated to 755-BCP modules within uncrosslinked four-component modular FMs, or conjugated to 755-BCP modules within four-component FMs of *in situ* crosslinked scaffolds. Radiant efficiency scaled per injection group. Reproduced from [216] licensed under [Creative Commons By 4.0](https://creativecommons.org/licenses/by/4.0/).

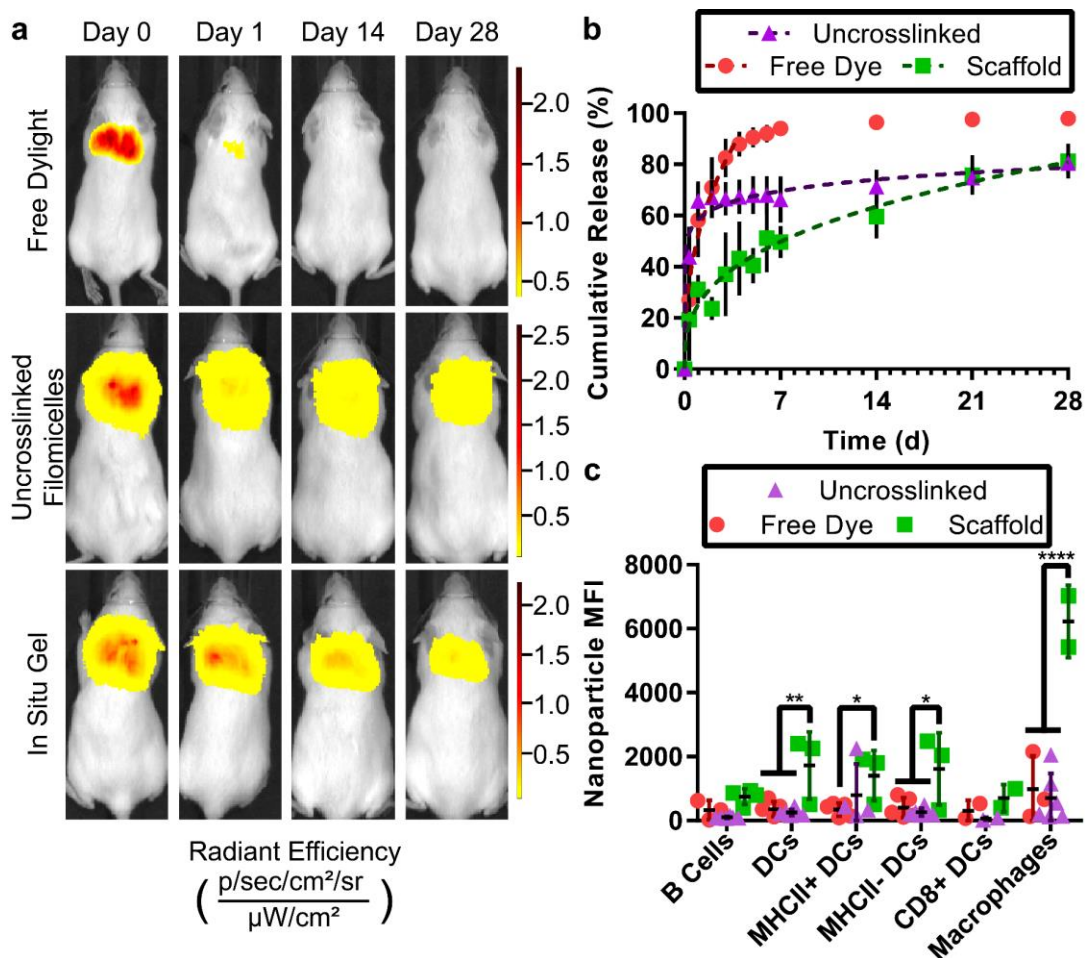


Figure 4-25. *In vivo* sustained release from *in situ* crosslinked FM-scaffolds over one month. (a) Representative IVIS images of Dylight 755 injections as: free solubilized dye, conjugated to 755-BCP modules within uncrosslinked four-component modular FMs, or conjugated to 755-BCP modules within four-component FMs of *in situ* crosslinked scaffolds. Radiant efficiency intensity scaled per individual mouse. (b) Cumulative release curves and power law model fits of MC (Dylight 755) release from FM-scaffolds ($n = 5$ mice for free dye and $n = 4$ mice for uncrosslinked and *in situ* groups). (c) Flow cytometric analysis of MC (Dylight 633) uptake by phagocytic immune cell populations in the draining lymph nodes ($n = 5$ mice for free dye and $n = 4$ mice for uncrosslinked and *in situ* groups). Significance determined by Tukey multiple comparison test: * $p < 0.05$, ** $p < 0.01$, **** $p < 0.0001$. For (b) and (c), error bars represent s.d. Reproduced from [216] licensed under [Creative Commons By 4.0](https://creativecommons.org/licenses/by/4.0/).

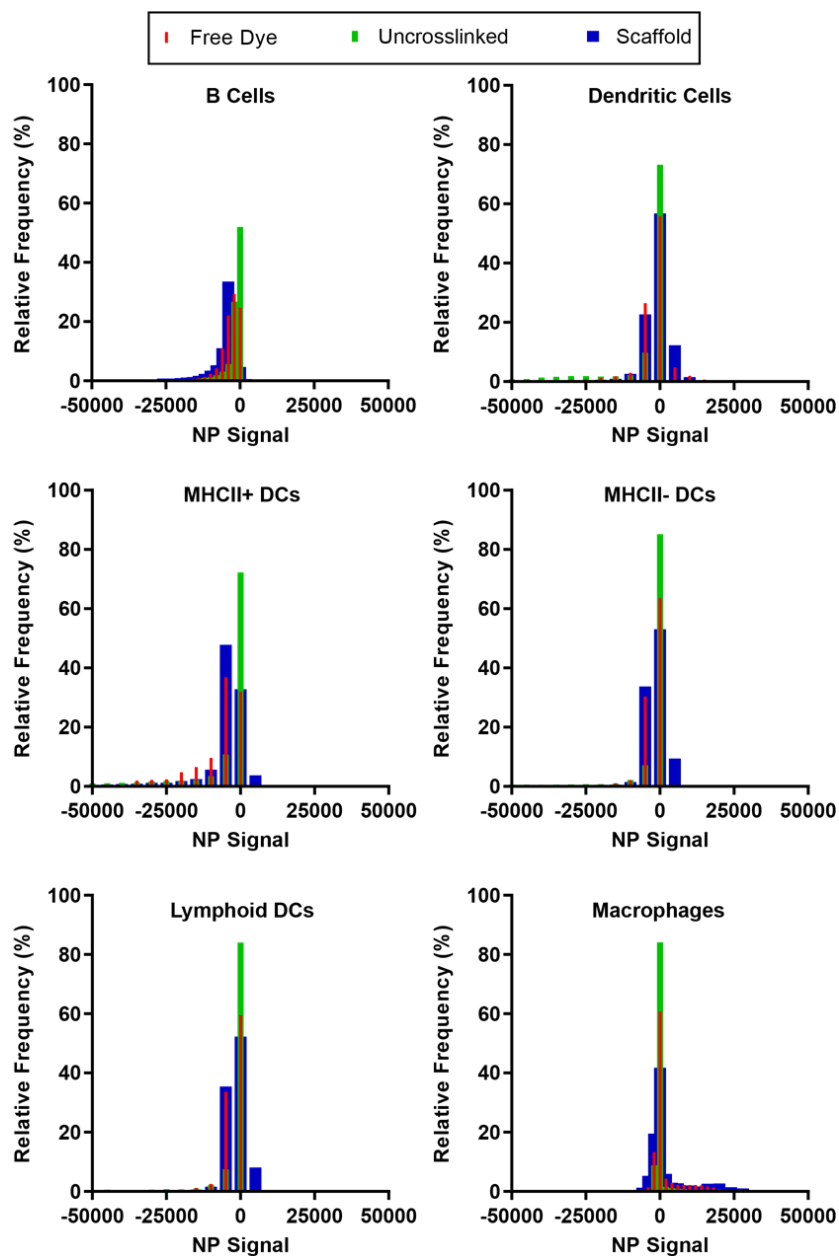


Figure 4-26. Additional flow cytometric analysis of the immune cell populations of the draining lymph nodes from the 28-day *in vivo* degradation study. Histograms of median fluorescence intensity (MFI) of DyLight 633 signal within the draining lymph nodes. MFI calculated after compensation, which leads to the presence of some cells exhibiting negative MFI values ($n = 5$ mice for free dye and $n = 4$ mice for uncrosslinked and scaffold groups). Reproduced from [216] licensed under [Creative Commons By 4.0](https://creativecommons.org/licenses/by/4.0/).

The *in situ* crosslinked scaffold and free FMs exhibited significantly slower release from the injection site in comparison to the free form DyLight control, which dispersed over 90% of the injected material within the first five days (**Figure 4-25b**). When comparing the *in situ* formed scaffolds to the non-crosslinked free form FMs, statistically significant differences in cumulative release were observed within 24 h, as the FM-scaffolds significantly reduced the amount of burst release from approximately 65% to only 31%. The difference in percent cumulative release between the free FMs and *in situ* formed scaffolds remained significant at every timepoint through the first week, eventually converging after 28 days.

The lymph nodes (axillary, brachial, and inguinal), spleens, and livers were harvested following the final one-month time point to assess cellular uptake of released MCs by flow cytometry. Tissue surrounding the injection site was recovered for histological analysis. Mice receiving *in situ* formed FM-scaffolds exhibited significantly greater uptake within the draining lymph nodes (axillary and brachial) than those receiving free DyLight or non-crosslinked FMs (**Figure 4-25c**, **Figure 4-26**). Specifically, MHCII⁺ dendritic cells and macrophages exhibited a discernible increase in MC fluorescence in comparison to free FM and DyLight controls. A statistically significant increase in MC fluorescence was also observed within MHCII⁺ dendritic cells when comparing mice receiving *in situ* formed FM-scaffolds in comparison to the free DyLight control. These differences in cell uptake at the 28-day time point likely reflect the differences in release rates between the crosslinked scaffolds ($\sim 0.07\%$ mass \cdot h⁻¹ following the burst release) and the free form FMs ($\sim 0.02\%$ mass h⁻¹ following the burst release). Uptake within the non-draining inguinal lymph nodes and liver was not statistically significant from background (**Figure 4-27**). Comparison of H&E and Masson's Trichrome stained tissue sections indicate only a mild increase in collagen deposition and macrophage infiltration for the mice receiving FM-scaffolds (**Figure 4-28a-f**). Neither multi-nucleated giant cells nor signs of fibrosis were detected.

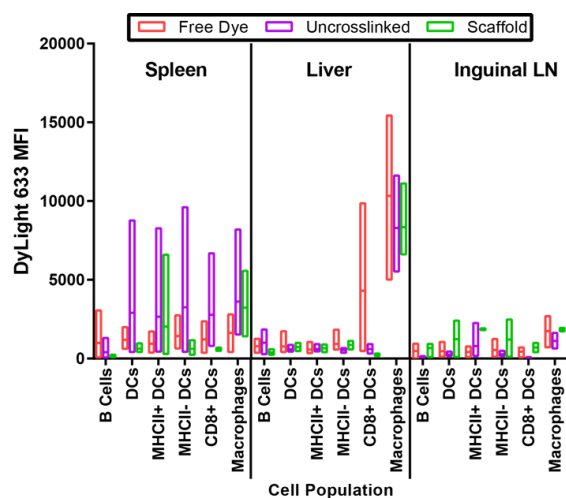


Figure 4-27. Additional flow cytometric analysis of the immune cell populations of the spleen, liver, and inguinal lymph nodes from the 28-day *in vivo* degradation study. Additional flow cytometric analysis of 633-BCP uptake by immune cell populations *in vivo* ($n = 5$ mice for free dye and $n = 4$ mice for FM and scaffold groups). Floating columns represent min, mean, and max. Adapted from [216] licensed under [Creative Commons By 4.0](https://creativecommons.org/licenses/by/4.0/).

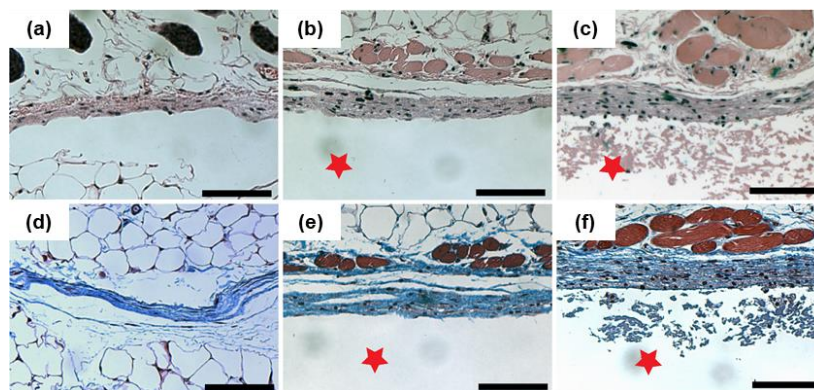


Figure 4-28. Histological analysis of the injection site. Representative images of H&E staining of the interface between skin and (a) the saline Dylight 633 solution-injected control; (b) uncrosslinked FMs; or (c) the *in situ* crosslinked FM-scaffold, respectively. (d), (e), (f) Representative images of Masson's Trichrome staining for the same groups listed above, respectively. The red star represents the scaffold or uncrosslinked FM side of the interface. All images shown are at 10x objective magnification, scale bars are 100 μm . Adapted from [216] licensed under [Creative Commons By 4.0](https://creativecommons.org/licenses/by/4.0/).

These results coupled with the lack of observable symptoms associated with an injection site reaction, such as redness, swelling, blistering, infection, or weight loss (data not shown, **Figure 4-29**), all highlight the non-immunogenic and non-inflammatory nature of the injected FMs in free or scaffold form.

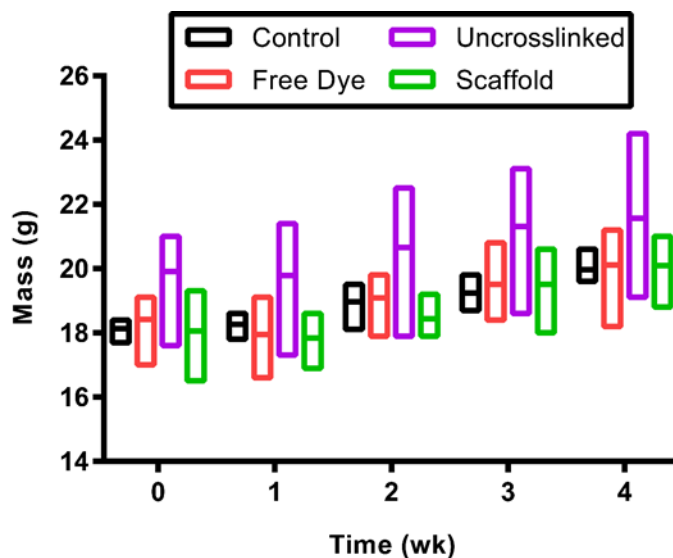


Figure 4-29. Comparison of mouse masses between treatments over the course of *in vivo* degradation study. Mouse masses were recorded weekly over the course of the *in vivo* degradation study. Comparison of the DPBS control mice to the free DyLight, uncrosslinked FMs, and *in situ* crosslinked scaffold treated mice revealed no statistically significant difference in average mouse mass within each time point (n = 3 mice for control group, n = 5 mice for the free dye group, and n = 4 mice for the uncrosslinked and *in situ* crosslinked scaffold groups). Floating columns represent min, mean, and max. Reproduced from [216] licensed under [Creative Commons By 4.0](https://creativecommons.org/licenses/by/4.0/).

This observed lack of an inflammatory response suggests that the gradual decrease in the release rate observed in **Figure 4-25b** is not due to walling-off of the scaffold by fibrous capsule formation and may instead simply reflect the reduction in total material at the injection site over time. Employment of the cylinder-to-sphere transition thus supports sustained micellar release with non-immunogenic scaffold bioresorption, which is not possible with current alternatives for long-term nanocarrier delivery.

4.5. Conclusion

When sustained nanocarrier release is achieved via entrapment within matrices [153, 336-339], the bulk of the construct serves no direct therapeutic role and may serve as a source for chronic inflammation. Here, we demonstrate that FM-scaffolds, composed of self-assembled PEG-*b*-PPS BCP modules, can support the sustained release of monodisperse micellar nanocarriers via the cylinder-to-sphere transition with no signs of chronic inflammation-related pathology. Unlike previous depot systems, FM-scaffolds can be prepared without employing an external matrix or network to control nanocarrier retention and release. Characterization of the oxidation-dependent FM-to-MC transition was achieved via complementary electron microscopy, SAXS, and thermodynamic modeling. Oxidation induced FM-scaffold degradation was confirmed *in vitro* through both incubation with H₂O₂ and photo-oxidation. Photo-oxidation via a loaded ethyl eosin payload within the FM core provided a highly reproducible and temporally controllable model system. FM-to-MC dependent degradation that would require weeks to occur under physiologic oxidative conditions was induced in a matter of hours, likely owing to the consistent ratio of ethyl eosin to PPS that was maintained by the high loading efficiency of ethyl eosin within the FM core. Following subcutaneous injection and *in situ* gelation in mice, our results suggest, although indirectly, that physiologic concentrations of ROS under homeostatic conditions are sufficient to induce the FM-to-MC transition *in vivo* for sustained release of nanocarriers.

Due to the size characteristics of the released MCs, FM-scaffolds injected subcutaneously are capable of efficiently delivering encapsulated payloads to lymphoid tissues such as the draining lymph nodes and spleen. The sustained *in vivo* release of DyLight-conjugated MCs resulted in discernible uptake within dendritic cells, particularly MHCII⁺ dendritic cells, and macrophages present in the draining lymph nodes. Dendritic cells and macrophages, which are professional APCs, are highly phagocytic and central players in the MPS where they are responsible for internalizing foreign material, processing antigen, and presenting antigen to T cells for activation. This ability to activate T cells coupled with their potency for cytokine release make them central figures in dictating the body's immune response [119]. Of the professional APCs, dendritic cells and macrophages exhibit the greatest phagocytic potential and as such, are expected to effectively phagocytose nanostructures within their surrounding environment if in fact micellar structures are present. When looking at dendritic cells, MHCII expression has been found to

increase during dendritic cell maturation [375] and it has been shown that mature dendritic cells may actually reduce their endocytic capacity [375]. Therefore, the statistically significant increase in nanoparticle MFI within dendritic cells, particularly MHCII⁺ dendritic cells, and macrophages described here is logical given the phagocytic capacity of these cells. Furthermore, this result highlights the potential usefulness of this construct in developing subunit vaccines and immunomodulatory treatments where the sustained delivery of encapsulated payloads to immature APCs is required. As such, these hydrogels permit highly efficient non-inflammatory bioresorption while achieving sustained nanocarrier delivery through a mechanism previously unexplored in an *in vivo* setting. FM-scaffolds offer an alternative to the currently employed entrapment matrices used for sustained nanoparticle delivery and have characteristics that make them well suited for the development of immunomodulatory treatments for cancer, cardiovascular disease, and diabetes.

4.6. Acknowledgements

We acknowledge staff and instrumentation support from the Structural Biology Facility at Northwestern University, the Robert H. Lurie Comprehensive Cancer Center of Northwestern University and NCI CCSG P30 CA060553. The Gatan K2 direct electron detector was purchased with funds provided by the Chicago Biomedical Consortium with support from the Searle Funds at The Chicago Community Trust. SAXS experiments were performed at the DuPont-Northwestern-Dow Collaborative Access Team (DND-CAT) located at Sector 5 of the Advanced Photon Source (APS). DND-CAT is supported by Northwestern University, E.I. DuPont de Nemours & Co., and The Dow Chemical Company. This research used resources of the Advanced Photon Source, a U.S. Department of Energy (DOE) Office of Science User Facility operated for the DOE Office of Science by Argonne National Laboratory under Contract No. DE-AC02-06CH11357. This work made use of the EPIC facility of Northwestern University's NUANCE Center, which has received support from the Soft and Hybrid Nanotechnology Experimental (SHyNE) Resource (NSF ECCS-1542205); the MRSEC program (NSF DMR-1121262) at the Materials Research Center; the International Institute for Nanotechnology (IIN); the Keck Foundation; and the State of Illinois, through the IIN. Histology services were provided by the Northwestern University Mouse Histology and Phenotyping Laboratory which is supported by NCI P30-CA060553 awarded to the Robert H. Lurie

Comprehensive Cancer Center. This work was supported by the Northwestern University – Flow Cytometry Core Facility supported by Cancer Center Support Grant (NCI CA060553). Imaging work was performed at the Northwestern University Center for Advanced Molecular Imaging generously supported by NCI CCSG P30 CA060553 awarded to the Robert H. Lurie Comprehensive Cancer Center.

I would like to acknowledge all the researchers who made this work possible. Jonathan Remis, who was instrumental to the early success of our lab, acquired the cryoTEM micrographs in this work. Dr. Reiner Bleher (NUANCE Center-EPIC, NU) taught me cryoSEM and, during my training, helped acquire the SEM micrographs of the FM-scaffolds. Dr. Emre Firlar and Shayan Shafiee provided their expertise in GLC-TEM. Dr. Ha-Kyung Kwon conducted the DSA experiments and thermodynamic modelling included in this work. Dr. Sharan Bobbala is the SAXS expert in our lab, and I would like to thank him for the time spent modeling the SAXS data presented here. Dr. Sean Allen completed the mouse injections, design of flow panels, and flow cytometry analysis. He has an exceptional talent for graphic design and is responsible for both the schematic illustrations and much of the figure layout design presented in this work. I would also like to acknowledge that Dr. Evan Scott was behind the conceptualization of this project, and I appreciate him allowing me to make this project my own and drive the direction this research was pursued.

4.7. Publication Information

Portions of this chapter have been previously published. The published works correspond to the following citations:

Karabin, N.B., et al., *Sustained micellar delivery via inducible transitions in nanostructure morphology*. Nat Commun, 2018. 9(1): p. 624. **[216]**

CHAPTER 5

Summary of Work and Future Directions

5.1. Summary of Work

The focus of this dissertation was to establish new functionalized PEG-*b*-PPS BCPs and to investigate how these BCPs could benefit PEG-*b*-PPS nanocarrier performance. In pursuit of these aims, I have established protocols for the preparation of six previously unreported PEG-*b*-PPS BCPs, explored how combinations of surface chemistry and morphology can influence PEG-*b*-PPS nanocarrier uptake within the cells of the MPS, and demonstrated how surface functionalized PEG-*b*-PPS nanocarriers can be employed for sustained delivery *in vivo*.

5.1.1. Synthesis of Functionally Diverse PEG-*b*-PPS BCPs

At the onset of this work, most studies utilizing PEG-*b*-PPS BCPs for the preparation of nanocarriers utilized its methoxy-functionalized derivative. Since PEG-*b*-PPS was first described in 2001, numerous works have suggested that nanocarrier surface chemistry plays a role in how the nanocarrier interacts with its biological surroundings. But limitations potentially imposed by the cost of heterobifunctional PEGs has led to only a few investigations that have explored alternative functional groups at the PEG terminus of PEG-*b*-PPS BCPs and, consequently, the nanocarrier surface. As such, a potentially useful nanocarrier design characteristic has remained under investigated within the PEG-*b*-PPS BCP system. I was able to prepare six previously unpublished functional derivatives of PEG-*b*-PPS. In my work, I established protocols that permit the incorporation of hydroxyl, vinyl sulfone, phosphate, mesylate, azide, and amine functional groups at the PEG terminus of PEG-*b*-PPS BCPs. Key to the development of these syntheses was the use of a previously published protocol for the asymmetric functionalization of commercial PEGs. Adaptation of this synthesis for my own work permitted the safe and economic preparation of heterobifunctional PEG. Through this synthesis, heterotelechelic PEG was prepared on a scale that permitted the exploration of several BCP chemistries that may be of use for the application of PEG-*b*-PPS nanocarriers in targeted or sustained delivery.

5.1.2. Exploring Surface Chemistry for the Passive Targeting of PEG-*b*-PPS Nanocarriers

Previous work in the Scott and Hubbell labs have demonstrated that changes in PEG-*b*-PPS nanocarrier morphology can result in differential cell uptake [33, 95, 204]. Altering nanocarrier uptake through the design and control of its physicochemical characteristics is a form of passive targeting. To further explore passive targeting strategies for PEG-*b*-PPS nanocarriers, I investigated whether surface chemistry could be coupled with morphology to further influence PEG-*b*-PPS nanocarrier internalization/association by monocytes, macrophages, and dendritic cells. This work compared the *in vitro* performance of PEG-*b*-PPS PSs, FMs, and MCs prepared with MeO-, OH-, and Phos-functionalized BCPs on their ability to induce cytokine secretion, to activate complement, and to associate with cells. I was able to show that irrespective of the combination of morphology and surface chemistry, PEG-*b*-PPS nanocarriers failed to elicit the secretion of pro-inflammatory cytokines to the extent of either TLR4 or TLR7/8 agonists in human whole blood. But both OH- and Phos-functionalized PSs did show an increased potential for activating complement in comparison to their MeO-functionalized counterparts. On the basis of cell uptake, nanocarrier morphology was the dominant physicochemical characteristic governing internalization within human monocytes, macrophages, and dendritic cells. But variations in nanocarrier uptake were observed due to changes in surface chemistry. Most interesting was the impact of nanocarrier surface chemistry on the internalization of PSs by dendritic cells. Dendritic cells were the lone cell type where both OH- and Phos-functionalized PSs outperformed their MeO-functionalized counterpart following plasma exposure. Given the importance of dendritic cells in governing the adaptive immune response, both the OH- and Phos-functionalized PSs may be of interest in the design of PEG-*b*-PPS-based vaccine constructs, wherein their ability to activate complement could actually be exploited as an advantage [300].

To better understand the differences in uptake between the nine nanocarrier formulations, I explored how the different combinations of morphology and surface chemistry influenced protein adsorption in human plasma over time. In the context of total protein, we observed a general decrease in protein adsorption on PEG-*b*-PPS nanocarriers over time. Following a two-hour incubation with human plasma, we observed decreasing amounts of total adsorbed protein with decreasing f_{PEG} as well as with decreasing polarity of the surface functional groups. Changes in the composition of the adsorbed proteins was also

assessed. Differential protein adsorption (as defined by the MW of the adsorbed species) was also observed, though general trends across morphology or surface chemistry were less apparent, save for the absence of high MW proteins (> 181 kDa) in the neutral PS formulations. More detailed analysis to identify the individual proteins within the PC of the nine formulations is currently underway.

5.1.3. Leveraging Surface Functionalized Nanocarriers for Sustained Delivery

Self-assembled BCP aggregates have proven to be dynamic in response to environmental changes. Several works stemming from the Hubbell and Scott labs have shown that PEG-*b*-PPS nanocarriers can undergo morphologic transitions in response to oxidation [32, 34, 60, 82]. This dynamic change in the self-assembled structure of PEG-*b*-PPS nanocarriers has been a key characteristic for achieving intracellular delivery. But in theory, these oxidation-induced transitions should occur wherever PEG-*b*-PPS nanocarriers are exposed to sufficient amounts of oxidant. I hypothesized that the oxidation-induced morphologic transitions achieved by PEG-*b*-PPS nanocarriers could be exploited for the development of a sustained nanocarrier delivery platform. This platform relied on VS-functionalized PEG-*b*-PPS FMs for the preparation of a scaffold. Because FMs require a narrow BCP compositional range for successful self-assembly, they are perceived to be the most susceptible PEG-*b*-PPS nanocarrier morphology to oxidation-induced transitions.

The successful crosslinking of VS-functionalized FM-scaffolds was confirmed through cryoSEM and rheology. I demonstrated that the mechanical properties of FM-scaffolds, like traditional hydrogels, can be modulated through scaffold crosslinking density. I also showed that oxidants either present in the surrounding medium or generated within the scaffold can be used to induce scaffold degradation *in vitro*. Furthermore, *in vitro* scaffold degradation resulted in the generation of monodisperse spherical MCs through both cryoTEM and DLS. The application of FM-scaffolds for sustained nanocarrier release was also assessed *in vivo* in a murine mouse model. The codelivery of both a dye covalently attached to the BCP and an encapsulated hydrophobic dye to immune cells within the spleen suggested the successful release of intact MCs *in vivo*. In addition to this proof of concept study, I demonstrated that FM-scaffolds could degrade in response to physiologic-levels of oxidant over the course of a month. The

fluorescent signal of dye covalently attached to the BCP was detected within various immune cell populations within the draining lymph nodes highlighting this platform's potential for sustained nanocarrier delivery.

5.2. Future Directions

While the work encompassed within this dissertation highlights the potential benefit of functionalized PEG-*b*-PPS BCPs, it, perhaps most importantly, presents several new directions for investigation into PEG-*b*-PPS nanocarriers. Much of my research efforts were focused on developing several PEG-*b*-PPS platforms to demonstrate the benefits that can be achieved by altering the construct's design at the BCP-level. Although I am confident that my efforts addressed questions pertaining to these benefits, I can appreciate the many questions concerning the application of PEG-*b*-PPS nanocarriers that remain and, in some case, have been generated by this work. In this final section, I will discuss some potential directions that I hope future investigators pursue as they explore the potential of PEG-*b*-PPS nanocarriers.

5.2.1. Additional PEG-*b*-PPS BCPs Worth Investigating

This dissertation presented syntheses for the preparation of six functionalized PEG-*b*-PPS BCPs, but there are several additional functional groups that are worth investigating and there are some alternative synthetic pathways that may be more efficient than what was relied upon in this work. In Chapter 2, I alluded to some of the difficulties encountered in my attempts to prepare NH₂-functionalized BCPs. Although I was able to find success through the Staudinger reduction, the multistep synthesis prevented the preparation of FM forming BCP. With each synthetic step and subsequent purification, slight changes to the BCP molecular weight distribution can occur. These changes may eventually lead to a shift in the f_{PEG} of the BCP batch such that it falls outside the narrow range required for the formation of PEG-*b*-PPS FMs. Thus, any synthetic pathway that reduces the number of steps required to achieve NH₂-functionalization could be beneficial. Although I did not have the opportunity to attempt this synthesis during my research, the synthesis I would be most interested in attempting next is depicted in **Figure 5-1**.

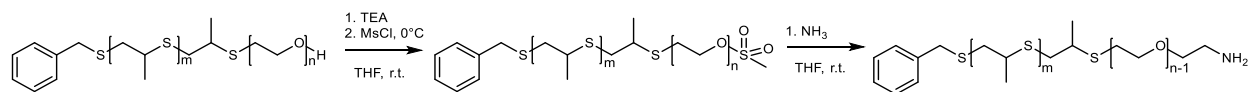


Figure 5-1. Proposed alternative synthetic pathway for preparing amine-functionalized PEG-*b*-PPS BCPs. Rather than utilizing the Staudinger reduction to generate a terminal amine on PEG-*b*-PPS, nucleophilic substitution of the terminal mesylate may be possible with an ammonia/THF solution.

In this proposed reaction, Bn-PPS-*b*-PEG-OMs is dissolved directly in an ammonia/tetrahydrofuran solution and allowed to react at room temperature for several days. If successful, one synthetic step would be removed from what I utilized in the Staudinger reduction, but this change in the pathway may be sufficient to generate NH₂-functionalized FMs.

Although I was unable to prepare this derivative, I believe aldehyde-functionalized PEG-*b*-PPS could be of use in future studies, particularly those investigating the FM-scaffold. Aldehydes, which react with amines and oxyamines to form imines, have been of recent interest in the biomaterials field [376]. Imines, also known as Schiff bases, are an appealing “click chemistry” that is also highly dynamic [377]. Unlike the covalent linkages formed by the VS- and N₃-BCPs described within this dissertation, imines are susceptible to hydrolysis. These hydrolytically labile linkages could permit an alternative strategy to control release from FM-scaffolds. By combining differing crosslinking mechanisms within the same construct, one could develop a combinatorial platform where surface attached proteins release at a rate that differs from the rate achieved through FM-scaffold oxidation. The pathways for generating an aldehyde often require the use of an oxidizing agent [378], which will require the preparation of aldehyde-PEG to take place prior to forming the BCP. While the synthesis of aldehyde-functionalized PEG-*b*-PPS is one example, I believe additional investigations concerning the chemical modification of PEG-*b*-PPS BCPs can be of value. Furthermore, I believe these investigations would be most beneficial if conducted with a specific application established at the onset.

5.2.2. Deconvoluting the Influence of Physicochemical Characteristics in PEG-*b*-PPS Nanocarrier Uptake

In Chapter 3, I investigated whether morphology could be combined with surface chemistry to alter PEG-*b*-PPS nanocarrier uptake within the cells that comprise the MPS. These studies demonstrated that differential uptake within a given morphology could be achieved by simply changing the surface chemistry. Within a given morphology, we gained insight as to how surface chemistry influenced protein adsorption and how changes in protein adsorption impacted the cell association of PEG-*b*-PPS nanocarriers. But, when assessing differences in performance between morphologies, understanding exactly why a given morphology outperforms another is less clear.

While morphology, in the context of nanocarrier performance, is often discussed as a single characteristic, it might be more appropriate to view morphology as a composite of several contributing factors. As such, I think our ability to design and optimize PEG-*b*-PPS nanocarriers could be greatly enhanced with a better understanding of what characteristics are really driving the morphology-based differences in performance. For example, Allen and Bobbala et al. showed that PEG-*b*-PPS PSs and BCNs exhibit different organ-level biodistributions following intravenous injection [33]. But what are the underlying characteristics that are most responsible for these differences? Both nanocarriers are spherical and share comparable chemical identities, but they exhibit differences in size and, most likely, in PEG density, hydrophobicity, and elasticity. Understanding which characteristics are driving the observed differences would allow for a more informed selection of nanocarrier morphology and would further permit optimization of the selected morphology for that application. For example, nanocarrier elasticity is a characteristic we have yet to explore in the Scott lab but has been observed to influence both cell interactions [379] and the nanocarrier biodistribution [380]. It would be interesting to explore how, for example, crosslinking self-assembled BCPs off their PPS block impacts the elasticity of nanocarriers, such as PSs and BCNs, and how these physical changes impact the nanocarrier's ability to interact with cells and deliver their encapsulated payload.

5.2.3. Research Directions for FM-scaffolds

I demonstrated that VS-functionalized FMs could be covalently crosslinked to form a scaffold capable of providing sustained nanocarrier delivery. This scaffold was unique in that it relied on oxidative stimuli to induce a morphologic transition for both scaffold degradation and nanocarrier release. This work largely focused on characterizing the transition of free and crosslinked PEG-*b*-PPS FMs to spherical MCs and determining whether this sustained micellar release could be achieved *in vivo*. While I am confident that my work demonstrated the potential usefulness of this platform, several investigatory routes, which include achieving stimuli-induced degradation and identifying the appropriate biological application, exist.

In the work regarding FM-scaffolds, I was able to demonstrate *in vitro* that photooxidation could trigger scaffold degradation and MC release. This proof of concept study used the photosensitizer ethyl eosin and the entire visible spectrum to generate singlet oxidation for PEG-*b*-PPS oxidation. When I applied this scaffold *in vivo*, the scaffold was formed subcutaneously. Human skin thickness, at the shoulder for example, can vary from approximately 1.9 up to 2.5 mm depending on individual body mass [381]. While much of the visible spectrum can penetrate human skin to a depth greater than or equal to 2 mm to some effect, longer wavelengths of light do so more efficiently and are capable of achieving greater penetrating depths [382]. For this reason, the “phototherapeutic window” is typically restricted to wavelengths between 650 nm and 1,000 nm [382]. Thus, attempts to exploit light for the photoinduced degradation of FM-scaffolds would benefit from the selection of a near infrared photosensitizer, such as pheophorbide A. Pheophorbide A continues to be investigated as an agent for photodynamic therapy [383]. I think it is interesting in the context of FM-scaffolds because it is hydrophobic and exhibits a carboxylic acid group that may allow it to be covalently conjugated to the end of PPS. But this represents simply one potential agent for light-induced oxidation of FM-scaffolds.

Obviously, the limitation of using light is the penetrating depth it can achieve. For the external stimuli-induced degradation of FM-scaffolds located at depths greater than several millimeters, the incorporation of sonodynamic agents may be worth investigating. Sonodynamic therapy, like photodynamic therapy, involves the generation of ROS for induced cell death [384]. But rather than inducing ROS generation through light exposure, sonodynamic therapy relies on low intensity ultrasound. Ultrasound has

a tissue penetrating depth on the scale of tens of centimeters [385, 386], which significantly expands the range of tissues where external stimuli can be used to generate ROS. Interestingly, there is overlap between the molecules used in both photo- and sonodynamic therapy [387]. As such, FM-scaffolds either encapsulating or covalently attached to a photo/sonosensitizer, such as pheophorbide A, could explore both strategies for stimuli induced oxidation in parallel.

I demonstrated that FM-scaffolds can sustain the release of PEG-*b*-PPS nanocarriers over the course of a month and that these nanocarriers can be taken up by immune cells either within the scaffold's immediate environment or within secondary lymphoid organs such as the lymph nodes. While these characteristics could potentially be useful, I did not have the opportunity to explore an application where this platform could make a meaningful difference in modulation of an immune response. An application I had always hoped to explore with the FM-scaffolds was as a single-shot vaccine system. This application always seemed logical as nanocarriers continue to be studied for the generation of subunit vaccines. Thus, the sustained nanocarrier delivery afforded by FM-scaffolds could potentially be tailored to replace the need for multiple booster administrations. A potential limitation of FMs in this role is their inability to simultaneously encapsulate both hydrophobic and hydrophilic molecules. As such, FMs are limited in their ability to codeliver adjuvant and antigen without modification due to the generally hydrophilic nature of peptide antigens. This constraint could inhibit their effectiveness in inducing MHC class II presentation of antigen [388], a process which benefits from the endosomal codelivery of adjuvant and antigen. But opportunities exist to design around these limitations. For example, FM-scaffolds could be applied toward the development of vaccines where a lipid, rather than peptide, antigen has been identified [389]. Unlike hydrophilic peptides, Shang and Kats et al., have demonstrated that lipid antigens can be stably incorporated into PEG-*b*-PPS nanocarriers. Additionally, the reactive BCPs described in Chapter 2 could be employed for the covalent attachment of antigenic peptide to the FM surface. But such strategies may require attachment through a cleavable linkage in order to permit the efficient processing and presentation of antigen [390].

5.2.4. PEG-*b*-PPS Nanocarriers for Active Targeting

To date, most studies involving PEG-*b*-PPS nanocarriers have relied on passive targeting strategies. As these works have typically relied on nanocarrier morphology, I attempted to demonstrate that control over additional physicochemical characteristics of PEG-*b*-PPS nanocarriers, such as surface chemistry, could provide another opportunity to tailor cellular uptake. While passive targeting has its merits, there are instances, such as achieving delivery to non-phagocytic cells, where active targeting strategies could be advantageous. Active targeting strategies involve the conjugation of a targeting ligand, such as a peptide [391], carbohydrate [392], or nucleic acid [393], to the nanocarrier surface that corresponds to a cognate receptor that exists only on or is upregulated upon the cell type of interest. Recently, the Scott lab has started to investigate the active targeting of PEG-*b*-PPS nanocarriers through two independent strategies.

Dr. Sijia Yi and Trevor Stack are exploring the incorporation of a secondary amphiphile, whose sole purpose is to provide cell targeting, within PEG-*b*-PPS constructs. The secondary amphiphile is composed of an application-specific targeting peptide, PEG spacer, and lipid tail. Utilization of this secondary amphiphile is advantageous as the amount incorporated into the PEG-*b*-PPS nanocarrier can be easily varied, allowing for rapid optimization. But, as was mentioned in Section 2.2.1., strategies relying on the incorporation of secondary amphiphiles are limited in how much of the amphiphile can be stably incorporated into the nanocarrier. Furthermore, optimization of the PEG spacer length is required for each new targeting peptide. This need for optimization of the PEG spacer length inhibits the swift implementation of this strategy for multiple applications.

Alternatively, several of the functionalized BCPs described in this dissertation can be used for the attachment of targeting ligands. Both the VS- and N₃-BCPs should theoretically permit the efficient attachment of thiol/amine- and alkyne/DBCO-modified ligands, respectively. As the reactive moieties exist at the PEG terminus of the BCPs, there is no need for including/optimizing a PEG spacer, which allows for the same batch of BCP to be utilized within several constructs with different ligands if the ligands exhibit the appropriate functional group. Both functional groups partake in “click chemistry”, and as such, ligand attachment can be completed in aqueous conditions and at a neutral pH following nanocarrier formation.

While I did not have the opportunity to thoroughly explore this area, I was able to generate some preliminary results that suggest further investigation. **Figure 5-2** depicts the percentage of nanocarrier positive cells for splenocytes treated with VS-functionalized PEG-*b*-PPS PSs presenting either the peptide P-D2 or the peptides P-D2 and CD47. PD-2 is a peptide with affinity for CD11c and has been used to increase dendritic cell uptake [394]. CD47 is a protein involved in self-recognition by immune cells and has been identified as a “don’t eat me signal.” The Discher group has previously identified and utilized a peptide of CD47 whose incorporation on nanoparticles reduces their ability to be phagocytosed [395]. The attachment of PD-2 to the surface of PEG-*b*-PPS PSs enhanced their *in vitro* cell uptake in comparison to unmodified PSs. Furthermore, the coattachment of these antithetical peptides led to modulated levels of uptake in comparison to the unmodified controls.

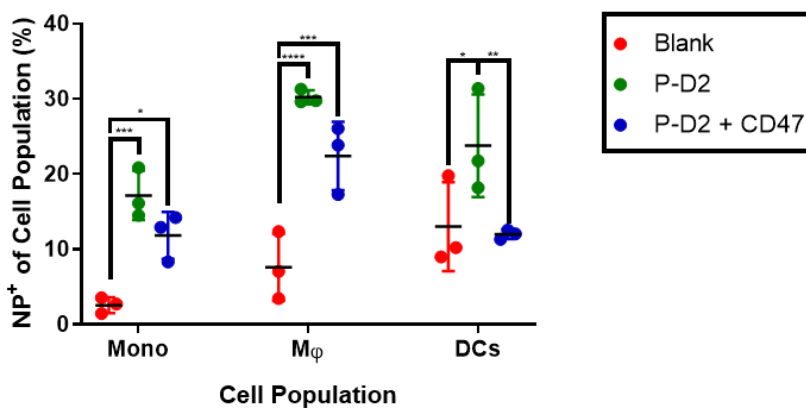


Figure 5-2. Flow cytometric analysis for the *in vitro* cell uptake of peptide-conjugated nanocarriers. Fresh splenocytes treated with blank (MeO-BCP; red) PSs, P-D2-conjugated PSs (MeO BCP/1% w/w VS-BCP; green), or dual P-D2- and CD47-conjugated PSs (MeO BCP/2% w/w VS-BCP; blue) ($n = 3$). The presence of P-D2 led to a statistically significant increase in uptake within monocytes, macrophages, and dendritic cells in comparison to the blank PS control. Coattachment of P-D2 and CD47 generally led to a decrease in uptake in comparison to the P-D2-conjugated PSs, but this decrease was only significant within dendritic cells. Significance determined by Tukey multiple comparison test: * $p < 0.05$, ** $p < 0.01$, *** $p < 0.001$, **** $p < 0.0001$. Error bars represent s.d.

While this initial study was promising, I have struggled to consistently replicate these results. I believe that the reactivity of the VS-BCP coupled with the presence of multiple cysteine and lysine residues within the selected peptides has caused stability issues within the formulations. As such, I would strongly suggest that future investigators interested in exploring the active targeting of PEG-*b*-PPS nanocarriers utilize the N₃-BCPs. The bioorthogonality of this chemistry will allow the investigator to specify precisely where on the ligand the covalent attachment will take place. This specificity should ameliorate concerns of nanocarrier-ligand crosslinking and reduced ligand activity.

5.3. Curriculum Vitae

Nicholas Karabin

EDUCATION

PhD: Northwestern University, 2019, Biomedical Engineering, *Anticipated*

M.S.: Northwestern University, 2017, Biomedical Engineering

B.S.: Carnegie Mellon University, 2013, Chemical Engineering with an Additional Major in Biomedical Engineering

RESEARCH EXPERIENCE

Graduate Researcher – Scott Lab, Northwestern University: 2014 – Current

Undergraduate Researcher: Washburn Lab, Carnegie Mellon University: 2011 - 2013

AWARDS, FELLOWSHIPS, & GRANTS

2018 – 2019, Terminal Year Fellowship Awardee, Northwestern University

2018, TGS Conference Travel Grant, Travel Expenses for both 2018 GRS and 2018 BMES Annual Meeting

2017, Ortho SIG STAR Abstract Award Recipient, 2017 Society for Biomaterials Annual Conference

2016 – 2017, Biotechnology Cluster Member, Northwestern University

PROFESSIONAL SOCIETY MEMBERSHIPS

2017 – Present: Society for Biomaterials Student Member

2016 – Present: Biomedical Engineering Society Student Member

TEACHING

Sep 2016 – Dec 2016, Biological Performance of Materials, Teaching Assistant, Northwestern University

Jan 2016 – Mar 2016, Systems Physiology, Teaching Assistant, Northwestern University

Sep 2015 – Dec 2015, Biological Performance of Materials, Teaching Assistant, Northwestern University

VOLUNTEERING & OUTREACH

Safety Volunteer, Research Student Safety Initiative, April 2018 – Present

Mentor, Graduates Mentoring Undergraduates, May 2017 - Present

Demo Leader, Biotechnology Day, November 2016

Mentor, NU-ETHS STEM Shadow Day, July 2016; Nov 2015; Nov 2014

PUBLICATIONS

Karabin, N. B., et al. Sustained micellar delivery via inducible transitions in nanostructure morphology. Nature Communications. 2018.

Allen, S.D.; Bobbala, S.; *Karabin, N.B.*; Modak, M.; Scott, E. A. Benchmarking bicontinuous nanospheres against polymersomes for in vivo biodistribution and dual intracellular delivery of lipophilic and water soluble payloads. ACS Applied Materials and Interfaces. 2018.

Scott, E.A., *Karabin, N.B.*, and Augsornworawat, P. Overcoming Immune Dysregulation with Immunoengineered Nanobiomaterials. Annual Review of Biomedical Engineering. 2017.

Frey, M.; Bobbala, S.; *Karabin, N.B.*; Scott, E. Influences of nanocarrier morphology on therapeutic immunomodulation. Nanomedicine. 2018.

MANUSCRIPTS IN PREPARATION

Karabin, N.B.; Vincent, M.P.; Allen, S.D.; Frey, M.; Bobbala, S.; Yi, S.; Yang, Y.; Scott, E.A. Achieving Differential protein adsorption and cellular uptake through combinations of nanocarrier morphology and surface chemistry. 2019.

Allen, S.D.; Bobbala, S.; Vincent, M.P.; *Karabin, N.B.*; Scott, E.A. Photo-oxidation responsive PEG-b-PPS bicontinuous nanospheres for triggerable morphological transition to micelles and release of cargo. 2019.

CONFERENCE PRESENTATIONS AND ABSTRACTS

Karabin, N.B.; Chen, S.; Li, S.; Yi, S.; Zhang, B.; Scott, E.A. Localized, Sustained Immunomodulation of Tumor Microenvironment via Micellar Delivery Vehicles. BMES Annual Meeting, 2018. Oral.

Allen, M.; Karabin, N.B.; Golding, A.; Scott, E.A.; Szeto, G. Targeted antimalarial delivery to inflammatory cells driving lupus pathogenesis. Autumn Immunology Conference, 2018.

Firlar, E.; Karabin, N.B.; Bogdanowicz, A.; Nadkarni, Y.; Scott, E.A.; Shahbazian-Yassar, R.; Shokuhfar, T. Investigation of in situ radiation effects in liquid cell electron microscopy. Microscopy and Microanalysis, 2018. Abstract.

Karabin, N. B.; Allen, S.D.; Kwon, H. K.; Bobbala, S.; Firlar, E.; Shokuhfar, T.; Shull, K. R.; Scott, E. A. Bioinspired in situ generation and release of monodisperse micellar vehicles for sustained therapeutic delivery. Gordon Research Seminar for Bioinspired Materials, 2018. Poster.

Karabin, N.B.; Allen, S.D.; Liu, Y.; Scott, E.A. A Dynamically Disassembling Filamentous Scaffold for Micellar Delivery. Society for Biomaterials Annual Meeting, 2017. Oral.

Yi, S.; Allen, S.D.; Karabin, N.B.; Liu, Y.; Scott, E.A. Engineering nanomaterial morphology to enhance immunotheranostic strategies. American Chemical Society, 2017. Abstract.

Karabin, N.B.; Firlar, E.; Shafiee, S.; Shokuhfar, T.; Scott, E.A. Development of a Photoresponsive Scaffold for the Induced Release of Self-assembled Nanostructures. BMES Annual Meeting, 2016. Oral.

Karabin, N.B. & Scott, E.A. Development of a Photoresponsive Scaffold Composed of Self-Assembled Nanostructures. Annual AIChE Midwest Regional Conference, 2016. Oral.

PATENTS

Self-assembled Particles for Targeted Delivery of Immunomodulators to Treat Cancer and Autoimmunity.

Gregory Szeto, Evan Scott, Amit Golding, Marilyn Allen, Nicholas Karabin.

REFERENCES

1. Kreyling, W.G., M. Semmler-Behnke, and Q. Chaudhry, *A complementary definition of nanomaterial*. *Nano Today*, 2010. **5**(3): p. 165-168.
2. Klaessig, F., M. Marrapese, and S. Abe, *Current perspectives in nanotechnology terminology and nomenclature*, in *Nanotechnology Standards*. 2011, Springer. p. 21-52.
3. Buzea, C., I.I. Pacheco, and K. Robbie, *Nanomaterials and nanoparticles: sources and toxicity*. *Biointerphases*, 2007. **2**(4): p. MR17-MR71.
4. Shubayev, V.I., T.R. Pisanic, 2nd, and S. Jin, *Magnetic nanoparticles for theragnostics*. *Adv Drug Deliv Rev*, 2009. **61**(6): p. 467-77.
5. Zhao, P., et al., *Near infrared quantum dots in biomedical applications: current status and future perspective*. *Wiley Interdiscip Rev Nanomed Nanobiotechnol*, 2018. **10**(3): p. e1483.
6. Whitesides, G.M. and B. Grzybowski, *Self-assembly at all scales*. *Science*, 2002. **295**(5564): p. 2418-2421.
7. Verma, G. and P.A. Hassan, *Self assembled materials: design strategies and drug delivery perspectives*. *Phys Chem Chem Phys*, 2013. **15**(40): p. 17016-28.
8. Lasic, D.D., *Novel applications of liposomes*. *Trends in Biotechnology*, 1998. **16**(7): p. 307-321.
9. Lombardo, D., et al., *Amphiphiles Self-Assembly: Basic Concepts and Future Perspectives of Supramolecular Approaches*. *Advances in Condensed Matter Physics*, 2015. **2015**: p. 1-22.
10. Bondi, C.A.M., et al., *Human and Environmental Toxicity of Sodium Lauryl Sulfate (SLS): Evidence for Safe Use in Household Cleaning Products*. *Environmental Health Insights*, 2015. **9**: p. 27-32.
11. McBain, J.W., *General discussion on colloids and their viscosity*. *Trans. Faraday Soc.*, 1913. **9**(99-101).
12. Nagarajan, R., *One Hundred Years of Micelles Evolution of the Theory of Micellization*, in *Surfactant Science and Technology: Retrospects and Prospects*, L.S. Romsted, Editor. 2014, CRC Press: Boca Raton, FL. p. 3-53.
13. Lucy, J.A., Glauert, Audrey M., *Structure and Assembly of Macromolecular Lipid Complexes composed of Globular Micelles*. *Journal of Molecular Biology*, 1964. **8**: p. 727-748.

14. Tanford, C., *Interfacial Free-Energy and the Hydrophobic Effect*. Proceedings of the National Academy of Sciences of the United States of America, 1979. **76**(9): p. 4175-4176.
15. Tanford, C., *Thermodynamics of Micelle Formation - Prediction of Micelle Size and Size Distribution*. Proceedings of the National Academy of Sciences of the United States of America, 1974. **71**(5): p. 1811-1815.
16. Tanford, C., *Theory of Micelle Formation in Aqueous-Solutions*. Journal of Physical Chemistry, 1974. **78**(24): p. 2469-2479.
17. Tritschler, U., et al., *50th Anniversary Perspective: Functional Nanoparticles from the Solution Self-Assembly of Block Copolymers*. Macromolecules, 2017. **50**(9): p. 3439-3463.
18. Feng, H., et al., *Block Copolymers: Synthesis, Self-Assembly, and Applications*. Polymers, 2017. **9**(12): p. 494.
19. Blanazs, A., S.P. Armes, and A.J. Ryan, *Self-Assembled Block Copolymer Aggregates: From Micelles to Vesicles and their Biological Applications*. Macromol Rapid Commun, 2009. **30**(4-5): p. 267-77.
20. Alexandridis, P.a.L., B., *Amphiphilic Block Copolymers: Self-Assembly and Applications*. 2000, Amsterdam: Elsevier.
21. Mai, Y. and A. Eisenberg, *Self-assembly of block copolymers*. Chem Soc Rev, 2012. **41**(18): p. 5969-85.
22. Discher, B.M., et al., *Polymersomes: Tough vesicles made from diblock copolymers*. Science, 1999. **284**(5417): p. 1143-1146.
23. Rideau, E., et al., *Liposomes and polymersomes: a comparative review towards cell mimicking*. Chem Soc Rev, 2018. **47**(23): p. 8572-8610.
24. Messenger, L., et al., *Novel aspects of encapsulation and delivery using polymersomes*. Current Opinion in Pharmacology, 2014. **18**: p. 104-111.
25. Israelachvili, J.N., *Special Interactions: Hydrogen-Bonding and Hydrophobic and Hydrophilic Interactions*, in *Intermolecular and Surface Forces*. 2011, Elsevier.

26. Gaucher, G., et al., *Block copolymer micelles: preparation, characterization and application in drug delivery*. J Control Release, 2005. **109**(1-3): p. 169-88.
27. Riess, G., *Micellization of block copolymers*. Progress in Polymer Science, 2003. **28**(7): p. 1107-1170.
28. Adams, M.L. and G.S. Kwon, *The effects of acyl chain length on the micelle properties of poly(ethylene oxide)-block-poly(N-hexyl-L-aspartamide)-acyl conjugates*. J Biomater Sci Polym Ed, 2002. **13**(9): p. 991-1006.
29. Owen, S.C., D.P.Y. Chan, and M.S. Shoichet, *Polymeric micelle stability*. Nano Today, 2012. **7**(1): p. 53-65.
30. Velluto, D., D. Demurtas, and J.A. Hubbell, *PEG-b-PPS diblock copolymer aggregates for hydrophobic drug solubilization and release: Cyclosporin A as an example*. Molecular Pharmaceutics, 2008. **5**(4): p. 632-642.
31. Oltra, N.S., et al., *Filomicelles in nanomedicine - from flexible, fragmentable, and ligand-targetable drug carrier designs to combination therapy for brain tumors*. Journal of Materials Chemistry B, 2013. **1**(39): p. 5177-5185.
32. Napoli, A., et al., *Glucose-oxidase based self-destructing polymeric vesicles*. Langmuir, 2004. **20**(9): p. 3487-91.
33. Allen, S.D., et al., *Benchmarking Bicontinuous Nanospheres against Polymersomes for in Vivo Biodistribution and Dual Intracellular Delivery of Lipophilic and Water-Soluble Payloads*. Acs Applied Materials & Interfaces, 2018. **10**(40): p. 33857-33866.
34. Bobbala, S., S.D. Allen, and E.A. Scott, *Flash nanoprecipitation permits versatile assembly and loading of polymeric bicontinuous cubic nanospheres*. Nanoscale, 2018. **10**(11): p. 5078-5088.
35. Barnhill, S.A., et al., *Phase Diagrams of Polynorbornene Amphiphilic Block Copolymers in Solution*. Macromolecules, 2015. **48**(4): p. 1152-1161.
36. Barnhill.

37. La, Y., et al., *A Morphological Transition of Inverse Mesophases of a Branched-Linear Block Copolymer Guided by Using Cosolvents*. *Angewandte Chemie-International Edition*, 2015. **54**(36): p. 10483-10487.
38. Lin, Z., et al., *Tunable Self-Assembly of Diblock Copolymers into Colloidal Particles with Triply Periodic Minimal Surfaces*. *Angew Chem Int Ed Engl*, 2017. **56**(25): p. 7135-7140.
39. Cho, A., et al., *Structural Requirements of Block Copolymers for Self-Assembly into Inverse Bicontinuous Cubic Mesophases in Solution*. *Macromolecules*, 2016. **49**(12): p. 4510-4519.
40. Allen, S.D., Bobbala, S., Karabin, N.B., Scott, E.A., *On the advancement of polymeric bicontinuous nanospheres toward biomedical applications*. *Nanoscale Horizons*, 2019. **4**: p. 258-272.
41. Israelachvili, J.N., *Soft and Biological Structures*, in *Intermolecular and Surface Forces*. 2011, Elsevier. p. 535-576.
42. Williams, D.F., *On the mechanisms of biocompatibility*. *Biomaterials*, 2008. **29**(20): p. 2941-2953.
43. Li, X.M., et al., *Biocompatibility and Toxicity of Nanoparticles and Nanotubes*. *Journal of Nanomaterials*, 2012.
44. Ilinskaya, A.N. and M.A. Dobrovolskaia, *Nanoparticles and the blood coagulation system. Part II: safety concerns*. *Nanomedicine*, 2013. **8**(6): p. 969-981.
45. Dobrovolskaia, M.A., D.R. Germolec, and J.L. Weaver, *Evaluation of nanoparticle immunotoxicity*. *Nature Nanotechnology*, 2009. **4**(7): p. 411-414.
46. Longmire, M., P.L. Choyke, and H. Kobayashi, *Clearance properties of nano-sized particles and molecules as imaging agents: considerations and caveats*. *Nanomedicine*, 2008. **3**(5): p. 703-717.
47. Wang, B., et al., *Metabolism of Nanomaterials in Vivo: Blood Circulation and Organ Clearance*. *Accounts of Chemical Research*, 2013. **46**(3): p. 761-769.
48. Nair, L.S. and C.T. Laurencin, *Biodegradable polymers as biomaterials*. *Progress in Polymer Science*, 2007. **32**(8-9): p. 762-798.
49. Marin, E., M.I. Briceno, and C. Caballero-George, *Critical evaluation of biodegradable polymers used in nanodrugs*. *International Journal of Nanomedicine*, 2013. **8**: p. 3071-3091.

50. Zhang, J.W. and W.M. Saltzman, *Engineering Biodegradable Nanoparticles for Drug and Gene Delivery*. Chemical Engineering Progress, 2013. **109**(3): p. 25-30.
51. Adams, M.L., A. Lavasanifar, and G.S. Kwon, *Amphiphilic block copolymers for drug delivery*. Journal of Pharmaceutical Sciences, 2003. **92**(7): p. 1343-1355.
52. Napoli, A., Tirelli, N., Kilcher, G., Hubbell, J.A., *New Synthetic Methodologies for Amphiphilic Multiblock Copolymers of Ethylene Glycol and Propylene Sulfide*. Macromolecules, 2001(34): p. 8913-8917.
53. Alexandridis, P. and J.F. Holzwarth, *Differential scanning calorimetry investigation of the effect of salts on aqueous solution properties of an amphiphilic block copolymer (Ploxamer)*. Langmuir, 1997. **13**(23): p. 6074-6082.
54. Coppola, L., et al., *A self-diffusion study in aqueous solution and lyotropic mesophases of amphiphilic block copolymers*. Colloid and Polymer Science, 2000. **278**(5): p. 434-442.
55. Svensson, B. and U. Olsson, *Thermotropic and lyotropic behavior of a PEO-PPO-PEO block copolymer*. Macromolecules, 2000. **33**(20): p. 7413-7419.
56. Napoli, A., Tirelli, N., Wehrli, E., Hubbell, J.A., *Lyotropic Behavior in Water of Amphiphilic ABA Triblock Copolymers Based on Poly(propylene sulfide) and Poly(ethylene glycol)*. Langmuir, 2002(18): p. 8324-8329.
57. Cerritelli, S., et al., *Aggregation Behavior of Poly(ethylene glycol-bi-propylene sulfide) Di- and Triblock Copolymers in Aqueous Solution*. Langmuir, 2009. **25**(19): p. 11328-11335.
58. Vo, C.D., G. Kilcher, and N. Tirelli, *Polymers and Sulfur: what are Organic Polysulfides Good For? Preparative Strategies and Biological Applications*. Macromol Rapid Commun, 2009. **30**(4-5): p. 299-315.
59. Flory, P.J., *Principles of Polymer Chemistry*. 1953, Ithaca, NY: Cornell University Press.
60. Napoli, A., et al., *Oxidation-responsive polymeric vesicles*. Nature Materials, 2004. **3**(3): p. 183-189.
61. Jannasch, P., *Preparation and characterisation of aggregating comblike poly(propylene oxide)*. Polymer, 2000. **41**(18): p. 6701-6707.

62. Nicol, E., T. Nicolai, and D. Durand, *Dynamics of poly(propylene sulfide) studied by dynamic mechanical measurements and dielectric spectroscopy*. *Macromolecules*, 1999. **32**(22): p. 7530-7536.
63. Lee, J.C.M., et al., *Preparation, stability, and in vitro performance of vesicles made with diblock copolymers*. *Biotechnology and Bioengineering*, 2001. **73**(2): p. 135-145.
64. Dimova, R., et al., *Hyperviscous diblock copolymer vesicles*. *European Physical Journal E*, 2002. **7**(3): p. 241-250.
65. Lappe, S., D. Mulac, and K. Langer, *Polymeric nanoparticles - Influence of the glass transition temperature on drug release*. *International Journal of Pharmaceutics*, 2017. **517**(1-2): p. 338-347.
66. Omelczuk, M.O. and J.W. McGinity, *The Influence of Polymer Glass-Transition Temperature and Molecular-Weight on Drug Release from Tablets Containing Poly(DI-Lactic Acid)*. *Pharmaceutical Research*, 1992. **9**(1): p. 26-32.
67. Apolinario, A.C., et al., *Challenges for the Self-Assembly of Poly(Ethylene Glycol)-Poly(Lactic Acid) (PEG-PLA) into Polymersomes: Beyond the Theoretical Paradigms*. *Nanomaterials*, 2018. **8**(6).
68. Ahmed, F. and D.E. Discher, *Self-porating polymersomes of PEG-PLA and PEG-PCL: hydrolysis-triggered controlled release vesicles*. *J Control Release*, 2004. **96**(1): p. 37-53.
69. Jain, J.P. and N. Kumar, *Self assembly of amphiphilic (PEG)(3)-PLA copolymer as polymersomes: preparation, characterization, and their evaluation as drug carrier*. *Biomacromolecules*, 2010. **11**(4): p. 1027-35.
70. Ghasemi, R., et al., *mPEG-PLA and PLA-PEG-PLA nanoparticles as new carriers for delivery of recombinant human Growth Hormone (rhGH)*. *Scientific Reports*, 2018. **8**.
71. Yu, K. and A. Eisenberg, *Multiple morphologies in aqueous solutions of aggregates of polystyrene-block-poly(ethylene oxide) diblock copolymers*. *Macromolecules*, 1996. **29**(19): p. 6359-6361.
72. Zhang, L.F. and A. Eisenberg, *Morphogenic effect of added ions on crew-cut aggregates of polystyrene-b-poly(acrylic acid) block copolymers in solutions*. *Macromolecules*, 1996. **29**(27): p. 8805-8815.

73. Zhang, L.F. and A. Eisenberg, *Multiple morphologies and characteristics of "crew-cut" micelle-like aggregates of polystyrene-b-poly(acrylic acid) diblock copolymers in aqueous solutions*. Journal of the American Chemical Society, 1996. **118**(13): p. 3168-3181.
74. Park, P.I.P. and S. Jonnalagadda, *Predictors of glass transition in the biodegradable polylactide and poly-lactide-co-glycolide polymers*. Journal of Applied Polymer Science, 2006. **100**(3): p. 1983-1987.
75. Discher, D.E. and F. Ahmed, *Polymersomes*. Annual Review of Biomedical Engineering, 2006. **8**: p. 323-341.
76. Hu, C.Y., et al., *Micelle or polymersome formation by PCL-PEG-PCL copolymers as drug delivery systems*. Chinese Chemical Letters, 2017. **28**(9): p. 1905-1909.
77. Grossen, P., et al., *PEG-PCL-based nanomedicines: A biodegradable drug delivery system and its application*. Journal of Controlled Release, 2017. **260**: p. 46-60.
78. Cheung, Y.W. and R.S. Stein, *Critical Analysis of the Phase-Behavior of Poly(Epsilon-Caprolactone) (Pcl)/Polycarbonate (Pc) Blends*. Macromolecules, 1994. **27**(9): p. 2512-2519.
79. Lallana, E. and N. Tirelli, *Oxidation-Responsive Polymers: Which Groups to Use, How to Make Them, What to Expect From Them (Biomedical Applications)*. Macromolecular Chemistry and Physics, 2013. **214**(2): p. 143-158.
80. Perell, G.T., et al., *Tuning Sulfur Oxidation States on Thioether-Bridged Peptide Macrocycles for Modulation of Protein Interactions*. Chembiochem, 2017. **18**(18): p. 1836-1844.
81. Napoli, A., H. Bermudez, and J.A. Hubbell, *Interfacial reactivity of block copolymers: understanding the amphiphile-to-hydrophile transition*. Langmuir, 2005. **21**(20): p. 9149-53.
82. Vasdekis, A.E., et al., *Precision Intracellular Delivery Based on Optofluidic Polymersome Rupture*. Acs Nano, 2012. **6**(9): p. 7850-7857.
83. Choi, H.S., et al., *Renal clearance of quantum dots*. Nature Biotechnology, 2007. **25**(10): p. 1165-1170.
84. Paiva, C.N. and M.T. Bozza, *Are Reactive Oxygen Species Always Detrimental to Pathogens? Antioxidants & Redox Signaling*, 2014. **20**(6): p. 1000-1037.

85. Hoffman, A.S., *The early days of PEG, PEGylation (1970s-1990s) (vol 40, pg 1, 2016)*. Acta Biomaterialia, 2017. **49**: p. 606-606.
86. Tirelli, N., et al., *Poly(ethylene glycol) block copolymers*. J Biotechnol, 2002. **90**(1): p. 3-15.
87. Knop, K., et al., *Poly(ethylene glycol) in Drug Delivery: Pros and Cons as Well as Potential Alternatives*. Angewandte Chemie-International Edition, 2010. **49**(36): p. 6288-6308.
88. Harris, J.M., ed. *Poly(Ethylene Glycol) Chemistry: Biotechnical and Biomedical Applications*. TOPICS IN APPLIED CHEMISTRY, ed. G.J.S. Alan R. Katritzky. 1992, Springer.
89. Yu, Q.A., et al., *Anti-fouling bioactive surfaces*. Acta Biomaterialia, 2011. **7**(4): p. 1550-1557.
90. Veronese, F.M. and G. Pasut, *PEGylation, successful approach to drug delivery*. Drug Discovery Today, 2005. **10**(21): p. 1451-1458.
91. Gref, R., et al., *Biodegradable Long-Circulating Polymeric Nanospheres*. Science, 1994. **263**(5153): p. 1600-1603.
92. van Vlerken, L.E., T.K. Vyas, and M.M. Amiji, *Poly(ethylene glycol)-modified nanocarriers for tumor-targeted and intracellular delivery*. Pharmaceutical Research, 2007. **24**(8): p. 1405-1414.
93. Gref, R., et al., *The Controlled Intravenous Delivery of Drugs Using Peg-Coated Sterically Stabilized Nanospheres*. Advanced Drug Delivery Reviews, 1995. **16**(2-3): p. 215-233.
94. Allen, S.D., O.A. Osorio, and E.A. Scott, *Rapid assembly and loading of theranostic polymersomes via multi-impingement flash nanoprecipitation*. Revised and Resubmitted, 2017.
95. Yi, S., et al., *Tailoring Nanostructure Morphology for Enhanced Targeting of Dendritic Cells in Atherosclerosis*. ACS Nano, 2016. **10**(12): p. 11290-11303.
96. Feynman, R.P., *There's plenty of room at the bottom*. Engineering and Science, 1959(23): p. 22-36.
97. Mishra, D., J.R. Hubenak, and A.B. Mathur, *Nanoparticle systems as tools to improve drug delivery and therapeutic efficacy*. Journal of Biomedical Materials Research Part A, 2013. **101**(12): p. 3646-3660.
98. Petros, R.A. and J.M. DeSimone, *Strategies in the design of nanoparticles for therapeutic applications*. Nature Reviews Drug Discovery, 2010. **9**(8): p. 615-627.

99. Demetzos, C. and N. Pippa, *Advanced drug delivery nanosystems (aDDnSs): a mini-review*. Drug Delivery, 2014. **21**(4): p. 250-257.
100. Blanco, E., et al., *Nanomedicine in cancer therapy: Innovative trends and prospects*. Cancer Science, 2011. **102**(7): p. 1247-1252.
101. Hawkins, M.J., P. Soon-Shiong, and N. Desai, *Protein nanoparticles as drug carriers in clinical medicine*. Advanced Drug Delivery Reviews, 2008. **60**(8): p. 876-885.
102. Maeda, H., et al., *Tumor vascular permeability and the EPR effect in macromolecular therapeutics: a review*. Journal of Controlled Release, 2000. **65**(1-2): p. 271-284.
103. Tietjen, G.T., et al., *Focus on Fundamentals: Achieving Effective Nanoparticle Targeting*. Trends in Molecular Medicine, 2018. **24**(7): p. 598-606.
104. Koo, O.M., I. Rubinstein, and H. Onyuksel, *Role of nanotechnology in targeted drug delivery and imaging: a concise review*. Nanomedicine-Nanotechnology Biology and Medicine, 2005. **1**(3): p. 193-212.
105. Alexis, F., et al., *New frontiers in nanotechnology for cancer treatment*. Urologic Oncology-Seminars and Original Investigations, 2008. **26**(1): p. 74-85.
106. Islam, M.A., et al., *Biomaterials for mRNA delivery*. Biomaterials Science, 2015. **3**(12): p. 1519-1533.
107. Yu, M.Y., et al., *Nanotechnology for protein delivery: Overview and perspectives*. Journal of Controlled Release, 2016. **240**: p. 24-37.
108. Houseley, J. and D. Tollervey, *The Many Pathways of RNA Degradation*. Cell, 2009. **136**(4): p. 763-776.
109. Jeong, K., et al., *Development of highly efficient nanocarrier-mediated delivery approaches for cancer therapy*. Cancer Letters, 2016. **374**(1): p. 31-43.
110. Mansoori, B., et al., *The Different Mechanisms of Cancer Drug Resistance: A Brief Review*. Advanced Pharmaceutical Bulletin, 2017. **7**(3): p. 339-348.

111. Kong, Y.W., Dreaden, Erik C., Hammond, Paula T., Yaffe, Michael B., *Exploiting Nanocarriers for Combination Cancer Therapy*, in *Intracellular Delivery III*, A. Prokop, Weissig, Volkmar, Editor. 2016, Springer International Publishing. p. 375-402.
112. Podder, H., et al., *Pharmacokinetic interactions augment toxicities of sirolimus/cyclosporine combinations*. *Journal of the American Society of Nephrology*, 2001. **12**(5): p. 1059-1071.
113. Matsumura, Y. and H. Maeda, *A New Concept for Macromolecular Therapeutics in Cancer-Chemotherapy - Mechanism of Tumorotropic Accumulation of Proteins and the Antitumor Agent Smancs*. *Cancer Research*, 1986. **46**(12): p. 6387-6392.
114. Danhier, F., *To exploit the tumor microenvironment: Since the EPR effect fails in the clinic, what is the future of nanomedicine?* *Journal of Controlled Release*, 2016. **244**: p. 108-121.
115. Nichols, J.W. and Y.H. Bae, *EPR: Evidence and fallacy*. *Journal of Controlled Release*, 2014. **190**: p. 451-464.
116. Shi, J.J., et al., *Cancer nanomedicine: progress, challenges and opportunities*. *Nature Reviews Cancer*, 2017. **17**(1): p. 20-37.
117. Chow, A., B.D. Brown, and M. Merad, *Studying the mononuclear phagocyte system in the molecular age*. *Nature Reviews Immunology*, 2011. **11**(11): p. 788-798.
118. Gustafson, H.H., et al., *Nanoparticle uptake: The phagocyte problem*. *Nano Today*, 2015. **10**(4): p. 487-510.
119. Scott, E.A., N.B. Karabin, and P. Augsornworawat, *Overcoming Immune Dysregulation with Immunoengineered Nanobiomaterials*. *Annu Rev Biomed Eng*, 2017.
120. Allen, S., Y.G. Liu, and E. Scott, *Engineering nanomaterials to address cell-mediated inflammation in atherosclerosis*. *Regen Eng Transl Med*, 2016. **2**(1): p. 37-50.
121. Swartz, M.A., S. Hirose, and J.A. Hubbell, *Engineering Approaches to Immunotherapy*. *Science Translational Medicine*, 2012. **4**(148).
122. Turvey, S.E. and D.H. Broide, *Innate immunity*. *The Journal of allergy and clinical immunology*, 2010. **125**(2 Suppl 2): p. S24-S32.

123. Fahy, J.V. and B.F. Dickey, *Airway Mucus Function and Dysfunction REPLY*. New England Journal of Medicine, 2011. **364**(10): p. 978-978.
124. Bustamante-Marin, X.M. and L.E. Ostrowski, *Cilia and Mucociliary Clearance*. Cold Spring Harbor Perspectives in Biology, 2017. **9**(4).
125. Wang, G., *Human antimicrobial peptides and proteins*. Pharmaceuticals (Basel, Switzerland), 2014. **7**(5): p. 545-594.
126. Dunkelberger, J.R. and W.C. Song, *Complement and its role in innate and adaptive immune responses*. Cell Research, 2010. **20**(1): p. 34-50.
127. Mogensen, T.H., *Pathogen Recognition and Inflammatory Signaling in Innate Immune Defenses*. Clinical Microbiology Reviews, 2009. **22**(2): p. 240-+.
128. Rosales, C., *Neutrophil: A Cell with Many Roles in Inflammation or Several Cell Types?* Frontiers in Physiology, 2018. **9**.
129. Kolaczkowska, E. and P. Kubes, *Neutrophil recruitment and function in health and inflammation*. Nature Reviews Immunology, 2013. **13**(3): p. 159-175.
130. Mayadas, T.N., X. Cullere, and C.A. Lowell, *The Multifaceted Functions of Neutrophils*. Annual Review of Pathology: Mechanisms of Disease, Vol 9, 2014. **9**: p. 181-218.
131. Lacy, P., *Mechanisms of degranulation in neutrophils*. Allergy Asthma Clin Immunol, 2006. **2**(3): p. 98-108.
132. Brinkmann, V., et al., *Neutrophil extracellular traps kill bacteria*. Science, 2004. **303**(5663): p. 1532-5.
133. Selders, G.S., et al., *An overview of the role of neutrophils in innate immunity, inflammation and host-biomaterial integration*. Regenerative Biomaterials, 2017. **4**(1): p. 55-68.
134. Jakubzick, C.V., G.J. Randolph, and P.M. Henson, *Monocyte differentiation and antigen-presenting functions*. Nat Rev Immunol, 2017. **17**(6): p. 349-362.
135. Zhu, Y.P., G.D. Thomas, and C.C. Hedrick, *2014 Jeffrey M. Hoeg Award Lecture: Transcriptional Control of Monocyte Development*. Arterioscler Thromb Vasc Biol, 2016. **36**(9): p. 1722-33.

136. Shi, C. and E.G. Pamer, *Monocyte recruitment during infection and inflammation*. Nat Rev Immunol, 2011. **11**(11): p. 762-74.
137. Boyette, L.B., et al., *Phenotype, function, and differentiation potential of human monocyte subsets*. PLoS One, 2017. **12**(4): p. e0176460.
138. Yang, J., et al., *Monocyte and macrophage differentiation: circulation inflammatory monocyte as biomarker for inflammatory diseases*. Biomark Res, 2014. **2**(1): p. 1.
139. Patel, A.A., et al., *The fate and lifespan of human monocyte subsets in steady state and systemic inflammation*. J Exp Med, 2017. **214**(7): p. 1913-1923.
140. Auffray, C., M.H. Sieweke, and F. Geissmann, *Blood monocytes: development, heterogeneity, and relationship with dendritic cells*. Annu Rev Immunol, 2009. **27**: p. 669-92.
141. Gordon, S., *Alternative activation of macrophages*. Nat Rev Immunol, 2003. **3**(1): p. 23-35.
142. Davies, L.C., et al., *Tissue-resident macrophages*. Nat Immunol, 2013. **14**(10): p. 986-95.
143. Murray, P.J., *Macrophage Polarization*. Annual Review of Physiology, Vol 79, 2017. **79**: p. 541-566.
144. Davies, L.C. and P.R. Taylor, *Tissue-resident macrophages: then and now*. Immunology, 2015. **144**(4): p. 541-548.
145. Mantovani, A., A. Sica, and M. Locati, *Macrophage polarization comes of age*. Immunity, 2005. **23**(4): p. 344-346.
146. Mosser, D.M. and J.P. Edwards, *Exploring the full spectrum of macrophage activation*. Nature Reviews Immunology, 2008. **8**(12): p. 958-969.
147. Mantovani, A., et al., *The chemokine system in diverse forms of macrophage activation and polarization*. Trends Immunol, 2004. **25**(12): p. 677-86.
148. Sprent, J., *Antigen-presenting cells. Professionals and amateurs*. Curr Biol, 1995. **5**(10): p. 1095-7.
149. Lin, A. and K. Lore, *Granulocytes: New Members of the Antigen-Presenting Cell Family*. Front Immunol, 2017. **8**: p. 1781.
150. Banchereau, J., et al., *Immunobiology of dendritic cells*. Annu Rev Immunol, 2000. **18**: p. 767-811.

151. Savina, A. and S. Amigorena, *Phagocytosis and antigen presentation in dendritic cells*. Immunol Rev, 2007. **219**: p. 143-56.
152. Segura, E., *Review of Mouse and Human Dendritic Cell Subsets*. Methods Mol Biol, 2016. **1423**: p. 3-15.
153. Lei, Y.G., et al., *Incorporation of active DNA/cationic polymer polyplexes into hydrogel scaffolds*. Biomaterials, 2010. **31**(34): p. 9106-9116.
154. Joffre, O.P., et al., *Cross-presentation by dendritic cells*. Nat Rev Immunol, 2012. **12**(8): p. 557-69.
155. Gilliet, M., W. Cao, and Y.J. Liu, *Plasmacytoid dendritic cells: sensing nucleic acids in viral infection and autoimmune diseases*. Nat Rev Immunol, 2008. **8**(8): p. 594-606.
156. Bonilla, F.A. and H.C. Oettgen, *Adaptive immunity*. J Allergy Clin Immunol, 2010. **125**(2 Suppl 2): p. S33-40.
157. Batista, F.D. and N.E. Harwood, *The who, how and where of antigen presentation to B cells*. Nature Reviews Immunology, 2009. **9**(1): p. 15-27.
158. Malhotra, S., et al., *B Cell Antigen Receptor Endocytosis and Antigen Presentation to T Cells Require Vav and Dynamin*. Journal of Biological Chemistry, 2009. **284**(36): p. 24088-24097.
159. Brynjolfsson, S.F., et al., *Long-Lived Plasma Cells in Mice and Men*. Frontiers in Immunology, 2018. **9**.
160. Sallusto, F., et al., *From vaccines to memory and back*. Immunity, 2010. **33**(4): p. 451-63.
161. Lanzavecchia, A. and F. Sallusto, *Dynamics of T lymphocyte responses: intermediates, effectors, and memory cells*. Science, 2000. **290**(5489): p. 92-7.
162. Luckheeram, R.V., et al., *CD4(+)T cells: differentiation and functions*. Clin Dev Immunol, 2012. **2012**: p. 925135.
163. Halle, S., O. Halle, and R. Forster, *Mechanisms and Dynamics of T Cell-Mediated Cytotoxicity In Vivo*. Trends Immunol, 2017. **38**(6): p. 432-443.
164. Durgeau, A., et al., *Recent Advances in Targeting CD8 T-Cell Immunity for More Effective Cancer Immunotherapy*. Front Immunol, 2018. **9**: p. 14.
165. Wan, Y.Y., *Multi-tasking of helper T cells*. Immunology, 2010. **130**(2): p. 166-71.

166. Sakaguchi, S., et al., *Regulatory T cells and immune tolerance*. Cell, 2008. **133**(5): p. 775-87.
167. Wang, J., et al., *More effective nanomedicines through particle design*. Small, 2011. **7**(14): p. 1919-31.
168. Xiang, S.D., et al., *Pathogen recognition and development of particulate vaccines: Does size matter?* Methods, 2006. **40**(1): p. 1-9.
169. Hettinger, J., et al., *Origin of monocytes and macrophages in a committed progenitor*. Nature Immunology, 2013. **14**(8): p. 821-+.
170. Kou, L., et al., *The endocytosis and intracellular fate of nanomedicines: Implication for rational design*. Asian Journal of Pharmaceutical Sciences, 2013. **8**(1): p. 1-10.
171. Rejman, J., et al., *Size-dependent internalization of particles via the pathways of clathrin-and caveolae-mediated endocytosis*. Biochemical Journal, 2004. **377**: p. 159-169.
172. Richards, D.M. and R.G. Endres, *The Mechanism of Phagocytosis: Two Stages of Engulfment*. Biophysical Journal, 2014. **107**(7): p. 1542-1553.
173. Firestein, G.S., *Evolving concepts of rheumatoid arthritis*. Nature, 2003. **423**(6937): p. 356-361.
174. Joyce, J.A. and D.T. Fearon, *T cell exclusion, immune privilege, and the tumor microenvironment*. Science, 2015. **348**(6230): p. 74-80.
175. Lavin, Y., et al., *Regulation of macrophage development and function in peripheral tissues*. Nat Rev Immunol, 2015. **15**(12): p. 731-44.
176. da Silva, H.B., et al., *Splenic macrophage subsets and their function during blood-borne infections*. Frontiers in Immunology, 2015. **6**.
177. Kurotaki, D., et al., *CSF-1-Dependent Red Pulp Macrophages Regulate CD4 T Cell Responses*. Journal of Immunology, 2011. **186**(4): p. 2229-2237.
178. Backer, R., et al., *Effective collaboration between marginal metallophilic macrophages and CD8(+) dendritic cells in the generation of cytotoxic T cells*. Proceedings of the National Academy of Sciences of the United States of America, 2010. **107**(1): p. 216-221.
179. Vasti, C., et al., *Relevance of protein-protein interactions on the biological identity of nanoparticles*. Colloids Surf B Biointerfaces, 2018. **166**: p. 330-338.

180. Nel, A.E., et al., *Understanding biophysicochemical interactions at the nano-bio interface*. Nat Mater, 2009. **8**(7): p. 543-57.
181. Walkey, C.D. and W.C. Chan, *Understanding and controlling the interaction of nanomaterials with proteins in a physiological environment*. Chem Soc Rev, 2012. **41**(7): p. 2780-99.
182. Wan, S., et al., *The "sweet" side of the protein corona: effects of glycosylation on nanoparticle-cell interactions*. ACS Nano, 2015. **9**(2): p. 2157-66.
183. Muller, J., et al., *Beyond the protein corona - lipids matter for biological response of nanocarriers*. Acta Biomater, 2018. **71**: p. 420-431.
184. Caracciolo, G., O.C. Farokhzad, and M. Mahmoudi, *Biological Identity of Nanoparticles In Vivo: Clinical Implications of the Protein Corona*. Trends Biotechnol, 2017. **35**(3): p. 257-264.
185. Duan, X. and Y. Li, *Physicochemical Characteristics of Nanoparticles Affect Circulation, Biodistribution, Cellular Internalization, and Trafficking*. Small, 2013. **9**(9-10): p. 1521-1532.
186. Cedervall, T., et al., *Understanding the nanoparticle-protein corona using methods to quantify exchange rates and affinities of proteins for nanoparticles*. Proceedings of the National Academy of Sciences of the United States of America, 2007. **104**(7): p. 2050-2055.
187. Nguyen, V.H. and B.J. Lee, *Protein corona: a new approach for nanomedicine design*. International Journal of Nanomedicine, 2017. **12**: p. 3137-3151.
188. Lundqvist, M., et al., *Nanoparticle size and surface properties determine the protein corona with possible implications for biological impacts*. Proceedings of the National Academy of Sciences of the United States of America, 2008. **105**(38): p. 14265-14270.
189. Saha, K., et al., *Regulation of Macrophage Recognition through the Interplay of Nanoparticle Surface Functionality and Protein Corona*. ACS Nano, 2016. **10**(4): p. 4421-30.
190. Gagner, J.E., et al., *Effect of gold nanoparticle morphology on adsorbed protein structure and function*. Biomaterials, 2011. **32**(29): p. 7241-7252.
191. Cerritelli, S., et al., *Thermodynamic and kinetic effects in the aggregation behavior of a poly(ethylene glycol-b-propylene sulfide-b-ethylene glycol) ABA triblock copolymer*. Macromolecules, 2005. **38**(18): p. 7845-7851.

192. Scott, E.A., et al., *Dendritic cell activation and T cell priming with adjuvant- and antigen-loaded oxidation-sensitive polymersomes*. *Biomaterials*, 2012. **33**(26): p. 6211-6219.
193. Stano, A., et al., *Tunable T cell immunity towards a protein antigen using polymersomes vs. solid-core nanoparticles*. *Biomaterials*, 2013. **34**(17): p. 4339-4346.
194. Cerritelli, S., D. Velluto, and J.A. Hubbell, *PEG-SS-PPS: Reduction-sensitive disulfide block copolymer vesicles for intracellular drug delivery*. *Biomacromolecules*, 2007. **8**(6): p. 1966-1972.
195. Dane, K.Y., et al., *Nano-sized drug-loaded micelles deliver payload to lymph node immune cells and prolong allograft survival*. *Journal of Controlled Release*, 2011. **156**(2): p. 154-160.
196. O'Neil, C.P., et al., *A Novel Method for the Encapsulation of Biomolecules into Polymersomes via Direct Hydration*. *Langmuir*, 2009. **25**(16): p. 9025-9029.
197. O'Neil, C.P., et al., *Extracellular matrix binding mixed micelles for drug delivery applications*. *Journal of Controlled Release*, 2009. **137**(2): p. 146-151.
198. Segura, T. and J.A. Hubbell, *Synthesis and in vitro characterization of an ABC triblock copolymer for siRNA delivery*. *Bioconjugate Chemistry*, 2007. **18**(3): p. 736-745.
199. Velluto, D., et al., *PEG-b-PPS-b-PEI micelles and PEG-b-PPS/PEG-b-PPS-b-PEI mixed micelles as non-viral vectors for plasmid DNA: Tumor immunotoxicity in B16F10 melanoma*. *Biomaterials*, 2011. **32**(36): p. 9839-9847.
200. Yu, S.S., et al., *Size- and charge-dependent non-specific uptake of PEGylated nanoparticles by macrophages*. *International Journal of Nanomedicine*, 2012. **7**: p. 799-813.
201. Yu, S.S., et al., *Enzymatic- and temperature-sensitive controlled release of ultrasmall superparamagnetic iron oxides (USPIOs) (vol 9, pg 7, 2011)*. *Journal of Nanobiotechnology*, 2011. **9**.
202. Du, F.F., Y.G. Liu, and E.A. Scott, *Immunotheranostic Polymersomes Modularly Assembled from Tetrablock and Diblock Copolymers with Oxidation-Responsive Fluorescence*. *Cellular and Molecular Bioengineering*, 2017. **10**(5): p. 357-370.

203. Bonnans-Plaisance, C., G. Levesque, and A. Midrak, *Polymerisation du methylthiirane par les sels d'ammonium quaternaire des (di)thioacides: Etude cinetique dans le THF*. European Polymer Journal, 1994. **30**(2): p. 239-244.
204. Dowling, D.J., et al., *Toll-like receptor 8 agonist nanoparticles mimic immunomodulating effects of the live BCG vaccine and enhance neonatal innate and adaptive immune responses*. J Allergy Clin Immunol, 2017.
205. van der Vlies, A.J., U. Hasegawa, and J.A. Hubbell, *Reduction-Sensitive Thioguanine Prodrug Micelles*. Molecular Pharmaceutics, 2012. **9**(10): p. 2812-2818.
206. Jeanbart, L., et al., *6-Thioguanine-loaded polymeric micelles deplete myeloid-derived suppressor cells and enhance the efficacy of T cell immunotherapy in tumor-bearing mice*. Cancer Immunology Immunotherapy, 2015. **64**(8): p. 1033-1046.
207. Acton, Q.A., *Glycols—Advances in Research and Application: 2013 Edition*. 2013: ScholarlyEditions.
208. Eby, J.K., et al., *Polymer micelles with pyridyl disulfide-coupled antigen travel through lymphatics and show enhanced cellular responses following immunization*. Acta Biomaterialia, 2012. **8**(9): p. 3210-3217.
209. Yu, S.S., et al., *Size- and charge-dependent non-specific uptake of PEGylated nanoparticles by macrophages*. Int J Nanomedicine, 2012. **7**: p. 799-813.
210. Thompson, M.S., et al., *Synthesis and applications of heterobifunctional poly(ethylene oxide) oligomers*. Polymer, 2008. **49**(2): p. 345-373.
211. Herzberger, J., et al., *Polymerization of Ethylene Oxide, Propylene Oxide, and Other Alkylene Oxides: Synthesis, Novel Polymer Architectures, and Bioconjugation*. Chemical Reviews, 2016. **116**(4): p. 2170-2243.
212. Vojkovsky, T., B. Sullivan, and K.N. Sill, *Synthesis of heterobifunctional polyethylene glycols: Polymerization from functional initiators*. Polymer, 2016. **105**: p. 72-78.
213. Mahou, R. and C. Wandrey, *Versatile Route to Synthesize Heterobifunctional Poly(ethylene glycol) of Variable Functionality for Subsequent Pegylation*. Polymers, 2012. **4**(1): p. 561-589.

214. Bouzide, A. and G. Sauve, *Silver(I) oxide mediated highly selective monotosylation of symmetrical diols. Application to the synthesis of polysubstituted cyclic ethers*. *Organic Letters*, 2002. **4**(14): p. 2329-2332.
215. Lutolf, M.P. and J.A. Hubbell, *Synthesis and physicochemical characterization of end-linked poly(ethylene glycol)-co-peptide hydrogels formed by Michael-type addition*. *Biomacromolecules*, 2003. **4**(3): p. 713-722.
216. Karabin, N.B., et al., *Sustained micellar delivery via inducible transitions in nanostructure morphology*. *Nat Commun*, 2018. **9**(1): p. 624.
217. Li, Z.Y. and Y. Chau, *A facile synthesis of branched poly(ethylene glycol) and its heterobifunctional derivatives*. *Polymer Chemistry*, 2011. **2**(4): p. 873-878.
218. Morales-Sanfrutos, J., et al., *Vinyl sulfone: a versatile function for simple bioconjugation and immobilization*. *Organic & Biomolecular Chemistry*, 2010. **8**(3): p. 667-675.
219. Sneh-Edri, H., D. Likhtenshtein, and D. Stepensky, *Intracellular Targeting of PLGA Nanoparticles Encapsulating Antigenic Peptide to the Endoplasmic Reticulum of Dendritic Cells and Its Effect on Antigen Cross-Presentation in Vitro*. *Molecular Pharmaceutics*, 2011. **8**(4): p. 1266-1275.
220. Yan, Z.Y., et al., *A novel peptide targeting Clec9a on dendritic cell for cancer immunotherapy*. *Oncotarget*, 2016. **7**(26): p. 40437-40450.
221. Mather, B.D., et al., *Michael addition reactions in macromolecular design for emerging technologies*. *Progress in Polymer Science*, 2006. **31**(5): p. 487-531.
222. Heggli, M., et al., *Michael-type addition as a tool for surface functionalization*. *Bioconjugate Chemistry*, 2003. **14**(5): p. 967-973.
223. Weber, E.J. and V.C. Stickney, *Hydrolysis Kinetics of Reactive Blue 19-Vinyl Sulfone*. *Water Research*, 1993. **27**(1): p. 63-67.
224. Mahato, R., W.Y. Tai, and K. Cheng, *Prodrugs for improving tumor targetability and efficiency*. *Advanced Drug Delivery Reviews*, 2011. **63**(8): p. 659-670.
225. Xiao, K., et al., *The effect of surface charge on in vivo biodistribution of PEG-oligocholic acid based micellar nanoparticles*. *Biomaterials*, 2011. **32**(13): p. 3435-46.

226. Hillaireau, H. and P. Couvreur, *Nanocarriers' entry into the cell: relevance to drug delivery*. Cellular and Molecular Life Sciences, 2009. **66**(17): p. 2873-2896.
227. Wei, X.W., et al., *Cationic nanocarriers induce cell necrosis through impairment of Na⁺/K⁺-ATPase and cause subsequent inflammatory response*. Cell Research, 2015. **25**(2): p. 237-253.
228. Hunter, T., *Why nature chose phosphate to modify proteins*. Philosophical Transactions of the Royal Society B-Biological Sciences, 2012. **367**(1602): p. 2513-2516.
229. Stockbridge, R.B. and R. Wolfenden, *Phosphate Monoester Hydrolysis in Cyclohexane*. Journal of the American Chemical Society, 2009. **131**(51): p. 18248-+.
230. Cleland, W.W. and A.C. Hengge, *Enzymatic mechanisms of phosphate and sulfate transfer*. Chemical Reviews, 2006. **106**(8): p. 3252-3278.
231. Lu, C.C., et al., *Carboxyl-polyethylene glycol-phosphoric acid: a ligand for highly stabilized iron oxide nanoparticles*. Journal of Materials Chemistry, 2012. **22**(37): p. 19806-19811.
232. Tang, W. and M.L. Becker, *"Click" reactions: a versatile toolbox for the synthesis of peptide-conjugates*. Chemical Society Reviews, 2014. **43**(20): p. 7013-7039.
233. Saxon, E. and C.R. Bertozzi, *Cell surface engineering by a modified Staudinger reaction*. Science, 2000. **287**(5460): p. 2007-2010.
234. Rostovtsev, V.V., et al., *A stepwise Huisgen cycloaddition process: Copper(I)-catalyzed regioselective "ligation" of azides and terminal alkynes*. Angewandte Chemie-International Edition, 2002. **41**(14): p. 2596-+.
235. Tornøe, C.W., C. Christensen, and M. Meldal, *Peptidotriazoles on solid phase: [1,2,3]-triazoles by regiospecific copper(I)-catalyzed 1,3-dipolar cycloadditions of terminal alkynes to azides*. Journal of Organic Chemistry, 2002. **67**(9): p. 3057-3064.
236. Agard, N.J., et al., *A comparative study of bioorthogonal reactions with azides*. Acs Chemical Biology, 2006. **1**(10): p. 644-648.
237. Hein, C.D., X.M. Liu, and D. Wang, *Click chemistry, a powerful tool for pharmaceutical sciences*. Pharmaceutical Research, 2008. **25**(10): p. 2216-2230.

238. Prescher, J.A. and C.R. Bertozzi, *Chemistry in living systems*. Nature Chemical Biology, 2005. **1**(1): p. 13-21.
239. Scriven, E.F.V. and K. Turnbull, *Azides - Their Preparation and Synthetic Uses*. Chemical Reviews, 1988. **88**(2): p. 297-368.
240. Frey, M., et al., *Influences of nanocarrier morphology on therapeutic immunomodulation*. Nanomedicine (Lond), 2018.
241. Bazak, R., et al., *Cancer active targeting by nanoparticles: a comprehensive review of literature*. Journal of Cancer Research and Clinical Oncology, 2015. **141**(5): p. 769-784.
242. Perry, J.L., et al., *Mediating Passive Tumor Accumulation through Particle Size, Tumor Type, and Location*. Nano Letters, 2017. **17**(5): p. 2879-2886.
243. Huynh, N.T., et al., *The rise and rise of stealth nanocarriers for cancer therapy: passive versus active targeting*. Nanomedicine, 2010. **5**(9): p. 1415-1433.
244. Su, G.X., et al., *Effects of Protein Corona on Active and Passive Targeting of Cyclic RGD Peptide-Functionalized PEGylation Nanoparticles*. Molecular Pharmaceutics, 2018. **15**(11): p. 5019-5030.
245. Salvati, A., et al., *Transferrin-functionalized nanoparticles lose their targeting capabilities when a biomolecule corona adsorbs on the surface*. Nat Nanotechnol, 2013. **8**(2): p. 137-43.
246. Mirshafiee, V., et al., *Protein corona significantly reduces active targeting yield*. Chemical Communications, 2013. **49**(25): p. 2557-2559.
247. Walczyk, D., et al., *What the Cell "Sees" in Bionanoscience*. Journal of the American Chemical Society, 2010. **132**(16): p. 5761-5768.
248. Diederichs, J.E., *Plasma protein adsorption patterns on liposomes: Establishment of analytical procedure*. Electrophoresis, 1996. **17**(3): p. 607-611.
249. Nierenberg, D., A.R. Khaled, and O. Flores, *Formation of a protein corona influences the biological identity of nanomaterials*. Reports of Practical Oncology and Radiotherapy, 2018. **23**(4): p. 300-308.
250. Milani, S., et al., *Reversible versus irreversible binding of transferrin to polystyrene nanoparticles: soft and hard corona*. ACS Nano, 2012. **6**(3): p. 2532-41.

251. Nanjappa, V., et al., *Plasma Proteome Database as a resource for proteomics research: 2014 update*. Nucleic Acids Research, 2014. **42**(D1): p. D959-D965.
252. Lynch, I. and K.A. Dawson, *Protein-nanoparticle interactions*. Nano Today, 2008. **3**(1-2): p. 40-47.
253. Vroman, L., *Effect of Adsorbed Proteins on the Wettability of Hydrophilic and Hydrophobic Solids*. Nature, 1962. **196**(4853): p. 476-477.
254. Vroman, L. and A.L. Adams, *Identification of rapid changes at plasma–solid interfaces*. Journal of Biomedical Materials Research, 1969. **3**(1): p. 43-67.
255. Tenzer, S., et al., *Rapid formation of plasma protein corona critically affects nanoparticle pathophysiology*. Nat Nanotechnol, 2013. **8**(10): p. 772-81.
256. Docter, D., et al., *The nanoparticle biomolecule corona: lessons learned - challenge accepted?* Chem Soc Rev, 2015. **44**(17): p. 6094-121.
257. Garcia-Alvarez, R., et al., *In vivo formation of protein corona on gold nanoparticles. The effect of their size and shape*. Nanoscale, 2018. **10**(3): p. 1256-1264.
258. Chen, D., et al., *The role of surface chemistry in serum protein corona-mediated cellular delivery and gene silencing with lipid nanoparticles*. Nanoscale, 2019.
259. Clemments, A.M., P. Botella, and C.C. Landry, *Protein Adsorption From Biofluids on Silica Nanoparticles: Corona Analysis as a Function of Particle Diameter and Porosity*. Acs Applied Materials & Interfaces, 2015. **7**(39): p. 21682-21689.
260. Ritz, S., et al., *Protein Corona of Nanoparticles: Distinct Proteins Regulate the Cellular Uptake*. Biomacromolecules, 2015. **16**(4): p. 1311-1321.
261. Schottler, S., et al., *Protein adsorption is required for stealth effect of poly(ethylene glycol)- and poly(phosphoester)-coated nanocarriers*. Nat Nanotechnol, 2016. **11**(4): p. 372-7.
262. Bertrand, N., et al., *Mechanistic understanding of in vivo protein corona formation on polymeric nanoparticles and impact on pharmacokinetics*. Nat Commun, 2017. **8**(1): p. 777.
263. Dreher, M.R., et al., *Tumor vascular permeability, accumulation, and penetration of macromolecular drug carriers*. Jnci-Journal of the National Cancer Institute, 2006. **98**(5): p. 335-344.

264. Kelly, C., C. Jefferies, and S.A. Cryan, *Targeted liposomal drug delivery to monocytes and macrophages*. J Drug Deliv, 2011. **2011**: p. 727241.
265. Devarajan, P.V., et al., *Particle shape: a new design parameter for passive targeting in splenotropic drug delivery*. J Pharm Sci, 2010. **99**(6): p. 2576-81.
266. Anselmo, A.C., et al., *Elasticity of nanoparticles influences their blood circulation, phagocytosis, endocytosis, and targeting*. ACS Nano, 2015. **9**(3): p. 3169-77.
267. Getts, D.R., et al., *Microparticles bearing encephalitogenic peptides induce T-cell tolerance and ameliorate experimental autoimmune encephalomyelitis*. Nat Biotech, 2012. **30**(12): p. 1217-1224.
268. Reddy, S.T., et al., *In vivo targeting of dendritic cells in lymph nodes with poly(propylene sulfide) nanoparticles*. Journal of Controlled Release, 2006. **112**(1): p. 26-34.
269. Han, J., et al., *A simple confined impingement jets mixer for flash nanoprecipitation*. J Pharm Sci, 2012. **101**(10): p. 4018-23.
270. Lund, M.E., et al., *The choice of phorbol 12-myristate 13-acetate differentiation protocol influences the response of THP-1 macrophages to a pro-inflammatory stimulus*. J Immunol Methods, 2016. **430**: p. 64-70.
271. Dauer, M., et al., *Mature dendritic cells derived from human monocytes within 48 hours: A novel strategy for dendritic cell differentiation from blood precursors*. Journal of Immunology, 2003. **170**(8): p. 4069-4076.
272. Rehbein, P. and H. Schwalbe, *Integrated protocol for reliable and fast quantification and documentation of electrophoresis gels*. Protein Expression and Purification, 2015. **110**: p. 1-6.
273. Schindelin, J., et al., *Fiji: an open-source platform for biological-image analysis*. Nature Methods, 2012. **9**(7): p. 676-682.
274. Nagarajan, R., *Molecular packing parameter and surfactant self-assembly: The neglected role of the surfactant tail*. Langmuir, 2002. **18**(1): p. 31-38.
275. Roy, M.T., M. Gallardo, and J. Estelrich, *Influence of size on electrokinetic behavior of phosphatidylserine and phosphatidylethanolamine lipid vesicles*. Journal of Colloid and Interface Science, 1998. **206**(2): p. 512-517.

276. Tseng, S., P.H. Yeh, and J.P. Hsu, *Simulation of Polyelectrolyte Electrophoresis: Effects of the Aspect Ratio, Double-Layer Polarization, Effective Charge, and Electroosmotic Flow*. Langmuir, 2014. **30**(27): p. 8177-8185.
277. Grossman, P.D. and D.S. Soane, *Orientation Effects on the Electrophoretic Mobility of Rod-Shaped Molecules in Free Solution*. Analytical Chemistry, 1990. **62**(15): p. 1592-1596.
278. Suttiponparnit, K., et al., *Role of Surface Area, Primary Particle Size, and Crystal Phase on Titanium Dioxide Nanoparticle Dispersion Properties*. Nanoscale Research Letters, 2011. **6**.
279. Tantra, R., P. Schulze, and P. Quincey, *Effect of nanoparticle concentration on zeta-potential measurement results and reproducibility*. Particuology, 2010. **8**(3): p. 279-285.
280. Medrzycka, K.B., *The Effect of Particle Concentration on Zeta-Potential in Extremely Dilute Solutions*. Colloid and Polymer Science, 1991. **269**(1): p. 85-90.
281. Wang, N., et al., *Influence of metal oxide nanoparticles concentration on their zeta potential*. Journal of Colloid and Interface Science, 2013. **407**: p. 22-28.
282. Tenzer, S., et al., *Nanoparticle Size Is a Critical Physicochemical Determinant of the Human Blood Plasma Corona: A Comprehensive Quantitative Proteomic Analysis*. Acs Nano, 2011. **5**(9): p. 7155-7167.
283. Lundqvist, M., et al., *The nanoparticle protein corona formed in human blood or human blood fractions*. Plos One, 2017. **12**(4).
284. Walkey, C.D., et al., *Nanoparticle Size and Surface Chemistry Determine Serum Protein Adsorption and Macrophage Uptake*. Journal of the American Chemical Society, 2012. **134**(4): p. 2139-2147.
285. Aggarwal, P., et al., *Nanoparticle interaction with plasma proteins as it relates to particle biodistribution, biocompatibility and therapeutic efficacy*. Adv Drug Deliv Rev, 2009. **61**(6): p. 428-37.
286. Yan, Y., et al., *Differential Roles of the Protein Corona in the Cellular Uptake of Nanoporous Polymer Particles by Monocyte and Macrophage Cell Lines*. Acs Nano, 2013. **7**(12): p. 10960-10970.

287. Deng, Z.J., et al., *Nanoparticle-induced unfolding of fibrinogen promotes Mac-1 receptor activation and inflammation*. *Nat Nanotechnol*, 2011. **6**(1): p. 39-44.
288. Worrall, J.W., et al., *"Cleaning" of nanoparticle inhibitors via proteolysis of adsorbed proteins*. *Chem Commun (Camb)*, 2006(22): p. 2338-40.
289. Lacerda, S.H., et al., *Interaction of gold nanoparticles with common human blood proteins*. *ACS Nano*, 2010. **4**(1): p. 365-79.
290. Fleischer, C.C. and C.K. Payne, *Secondary Structure of Corona Proteins Determines the Cell Surface Receptors Used by Nanoparticles*. *Journal of Physical Chemistry B*, 2014. **118**(49): p. 14017-14026.
291. Elsabahy, M. and K.L. Wooley, *Cytokines as biomarkers of nanoparticle immunotoxicity*. *Chem Soc Rev*, 2013. **42**(12): p. 5552-76.
292. Renner, L., et al., *Control of fibronectin displacement on polymer substrates to influence endothelial cell behaviour*. *Journal of Materials Science-Materials in Medicine*, 2004. **15**(4): p. 387-390.
293. Renner, L., et al., *Fibronectin displacement at polymer surfaces*. *Langmuir*, 2005. **21**(10): p. 4571-4577.
294. Turner, M.D., et al., *Cytokines and chemokines: At the crossroads of cell signalling and inflammatory disease*. *Biochim Biophys Acta*, 2014. **1843**(11): p. 2563-2582.
295. Ember, J.A., et al., *Induction of Interleukin-8 Synthesis from Monocytes by Human C5a Anaphylatoxin*. *American Journal of Pathology*, 1994. **144**(2): p. 393-403.
296. Kilgore, K.S., et al., *The membrane attack complex of complement induces interleukin-8 and monocyte chemoattractant protein-1 secretion from human umbilical vein endothelial cells*. *American Journal of Pathology*, 1996. **149**(3): p. 953-961.
297. Wang, L., et al., *Regulation of IL-8 production by complement-activated product, C5a, in vitro and in vivo during sepsis*. *Clin Immunol*, 2010. **137**(1): p. 157-65.
298. Moghimi, S.M., et al., *Material properties in complement activation*. *Adv Drug Deliv Rev*, 2011. **63**(12): p. 1000-7.

299. Dobrovolskaia, M.A. and S.E. McNeil, *Handbook of Immunological Properties of Engineered Nanomaterials*. 2013: World Scientific.
300. Thomas, S.N., et al., *Engineering complement activation on polypropylene sulfide vaccine nanoparticles*. *Biomaterials*, 2011. **32**(8): p. 2194-203.
301. Reddy, S.T., et al., *Exploiting lymphatic transport and complement activation in nanoparticle vaccines*. *Nature Biotechnology*, 2007. **25**(10): p. 1159-1164.
302. Salvador-Morales, C., et al., *Immunocompatibility properties of lipid-polymer hybrid nanoparticles with heterogeneous surface functional groups*. *Biomaterials*, 2009. **30**(12): p. 2231-40.
303. Ricklin, D., et al., *Complement: a key system for immune surveillance and homeostasis*. *Nat Immunol*, 2010. **11**(9): p. 785-97.
304. Wibroe, P.P. and S.M. Moghimi, *Complement Sensing of Nanoparticles and Nanomedicines*, in *Functional Nanoparticles for Bioanalysis, Nanomedicine, and Bioelectronic Devices Volume 2*. 2012, American Chemical Society. p. 365-382.
305. Thielens, N.M., et al., *Impact of the surface charge of polydiacetylene micelles on their interaction with human innate immune protein C1q and the complement system*. *Int J Pharm*, 2018. **536**(1): p. 434-439.
306. Sou, K. and E. Tsuchida, *Electrostatic interactions and complement activation on the surface of phospholipid vesicle containing acidic lipids: effect of the structure of acidic groups*. *Biochim Biophys Acta*, 2008. **1778**(4): p. 1035-41.
307. Owens, D.E. and N.A. Peppas, *Opsonization, biodistribution, and pharmacokinetics of polymeric nanoparticles*. *International Journal of Pharmaceutics*, 2006. **307**(1): p. 93-102.
308. Du, F., Y.G. Liu, and E.A. Scott, *Immunotheranostic Polymersomes Modularly Assembled from Tetrablock and Diblock Copolymers with Oxidation-Responsive Fluorescence*. *Cell Mol Bioeng*, 2017. **10**(5): p. 357-370.
309. Monopoli, M.P., et al., *Biomolecular coronas provide the biological identity of nanosized materials*. *Nature Nanotechnology*, 2012. **7**(12): p. 779-786.

310. Mirshafiee, V., et al., *The importance of selecting a proper biological milieu for protein corona analysis in vitro: Human plasma versus human serum*. Int J Biochem Cell Biol, 2016. **75**: p. 188-95.
311. Bosshart, H. and M. Heinzelmann, *THP-1 cells as a model for human monocytes*. Ann Transl Med, 2016. **4**(21): p. 438.
312. Lunov, O., et al., *Differential uptake of functionalized polystyrene nanoparticles by human macrophages and a monocytic cell line*. ACS Nano, 2011. **5**(3): p. 1657-69.
313. Kettler, K., et al., *Uptake of silver nanoparticles by monocytic THP-1 cells depends on particle size and presence of serum proteins*. J Nanopart Res, 2016. **18**(9): p. 286.
314. Ulery, B.D., et al., *Polymer chemistry influences monocytic uptake of polyanhydride nanospheres*. Pharm Res, 2009. **26**(3): p. 683-90.
315. Yang, H., et al., *Endosomal pH modulation by peptide-gold nanoparticle hybrids enables potent anti-inflammatory activity in phagocytic immune cells*. Biomaterials, 2016. **111**: p. 90-102.
316. Shiratori, H., et al., *THP-1 and human peripheral blood mononuclear cell-derived macrophages differ in their capacity to polarize in vitro*. Molecular Immunology, 2017. **88**: p. 58-68.
317. Tedesco, S., et al., *Convenience versus Biological Significance: Are PMA-Differentiated THP-1 Cells a Reliable Substitute for Blood-Derived Macrophages When Studying in Vitro Polarization?* Frontiers in Pharmacology, 2018. **9**.
318. Chinen, A.B., et al., *The Impact of Protein Corona Formation on the Macrophage Cellular Uptake and Biodistribution of Spherical Nucleic Acids*. Small, 2017. **13**(16).
319. Forrester, M.A., et al., *Similarities and differences in surface receptor expression by THP-1 monocytes and differentiated macrophages polarized using seven different conditioning regimens*. Cellular Immunology, 2018. **332**: p. 58-76.
320. Reddy, S.T., M.A. Swartz, and J.A. Hubbell, *Targeting dendritic cells with biomaterials: developing the next generation of vaccines*. Trends in Immunology, 2006. **27**(12): p. 573-579.

321. Gessner, A., et al., *Influence of surface charge density on protein adsorption on polymeric nanoparticles: analysis by two-dimensional electrophoresis*. European Journal of Pharmaceutics and Biopharmaceutics, 2002. **54**(2): p. 165-170.
322. Huang, H.Y. and J.F. Lovell, *Advanced Functional Nanomaterials for Theranostics*. Advanced Functional Materials, 2017. **27**(2).
323. Nandwana, V., et al., *High-Density Lipoprotein-like Magnetic Nanostructures (HDL-MNS): Theranostic Agents for Cardiovascular Disease*. Chemistry of Materials, 2017. **29**(5): p. 2276-2282.
324. Pitorre, M., et al., *Recent advances in nanocarrier-loaded gels: Which drug delivery technologies against which diseases?* J Control Release, 2017. **266**: p. 140-155.
325. Jiang, B., G.H. Zhang, and E.M. Brey, *Dual delivery of chlorhexidine and platelet-derived growth factor-BB for enhanced wound healing and infection control*. Acta Biomaterialia, 2013. **9**(2): p. 4976-4984.
326. Briquez, P.S., J.A. Hubbell, and M.M. Martino, *Extracellular Matrix-Inspired Growth Factor Delivery Systems for Skin Wound Healing*. Adv Wound Care (New Rochelle), 2015. **4**(8): p. 479-489.
327. Park, M.R., B.B. Seo, and S.C. Song, *Dual ionic interaction system based on polyelectrolyte complex and ionic, injectable, and thermosensitive hydrogel for sustained release of human growth hormone*. Biomaterials, 2013. **34**(4): p. 1327-36.
328. Gao, Y.H., et al., *Sustained Release of Recombinant Human Growth Hormone from Bioresorbable Poly(ester urea) Nanofibers*. Acs Macro Letters, 2017. **6**(8): p. 875-880.
329. Gajanayake, T., et al., *A single localized dose of enzyme-responsive hydrogel improves long-term survival of a vascularized composite allograft*. Science Translational Medicine, 2014. **6**(249).
330. Liu, J.M.H., et al., *Transforming growth factor-beta 1 delivery from microporous scaffolds decreases inflammation post-implant and enhances function of transplanted islets*. Biomaterials, 2016. **80**: p. 11-19.
331. Berthet, M., et al., *Nanoparticle-Based Dressing: The Future of Wound Treatment?: (Trends in Biotechnology 35, 770-784, 2017)*. Trends Biotechnol, 2017.

332. Fisher, J.D., A.P. Acharya, and S.R. Little, *Micro and nanoparticle drug delivery systems for preventing allotransplant rejection*. Clin Immunol, 2015. **160**(1): p. 24-35.
333. Irvine, D.J., et al., *Synthetic Nanoparticles for Vaccines and Immunotherapy*. Chemical Reviews, 2015. **115**(19): p. 11109-11146.
334. Benne, N., et al., *Orchestrating immune responses: How size, shape and rigidity affect the immunogenicity of particulate vaccines*. Journal of Controlled Release, 2016. **234**: p. 124-134.
335. Scott, E.A., et al., *Modular scaffolds assembled around living cells using poly(ethylene glycol) microspheres with macroporation via a non-cytotoxic porogen*. Acta Biomater, 2010. **6**(1): p. 29-38.
336. Segovia, N., et al., *Hydrogel Doped with Nanoparticles for Local Sustained Release of siRNA in Breast Cancer*. Advanced Healthcare Materials, 2015. **4**(2): p. 271-280.
337. Lei, Y.G., et al., *Hyaluronic acid and fibrin hydrogels with concentrated DNA/PEI polyplexes for local gene delivery*. Journal of Controlled Release, 2011. **153**(3): p. 255-261.
338. Rossi, F., et al., *Polymer hydrogel functionalized with biodegradable nanoparticles as composite system for controlled drug delivery*. Nanotechnology, 2015. **26**(1).
339. Rossi, F., et al., *Tunable hydrogel-Nanoparticles release system for sustained combination therapies in the spinal cord*. Colloids and Surfaces B-Biointerfaces, 2013. **108**: p. 169-177.
340. Anderson, J.M., A. Rodriguez, and D.T. Chang, *Foreign body reaction to biomaterials*. Semin Immunol, 2008. **20**(2): p. 86-100.
341. Zhang, L., et al., *Zwitterionic hydrogels implanted in mice resist the foreign-body reaction*. Nat Biotechnol, 2013. **31**(6): p. 553-6.
342. Ward, W.K., *A Review of the Foreign-body Response to Subcutaneously-implanted Devices: The Role of Macrophages and Cytokines in Biofouling and Fibrosis*. Journal of Diabetes Science and Technology, 2008. **2**(5): p. 768-777.
343. Bastiancich, C., et al., *Injectable nanomedicine hydrogel for local chemotherapy of glioblastoma after surgical resection*. J Control Release, 2017. **264**: p. 45-54.

344. Vegas, A.J., et al., *Combinatorial hydrogel library enables identification of materials that mitigate the foreign body response in primates*. Nat Biotechnol, 2016. **34**(3): p. 345-52.
345. Hayward, R.C. and D.J. Pochan, *Tailored Assemblies of Block Copolymers in Solution: It Is All about the Process*. Macromolecules, 2010. **43**(8): p. 3577-3584.
346. Wang, L.L., H.Y. Huang, and T.B. He, *Rayleigh Instability Induced Cylinder-to-Sphere Transition in Block Copolymer Micelles: Direct Visualization of the Kinetic Pathway*. ACS Macro Letters, 2014. **3**(5): p. 433-438.
347. Lund, R., et al., *Kinetic Pathway of the Cylinder-to-Sphere Transition in Block Copolymer Micelles Observed in Situ by Time-Resolved Neutron and Synchrotron Scattering*. ACS Macro Letters, 2013. **2**(12): p. 1082-1087.
348. Lund, R., et al., *Structural and thermodynamic aspects of the cylinder-to-sphere transition in amphiphilic diblock copolymer micelles*. Soft Matter, 2011. **7**(4): p. 1491-1500.
349. Loverde, S.M., et al., *Curvature-driven molecular demixing in the budding and breakup of mixed component worm-like micelles*. Soft Matter, 2010. **6**(7): p. 1419-1425.
350. Jain, S. and F.S. Bates, *Consequences of nonergodicity in aqueous binary PEO-PB micellar dispersions*. Macromolecules, 2004. **37**(4): p. 1511-1523.
351. Burke, S.E. and A. Eisenberg, *Kinetics and mechanisms of the sphere-to-rod and rod-to-sphere transitions in the ternary system PS310-b-PAA(52)/dioxane/water*. Langmuir, 2001. **17**(21): p. 6705-6714.
352. Chen, Y.Y. and K.R. Shull, *High-Toughness Polycation Cross-Linked Triblock Copolymer Hydrogels*. Macromolecules, 2017. **50**(9): p. 3637-3646.
353. Henderson, K.J. and K.R. Shull, *Effects of Solvent Composition on the Assembly and Relaxation of Triblock Copolymer-Based Polyelectrolyte Gels*. Macromolecules, 2012. **45**(3): p. 1631-1635.
354. Henderson, K.J., et al., *Ionically Cross-Linked Triblock Copolymer Hydrogels with High Strength*. Macromolecules, 2010. **43**(14): p. 6193-6201.
355. Rikken, R.S., et al., *Shaping polymersomes into predictable morphologies via out-of-equilibrium self-assembly*. Nat Commun, 2016. **7**: p. 12606.

356. Salva, R., et al., *Polymersome shape transformation at the nanoscale*. ACS Nano, 2013. **7**(10): p. 9298-311.
357. Wang, C., et al., *High-resolution electron microscopy and spectroscopy of ferritin in biocompatible graphene liquid cells and graphene sandwiches*. Adv Mater, 2014. **26**(21): p. 3410-4.
358. Yu, Y.R., et al., *A Protocol for the Comprehensive Flow Cytometric Analysis of Immune Cells in Normal and Inflamed Murine Non-Lymphoid Tissues*. PLoS One, 2016. **11**(3): p. e0150606.
359. Kotecha, N., P.O. Krutzik, and J.M. Irish, *Web-based analysis and publication of flow cytometry experiments*. Curr Protoc Cytom, 2010. **Chapter 10**: p. Unit10 17.
360. Draper, E.R., et al., *Opening a Can of Worm(-like Micelle)s: The Effect of Temperature of Solutions of Functionalized Dipeptides*. Angewandte Chemie-International Edition, 2017. **56**(35): p. 10467-10470.
361. Nair, R.R., et al., *Graphene as a transparent conductive support for studying biological molecules by transmission electron microscopy*. Applied Physics Letters, 2010. **97**(15).
362. Kim, Y.D., et al., *Bright visible light emission from graphene*. Nature Nanotechnology, 2015. **10**(8): p. 676-681.
363. Zhulina, E.B., et al., *Diblock copolymer micelles in a dilute solution*. Macromolecules, 2005. **38**(12): p. 5330-5351.
364. Semenov, A.N., *Contribution to the Theory of Microphase Layering in Block-Copolymer Melts*. Zhurnal Eksperimentalnoi I Teoreticheskoi Fiziki, 1985. **88**(4): p. 1242-1256.
365. Carvajal, D., et al., *Mechanics of pendant drops and axisymmetric membranes*. Soft Matter, 2011. **7**(22): p. 10508-10519.
366. Brubaker, C.E., et al., *Crystalline Oligo(ethylene sulfide) Domains Define Highly Stable Supramolecular Block Copolymer Assemblies*. Acs Nano, 2015. **9**(7): p. 6872-6881.
367. Verber, R., A. Blanazs, and S.P. Armes, *Rheological studies of thermo-responsive diblock copolymer worm gels*. Soft Matter, 2012. **8**(38): p. 9915-9922.
368. Won, Y.Y., H.T. Davis, and F.S. Bates, *Giant wormlike rubber micelles*. Science, 1999. **283**(5404): p. 960-3.

369. Sterling, T. and J.J. Irwin, *ZINC 15--Ligand Discovery for Everyone*. J Chem Inf Model, 2015. **55**(11): p. 2324-37.
370. Pinol, R., et al., *Self-assembly of PEG-b-Liquid crystal polymer: The role of smectic order in the formation of nanofibers*. Macromolecules, 2007. **40**(16): p. 5625-5627.
371. Oussoren, C., et al., *Lymphatic uptake and biodistribution of liposomes after subcutaneous injection .2. Influence of liposomal size, lipid composition and lipid dose*. Biochimica Et Biophysica Acta-Biomembranes, 1997. **1328**(2): p. 261-272.
372. Schmitt, F.J., et al., *Reactive oxygen species: re-evaluation of generation, monitoring and role in stress-signaling in phototrophic organisms*. Biochim Biophys Acta, 2014. **1837**(6): p. 835-48.
373. Winterbourn, C.C., *Reconciling the chemistry and biology of reactive oxygen species*. Nat Chem Biol, 2008. **4**(5): p. 278-86.
374. de Gracia Lux, C., et al., *Biocompatible polymeric nanoparticles degrade and release cargo in response to biologically relevant levels of hydrogen peroxide*. J Am Chem Soc, 2012. **134**(38): p. 15758-64.
375. Shin, J.S., et al., *Surface expression of MHC class II in dendritic cells is controlled by regulated ubiquitination*. Nature, 2006. **444**(7115): p. 115-118.
376. Wu, X., et al., *Synergistic therapeutic effects of Schiff's base cross-linked injectable hydrogels for local co-delivery of metformin and 5-fluorouracil in a mouse colon carcinoma model*. Biomaterials, 2016. **75**: p. 148-162.
377. Belowich, M.E. and J.F. Stoddart, *Dynamic imine chemistry*. Chemical Society Reviews, 2012. **41**(6): p. 2003-2024.
378. Deng, Y., et al., *Injectable in situ cross-linking chitosan-hyaluronic acid based hydrogels for abdominal tissue regeneration*. Sci Rep, 2017. **7**(1): p. 2699.
379. Banquy, X., et al., *Effect of mechanical properties of hydrogel nanoparticles on macrophage cell uptake*. Soft Matter, 2009. **5**(20): p. 3984-3991.
380. Guo, P., et al., *Nanoparticle elasticity directs tumor uptake*. Nature Communications, 2018. **9**.

381. Laurent, A., et al., *Echographic measurement of skin thickness in adults by high frequency ultrasound to assess the appropriate microneedle length for intradermal delivery of vaccines*. Vaccine, 2007. **25**(34): p. 6423-30.
382. Ruggiero, E., et al., *Upconverting nanoparticles for the near infrared photoactivation of transition metal complexes: new opportunities and challenges in medicinal inorganic photochemistry*. Dalton Trans, 2016. **45**(33): p. 13012-20.
383. Li, L., et al., *GSH-mediated photoactivity of pheophorbide a-conjugated heparin/gold nanoparticle for photodynamic therapy*. J Control Release, 2013. **171**(2): p. 241-50.
384. Xu, H.Y., et al., *Nanoparticles in sonodynamic therapy: state of the art review*. Rsc Advances, 2016. **6**(56): p. 50697-50705.
385. Nomikou, N., et al., *Microbubble-sonosensitiser conjugates as therapeutics in sonodynamic therapy*. Chemical Communications, 2012. **48**(67): p. 8332-8334.
386. McEwan, C., et al., *Comparing the efficacy of photodynamic and sonodynamic therapy in non-melanoma and melanoma skin cancer*. Bioorganic & Medicinal Chemistry, 2016. **24**(13): p. 3023-3028.
387. Pang, X., et al., *Natural products in the discovery of novel sonosensitizers*. Pharmacology & Therapeutics, 2016. **162**: p. 144-151.
388. Blander, J.M. and R. Medzhitov, *Toll-dependent selection of microbial antigens for presentation by dendritic cells*. Nature, 2006. **440**(7085): p. 808-812.
389. Shang, S.B., et al., *Induction of Mycobacterium Tuberculosis Lipid-Specific T Cell Responses by Pulmonary Delivery of Mycolic Acid-Loaded Polymeric Micellar Nanocarriers*. Frontiers in Immunology, 2018. **9**.
390. Kramer, K., et al., *Intracellular Cleavable CpG Oligodeoxynucleotide-Antigen Conjugate Enhances Anti-tumor Immunity*. Molecular Therapy, 2017. **25**(1): p. 62-70.
391. Zhang, H., et al., *The Improved Delivery to Breast Cancer Based on a Novel Nanocarrier Modified with High-Affinity Peptides Discovered by Phage Display*. Adv Healthc Mater, 2018. **7**(20): p. e1800269.

392. Han, L., C. Tang, and C. Yin, *pH-Responsive Core-Shell Structured Nanoparticles for Triple-Stage Targeted Delivery of Doxorubicin to Tumors*. ACS Appl Mater Interfaces, 2016. **8**(36): p. 23498-508.
393. Prusty, D.K., et al., *Supramolecular aptamer nano-constructs for receptor-mediated targeting and light-triggered release of chemotherapeutics into cancer cells*. Nature Communications, 2018. **9**.
394. Lewis, J.S., et al., *Microparticle surface modifications targeting dendritic cells for non-activating applications*. Biomaterials, 2012. **33**(29): p. 7221-32.
395. Rodriguez, P.L., et al., *Minimal "Self" Peptides That Inhibit Phagocytic Clearance and Enhance Delivery of Nanoparticles*. Science, 2013. **339**(6122): p. 971-975.

APPENDIX A

Methods Development for PC Analysis

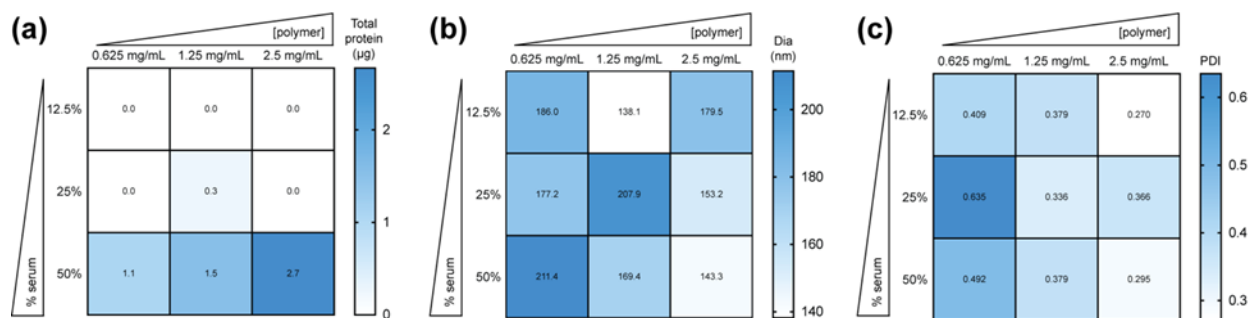


Figure A-1. Determination of the protein:polymer ratio for use in the protein adsorption studies.

MeO-PS were incubated with heat-inactivated fetal bovine serum (FBS) for 2 hours under the specified serum and nanocarrier polymer concentrations. The concentration of 100% FBS is $\sim 20 \text{ mg mL}^{-1}$ (data not shown). Nanocarrier-protein complexes were isolated following three rounds of centrifugation ($100,000 \times g$ for 45 min at 4°C) and PBS washing. (a) Total protein recovered per 200 μl . Protein concentration was determined using the A660 assay. (b) Diameter and (c) PDI of recovered nanocarrier-protein complexes determined by DLS.

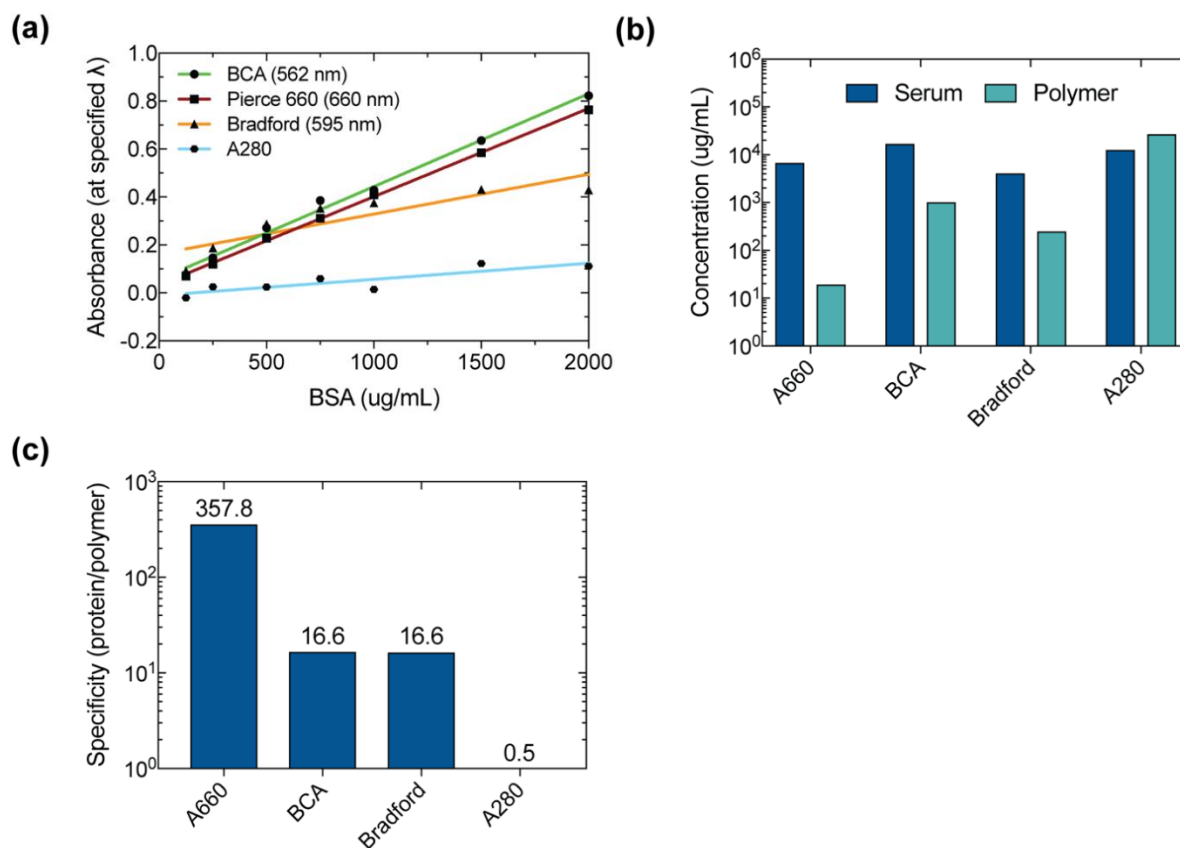


Figure A-2. Identification of a protein concentration assay with minimal interference by PEG-*b*-PPS polymer. (a) BSA calibration curves for each assay. A660: Pierce 660 nm reagent ($y = 3.7e-4x + 3.4e-2$; $r^2 = 0.99$; $F = 5292$, $p < 0.0001$); BCA: Bicinchoninic acid assay (562 nm; $y = 3.9e-4x + 5.6e-2$; $r^2 = 0.76$; $F=666.7$, $p < 0.0001$); Bradford assay (595 nm; $y = 1.7e-4x + 1.6e-1$; $r^2 = 0.81$; $F=17.8$, $p = 0.0084$); A280: concentration determination by absorbance of 280 nm light ($y = 6.71e-5x - 1.0e-2$; $r^2 = 0.76$; $F =15.88$, $p =0.0107$). (b) Serum and Polymer are Fetal Bovine Serum (FBS; 14.5 mg mL^{-1}) and PEG-*b*-PPS MeO-PPSs BCP (5 mg mL^{-1}), respectively. (c) Polymer interference assessed through the ratio of protein/polymer for the protein concentrations determined in (b).

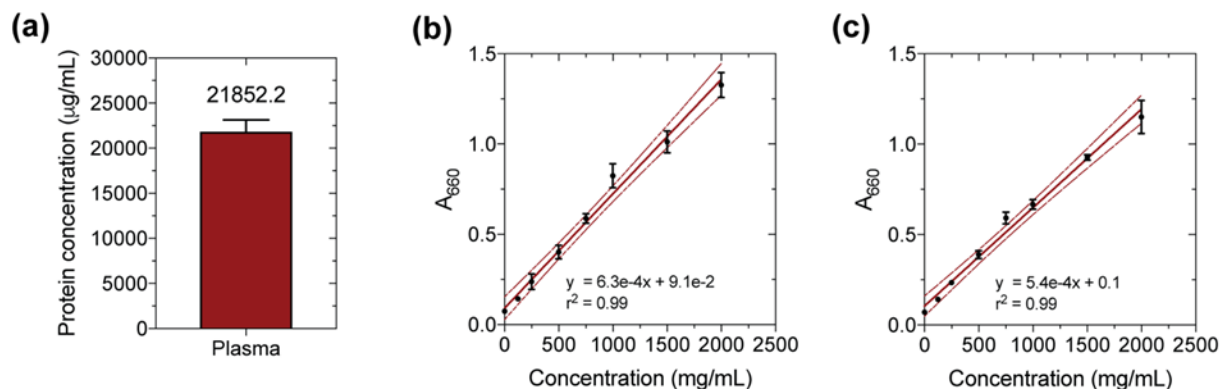


Figure A-3. Human plasma protein concentration and calibration curves used for the A660 assay.

(a) Protein concentration determined for human plasma samples used in this study. The mean protein concentration is displayed above the bar ($n = 6$). BSA calibration curves for quantifying protein concentrations of nanocarrier samples incubated with human plasma for (b) 2 hours at 37°C , 220 rpm ($F = 612.4$, $p < 0.0001$, $n = 3$) and (c) 24 hours at 37°C , 220 rpm ($F = 575.5$, $p < 0.0001$, $n = 3$). Replicates (black circles) display the mean value. Error bars represent the s.d.. The regression equation and the coefficient of determination (r^2) are displayed within each plot. The linear regression models (solid red lines) and the 95% confidence bands (red dashed lines) are also plotted.

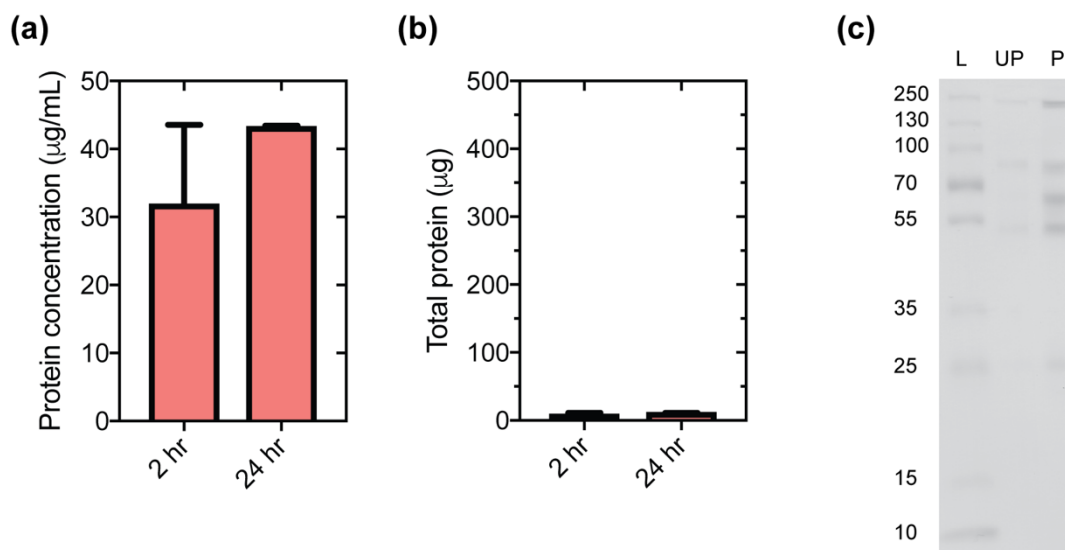


Figure A-4. Ultracentrifugation of plasma proteins without nanocarriers. (a) A660 determination of protein concentration of ultracentrifuged human plasma. (b) Total isolated protein (μg) in ultracentrifuged plasma at the 2-hour and 24-hour timepoints. The total protein was calculated for a 250 μl volume. For (a) and (b), error bars represent the s.e.m. determined in three replicates. (c) SDS-PAGE gel of ultracentrifuged plasma protein versus input plasma. The gel shows the MW ladder (L; Lane 1), ultracentrifuged plasma after incubation at 37°C, 220 rpm for 24 hours (UP; Lane 2), and the input (uncentrifuged) human plasma (P; Lane 3). Ultracentrifugation, SDS-PAGE, and silver staining was performed as described in Materials and Methods.

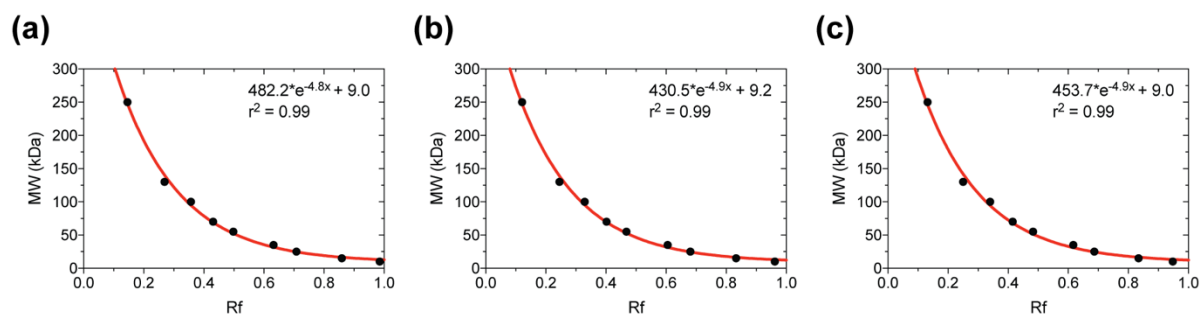


Figure A-5. Representative calibration curves used to determine the molecular weight of stained protein species. To determine the MW of unknown species, non-linear regression models were fit using the R_f values of each protein of known molecular weight in the ladder. The fit models and r^2 values are shown for a (a) MC, (b) FM, and (c) PS gel. This process was performed for all gels individually.